



HAL
open science

3D wind vectors measurement with remotely piloted aircraft system for aerosol-cloud interaction study

Radiance Calmer

► **To cite this version:**

Radiance Calmer. 3D wind vectors measurement with remotely piloted aircraft system for aerosol-cloud interaction study. Earth Sciences. Institut National Polytechnique de Toulouse - INPT, 2018. English. NNT : 2018INPT0021 . tel-04199476

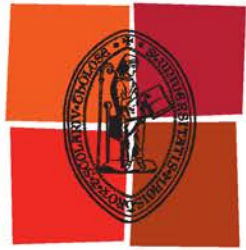
HAL Id: tel-04199476

<https://theses.hal.science/tel-04199476v1>

Submitted on 7 Sep 2023

HAL is a multi-disciplinary open access archive for the deposit and dissemination of scientific research documents, whether they are published or not. The documents may come from teaching and research institutions in France or abroad, or from public or private research centers.

L'archive ouverte pluridisciplinaire **HAL**, est destinée au dépôt et à la diffusion de documents scientifiques de niveau recherche, publiés ou non, émanant des établissements d'enseignement et de recherche français ou étrangers, des laboratoires publics ou privés.



Université
de Toulouse

THÈSE

En vue de l'obtention du

DOCTORAT DE L'UNIVERSITÉ DE TOULOUSE

Délivré par :

Institut National Polytechnique de Toulouse (INP Toulouse)

Discipline ou spécialité :

Océan, atmosphère, climat

Présentée et soutenue par :

Mme RADIANCE CALMER

le mardi 20 mars 2018

Titre :

Mesure du vecteur tridimensionnel du vent à partir de drones pour l'étude
des interactions aérosol-nuage

Ecole doctorale :

Sciences de l'Univers de l'Environnement et de l'Espace (SDUEE)

Unité de recherche :

Groupe d'étude de l'Atmosphère Météorologique (CNRM-GAME)

Directeur(s) de Thèse :

M. GREGORY ROBERTS

Rapporteurs :

M. BRUNO NEININGER, UNIVERSITE DE ZURICH

Mme ANDREA FLOSSMANN, UNIVERSITE CLERMONT-FERRAND 1

M. WOLFGANG JUNKERMANN, KARLSRUHE INSTITUTE OF TECHNOLOGY

Membre(s) du jury :

Mme CELINE MARI-BONTOUR, CNRS TOULOUSE, Président

M. GREGORY ROBERTS, METEO FRANCE TOULOUSE, Membre

Mme MARIE LOTHON, CNRS TOULOUSE, Membre

Abstract

Mesures du vecteur tridimensionnel du vent à partir de drones pour l'étude des interactions aérosol-nuage

by Radiance CALMER

The European project BACCHUS (impact of Biogenic versus Anthropogenic emissions on Clouds and Climate: towards a Holistic UnderStanding) focuses on aerosol-cloud interactions. Vertical wind velocities near cloud base, and cloud condensation nuclei (CCN) spectra, are the two most important input parameters for aerosol-cloud parcel models in determining cloud microphysical and optical properties. Therefore, the present study focuses on the instrumental development for vertical wind measurements to improve aerosol-cloud closure studies. Enhancements in Remotely Piloted Aircraft Systems (RPAS) have demonstrated their potential as tools in atmospheric research to study the boundary layer dynamics, aerosols and clouds. However, as a relatively new tool for atmospheric research, RPA require instrumental development and validation to address current observational needs. A 5-hole probe is implemented on a remotely piloted aircraft (RPA) platform, with an inertial navigation system (INS) to obtain atmospheric wind vectors. The 5-hole probe is first calibrated in a wind tunnel (at Météo-France, Toulouse, France), and an error analysis is conducted on the vertical wind measurement. Atmospheric wind vectors obtained from RPA flights are compared with wind vectors determined from sonic anemometers located at different levels on a 60 m meteorological mast (Centre de Recherches Atmosphériques, Lannemezan, France). Good agreements between vertical wind velocity probability density functions are obtained. The power spectral density of the three wind components follow the $-5/3$ line for the established regime of turbulence (Kolmogorov law). Turbulent kinetic energy (TKE) values calculated from the RPA are somewhat higher than TKE compared to the sonic anemometer; however, the results agree with those reported in other experiments that compare RPA platforms and sonic anemometers (Lampert et al. (2016), Båserud et al. (2016)). As the RPA equipped with a 5-hole probe (defined as the “wind-RPA”) is developed for aerosol-cloud observations, updraft velocities near cloud base are compared with cloud radar data during a BACCHUS field campaign (Mace Head Research Station, Ireland). Three case studies illustrate the similarity of in-cloud updrafts measured between the wind-RPA and the cloud radar. A good agreement between vertical velocities of both instruments over a range of different meteorological conditions is found. Updraft velocity measurements from the wind-RPA are implemented in the aerosol-cloud parcel model to conduct a closure study for stratocumulus case with convection sampled during a BACCHUS field campaign in Cyprus. Aerosol size distributions and CCN were measured at a ground-site, which served as input to the aerosol-cloud parcel model along with the updraft velocities at cloud base measured by the RPA. In addition, the RPA conducted a vertical profile through the cloud layer and measured the shortwave transmission of solar irradiance during the ascent. The aerosol-cloud parcel model also shows that entrainment has a greater impact on cloud optical properties than variability in updraft velocity and aerosol particle concentration. Results of the case study for the Cyprus field experiment are consistent with results for similar closure studies conducted during the Mace Head field campaign (Sanchez et al., 2017), and reinforce the significance of including entrainment processes in cloud models to reduce uncertainties in aerosol-cloud interactions.

Résumé en Français

Le projet européen BACCHUS (impact of Biogenic versus Anthropogenic emissions on Clouds and Climate: towards a Holistic UnderStanding) porte sur les interactions aérosols-nuages. Les vitesses du vent vertical à proximité de la base des nuages et les spectres des noyaux de condensation des nuages (CCN) sont deux paramètres d'entrée importants pour les modèles de parcelle aérosol-nuage dans la détermination des propriétés microphysiques et optiques des nuages. Par conséquent, la présente étude se concentre sur le développement et la mise en œuvre de mesures de vent atmosphérique afin d'améliorer les études de fermeture aérosol-nuage. Les systèmes d'aéronefs pilotés à distance (RPAS) ont démontré leur potentiel en tant qu'outils pour la recherche atmosphérique dans l'étude de la couche limite, des aérosols et des nuages. Cependant, en tant qu'outil récent en recherche atmosphérique, le RPAS nécessite un développement instrumental pour répondre aux besoins d'observation actuels. Une sonde à 5 voies est développée pour une plateforme d'aéronef piloté à distance (RPA), assistée par un système de navigation inertiel (INS) pour obtenir les trois vecteurs du vent atmosphérique. La sonde à 5 voies est d'abord calibrée dans une soufflerie (à Météo-France, Toulouse, France), et une analyse d'erreur est effectuée sur la mesure du vent vertical. Les vecteurs de vent obtenus à partir de vols de RPA sont comparés à des vecteurs de vent déterminés à partir d'anémomètres soniques situés à différents niveaux d'un mât météorologique de 60 m (Centre de Recherches Atmosphériques, Lannemezan, France). Une bonne concordance entre les fonctions de densité de probabilité de la vitesse verticale du vent est obtenue. La densité spectrale de puissance des trois composantes du vent suit la ligne $-5/3$ en régime de turbulence établie (loi de Kolmogorov). Les valeurs d'énergie cinétique turbulente (TKE), calculées à partir du RPA, sont légèrement supérieures à celles de l'anémomètre sonique. Cependant, les résultats concordent avec ceux rapportés dans d'autres expériences comparant les plateformes RPAs à des anémomètres soniques (Lampert et al. (2016), Båserud et al. (2016)). Comme le RPA équipé d'une sonde à 5 voies (définie comme le "wind-RPA") est développé pour les observations aérosol-nuage, les vitesses verticales (updraft) près de la base des nuages sont comparées avec les données d'un radar de nuage au cours d'une campagne de mesures BACCHUS (Mace Head Research Station, Irlande). Trois études de cas illustrent la similitude des vitesses verticales dans les nuages mesurées par le wind-RPA et le radar de nuage. Une bonne concordance entre les vitesses verticales des deux instruments à travers différentes conditions météorologiques est établie. Les mesures de vitesse verticale du wind-RPA sont implémentées dans le modèle de parcelle aérosol-nuage pour mener une étude de fermeture (campagne de mesures BACCHUS à Chypre). Les distributions de taille des aérosols et les CCN mesurés par un site au sol servent de paramètres d'entrée au modèle avec les vitesses verticales mesurées par le RPA. Le modèle de parcelle aérosol-nuage montre que l'entraînement dans les nuages a un impact plus important sur les propriétés optiques des nuages que la variabilité de la vitesse verticale et que la concentration en aérosols. Les résultats du cas d'étude de Chypre sont cohérents avec les résultats des études de fermeture similaires de la campagne de mesures à Mace Head (Sanchez et al., 2017) et renforcent l'importance d'inclure les processus d'entraînement dans les modèles de nuages pour réduire les incertitudes liées aux interactions aérosol-nuage.

Acknowledgements

What would be the most impressive memory of my PhD years? When I crossed the channel between our operation field and the Mace Head Research Station, in Ireland, at high tide with water up to my chest and a toolbox above my head? Or when we tried to fix a Paparazzi autopilot electronics board until 1 a.m. after one of our RPA decided to go for a swim? It might also have been the miraculous recovery of a RPA in Cyprus when the power board fried and the RPA landed, intact, on a moon field after an 800 m fall. . . It could also have been when I received my Fulbright scholarship, which opened to me its international network and funded my stay at Scripps Institution of Oceanography, in California. None of these memories would exist without the energy, the visionary ideas and the support of my PhD adviser, Greg Roberts. I warmly thank him for his teaching, his patience and his encouragement all along my PhD. He will remain for me a model of achievement in science, research and life.

My thanks to Kevin Sanchez, who was PhD student at Scripps Institution of Oceanography and visited Météo-France during his thesis. His steadiness of mood, his humor, and his skills were precious during the BACCHUS field campaign in Ireland. His help during my stay in San Diego at Scripps made my daily life so much easier. And thanks to him, I met friends I will keep for a long time. I hope I was able to cheer him up a little bit when time was hard during his thesis, too.

I deeply thank the MNPCA group, Grégoire Cayez, Frédéric Burnet, Thierry Bourriane, Fabrice Julien, Brigitte Gaillard, Jean-Michel Etcheberry, Cyrielle Denjean, Pauline Martinet. It is exceptional to conduct a PhD thesis in France on instrumental development, and their support made it possible. Thanks to Sébastien Barrau and Laurent Gustave for their patience and their administrative support during the preparation of the field campaigns and the conferences.

My sincere thanks to the BACCHUS committee to have led such a global project at the European level and introduced me to the international community of aerosol scientists. My gratitude to the leaders and the dynamic groups who conducted the BACCHUS field campaigns in Ireland at Mace Head and in Cyprus. These field experiences were life-changing for me. I realized that I could become both scientist and engineer, and work in the field, facing Nature in its most beautiful and terrific aspects.

I thank Marie Lothon, Solène Derrien, and all the people who work at the CRA in Lannemezan for their scientific and technique advises, their welcome during our field tests with the RPAs. Lannemezan is a unique place in Europe to fly RPA up to 2280 m.asl, and we are lucky to be able to visit this site so often.

I am profoundly grateful to the ENAC team, and particularly Murat Bronz and Gauthier Hattenberger. They taught me how to use the Paparazzi autopilot, and guided my first steps as a ground-station pilot. The tenacity of the ENAC team to develop an open-source autopilot, whatever

the cost, the difficulties, demonstrated for me the bases of research: sharing knowledge. Yet, I'm sure they will always remember me as my blood imprinted the floor of their office, memory of the common meeting between RPA propellers and a finger, mine in this case. . .

Another turning-point in my thesis was to receive a Fulbright grant to spend six months studying at Scripps Institution of Oceanography, San Diego, California. French people may have never heard about this program, but I will always remember the reaction of a group of American students met in a youth hostel in Philadelphia during a snowy night when I told them I was a Fulbright grantee. Surprise, admiration, respect, dream. I thank la Commission Franco-Américaine for trusting me, and for making a dream become real.

I would like to thank my thesis committee for their insightful comments, but also for their challenging questions, which incited me to widen my research to atmospheric modelling and research with manned aircraft.

I would like to thank my family and my friends for their unfailing and steadfast support throughout my PhD years, and for making fun of me when I was overwhelmed just to remind me that Love is essential.

Contents

Abstract	iv
Acknowledgements	vii
Contents	ix
List of Figures	xiii
List of Tables	xv
List of Abbreviations	xvii
1 Introduction	1
1.1 Introduction en Français	1
1.1.1 Les interactions aerosol-nuage	1
1.1.2 Les effets du forçage radiatif effectif dû aux interactions aérosol-nuage	2
1.1.3 Les objectifs de la thèse	2
1.2 English introduction	6
1.2.1 Aerosol-cloud interactions	6
1.2.2 Effective radiative forcing from aerosol-cloud interactions	7
1.2.3 Thesis objectives	7
2 Instrument development	13
2.1 Historical background of wind measurements from airborne platforms	13
2.2 Wind measurements with remotely piloted aircraft system (RPAS)	15
2.2.1 3D wind vector equations	15
The air velocity from the aerodynamic coordinate system F_a to the RPA coordinate system F_b	16
From the RPA coordinate system F_b to the Earth's coordinate system F_0	16
Angular acceleration in the Earth's coordinate system	17
Wind vectors in the Earth's coordinate system	17
Assumptions to simplify wind vector equations	18
2.2.2 5-hole probe	19
2.2.3 Inertial navigation system (INS)	19
2.3 Calibration in wind tunnel	20
2.3.1 Wind tunnel installation	21

2.3.2	Calibration of 5-hole probe	21
	Determination of angle of attack and angle of sideslip of the 5-hole probe	22
	Determination of airspeed of the 5-hole probe	24
2.3.3	Experimental error analysis on vertical wind velocity	25
2.3.4	Gaussian error propagation on vertical wind speed	26
2.4	Wind-RPAS platform	27
2.4.1	Skywalker X6 airframe	27
2.4.2	The open-source autopilot Paparazzi	27
2.4.3	Overview of flight operations	28
2.4.4	Instrumentation challenges	28
2.5	The BACCHUS field campaigns challenges	29
2.6	Conclusions and perspectives	30
3	Validation of RPA wind measurements in the atmospheric boundary layer	31
3.1	Centre de Recherches Atmospheriques de Lannemezan — Validation of RPA wind measurements	33
3.2	Vertical wind velocity distributions	34
3.3	Power spectral density functions	37
3.4	Turbulent kinetic energy (TKE)	41
3.5	Conclusions and perspectives	45
4	Comparison of vertical wind velocities from RPA and cloud radar	47
4.1	Vertical wind measurement for aerosol-cloud closure study	47
4.2	Mace Head field campaign, Ireland	48
4.3	Stratocumulus deck with light precipitation (Flight 26: 2015/08/11)	49
4.4	Cloud fields within changing meteorology (Flight 38: 2015/08/21)	51
4.5	Fair weather cumulus clouds (Flight 30: 2015/08/15)	53
4.6	Conclusion and perspectives	54
5	Closure study, Cyprus field experiment	57
5.1	From updraft velocity measurements to aerosol-cloud closure study	57
5.2	Overview of the BACCHUS field campaign in Cyprus	59
	5.2.1 Ground-based measurements	59
	5.2.2 RPAS Operations	60
	5.2.3 Case study : stratocumulus layer	60
5.3	Aerosol-Cloud Parcel Model	61
	5.3.1 Description of the Aerosol-Cloud Parcel Model (ACPM)	62
	5.3.2 Model inputs from ground measurements and RPAs	64
5.4	Ground-based measurements	65
	5.4.1 Particle size distribution	65
	5.4.2 Aerosol-CCN closure	67
5.5	RPA measurements and in-cloud extinction	67

5.5.1	RPA vertical profiles	67
5.5.2	Updraft velocity measurements and in-cloud extinction	69
5.6	Aerosol-cloud closure study	72
5.6.1	Cloud droplet number concentration	72
5.6.2	Cloud optical properties	75
5.6.3	Sensitivity study on cloud optical properties	77
5.7	Concluding remarks	77
6	Conclusions	79
6.1	Conclusion	79
6.2	Conclusion en Français	81
A	Vertical Wind Velocity Measurements using a 5-hole Probe with Remotely Piloted Aircraft to Study Aerosol-Cloud Interactions, AMT journal	85
B	Top-down and bottom-up aerosol–cloud closure: towards understanding sources of uncertainty in deriving cloud shortwave radiative flux, ACP journal	103
	Bibliography	123

List of Figures

1.1	Aerosol-radiation and aerosol-cloud interactions	7
2.1	Aerodynamic frame F_a relative to the RPA frame F_b	17
2.2	RPA frame F_b relative to the Earth's coordinate frame F_0	18
2.3	Schematic of the 5-hole probe	20
2.4	Wind tunnel installation	20
2.5	Calibration of the pressure sensors	21
2.6	Calibration coefficients C_α and C_β of the 5-hole probe	22
2.7	Linearity domain of the 5-hole probe calibration coefficients	23
2.8	Dynamic C_q and static C_s pressure coefficients	24
2.9	Standard deviation of w function of rate of change	25
2.10	Paparazzi ground station	28
2.11	Flight plan patterns	29
3.1	Flight plan, CRA Lannemezan	35
3.2	Vertical wind velocity distributions, comparison between sonic anemometers and wind-RPA	36
3.2	Power spectral density function, comparison between sonic anemometer and wind-RPAS	39
3.3	Investigation of the origin of difference in energy level in the PSDs	40
3.4	Variances on u, v, w and TKE for the mast and the RPA	42
3.5	Comparison of the horizontal wind variances from the mast	43
3.6	Variances on u, v, w and TKE for the mast and the RPA with the isotropy assumption	44
3.7	Comparison of TKE between sonic anemometers and RPA	45
4.1	Time series of vertical wind velocity for a stratocumulus deck with light precipitation (Flight 26)	50
4.2	Comparison of vertical wind velocity distribution between RPA and cloud radar (Flight 26)	51
4.3	Coastal map and flight tracks (Flight 38)	52
4.4	Time series of vertical wind velocity (Flight 38)	53
4.5	Comparison of vertical wind velocity distribution between RPA and cloud radar (Flight 38)	54
4.6	Coastal map and flight tracks (Flight 30)	55
4.7	Time series of vertical wind velocity (Flight 30)	56

4.8	Comparison of vertical wind velocity distribution between RPA and cloud radar (Flight 30)	56
5.1	Cyprus Atmospheric Observatory	59
5.2	Cyprus case study, flight plan	60
5.3	Pictures of clouds, Cyprus Flight 67	61
5.4	Hysplit model for Cyprus case study	63
5.5	Contour plot showing time series of SMPS, 1 April 2015	65
5.6	Particle size ditribution	66
5.7	Aerosol chemical speciation monitor (ACSM) distributions	68
5.8	Profiles of PTU, Cyprus flight 67	69
5.9	Skew-T lop-P diagram, Cyprus Flight 67	69
5.10	Profiles of aerosol number concentration	70
5.11	Vertical wind distribution, Cyprus Flight 67	71
5.12	Solar irradiance profile, Cyprus Flight 67	71
5.13	Simulated CDNC and r_e for aerosol-cloud parcel model, and variability of cloud droplet number with small variations of liquid water content	73
5.14	Cloud droplet spectra in the adiabatic and entrainment cases	74
5.15	Optical cloud profile	76

List of Tables

2.1	Uncertainty associated with vertical wind velocity w	27
3.1	Description of flights conducted at P2OA, Lannemezan, France.	34
3.2	Intersection numbers for comparison of PDFs for five flights conducted at P2OA, Lannemezan, France.	35
4.1	Description of BACCHUS case study flights, Mace Head, Ireland.	49
4.2	BACCHUS field campaign at Mace Head, Ireland. The intersection number compares vertical wind velocity distributions between RPA and cloud radar.	50
5.1	Profile history from cloud base (1000 m.asl) to the ceiling (2100 m.asl) and down near cloud base again (950 m.asl) during Flight 67	62
5.2	Particle number distribution from SMPC and OPC during the 3-hour period including Flight 67	66

List of Abbreviations

5HP	5-Hole Probe
ABL	Atmospheric Boundary Layer
ACI	Aerosol-Cloud Interactions
ACPM	Aerosol-Cloud Parcel Model
ACSM	Aerosol Chemical Speciation Monitor
ACTOS	Airborne Cloud Turbulence Observation System
ALADINA	Application of Light-weight Aircraft for Detecting IN situ Aerosol
AUAV	Autonomous Unmanned Aerial Vehicles
BACCHUS	impact of Biogenic versus Anthropogenic emissions on Clouds and Climate: towards a Holistic UnderStandig
BAT-probe	“Best Air Turbulence” probe
BLLAST	Boundary Layer Afternoon and Sunset Turbulence
CAO	Cyprus Atmospheric Observatory
CARRIBA	Cloud, Aerosol, Radiation and tuRbulence in the trade wInd regime over BARbados
CCN	Cloud Condensation Nuclei
CDND	Cloud Droplet Number Concentration
CNRM	Centre National de Recherches Météorologiques
CPC	Condensation Particles Counter
CRA	Centre de Recherches Atmosphériques
CRISTAL-FACE	Cirrus Regional Study of Tropical Anvils and Cirrus Layers – Florida Area Cirrus Experiment
dGPS	Differential Global Positioning System
ENAC	Ecole National de l’Aviation Civile
ERF	Effective Radiative Forcing
ERF_{aci}	Aerosol-Cloud Interaction Effective Radiative Forcing
EUCAARI	European Aerosol Cloud Climate and Air Quality Interactions project
GCM	Global Climate Model
GCS	Ground Control Station
GIEC	Groupe d’experts Intergouvernemental sur l’Évolution du Climat
GPS	Global Positing System
ICARTT	Atmospheric Research on Transport and Transformation
IMU	Inertial Measurement Unit
INS	Inertial Navigation System

IPCC	International Panel for Climate Change
LLJ	Low Level Jet
M²AV	Meteorological Mini unmanned Aerial Vehicle
MAC	Maldives AUAV Campaign
MASC	Multi-purpose Airborne Sensor Carrier
MEMS	MicroElectroMechanical System
NCAR	National Center for Atmospheric Research
OPC	Optical Particle Counter
P2OA	Pyrenean Platform of Observation of the Atmosphere
PDF	Probability Density Function
PSD	Power Spectral Density
RPA	Remotely Piloted Aircraft
RPAS	Remotely Piloted Aircraft System
SAFIRE	Service des Avions Français Instrumentés pour la Recherche en Environnement
SMPS	Scanning Mobility Particle Sizer
SUMO	Small Unmanned Meteorological Observer
TKE	Turbulent Kinetic Energy
UAV	Unmanned Aerial Vehicle
UTC	Coordinated Universal Time

Chapter 1

Introduction

Contents

1.1	Introduction en Français	1
1.1.1	Les interactions aerosol-nuage	1
1.1.2	Les effets du forçage radiatif effectif dû aux interactions aerosol-nuage	2
1.1.3	Les objectifs de la thèse	2
1.2	English introduction	6
1.2.1	Aerosol-cloud interactions	6
1.2.2	Effective radiative forcing from aerosol-cloud interactions	7
1.2.3	Thesis objectives	7

1.1 Introduction en Français

1.1.1 Les interactions aerosol-nuage

Le Groupe d'experts Intergouvernemental sur l'Évolution du Climat (GIEC) consacre un chapitre de la Cinquième évaluation à l'état de l'art en matière de recherche scientifique sur les aérosols et les nuages (Boucher et al., 2013). Cette section présente les connaissances actuelles sur les interactions aerosol-nuage, soulignant dans sa conclusion la possibilité que des “interactions mal comprises et non représentées” biaisent les prédictions des modèles climatiques globaux (GCMs) sur les effets du forçage radiatif effectif (ERF). Par conséquent, la quantification des paramètres ayant un impact sur le forçage radiatif effectif est une priorité pour comprendre comment l'atmosphère réagit à la modification anthropique du climat. Alors que l'atmosphère est principalement composée de gaz, des particules liquides ou solides sont également présentes, et sont distinguées en tant que particules d'aérosols, particules de nuages et hydrométéores en chute. Les particules d'aérosols sont classées selon leur taille, leur composition chimique, leur teneur en eau et leur vitesse de chute (Boucher et al., 2013) et ont un impact profond sur le climat de la Terre. Les aérosols sont considérés comme des particules primaires si leur origine provient de la surface de la Terre, sans transformation chimique, telle que la poussière, la combustion de biomasse ou le sel marin. Les particules secondaires proviennent de précurseurs atmosphériques gazeux, tels que les sulfates, les nitrates ou le carbone organique volatil. Les effets des aérosols dans l'atmosphère sont définis dans l'évaluation du GIEC en tant qu'interactions aerosol-rayonnement (effet direct) et aerosol-nuage (effet indirect).

Il existe également une sous-catégorie appelée «effet semi-direct», qui se rapporte au changement de la structure thermodynamique de l'atmosphère dû au réchauffement par les aérosols absorbants (Fig.1.1). Ce travail se concentre sur les interactions aérosol-nuage liées aux mécanismes qui déterminent l'impact de l'effet indirect sur le climat de la Terre.

Les nuages sont formés par la vapeur d'eau qui se condense sur les noyaux activés à une sursaturation donnée. Les particules activées sont appelées noyaux de condensation de nuages (CCN), et représentent les particules qui forment des gouttelettes de nuages sous une sursaturation atmosphérique raisonnable (Seinfeld et al., 2006). La capacité d'une particule d'aérosol à s'activer et condenser la vapeur d'eau pour créer une gouttelette dépend de la sursaturation, mais aussi de sa taille (tension superficielle) et de sa composition chimique (c'est-à-dire, activité des ions solubles dans l'eau). La pression de vapeur de saturation d'un soluté A dans l'air à la température T est $S = p_A/p_A^s(T)$, où p_A est la pression partielle de A et $p_A^s(T)$ est la pression partielle de A en équilibre avec sa phase liquide sur une surface plane à T. La sursaturation se produit quand $S > 1$ (Seinfeld et al., 2006). Par exemple, un rapport de pression de vapeur saturante pour l'eau de 1.01 correspond à une humidité relative de 101 % et à une sursaturation de 1 %.

1.1.2 Les effets du forçage radiatif effectif dû aux interactions aérosol-nuage

L'effet des aérosols sur les propriétés radiatives des nuages a d'abord été identifié par Twomey (1974), et fait référence à une augmentation du rayonnement solaire réfléchi vers l'espace (ou albédo) pour une augmentation donnée du nombre de gouttelettes de nuage et une diminution de leur taille associée à une teneur en eau liquide constante. D'autres effets des aérosols sur les nuages et la rétroaction des nuages sur les aérosols ont été mis en évidence (c.-à-d., durée de vie des nuages (Albrecht, 1989)) et sont résumés dans Lohmann et al. (2004). Chaque rapport du GIEC a évalué l'impact des effets des aérosols sur le forçage radiatif effectif (ERF), qui reste le paramètre le moins contraint dans l'évaluation du changement climatique anthropique. La cinquième évaluation du GIEC a rapporté une valeur médiane de ERF de -1.4 W m^{-2} . Cependant, une grande incertitude est encore associée au forçage radiatif effectif dû aux interactions aérosol-nuage (ERF_{aci}), et les modèles climatiques globaux ne considèrent pas les processus secondaires, ce qui conduit à un ERF_{aci} modélisé relativement faible (-0.45 W m^{-2} ; Boucher et al. (2013)).

1.1.3 Les objectifs de la thèse

Pour aborder les incertitudes liées au forçage radiatif effectif dû aux aérosols et aux nuages, cette thèse se base sur le développement instrumental et le déploiement d'une sonde multi-voies pour mesurer les trois composantes du vent atmosphérique afin d'étudier les interactions aérosol-nuage à l'aide d'un aéronef télépiloté. Les mesures de vent 3D, en particulier les vitesses verticales, sont utilisées pour estimer les propriétés microphysiques des nuages dans les études de fermeture aérosol-nuage. Les études de fermeture combinent des observations (concentrations en aérosols,

vitesse ascendantes et paramètres atmosphériques) et des modèles air-parcelle détaillés pour simuler les processus atmosphériques (formation de nuages) et comparer les résultats simulés à ceux observés (propriétés radiatives des nuages). La mesure des vitesses verticales est un élément important de la compréhension des interactions aérosol-nuage.

Pour répondre aux incertitudes liées au forçage radiatif effectif (ERF) des nuages, le projet BACCHUS (impact of Biogenic versus Anthropogenic emissions on Clouds and Climate: towards a Holistic UnderStandig), financé par l'Union européenne (FP7), réunit une communauté internationale de scientifiques ayant des expertises complémentaires dans l'expérimentation et la modélisation des interactions aérosol-nuage (ACI). La télédétection par satellite, la télédétection au sol et les mesures microphysiques in situ fournissent un grand nombre d'observations à comparer et à paramétrer dans les modèles pour améliorer les simulations, évaluer la sensibilité et quantifier l'incertitude associée aux études ACI.

Le processus d'activation des particules d'aérosol en gouttelettes de nuage constitue le lien microphysique direct entre les aérosols et les nuages. La distribution de la sursaturation du nuage est largement contrôlée par la vitesse verticale à proximité de la base du nuage (par exemple, Sullivan et al. (2016)), en raison du refroidissement par détente induite de la masse d'air. La sursaturation maximale détermine alors le nombre d'aérosols qui sont activés en gouttelettes de nuage. La concentration en nombre de gouttelettes du nuage (CDNC) influe sur le rayon effectif du nuage, car les concentrations en gouttelettes plus élevées produisent des rayons effectifs plus petits et une augmentation de l'albedo (Twomey, 1974) et de la durée de vie des nuages (Albrecht, 1989). Pour calculer le forçage radiatif effectif (ERF), les modèles climatiques globaux utilisent des paramétrisations de l'activation des aérosols reliant la formation de gouttelettes aux spectres CCN et la vitesse verticale (Sullivan et al., 2016). Plusieurs études présentent les différences dans la paramétrisation des gouttelettes de nuage (les propriétés des aérosols en mode grossier et le diamètre moyen géométrique des aérosols) dans les GCMs (Morales-Betancourt et al., 2014), et le rôle de la vitesse ascendante (Morales et al. (2010); Sullivan et al. (2016)). Dans une autre étude, Reutter et al. (2009) étudient la formation de gouttelettes de nuage pour un large éventail de vitesses verticales et de concentrations en nombre d'aérosols. Trois régimes différents sont définis, un régime limité par le nombre d'aérosols, où la concentration en gouttelettes est directement proportionnel au nombre d'aérosols, un régime limité par les vitesses verticales, où CDNC est directement proportionnel aux vitesses verticales, et un régime sensible aux aérosols et aux vitesses verticales, où CDNC varie non-linéairement avec le nombre d'aérosols et les vitesses verticales. Le paramètre d'hygroscopicité, qui exprime la composition des particules, joue un rôle important à faible sursaturation ($S < 0.1$ %) dans le régime limité par les vitesses verticales. Pour améliorer les estimations du forçage radiatif effectif des nuages des modèles GCM et air-parcelle, Morales et al. (2010), Peng et al. (2005), Reutter et al. (2009), Sullivan et al. (2016) citent le besoin de mesures expérimentales plus poussées sur les nuages de types différents afin de compléter les observations actuelles trop éparées.

Les vents verticaux proches de la base des nuages sont souvent mesurés directement à l'aide d'une sonde multi-voies couplée à un système inertiel de navigation¹ (INS) sur les avions de recherche traditionnels. Par exemple, la vitesse verticale du vent a été mesurée avec une sonde à 5 voies pour étudier les interactions aérosol-nuage dans Conant et al. (2004) (projet CRISTAL-FACE, avion Twin Otter), Fountoukis et al. (2007) (projet ICARTT, avion Twin Otter), ou Crumeyrolle et al. (2010) (projet EUCAARI, avion ATR42). Les mesures aéroportées avec des avions de recherche pilotés couvrent une grande région de nuages. Cependant, la résolution spatiale des propriétés microphysiques des nuages, des vitesses verticales et des mesures radiatives est relativement faible en raison de leur vitesse-air rapide (environ 100 m s^{-1}). Pour pallier à ces limitations en obtenant des mesures de haute résolution spatiale des nuages et des vents atmosphériques, en particulier à l'interface des nuages, des mesures héliportées ont été développées (Airborne Cloud Turbulence Observation System (ACTOS)). Siebert et al. (2006) présente une nacelle instrumentée suspendue à un hélicoptère qui vole horizontalement à 15 m s^{-1} . ACTOS transporte des instruments pour mesurer les propriétés microphysiques des aérosols et des nuages, les vecteurs 3D de vent et les paramètres d'état de l'atmosphère. Les vecteurs 3D de vent sont obtenus à partir d'un anémomètre sonique monté à l'avant de la nacelle. ACTOS a été déployé sur la mer Baltique pour étudier les nuages de type stratocumulus (Ditas et al., 2012), et à la Barbade pendant la campagne de mesures CARRIBA (Siebert et al., 2013) pour mener des études de fermeture aérosol-nuage. Les résultats montrent une étroite concordance entre les mesures in situ et les simulations de modèles air-parcelle du rayon effectif des gouttelettes (Werner et al., 2014).

Au cours de la dernière décennie, les systèmes d'aéronefs pilotés à distance² sont devenus des outils efficaces en science atmosphérique. Les RPAS légers ($<25 \text{ kg}$) présentent une capacité de charge utile limitée par rapport aux avions de recherche traditionnels et aux plateformes héliportées. Cependant, les RPAS sont logistiquement plus faciles et moins coûteux à déployer. L'utilisation des RPAS pour étudier les aérosols et les nuages est encore récente et relativement peu d'études sont cités dans la littérature. Par exemple, trois Manta RPAs avec des charges utiles pour étudier les flux aérosol-nuage-rayonnement solaire ont été déployés pendant la Campagne AUAV aux Maldives (MAC) (Ramanathan et al. (2007); Ramana et al. (2007); Corrigan et al. (2007); Roberts et al. (2008)). Corrigan et al. (2007) met en évidence des divergences dans les mesures des profils verticaux atmosphériques entre les mesures de surface et de RPA (importantes pour l'utilisation de mesures au sol dans les études sur les aérosols et nuages). Roberts et al. (2008) quantifie l'augmentation de l'albédo des nuages due à l'augmentation des concentrations en aérosols. Dans Altstädter et al. (2015), une autre étude portant sur les particules d'aérosol dans la couche limite avec la plateforme ALADINA (Application of Light-weight Aircraft for Detecting IN situ Aerosol), démontre la capacité des RPAs à étudier la formation de nouvelles particules dans les couches de nuage. Sanchez et al. (2017) est la première étude à présenter une fermeture bottom-up et top-down sur les interactions aérosol-nuage en utilisant des mesures au sol des spectres CCN, des mesures de

¹Dans ce travail, INS représente un système fusionnant les données du système de positionnement global (GPS) et l'unité de mesures inertielles (IMU) par un filtre de Kalman.

²Le système d'aéronef piloté à distance (RPAS) représente l'aéronef et la station de contrôle au sol, l'aéronef piloté à distance (RPA) représente uniquement l'aéronef.

vents verticaux de radar de nuage, des mesures in situ de RPA sur les propriétés des nuages, comparées aux mesures d'un satellite sur les propriétés optiques des nuages. Le processus d'entraînement aux extrémités des nuages est identifié comme une source majeure de discordance entre les observations et les simulations des propriétés optiques des nuages. Un accord de fermeture de moins de 30 % d'écart est obtenu entre la concentration en nombre de gouttelettes de nuage (CDNC) mesurée par satellite et simulée.

Dans le cadre du projet BACCHUS, la contribution des RPAs du CNRM (Centre National de Recherches Météorologiques) est de compléter les observations au sol d'aérosol/CCN pour caractériser la distribution verticale des paramètres aérosols, flux radiatifs, turbulence et état météorologique. Comme indiqué dans Sanchez et al. (2017), Roberts et al. (2008) et Corrigan et al. (2007), les observations au sol ont besoin de la structure verticale de l'atmosphère pour faire des hypothèses sur le mélange dans la basse troposphère et sur les interactions aérosol-nuage. Pendant les campagnes de mesures BACCHUS, les RPAS ont été déployés sur deux sites contrastés: 1) à Chypre, en Méditerranée au carrefour de la pollution en provenance de l'Europe et du Moyen-Orient et soumis à la poussière du Sahara, et 2) en Irlande, à la station de recherche de Mace Head exposée à des masses d'air provenant de l'océan Atlantique, dont l'influence est beaucoup moins anthropique. Quatre plateformes RPA ont été développées avec une instrumentation spécifique, qui a nécessité une adaptation des produits commerciaux pour minimiser leur taille, leur poids et leur puissance, et créer un lien avec le système d'acquisition des données. L'aéronef a été construit avec la participation de l'Ecole Nationale de l'Aviation Civile (ENAC, Toulouse). Le pilote automatique Paparazzi, qui contrôle les RPAS pour BACCHUS, est développé par ENAC (Brisset et al., 2006).

Les motivations du travail présent se portent sur le besoin de mesures de vent vertical pour mieux quantifier les interactions aérosol-nuage. Il existe des sondes commerciales multi-voies (par exemple Aeroprobe Corporation et Vectoflow). Cependant, l'intégration des capteurs, de la sonde multi-voies, de l'INS et leur couplage pour assurer la synchronisation des données a été développé pour cette thèse. Actuellement, seuls quatre groupes de recherche à l'échelle internationale, y compris le CNRM, ont publié les résultats de sondes multi-voies intégrées à des RPAS; et ces groupes se concentrent sur les mesures de turbulence dans la couche limite atmosphérique. Pour améliorer notre compréhension des interactions aérosol-nuage, des mesures des vitesses verticales à la base des nuages sont nécessaires et se situent au centre du travail de cette thèse.

L'étude présentée ci-après est divisée en quatre chapitres; le Chapitre 2 se concentre sur le développement instrumental des mesures de vent atmosphérique par la plateforme RPA. La sonde à 5 voies est d'abord étalonnée et validée dans une soufflerie à Météo-France (Toulouse, France). Le Chapitre 3 compare les résultats des vitesses de vent mesurées par le RPA avec ceux des anémomètres soniques positionnés sur un mât météorologique au Centre de Recherches Atmosphériques (CRA, Lannemezan, France). Trois paramètres sont sélectionnés pour la validation de la sonde à 5 voies: les fonctions de densité de probabilité (PDF) de la vitesse verticale du vent, la densité spectrale de puissance (PSD) de chaque composante du vent et le calcul de l'énergie

cinétique turbulente (TKE). Le Chapitre 4 présente des mesures de vent vertical déterminées lors de la campagne de mesures BACCHUS à la station de recherche de Mace Head. Les mesures sont validées par la comparaison avec un radar de nuage par trois cas d'étude de nuages dans des conditions météorologiques différentes. Le Chapitre 5 présente une étude de fermeture des interactions aérosol-nuage entre les mesures d'aérosols au sol, les mesures de RPA des vitesses verticales et les propriétés optiques des nuages, et un modèle de parcelle aérosol-nuage. L'étude de cas se concentre sur une couche de stratocumulus – échantillonnée lors d'une campagne de mesures BACCHUS à Chypre.

1.2 English introduction

1.2.1 Aerosol-cloud interactions

The International Panel for Climate Change (IPCC) dedicates one chapter of the Fifth Assessment on the state of the art on aerosol and cloud scientific research (Boucher et al., 2013). This section reports the current knowledge about aerosol-cloud interactions, emphasizing in its conclusion the possibility that “poorly understood and unrepresented interactions” bias the predictions of global climate models (GCM) on the cloud effective radiative forcing (ERF) impacts. Consequently, quantifying parameters that impact ERF is a priority to understand how the atmosphere responds to the anthropogenic modification of climate. While the atmosphere is mainly composed of gases, liquid or solid particles are also present, and are distinguished as aerosol particles, cloud particles, and falling hydrometeors. Aerosol particles are classified according to their size, chemical composition, water content and fall velocity (Boucher et al., 2013) and have a profound impact on the Earth's climate. Aerosols are considered as primary particulate matter if they originate from the Earth's surface, without chemical transformation such as dust, biomass burning or sea salt. Secondary particulate matter derives from gaseous atmospheric precursors, such as sulfate, nitrates or volatile organic carbon. The effects of aerosols in the atmosphere are defined in the Fifth IPCC Assessment as aerosol-radiation (direct effect) and aerosol-cloud interactions (indirect effect). There is also a sub-category called the ‘semi-direct-effect’, which relates to the change in the thermodynamic structure of the atmosphere owing to heating from absorbing aerosol (Fig.1.1). This work focuses on mechanisms related to aerosol-cloud interactions.

Clouds are formed by water vapor, which condense on activated nuclei at a given supersaturation. These activated particles are called cloud condensation nuclei (CCN), and represent the particles that form cloud droplets under reasonable atmospheric supersaturation (Seinfeld et al., 2006). The capacity of an aerosol particle to become activated and condense water vapor to create a cloud droplet depends on the supersaturation, but also on its size (i.e., surface tension) and chemical composition (i.e., water activity of soluble ions). The saturation vapor pressure of a solute A in air at temperature T is $S = p_A/p_A^s(T)$, where p_A is the partial pressure of A and $p_A^s(T)$ is the partial pressure of A in equilibrium with its liquid phase over a flat surface at T; supersaturation occurs when $S > 1$ (Seinfeld et al., 2006). For example, a ratio of saturation

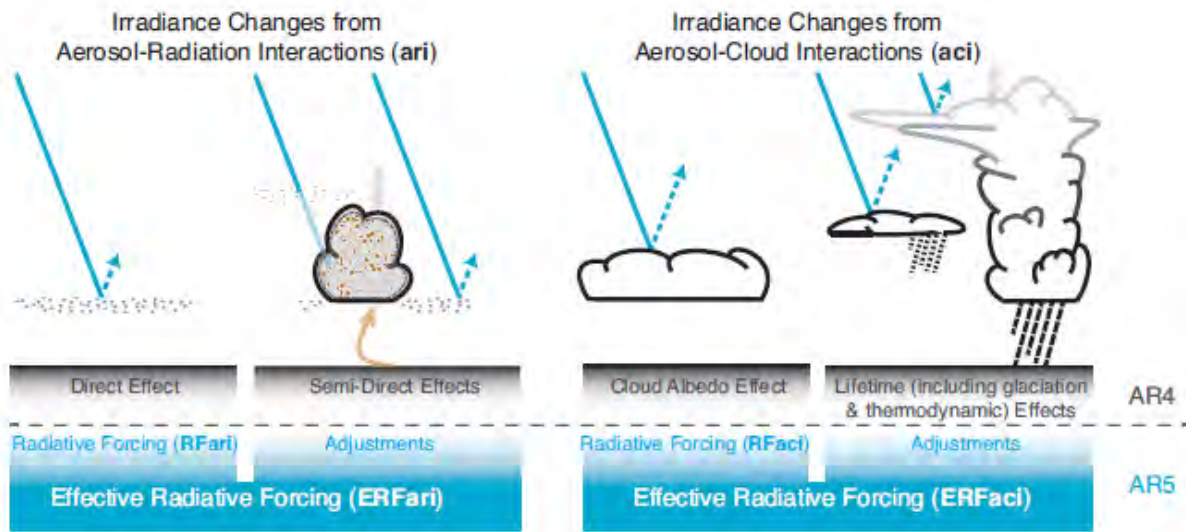


FIG. 1.1: Schematic of the new terminology used in the Fifth IPCC assessment (AR5) for aerosol-radiation and aerosol-cloud interactions and how relate to the terminology used in the Fourth IPCC assessment (AR4). The blue arrows depict solar radiation, the gray arrows terrestrial radiation and the brown arrow symbolizes the importance of couplings between the surface and the cloud layer for rapid adjustments (Boucher et al., 2013).

vapor pressure for water that is 1.01 corresponds to a relative humidity of 101 % and a supersaturation of 1 %.

1.2.2 Effective radiative forcing from aerosol-cloud interactions

The effect of aerosols on cloud radiative properties was first identified by Twomey (1974), and refers to an enhancement of solar radiation reflected back into space (or albedo) for a given increase in number of cloud droplets and associated decrease in their size at a constant liquid water content. Other aerosol effects on cloud and the feedback of clouds on aerosols have been included (i.e., cloud lifetime (Albrecht, 1989)) and are summarized in Lohmann et al. (2004). Each IPCC report has assessed the impact of aerosol effects on effective radiative forcing (ERF), which has remained the least constrained parameter in assessing anthropogenic climate change. The Fifth IPCC assessment reported a median value of ERF of -1.4 W m^{-2} . However, a large uncertainty is still associated with aerosol-cloud interaction ERF (ERF_{aci}), and global climate models (GCMs) do not consider secondary processes, which leads to a relatively low ERF_{aci} (-0.45 W m^{-2} ; Boucher et al. (2013)).

1.2.3 Thesis objectives

Ultimately, to address the uncertainties related to aerosol and cloud ERF, this thesis is based on instrumental development and deployment of a multi-hole probe to measure vertical wind velocity to study aerosol-cloud interactions using a remotely piloted aircraft (RPA). Atmospheric wind

measurements, particularly updraft velocities, are used to estimate cloud microphysical properties in aerosol-cloud closure studies. Closure studies combine observations (such as aerosol concentrations, updraft velocities and atmospheric state parameters) and detailed air-parcel models to simulate atmospheric processes (i.e., cloud formation) and compare the simulated results to those observed (i.e., cloud radiative properties). The measurement of updraft velocities is an important component of understanding aerosol-cloud interactions.

To address the uncertainties associated with effective radiative forcing (ERF) of clouds, the BACCHUS project (impact of Biogenic versus Anthropogenic emissions on Clouds and Climate: towards a Holistic UnderStandig), funded by the European Union's Seventh Framework Programme (FP7), gathers an international community of scientists with complementary expertise in experimental and modeling of aerosol-cloud interactions (ACI). Satellite remote sensing, ground-based remote sensing, in-situ microphysical measurements provide a large number of observations to be compared and parameterized in models to improve simulations, assess sensitivity and quantify the uncertainty associated with ACI studies.

The activation process of aerosol particles into cloud droplets constitutes the direct microphysical link between aerosols and clouds. The cloud's supersaturation distribution is largely controlled by the vertical wind velocity near cloud base (e.g., Sullivan et al. (2016)), owing to the induced expansion cooling of the air mass. The maximum supersaturation then determines the number of aerosols that activate into cloud droplets. The cloud droplet number concentration (CDNC) impacts the cloud droplet effective radii as higher CDNC results in smaller effective radii and an increased cloud albedo (Twomey, 1974), and possibly cloud life time (Albrecht, 1989). To calculate the effective radiative forcing (ERF), global climate models use parameterizations of aerosol activation linking droplet formation to CCN spectra and vertical velocity (Sullivan et al., 2016). Several studies investigate the discrepancies in cloud droplet parameterization (the coarse mode aerosol properties and the accumulation mode aerosol geometric mean diameter) in GCM (Morales-Betancourt et al., 2014), and the role of updraft velocity (Morales et al. (2010); Sullivan et al. (2016)). In another study, Reutter et al. (2009) investigate the formation of cloud droplets for a wide range of updrafts and aerosol number concentrations. Three different regimes are defined, an aerosol-limited regime, where CDNC is directly proportional to the aerosol number, an updraft-limited regime, where CDNC is directly proportional to the updraft, and an aerosol- and updraft-sensitive regime, where CDNC depends non-linearly on aerosol numbers and updraft. The hygroscopicity parameter, which expresses the particle composition, is found to play an important role at low supersaturation ($S < 0.1$ %) in the updraft-limited regime. To improve estimates of cloud radiative forcing in GCM and air parcel models, Morales et al. (2010), Peng et al. (2005), Reutter et al. (2009), Sullivan et al. (2016) cite the need for more experimental updraft measurements over a range of cloud types as observations are too sparse.

Vertical winds near cloud base are often measured directly using a multi-hole probe paired with

an inertial navigation system³ (INS) on traditional piloted research aircraft. For example, vertical wind velocity was measured with a 5-hole probe to study aerosol-cloud interactions in Conant et al. (2004) (CRISTAL-FACE experiment, Twin Otter aircraft), Fountoukis et al. (2007) (ICARTT experiment, Twin Otter aircraft), or Crumeyrolle et al. (2010) (EUCAARI experiment, ATR42 aircraft). Airborne measurements with piloted research aircraft cover a large cloud field region; however the spatial resolution of cloud microphysical properties, vertical velocities, and radiative measurements is relatively low owing to their fast airspeed (ca. 100 m s⁻¹). To tackle these limitations in obtaining high spacial resolution measurements of clouds and atmospheric winds, particularly at the cloud's interface, helicopter-borne measurements have been developed (Airborne Cloud Turbulence Observation System (ACTOS)). Siebert et al. (2006) present an instrumented pod suspended from a helicopter which flies horizontally at 15 m s⁻¹. The ACTOS carries instrumentation for measuring aerosol and cloud microphysical properties instruments, 3D wind vectors and atmospheric state parameters. 3D wind vectors are obtained from an ultrasonic anemometer mounted at the front edge of the pod. ACTOS has been deployed over the Baltic sea to study turbulent marine stratocumulus clouds (Ditas et al., 2012), and in Barbados during the CARRIBA field campaign (Siebert et al., 2013) to conduct aerosol-cloud closure studies. Results show a close agreement between in situ measurements and air-parcel model simulations of droplet effective radius (Werner et al., 2014).

Over the past decade, remotely piloted aircraft systems⁴ (RPAS) have become useful tools in atmospheric science. Lightweight RPAS (<25 kg) present limited payload capacity compared to traditional research aircraft and helicopter-borne platforms; however RPAS are logistically easier and less expensive to operate. The use of RPAS to study aerosols and clouds is still recent, and relatively few studies are cited in the literature. For example, three RPA platforms of the Manta model with aerosol-cloud-solar flux payloads were deployed during the Maldives AUAV Campaign (MAC) (Ramanathan et al. (2007); Ramana et al. (2007); Corrigan et al. (2007); Roberts et al. (2008)). Corrigan et al. (2007) highlights discrepancies in measurements of atmospheric vertical profiles between surface and RPA measurements (important for using ground-based measurements in aerosol-cloud studies). Roberts et al. (2008) quantifies cloud albedo enhancement due to increasing aerosol concentrations. Another study focusing on aerosol particles within the boundary layer with the ALADINA platform (Application of Light-weight Aircraft for Detecting IN situ Aerosol) in Altstädter et al. (2015), demonstrates the capability of RPA to study new particle formation in the region of a cloud layer. Sanchez et al. (2017) is the first study to present a bottom-up and top-down aerosol-cloud closure using ground-based measurements of CCN spectra, cloud radar measurements of vertical winds, in situ RPA of cloud properties, and satellite derived cloud optical properties. Cloud-top entrainment is identified as a major source of discrepancy between observations and simulations of cloud optical properties. A closure agreement within 30 %

³In the present work, INS represents a unit merging global positioning system (GPS) data and inertial measurement unit (IMU) with an extended Kalman filter.

⁴Remotely piloted aircraft system (RPAS) represents the airframe and the ground control station, remotely piloted aircraft (RPA) represents only the aircraft.

is obtained between satellite-retrieved and simulated cloud droplet number concentration (CDNC).

Within the BACCHUS project, the CNRM (Centre National de Recherches Météorologiques) contribution of RPA is to complement the ground-based observations of aerosol/CCN to characterize the vertical distribution of aerosol, radiative fluxes, turbulence and meteorological state parameters. As shown in Sanchez et al. (2017), Roberts et al. (2008), and Corrigan et al. (2007), ground-based observations need the vertical structure of the atmosphere to make assumptions about mixing in the lower troposphere and aerosol-cloud interactions. During BACCHUS field campaigns, RPAS were deployed on two contrasting field sites, 1) in Cyprus, in the Mediterranean Sea at the intersection of pollution from Europe and Middle East, and subjected to dust from Sahara, and 2) in Ireland, at the Mace Head Atmospheric Research Station exposed to air masses originating from the Atlantic Ocean, with much less influence of anthropogenic activity. Four RPA platforms were developed with specific instrumentation, which required adaptation from commercial products to minimize size, weight, and power, and link to the data acquisition system. The airframe was constructed with the participation of the Ecole Nationale de l'Aviation Civile (ENAC, Toulouse). The Paparazzi autopilot, which controls the RPAs for BACCHUS, is developed by ENAC (Brisset et al., 2006).

Motivations of the present work are driven in particular by the need for vertical wind measurements to better quantify aerosol-cloud interactions. Commercial multi-holes probes do exist (i.e., Aeroprobe Corporation, and Vectroflow); however, supporting sensor measurements, and coupling with an INS and integration into a RPA had to be developed for this thesis research. Currently, only four research groups internationally, including CNRM, have published results for multi-hole probes integrated in a RPA; and these groups focus on turbulence measurements in the boundary layer. To improve our understanding of aerosol-cloud interactions, vertical wind measurements near cloud base are needed and are the focus of this thesis research.

The study presented hereafter is divided in four chapters; the Chapter 2 focuses on the instrumental development of atmospheric wind measurements on the RPA platform. The 5-hole probe is first calibrated and validated in a wind-tunnel at Météo-France (Toulouse, France). Chapter 3 compares the results of measured wind velocities with the wind-RPA to sonic anemometers on a meteorological tower at the Centre de Recherches Atmosphériques (CRA, Lannemezan, France). Three parameters are selected for the validation of the 5-hole probe, i.e. probability density functions (PDF) of the vertical wind velocity, the power spectral density (PSD) function of each wind component, and the calculation of turbulent kinetic energy (TKE). Chapter 4 presents vertical wind measurements sampled during the BACCHUS field campaign at the Mace Head Atmospheric Research Station. Measurements are validated with a cloud radar for three different meteorological conditions of cloud fields. Chapter 5 presents an aerosol-cloud closure study between ground-based aerosol measurements, RPA measurements of updraft velocities and cloud optical properties, and an aerosol-cloud parcel model. The case study focuses on a stratocumulus cloud layer – sampled during a BACCHUS field campaign in Cyprus.

Chapter 2

Instrument development

Contents

2.1	Historical background of wind measurements from airborne platforms .	13
2.2	Wind measurements with remotely piloted aircraft system (RPAS) . . .	15
2.2.1	3D wind vector equations	15
2.2.2	5-hole probe	19
2.2.3	Inertial navigation system (INS)	19
2.3	Calibration in wind tunnel	20
2.3.1	Wind tunnel installation	21
2.3.2	Calibration of 5-hole probe	21
2.3.3	Experimental error analysis on vertical wind velocity	25
2.3.4	Gaussian error propagation on vertical wind speed	26
2.4	Wind-RPAS platform	27
2.4.1	Skywalker X6 airframe	27
2.4.2	The open-source autopilot Paparazzi	27
2.4.3	Overview of flight operations	28
2.4.4	Instrumentation challenges	28
2.5	The BACCHUS field campaigns challenges	29
2.6	Conclusions and perspectives	30

2.1 Historical background of wind measurements from airborne platforms

Tracing the evolution of wind measurements in the atmosphere from aircraft, three axes of development have been pursued over the past 60 years including advancement in airborne platforms, inertial navigation systems (INS) and instruments for wind measurements. Clearly, the accuracy of wind measurements improved with the development of instrumentation along these three axes. The values of uncertainties reported here are found in the literature, and show the evolution of atmospheric wind measurements. Early methods to calculate the vertical wind velocity from airborne platforms were described in Jones (1954) and Bunker (1955), based on the integration of

the aircraft's acceleration, which yielded the vertical velocity of the aircraft. The flight characteristics were then used to obtain the velocity of the air relative to the aircraft and the sum of two provided the vertical wind velocity. Telpord et al. (1962) also used the integration of the accelerations to obtain the aircraft vertical velocity, however an angle of attack vane was developed to measure the air velocity. Axford (1968) described the first implementation of an INS platform on a meteorological aircraft (Canberra PR3) to obtain more accurate wind measurements. At that time, wind vanes were set up at the tip of a nose boom to determine three-dimensional wind velocities. Lenschow (1971) described the characteristics of rotating and constrained vanes using NCAR's Buffalo aircraft to achieve absolute wind measurement accuracy of 1 m s^{-1} (Lenschow, 1972). Lawson (1979) published vertical wind velocity calculated with higher accuracy gyroscopes for pitch and roll measurements, which reduced the standard deviation of the 3D wind measurements to 0.7 m s^{-1} (NCAR Queen Air aircraft). In 1980s, multi-hole probes with differential pressure sensors were developed for wind measurements, and positioned either on a nose boom (e.g., Rosemount sensor) or on the nose of the aircraft itself (i.e., radome). Comparison of the two instruments installed at two different locations on the same aircraft (NCAR Sabreliner) was presented in Brown et al. (1983). A superior frequency response of the radome system was found compared to the probe on the nose boom due to the shorter pressure lines for the radome (less distance between the probe and the sensors for the radome compared to the nose boom). Global Positioning Systems (GPS) brought further improvements in wind measurements when GPS data were used in a postflight filtering method to complement inertial measurement results (Khelif et al., 1999). However, improvements were still necessary, particularly in reducing the uncertainty associated with the heading measurements (pointing direction of the aircraft trajectory), and merging GPS and IMU (Inertial Measurement Unit) data in real time. The Dornier aircraft (Corsmeier et al., 2001) achieved an accuracy of 0.5 m s^{-1} for the horizontal wind and 0.1 m s^{-1} for the vertical wind estimate with the integration of fast GPS data combined in real time with IMU output. In Crawford et al. (1992), a custom 9-hole probe with differential pressure sensors was developed on a light airplane (Long-EZ), which became the BAT probe ("Best Air Turbulence" probe). The BAT probe was later adapted for different aircraft types (Hacker et al., 1999), and had an error associated with the vertical wind measurement of 0.03 m s^{-1} (Garman et al., 2006). Over the past decade, GPS, IMU, INS, multi-hole probes, and pressure sensors have become sufficiently miniaturized to be integrated on ultra-light remotely piloted aircrafts (RPA) — commonly called unmanned aerial vehicles (UAV) and drones. Such advances have extended observational capabilities previously limited to traditional piloted research aircraft.

A wide size-range of RPAS has been used to measure atmospheric winds, from a 600 g RPA named SUMO (Small Unmanned Meteorological Observer, Reuder et al. (2016)) to a 30 kg Manta RPA (BAE Systems Manta C1 RPA model, Thomas et al. (2012)). In particular, a multi-hole probe paired with an inertial navigation system has been the main mechanism from obtaining 3D winds in fixed-wing RPA. Ultimately, the combination of a multi-hole probe, the differential pressure measurements and the INS dictate the precision of atmospheric wind measurements. The following wind accuracies were found in the literature for different RPA platforms; they were obtained by

different methods. The authors provided either 1-sigma uncertainty or systematic errors associated with a specific probe/INS pair. For example, in Kroonenberg et al. (2008), a custom 5-hole probe on the M²AV (Meteorological Mini unmanned Aerial Vehicle), implemented with a GPS-MicroElectroMechanical System (MEMS)-IMU was reported with an accuracy for w within 0.5 m s⁻¹. The accuracy was based on a systematic error estimation using characteristic flight parameters with a reference state of $w=1$ m s⁻¹. The uncertainty in w reported for the SUMO (Båserud et al., 2016) is ± 1 m s⁻¹ as given by the manufacturer; however, the impact of the INS was not included in their analysis. In Thomas et al. (2012), the Manta RPA was equipped with a commercial 5-hole probe from Aeroprobe Corporation and a C-Migits-III tactical sensor (INS unit) to obtain a minimum resolvable w of 0.17 m s⁻¹ (1-sigma). The method of determination, described in Garman et al. (2006), is based on the error propagation of the contribution of each individual measurements: RPA vertical velocity, pitch angle, angle of attack and airspeed. The Manta and ScanEagle RPAs described in Reineman et al. (2013) achieved precise wind measurements with a custom 9-hole probe and NovAtel INS with reported uncertainties in w within ± 0.021 m s⁻¹. Their uncertainty was obtained from a Monte-Carlo simulation, and was also consistent with the reverse-heading maneuvers (flight legs in opposite directions). The higher precision of the latter study (Reineman et al., 2013) is mostly due to the much higher precision of the dGPS/IMU used in this study. At the time of the development of their multi-hole probes, such dGPS/IMU systems were too large to be placed in the ultralight RPA. The technology is rapidly changing and there are now dGPS/IMU systems that are available for use in the ultralight RPA.

The study hereafter presents the development of a RPA for atmospheric wind measurements. The RPA is an ultralight platform (<2.5 kg), instrumented with a 5-hole probe designed by Aeroprobe Corporation, but with custom electronics composed of differential and absolute pressure sensors. An INS, combining GPS and IMU data, is added in the RPA. The calibration of the 5-hole probe is conducted in wind tunnel, and an uncertainty analysis assesses the accuracy of the vertical wind measurement for the INS/5-hole probe implemented on the present wind-RPA.

2.2 Wind measurements with remotely piloted aircraft system (RPAS)

2.2.1 3D wind vector equations

3D wind vectors in the Earth's coordinate system are obtained by subtracting the measured motion of the RPA (given by the INS), from the motion of the air (given by the 5-hole probe), as stated in Lenschow et al. (1989). The angle of attack α , the angle of sideslip β , and the airspeed V_a are measured by the 5-hole probe in the probe coordinate system and then transformed to the RPA coordinate system; while the attitude angles from the INS provide the transformation of α , β and V_a from the RPA coordinate system to the Earth's coordinate system. Lenschow equations (Lenschow et al., 1989) are therefore followed to calculate the wind vector in the Earth's coordinate system.

$$\vec{V}_e = \vec{V}_{air/RPA} + \vec{V}_{RPA/earth} + \vec{\Omega} \wedge \vec{R} \quad (2.1)$$

with \vec{V}_e the wind vector in the Earth's coordinate system F_e , $\vec{V}_{air/RPA}$ the air speed relative to the RPA, $\vec{V}_{RPA/earth}$ the velocity of the RPA relative to the ground, $\vec{\Omega}$ the angular acceleration of the RPA with respect to its axes, and \vec{R} the distance from the accelerometers (IMU) to the 5-hole probe. Transformations between the different coordinate systems are detailed in the following subsections.

The air velocity from the aerodynamic coordinate system F_a to the RPA coordinate system F_b

Considering the angle of attack α , the angle of sideslip β and the airspeed V_a , given in the aerodynamic frame F_a , the air velocity vector is expressed in the RPA frame F_b as (Fig.2.1):

$$\vec{V}_{air/RPA} = \frac{-V_a}{D} \begin{pmatrix} 1 \\ \tan \beta \\ \tan \alpha \end{pmatrix} \quad (2.2)$$

with the normalization factor $D = \sqrt{1 + \tan^2 \alpha + \tan^2 \beta}$.

From the RPA coordinate system F_b to the Earth's coordinate system F_0

Three rotations angles are required to transform vectors from F_b to F_0 (Fig.2.2). The first rotation is around the RPA fuselage axis x_b of the roll angle ϕ . The rotation of the pitch angle θ is around the right wing axis y_b , and finally, the rotation of the yaw angle ψ in the horizontal plane. From the three rotations, the matrix of transformation T_{pe} applied to $\vec{V}_{air/RPA}$ is defined as:

$$T_{pe} = \begin{pmatrix} \sin \psi & \cos \psi & 0 \\ \cos \psi & -\sin \psi & 0 \\ 0 & 0 & -1 \end{pmatrix} \begin{pmatrix} \cos \theta & 0 & \sin \theta \\ 0 & 1 & 0 \\ -\sin \theta & 0 & \cos \theta \end{pmatrix} \begin{pmatrix} 1 & 0 & 0 \\ 0 & \cos \phi & -\sin \phi \\ 0 & \sin \phi & \cos \phi \end{pmatrix} \quad (2.3)$$

Of note, the meteorological and aircraft navigation frames are slightly different, so we clarify the differences here. In the aeronautic literature, the w -component on the z -axis of the Earth's coordinate system is positive down, however in the meteorological frame used in the present work, w is positive up. The vector of ground velocities $\vec{V}_{RPA/earth}$ given by the INS is already in the Earth's frame, and do not need further transformation.

$$\vec{V}_{RPA/earth} = \begin{pmatrix} V_x \\ V_y \\ V_z \end{pmatrix} \quad (2.4)$$

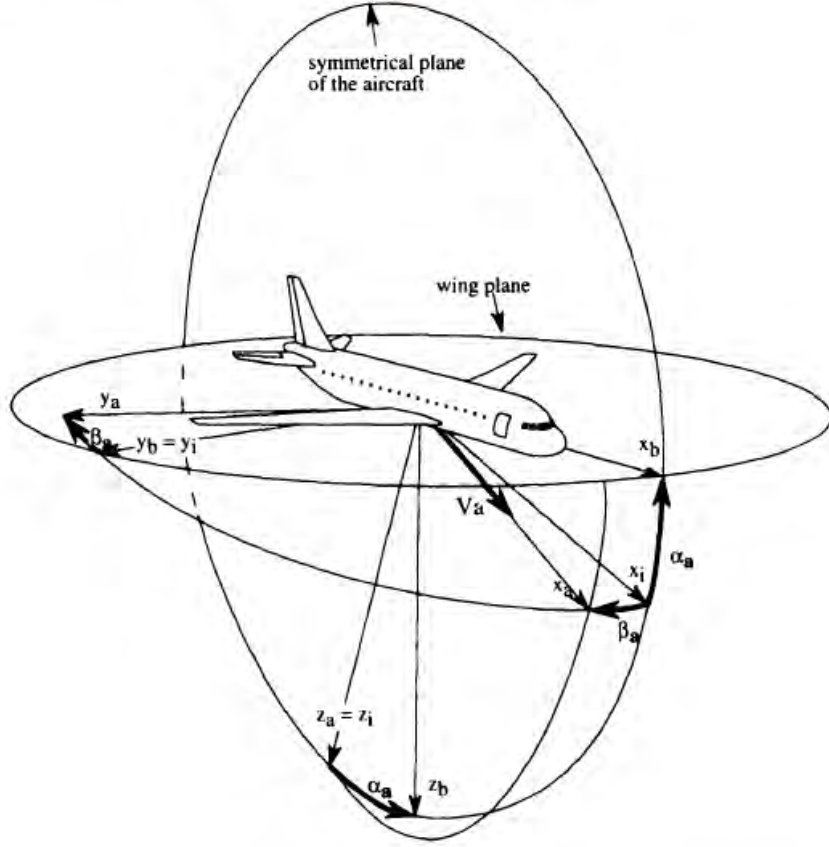


FIG. 2.1: Identification of the angle of attack α , the angle of sidesplit β , and the airspeed V_a in the aerodynamic coordinate system $F_a (x_a, y_a, z_a)$ relative to the RPA coordinate system $F_b (x_b, y_b, z_b)$. The figures is from Boiffier (1998).

Angular acceleration in the Earth's coordinate system

$$\vec{\Omega} \wedge \vec{R} = -L \begin{pmatrix} \dot{\theta} \sin \theta \sin \psi - \dot{\psi} \cos \psi \cos \theta \\ \dot{\psi} \sin \psi \cos \theta + \dot{\theta} \cos \psi \sin \theta \\ -\dot{\theta} \cos \theta \end{pmatrix} \quad (2.5)$$

with L the distance between the IMU accelerometers and the pressure sensors of the 5-hole probe.

Wind vectors in the Earth's coordinate system

$$u = -V_a D^{-1} [\sin \psi \cos \theta + \tan \beta (\cos \psi \cos \phi + \sin \psi \sin \theta \sin \phi) + \tan \alpha (\sin \psi \sin \theta \cos \phi - \cos \psi \sin \phi)] + V_x - L(\dot{\theta} \sin \theta \sin \psi - \dot{\psi} \cos \psi \cos \theta) \quad (2.6)$$

$$v = -V_a D^{-1} [\cos \psi \cos \theta - \tan \beta (\sin \psi \cos \phi - \cos \psi \sin \theta \sin \phi) + \tan \alpha (\cos \psi \sin \theta \cos \phi + \sin \psi \sin \phi)] + V_y - L(\dot{\psi} \sin \psi \cos \theta + \dot{\theta} \cos \psi \sin \theta) \quad (2.7)$$

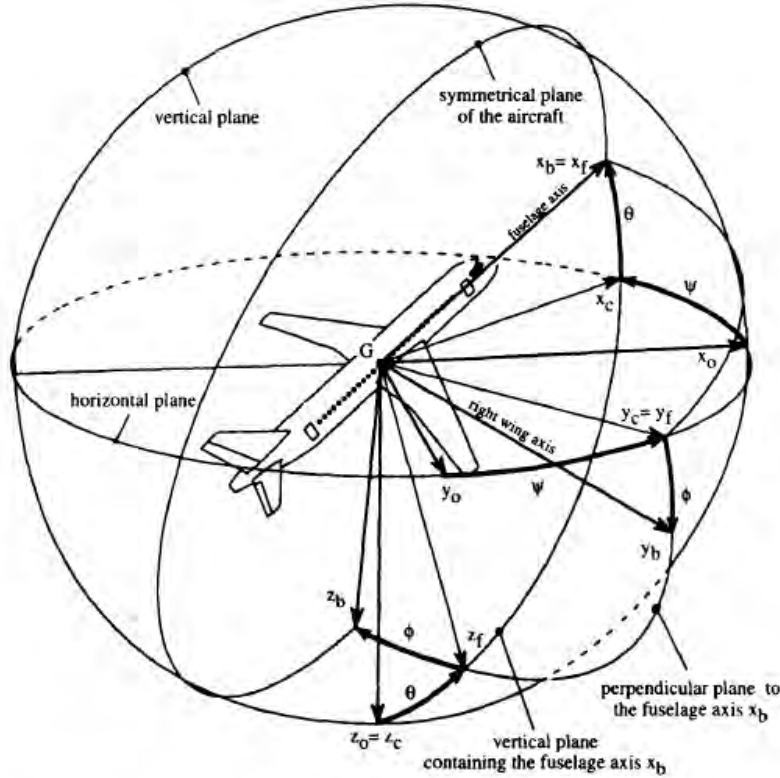


FIG. 2.2: Identification of attitude angles, the pitch angle θ , the roll angle ϕ , and the yaw angle ψ in the RPA coordinate system $F_b (x_b, y_b, z_b)$ relative to the Earth's coordinate system $F_0 (x_0, y_0, z_0)$. The figures is from Boiffier (1998).

$$w = -V_a D^{-1} (\sin \theta - \tan \beta \cos \theta \sin \phi - \tan \alpha \cos \theta \cos \psi) + V_z + L \dot{\theta} \cos \theta \quad (2.8)$$

Assumptions to simplify wind vector equations

As the calibration coefficients are non-linear, we need to minimize uncertainties in the method in which we retrieve 3D winds. This can be done by designing the flights plans such that the RPA flies along straight-and-level legs. Pitch and roll variations are substantially reduced, which constrains measurements and uncertainties in the quasi-linear regime of the calibration coefficients. The separation, which is the distance L between the IMU and the 5-hole probe, is small, less than 10 cm, therefore the angular acceleration $\vec{\Omega} \wedge \vec{R}$ is negligible. In general, the angular acceleration is only relevant in large aircraft with distances superior than 10 m, or during extreme pitch maneuvers. When the RPA flies along straight-and-level legs, the small-angle approximations simplify the full set of equations (ultimately, these simplified equations facilitate error analysis and may also be used for online calculations of wind vectors in real-time). In the calculation of horizontal winds, u and v , and as the angle of attack (α), pitch (θ), and roll (ϕ) approach zero, $\cos \alpha$, $\cos \theta$ and $\cos \phi$ approach unity, and the products of sines of two of the angles α , θ , and ϕ are negligible. Finally, $\tan(\alpha, \beta) \approx \sin(\alpha, \beta)$ (Lenschow et al., 1989). For the vertical wind w , the same assumptions are

used for the angles β , θ , and ϕ . Ultimately, the wind vectors are simplified to the following equations:

$$u = -V_a \sin(\psi + \beta) + V_x \quad (2.9a)$$

$$v = -V_a \cos(\psi + \beta) + V_y \quad (2.9b)$$

$$w = -V_a \sin(\theta - \alpha) + V_z \quad (2.9c)$$

More details on wind equations, and schematics of coordinate systems are found in Lenschow et al. (1989), Boiffier (1998), or Kroonenberg et al. (2008).

2.2.2 5-hole probe

The 5-hole probe, used for this research, has been constructed by the Aeroprobe Corporation (Christiansburg, Virginia, United-States), and consists of a stainless tube with a semi-spherical tip (Fig.2.3). The electronics provided by the constructor was inadequate for the operating conditions of the wind-RPA. Therefore, it has been decided to replace the electronics, which led to calibrate the manufactured probe and the new custom electronics in wind tunnel. The custom electronics have been designed at the Centre National de Recherches Météorologiques (CNRM) laboratory, and consist of three differential pressure sensors (All-Sensors 5inch-D1-MV) and one absolute pressure sensor (All Sensors MLV-015A) linked by tubing to the probe (less than 15 cm length). Figure 2.3a illustrates the probe design: hole 1 measures the pressure at the stagnation point of the tip; the differential pressure between holes 2 and 3 provides β , the angle of sideslip; the differential pressure between 4 and 5 gives α , the angle of attack; and hole 6, a ring around the probe, corresponds to the static pressure port. The airspeed, V_a , is calculated from the dynamic and static pressure obtained from a combination of the differential pressures to take into account the influence of inclination of the probe. To obtain angles in degrees and airspeed in m s^{-1} , the 5-hole probe system must be calibrated in the probe's coordinate system (aerodynamic frame F_a) and converted to the Earth's coordinate system (F_0).

2.2.3 Inertial navigation system (INS)

The inertial navigation system, INS (Lord Sensing Microstrain 3DM-GX4-45) is a combination of a GPS and an inertial measurement unit (IMU), with an extended Kalman filter. The IMU is composed of a triaxial accelerometer, a gyroscope, a magnetometer, and the INS hosts an integrated GPS receiver. The extended Kalman filter is an optimal estimation algorithm, which combines measurements from the different processors that are subjected to noise or drift to estimate position, attitude angles and ground velocities. The uncertainties of the INS are provided by the constructor as : ± 2.5 m RMS horizontal and ± 5 m RMS vertical for position accuracy, ± 0.1 m s^{-1} RMS for velocity, ± 0.25 deg RMS for roll and pitch for attitude angles, and ± 0.8 deg RMS for the heading angle. The data from the INS, as well as the 5-hole probe, are recorded by the Mbed microcontroller acquisition system, to ensure synchronization between the instruments. The

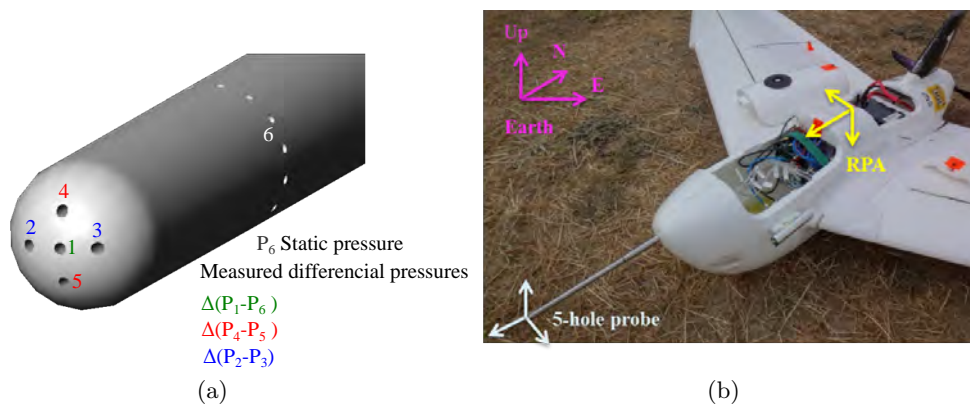


FIG. 2.3: (a) 5-hole probe tip, schematic representation of pressure holes. (b) 5-hole probe mounted on a Skywalker X6 RPA.

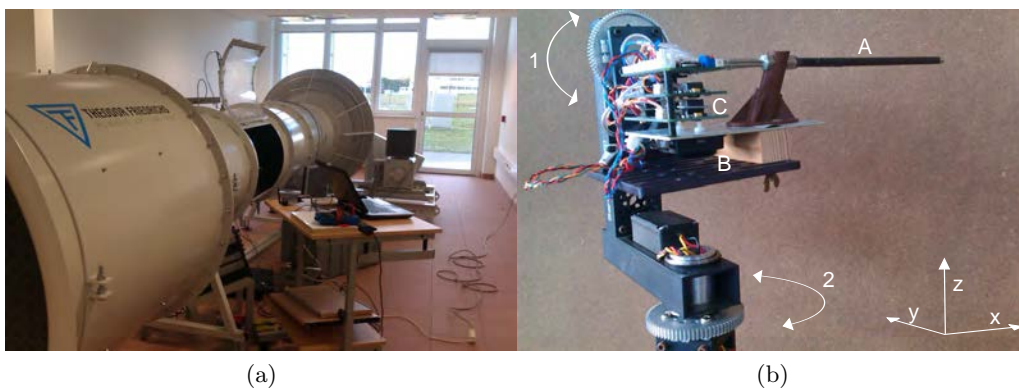


FIG. 2.4: (a) Theodor Friedrichs wind tunnel, Météo-France, Toulouse. (b) Two-axis platform for wind tunnel experiment, 1: rotation on pitch axis, 2: rotation on yaw axis, A: 5-hole probe, B: IMU, C: pressure sensors.

acquisition frequency is 30 Hz (oversampled 30 times), and data are averaged to 10 Hz for analysis. The measurements saved from the INS include the attitude angles, roll ϕ , yaw ψ and pitch θ , GPS time and GPS position and altitude, and ground speeds of the RPA in Earth's coordinate system. The INS is a miniature instrument and fits in the nose of the RPA, close to the probe mount.

2.3 Calibration in wind tunnel

The calibration of the 5-hole probe consists of a series of experiments in a wind tunnel (Theodor Friedrichs & Co) with a cross section of 70 cm, and a range of wind velocities between 0.15 to 50 m s^{-1} . The uncertainty associated with the wind velocity in the wind tunnel is less than 2 %. The calibration of the 5-hole probe is a two-step process : 1) determining the linear relationship between the absolute and differential pressure sensors' raw voltages to Pa with a reference barometer, and 2) associating the differential pressure measurements in Pa to angles (α and β) or velocity (V_a) in degree or m s^{-1} , respectively.

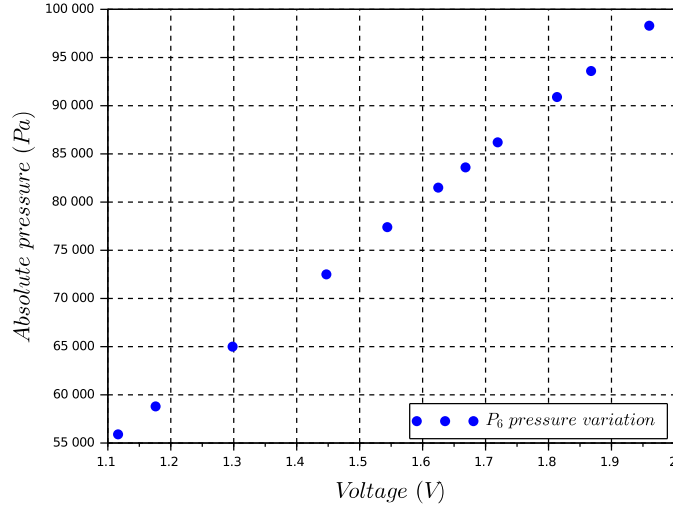


FIG. 2.5: Calibration of the pressure sensor from voltage to Pa with a barometer as a reference of the absolute pressure in Pa.

2.3.1 Wind tunnel installation

The 5-hole probe, the pressure sensors, and the INS are installed on a two-axis platform with motion in vertical and horizontal planes. The two-axis platform rotates in the pitch axis (motion in the vertical plane) and yaw axis (motion in the horizontal plane), controlled with a LabView program (Fig.2.4). The amplitude of pitch and yaw angles varies from ± 15 deg.

The first step of the calibration is to determine the relationship of pressure in Pa to the voltage variation of the pressure sensors recorded by the data acquisition system (Fig.2.5). The following regressions are calculated and used in the next steps of the calibration:

$$P_{6,Pa} = 2.5P_{6,V} - 264 \quad (2.10a)$$

$$\Delta(P_1 - P_6)_{Pa} = 341\Delta(P_1 - P_6)_V - 365 \quad (2.10b)$$

$$\Delta(P_2 - P_3)_{Pa} = 744\Delta(P_4 - P_5)_V - 1241 \quad (2.10c)$$

$$\Delta(P_4 - P_5)_{Pa} = 742\Delta(P_4 - P_5)_V - 1225 \quad (2.10d)$$

with P_6 the pressure given by the static ring, $\Delta(P_2 - P_3)$ is the differential pressure between holes 2 and 3, related to the calculation of the angle of sideslip β ; $\Delta(P_4 - P_5)$ is the differential pressure between holes 4 and 5, related to the calculation of the angle of attack α ; and $\Delta(P_1 - P_6)$ is the differential pressure between holes 1 and 6.

2.3.2 Calibration of 5-hole probe

The calibration of the 5-hole probe is based on a method described in Treaster et al. (1978), and also used in Wildmann et al. (2014). The calibration provides a procedure to measure the probe response in a controlled environment. The determination of α , β , and V_a from the 5-hole probe depends on four

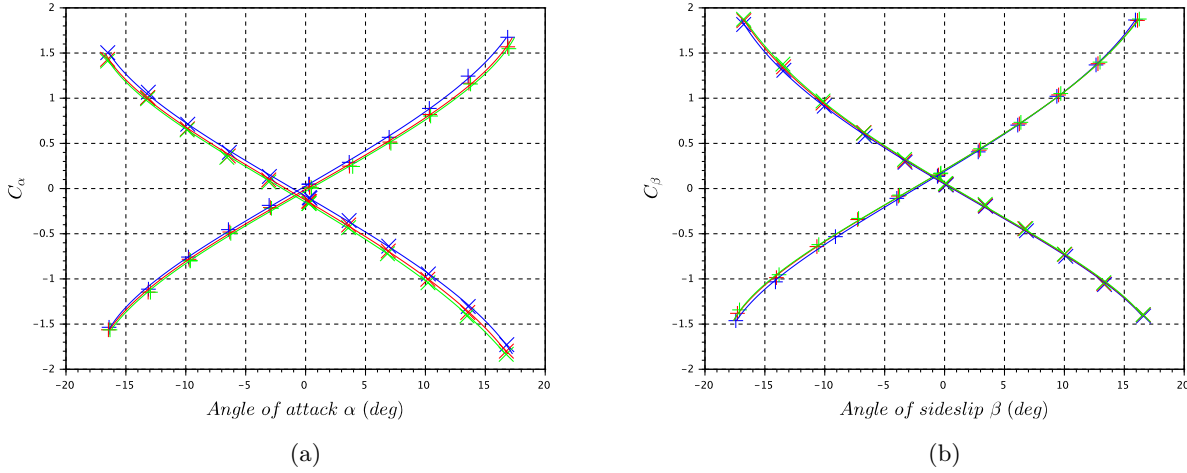


FIG. 2.6: (a) Calibration coefficients C_α for the calculation of the angle of attack α (INS pitch angles as a reference) at different wind tunnel velocities, blue: 15 m s⁻¹, red: 20 m s⁻¹, green: 25 m s⁻¹. The positive slope corresponds to the probe in standard orientation, + markers. The negative slope corresponds to the probe in inverted orientation, x markers. (b) Calibration coefficients C_β for the calculation of the angle of sideslip β (INS yaw angles as a reference) at different wind tunnel velocities, blue: 15 m s⁻¹, red: 20 m s⁻¹, green: 25 m s⁻¹. The positive slope corresponds to the probe in standard orientation, + markers. The negative slope corresponds to the probe in inverted orientation, x markers.

coefficients C_α , C_β , C_q for the dynamic pressure, and C_s for the static pressure. The INS mounted on the two-axis platform is the reference for the angles of the probe.

Determination of angle of attack and angle of sideslip of the 5-hole probe

To obtain α and β , the following coefficients are defined (Treaster et al., 1978):

$$C_\alpha = \frac{\Delta(P_4 - P_5)}{\Delta(P_1 - P_6) - \Delta P} \quad \text{and} \quad C_\beta = \frac{\Delta(P_2 - P_3)}{\Delta(P_1 - P_6) - \Delta P} \quad (2.11)$$

with $\Delta P = \frac{1}{4}(|\Delta(P_4 - P_5)| + |\Delta(P_2 - P_3)|)$. A polynomial fit is obtained for C_α and C_β to determine the angles α and β . For α and β within ± 10 deg, the calibration shows a nearly linear relationship (Fig.2.6). In the wind tunnel, the angle of attack α (5-hole probe) and the pitch angle θ (INS) are the same; as for the angle of sideslip β (5-hole probe) and the yaw angle ψ (INS) as the wind tunnel flow is laminar. The INS is used as a reference angle measurement between the 5-hole probe and the flow in the wind tunnel. Coefficients of a polynomial regression between α and C_α , and β and C_β are determined using a least squares minimization. To account for offsets in the alignment, experiments are performed with the probe in the standard orientation shown in Fig.2.3, with roll angle equal to 0 deg (markers + in Fig.2.6), and the probe in inverted orientation for the roll angle equal to 180 deg (markers x in Fig.2.6). Likewise, the same procedure is followed by rotating the 5-hole probe by 90 deg and -90 deg to determine the offset in the horizontal plane. INS angles and

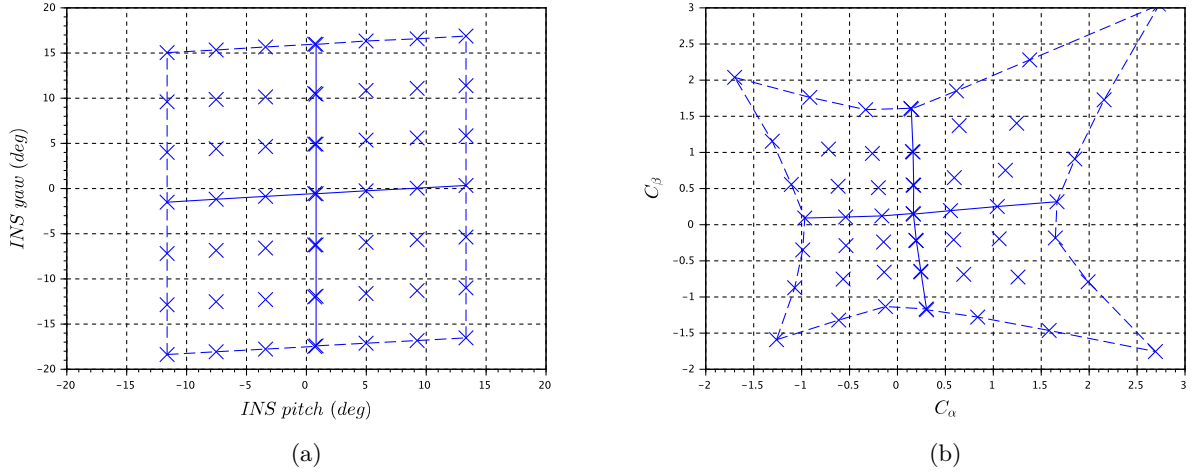


FIG. 2.7: (a) Variation by step of pitch and yaw angles of the multi-axis platform in wind tunnel, wind speed 15 m s^{-1} . (b) Corresponding C_α and C_β of the 5-hole probe to steps of the platform.

ratios of differential pressure sensors are recorded for platform positions between ± 15 deg for three air speeds in the wind tunnel. Figure 2.6 shows that calibration coefficients for the range of airspeeds in these experiments (between 15 and 25 m s^{-1}) are within instrument uncertainty, inducing less than 0.1 m s^{-1} difference in wind calculation. As the calibration coefficients are then similar in the range of operational airspeeds of the RPA, an average of the coefficients is selected for the flight analysis, and leads to a polynomial expression for determining α and β :

$$\alpha = 0.03C_\alpha^4 - 1.08C_\alpha^3 - 0.037C_\alpha^2 + 13.18C_\alpha + 0.046 \quad (2.12a)$$

$$\beta = 0.15C_\beta^4 - 1.05C_\beta^3 - 0.084C_\beta^2 + 12.83C_\beta - 2.57 \quad (2.12b)$$

The pitch and yaw angles of the two-axis platform are varied concurrently (Fig.2.7a), and the corresponding differential pressure coefficients C_α and C_β are measured (Fig.2.7b). This yields a matrix relating the probe's response to the relative vertical (α) and horizontal (β) winds on the probe (Fig.2.7). The grid in Fig.2.7a is due to the discrete 5 deg steps in pitch and yaw angles to create a 5×5 calibration matrix. The experiment is conducted at a constant wind speed of 15 m s^{-1} . The small angular bias in Fig.2.7 is due to a 3 deg roll angle in the mounting of the two-axis platform in the wind tunnel. The zero-angle offset between the probe and the INS is also visible as the grid of coefficients in Fig.2.7b is not centered on 0 . From Fig.2.7, the calibration coefficients show a nearly linear relationship C_α and C_β between ± 0.5 , which corresponds to α and β within ± 10 deg.

Determination of airspeed of the 5-hole probe

The measurement of airspeed by the 5-hole probe has been calibrated following the method described by Treaster et al. (1978). The coefficients C_q and C_s for calculation of dynamic and static pressures are defined :

$$C_q = \frac{\Delta(P_1 - P_6) - \Delta P_q}{\Delta(P_1 - P_6) - \Delta P} \quad \text{and} \quad C_s = \frac{P_6 + \Delta P - P_s}{\Delta(P_1 - P_6) - \Delta P} \quad (2.13)$$

The calibration coefficients account for the pitch and roll of the RPA during flights. There were no independent external measurements of the dynamic and static pressure in the wind tunnel during the experiment. Consequently, ΔP_q and P_s are calculated from the probe without any inclination (i.e., pitch and yaw equal zero), as the pressure in the wind tunnel remains constant for fixed wind speed:

$$\Delta P_q = \Delta(P_1 - P_6)_{\alpha=\beta=0} + (\Delta P)_{\alpha=\beta=0} \quad \text{and} \quad P_s = (P_6)_{\alpha=\beta=0} \quad (2.14)$$

As the angle of sideslip shows larger variations than the angle of attack during straight and level legs, the polynomial coefficients of C_q and C_s function of β have been averaged for α in the regime within ± 5 deg (Fig.2.8). The dynamic and static pressures are then calculated :

$$P_q = \Delta(P_1 - P_6) - C_q(\Delta(P_1 - P_6) - \Delta P) \quad (2.15a)$$

$$P_s = P_6 + \Delta P - C_s(\Delta(P_1 - P_6) - \Delta P) \quad (2.15b)$$

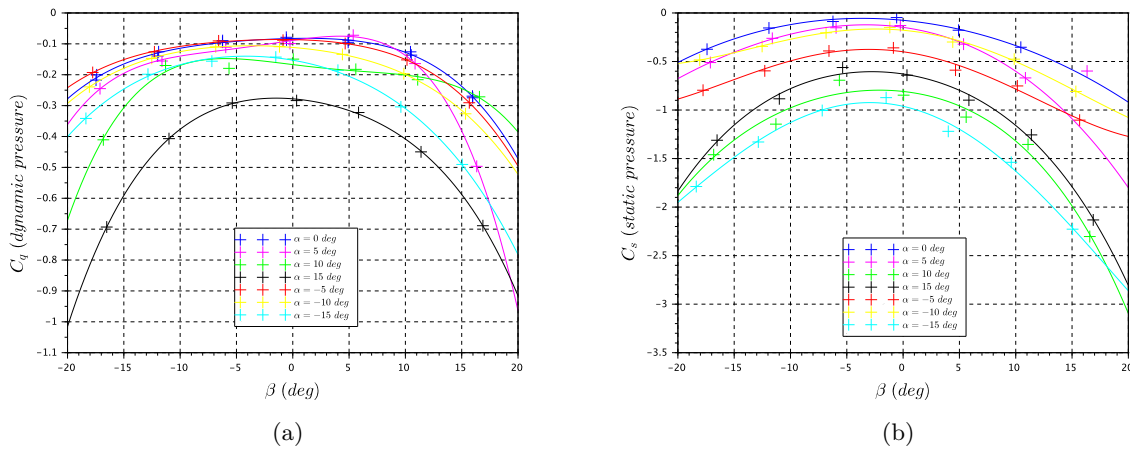


FIG. 2.8: Dynamic and static pressure coefficients function of angle of sideslip. Crosses correspond to measurement points, and the solid lines correspond to polynomial best fit.

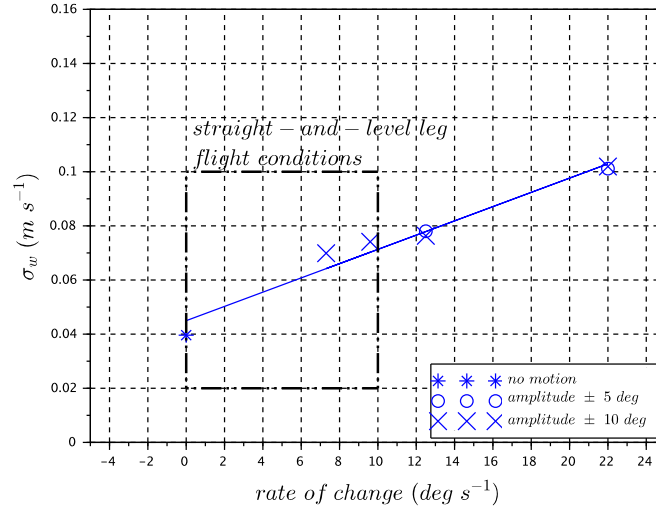


FIG. 2.9: Standard deviation of vertical wind vector w for each rate of change of the pitch angles on the two-axis platform. For the flight conditions presented in this study, the rate of change does not exceed 10 deg s^{-1} .

Finally, the airspeed, V_a , is calculated with the static pressure P_s and the dynamic pressure P_q (Eq.2.8) from Anderson (2001) (Eq.2.16a to 2.16c), with speed of sound a , Mach number M :

$$V_a = a \times M \quad (2.16a)$$

$$a = \sqrt{\gamma RT} \quad (2.16b)$$

$$M = \sqrt{\frac{2}{\gamma - 1} \left(\left(\frac{P_s + P_q}{P_s} \right)^{\frac{(\gamma-1)}{\gamma}} - 1 \right)} \quad (2.16c)$$

where $\gamma = 1.4$ is the specific heat ratio, $R = 287.07 \text{ J kg}^{-1} \text{ K}^{-1}$, T is the temperature in Kelvin, P_q is the dynamic pressure in Pa (Eq.2.15a), and P_s is the static pressure in Pa (Eq.2.15b). Variations of the wind tunnel airspeed between 12 and 34 m s^{-1} (operational range of RPA airspeed) provide an experimental estimation of the uncertainty associated with the probe airspeed. A systematic offset of 7 % has been found between the calculation of V_a and the wind tunnel airspeed. The 1- σ uncertainty in V_a is 0.1 m s^{-1} .

2.3.3 Experimental error analysis on vertical wind velocity

The performance of the 5-hole probe/INS pair is verified by using a dynamic platform to generate motion in the controlled environment of the wind tunnel. The wind tunnel provides a laminar flow, thus vertical wind velocity is, by definition, zero even when the two-axis platform is in motion. Therefore, the response of the 5-hole probe can be validated in the wind tunnel by controlling the amplitude (up to $\pm 15 \text{ deg}$) and the angular rate of change (up to 22 deg s^{-1}) of the platform in the vertical (pitch) axis. As expected, the estimates of vertical wind velocity, w , in the wind tunnel are

close to zero. The 1- σ standard deviation of w increases with the angular rate of change of the platform (Fig.2.9), which seems to be related to a lag in the INS's Kalman filtering process. Under the flight conditions reported in this work, the pitch angle rate of change rarely exceeds $\pm 10 \text{ deg s}^{-1}$ during straight-and-level legs, implying the minimum resolution of vertical wind velocity measurement with the 5-hole probe/INS system is 0.07 m s^{-1} . The uncertainties in w increase when accounting for all parameters, as shown in the next section.

2.3.4 Gaussian error propagation on vertical wind speed

As the RPA is specifically operated on straight-and-level legs to reduce the uncertainty in deriving 3D winds, the operational domain lies in the quasi-linear regime of the calibration coefficients (Fig.2.7). Therefore, the analysis described in Section 2.2.1 is used to conduct an uncertainty analysis on the simplified vertical wind equation (Lenschow et al., 1989) :

$$w = -V_a \sin(\theta - \alpha) + V_z \quad (2.17)$$

From Gaussian error propagation, 1-sigma uncertainty is determined by:

$$\sigma_w = \sqrt{\left(\frac{\partial w}{\partial \alpha} \sigma_\alpha\right)^2 + \left(\frac{\partial w}{\partial V_a} \sigma_{V_a}\right)^2 + \left(\frac{\partial w}{\partial \theta} \sigma_\theta\right)^2 + \left(\frac{\partial w}{\partial V_z} \sigma_{V_z}\right)^2} \quad (2.18)$$

1- σ of V_a is 0.1 m s^{-1} . σ_θ is provided by the INS manufacturer as 0.25 deg , and the uncertainty for the INS vertical velocity V_z is 0.1 m s^{-1} . The uncertainties are summarized in Table 2.1. The error propagation is conducted for α based on C_α in the linear regime (with the slope a_α , and the intersect b_α) :

$$\alpha = a_\alpha C_\alpha + b_\alpha \quad (2.19)$$

To be:

$$\sigma_\alpha = a_\alpha \sigma_{C_\alpha} \quad (2.20)$$

and, as C_α is calculated based on the differential pressures measured by the 5-hole probe :

$$\sigma_{C_\alpha} = \sqrt{\left(\frac{\partial C_\alpha}{\partial \Delta(P_4 - P_5)} \sigma_{\Delta(P_4 - P_5)}\right)^2 + \left(\frac{\partial C_\alpha}{\partial \Delta(P_2 - P_3)} \sigma_{\Delta(P_2 - P_3)}\right)^2 + \left(\frac{\partial C_\alpha}{\partial \Delta(P_1 - P_6)} \sigma_{\Delta(P_1 - P_6)}\right)^2} \quad (2.21)$$

TABLE 2.1: Uncertainty ($1\text{-}\sigma$) associated with parameters from 5-hole probe (5HP) and inertial navigation system (INS) for the calculation of error associated with the vertical wind velocity w .

Variable	Symbol	precision/value
differential pressure between holes 1 and 6 (5HP)	$\sigma_{\Delta(P_1-P_6)}$	1.2 Pa
differential pressure between holes 2 and 3 (5HP)	$\sigma_{\Delta(P_2-P_3)}$	1.4 Pa
differential pressure between holes 4 and 5 (5HP)	$\sigma_{\Delta(P_4-P_5)}$	1.2 Pa
ratio of differential pressures (5HP)	σ_{C_α}	0.013
angle of attack (5HP)	σ_α	0.16 deg
pitch angle (INS)	σ_θ	0.25 deg
airspeed (5HP)	σ_{V_a}	0.1 m s ⁻¹ systematic 7 %
vertical ground speed (INS)	σ_{V_z}	0.1 m s ⁻¹
coefficient calibration - slope	a_α	12.52
coefficient calibration - intersect	b_α	0.039
calculated vertical velocity	σ_w	0.12 m s ⁻¹

Finally, the Gaussian error propagation provides $\sigma_w=0.12\text{ m s}^{-1}$, which is in agreement with the experimental estimation of the uncertainty determined in Section 2.3.3.

2.4 Wind-RPAS platform

2.4.1 Skywalker X6 airframe

The RPA used here to measure the atmospheric wind is based on the commercially available Skywalker X6 model (Fig.2.3a); wingspan is 1.5 m. The take-off weight of the Skywalker X6 is 2.5 kg with a payload of 500 g. The cruise airspeed is approximately 16 m s⁻¹. The RPA is equipped with propellers at the back of the fuselage as to not perturb measurements of the 5-hole probe. Electric batteries (12000 mAh, 3S) allow the RPA to profile the atmosphere up to ca. 3000 m.asl or fly along straight-and-level legs for a total flight time of 1 hour to 1.75 hours depending on the meteorological conditions.

2.4.2 The open-source autopilot Paparazzi

The navigation system is the open source autopilot Paparazzi from Ecole Nationale de l'Aviation Civile in Toulouse (Brisset et al., 2006). The parameters for the flight operation of the RPA are defined before the flight and are uploaded to the Paparazzi autopilot. During the flight, modifications of the trajectories are possible; for example to change the altitude or direction of the legs depending on the location of cloud base, or to adapt the RPA parameters to meteorological conditions (particularly wind speed). The Paparazzi interface on the ground control station (GCS) during the flight is shown in Fig.2.10. The map allows to follow the RPA trajectory and to command the RPA during flight. Communication through the autopilot between the RPA and the ground control station is done by radio link. The radio link also allows a visualization, in real time, of the payload measurements on the GCS. Real time data are used to verify state of the instruments and to follow the evolution of the meteorological conditions (level of inversion, in/out of cloud, height of cloud base, etc.).

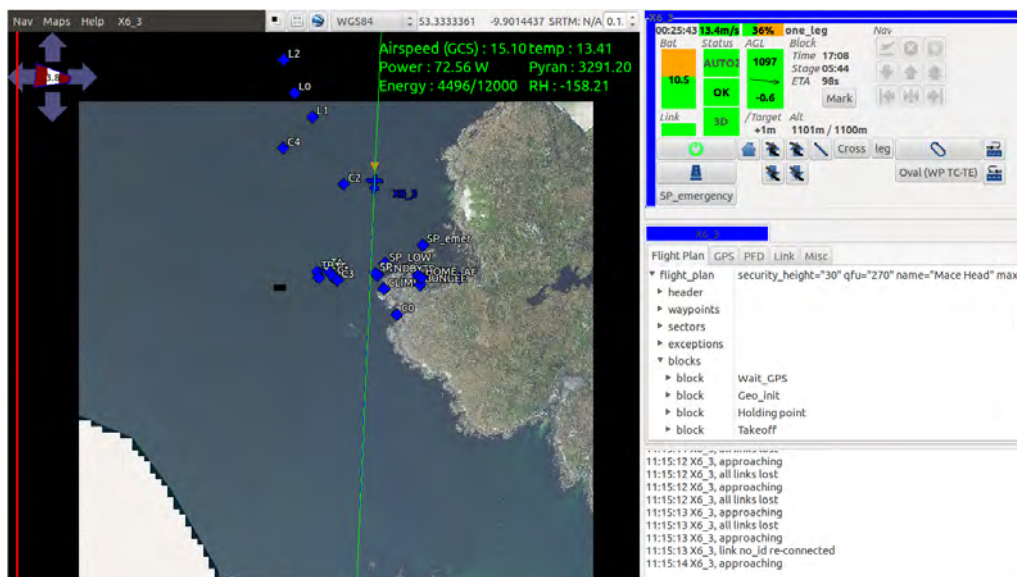


FIG. 2.10: Paparazzi ground control station screenshot during a flight.

2.4.3 Overview of flight operations

Fight operations are designed to conduct straight-and-level legs near cloud base for aerosol-cloud interaction studies. Flight plans of hippodromes or legs around a meteorological mast are implemented for comparison with sonic anemometers (Fig.3.1), and cross patterns for in-flight wind measurement calibration (Fig.2.11). A simulation of the flight plan finalizes each step of the flight to ensure well-prepared operations. The safety pilot is in charge of the take off before sending the RPA on the predefined scientific mission. The ground control station pilot watches over the automatic flight and adjusts the RPA parameters or the flight plan as necessary. During the flight, GCS and safety pilots communicate to ensure safety. A net landing system provides protection of the 5-hole probe mounted at the front of the RPA. After the flight, the high resolution payload data are recovered, and the RPA and instruments are prepared for the next flight. This routine includes detailed pre-and post-flight procedures and reports of the meteorological conditions, which provide complementary information for the data analysis. The small size of the RPAs allows us to operate on our own; however, this does require mastering flight operations, including understanding the autopilot, security checks and airspace regulations. Becoming a certified ground station pilot was necessary to conduct the experiments, which also helped understand to design the flight strategy and conduct the analysis of the atmospheric wind measurements with the RPA.

2.4.4 Instrumentation challenges

Ultra-light RPA (<2.5 kg) are easier to operate compared to bigger RPA as the logistic and the cost scale exponentially with the RPA weight. Consequently, this technical choice implies compromises for the payload, which is then limited to about 800 g. Commercially available instrument must be adapted to the small space available in the nose of the Skywalker X6 and the weight that the RPA is able to embark. Therefore, miniaturization of instruments is a key factor that has allowed the deployment of ultra-light RPAs for atmospheric science. For example, housings for the MetOne

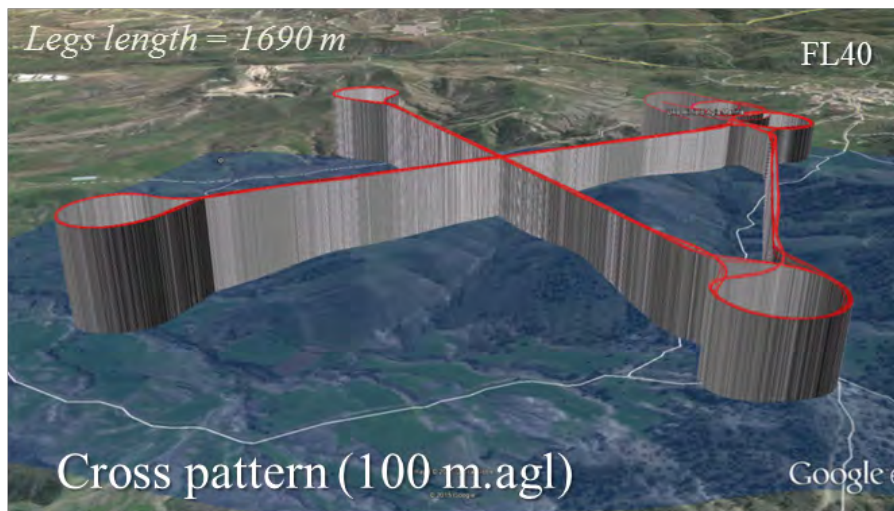


FIG. 2.11: Flight plan in cross pattern for in-flight wind measurement calibration, BACCHUS field campaign, Agia Marina, Cyprus, March 2015.

optical particle counter were removed and the electronics repackaged to fit inside the fuselage. On the other hand, some miniature instruments, such as the Lord MicroStrain INS (4.4x2.4 cm, 20 g), which was used for atmospheric wind measurements are not as accurate as larger INS (17x9 cm, 2 kg) that have been deployed in larger RPAs or research aircraft. For example, the accuracy on heading measurements improves from 0.8 deg for small INS to 0.025 deg for larger, more expensive models. Therefore, it is important to assess if the instrument provides measurements accurate enough for the expected scientific results. Calibration in a controlled environment and comparison with other instruments (sonic anemometers on a tower) are essential steps to validate the measurements, such as in the present case, the 5-hole probe/INS combination for atmospheric wind velocities.

2.5 The BACCHUS field campaigns challenges

For scientific reasons, it was essential to operate next to the Mace Head Research Station to insure that the RPA measurements were characterizing the same aerosol populations as the ground-based instruments. Risk assessment is also part of the decision for conducting operations based on environment factors. For example, the team was required to development a net landing system to protect the 5-hole probe as there was no runway or flat field suitable for normal operations surrounding the Mace Head Research station. Insuring the vertical mixing of the atmosphere is also important to verifying that the ground-based instruments are measuring the same parameters as the RPAs, particularly at cloud base. Consequently, flight operations often start with a vertical profile to check the mixing stated of the boundary layer. Meteorological conditions also dictate the RPA measurements, the main constraint being wind, as the RPAs we used in these experiments do not handle well wind speeds higher than 15 m s^{-1} . In addition, operations in the marine environment at Mace Head sped up the deterioration of the electronics as sea salt corroded circuit boards and cables.

2.6 Conclusions and perspectives

This instrument development chapter describes the implementation of a commercial 5-hole probe with custom electronics, paired with an INS (GPS/IMU), on a RPA. The aim of the instrument development is to develop a probe that measures 3D atmospheric wind vector, with a particular focus on the measurement of vertical wind velocity for aerosol-cloud interaction studies. The calibration of the 5-hole probe in wind tunnel provides the polynomial coefficients for the calculation of the angle of attack (vertical axis; α), the angle of sideslip (horizontal axis; β), and the airspeed V_a based on the differential pressure measurements for each of the three axes on the probe. Lenschow et al. (1989) describe a method to transform wind measurements from the multi-probe coordinate system to the Earth's coordinate system. We show that for conditions of straight-and-level legs (e.g., pitch and roll are less than 10 deg), simplified equations may be used to calculate 3D winds and perform an uncertainty analysis. The minimum resolution for measuring vertical wind velocity w is ca. 0.12 m s^{-1} . The error associated with w in our study is sufficient for aerosol-cloud closure studies; nonetheless, higher resolutions have been achieved in other studies (Reineman et al., 2013). The main difference lies in the choice of INS units for wind measurements. The RPAs used in Reineman et al. (2013) were equipped with high accuracy dGPS/IMU, providing precision of aircraft motion on velocity scales of cm s^{-1} and attitude angles less than 0.01 deg. Such technology now exists in smaller packages, which are deployable on ultralight RPA. One SBG System dGPS/IMU unit is currently under test to improve wind measurements for the ultralight wind-RPA. Developments are also on-going to design a custom probe with optimized hole placement and embedded electronics, which will further improve the wind measurement resolution and provide higher accurate vertical wind results.

Chapter 3

Validation of RPA wind measurements in the atmospheric boundary layer

Contents

3.1	Centre de Recherches Atmospheriques de Lannemezan — Validation of RPA wind measurements	33
3.2	Vertical wind velocity distributions	34
3.3	Power spectral density functions	37
3.4	Turbulent kinetic energy (TKE)	41
3.5	Conclusions and perspectives	45

Since mid-2000s, RPAS have been successfully deployed to study the atmospheric boundary layer (ABL), with a focus mainly on turbulence and heat fluxes measurements. These measurements have been conducted using lightweight RPAS (< 25 kg) equipped with multi-hole probes (described in Chapter 2). As the RPA platforms for ABL studies carry similar instrumentation (5-hole probe and INS), it is interesting to compare our own results with the peer-reviewed literature.

One of the first studies to demonstrate the ability of RPA to measure turbulent properties and latent heat fluxes is presented in Thomas et al. (2012). The Manta RPA was developed with a payload composed of a turbulence probe (Aeroprobe Corporation), dGPS/IMU, and a fast response water vapor sensor. A good agreement with sonic anemometers was obtained on turbulence measurements, and the uncertainty associated with the vertical wind velocity was low, 0.17 m s^{-1} . Further payload instruments are implemented on RPA to extend the analysis of ABL to measure momentum fluxes, latent, sensible and radiative heat fluxes, as for the Manta and the ScanEagle RPAs for example (Reineman et al., 2013). Three types of payload are presented (flux, radiometric and imaging payloads) achieving a details investigation of the boundary layer fluxes and wave field kinematics.

The Meteorological Mini unmanned Aerial Vehicle (M^2AV), a lightweight RPA, developed by the University of Tübingen in Germany is equipped with high resolution wind and temperature measurements (a custom 5-hole probe (Kroonenberg et al., 2008), a Vaisala HMP 50 for temperature and humidity measurements, and a thermocouple for temperature fluctuations (Spiess

et al., 2007)). To study the morning and evening transitions in ABL, profiles of temperature, relative humidity, wind direction and horizontal wind speed of the M²AV are compared with in-situ and remote sensing systems (Martin et al., 2011). The M²AV measurements show a good agreement with the reference platforms. Further analysis of the transition zone between the convective boundary layer and the stably stratified free atmosphere are presented in Martin et al. (2014) with the ability for the M²AV to capture small-scale turbulence processes and sharp gradients. Successful calculation of vertical velocity variance and sensible heat flux, in agreement with the literature (Lenschow et al., 1980), demonstrates an accurate measurement of vertical wind velocity.

Morning transition of the ABL is also studied in Wildmann et al. (2015) with the Multi-purpose Airborne Sensor Carrier (MASC). The thermodynamic payload development and validation is described for the 5-hole probe in Wildmann et al. (2014) and Kroonenberg et al. (2008), and for the thermometer and the thermocouple in Wildmann et al. (2013). The MASC successfully observe the development of thermal stratification of the atmosphere, along with sensible heat flux in agreement with analysis based on helicopter-borne measurement (Bange et al., 2007). The Small Unmanned Meteorological Observer (SUMO) RPA is developed by the University of Bergen, Norway. The platform is initially deployed to complement meteorological towers and radiosondes measurements (Reuder et al., 2008). Arctic zones, with profiles of temperature, relative humidity and wind are studied in Reuder et al. (2012), and are validated with sonic anemometer comparison.

During the BLLAST field experiment (Lothon et al., 2014), the SUMO, the MASC and the M²AV RPAs provided an extensive study of the ABL. In Reuder et al. (2016), a high temporal resolution of the atmosphere is provided by intensive flights of the SUMO. Profiles of energy fluxes present detailed information on diurnal development of the ABL. Wind measurements on horizontal legs are used for calculation of turbulent kinetic energy (TKE). Båserud et al. (2016) then focuses on TKE calculation with the SUMO during the BLLAST campaign, addressing uncertainties and limitations of the platform. These results are compared to our results in Section 3.7 of the thesis. The M²AV is deployed to study the transition between a turbulently mixed atmosphere to a stably stratified atmosphere (afternoon-evening transition) during BLLAST. Profiles of temperature, wind speed and direction are shown in Lampert et al. (2016), results of TKE study and anisotropy are also presented, with a clear identification of the influence of a low level jet (LLJ) on these parameters —anisotropy ratio enhanced by LLJ and TKE incremented after sunset by its presence.

RPA platforms carrying wind payload measurements are also used in aerosol-cloud field (Manta in Ramanathan et al. (2007), Corrigan et al. (2007) and Roberts et al. (2008), and ALADINA in Altstädter et al. (2015)), however more wind measurement results are available in the ABL field to compare and validate the development of a new RPA platform. The studies in ABL cited previously show extensive comparisons between the RPA and ground-based instruments (sonic anemometers on towers or cars), remote-sensing instruments (wind profiler and sodar), or other airborne measurements (tethered balloon, helicopter-borne instruments, radiosonde, or manned aircraft). Therefore, to validate the present RPA wind measurements, a comparison with sonic anemometers

on a mast at 30 and 60 m.agl (meters above ground level) is conducted. The results presented here only aim to assess the ability of the wind-RPA to measure 3D wind vectors compared to the literature. As the scientific objectives focus on aerosol-cloud interactions, high resolution is not expected as for turbulence measurements, and parameters presented hereafter do not constitute a scientific study of the ABL.

3.1 Centre de Recherches Atmospheriques de Lannemezan — Validation of RPA wind measurements

The purpose of the comparison between the wind-RPA and sonic anemometers is to validate atmospheric wind measurements with RPA. We concentrate on the analysis of three parameters: 1) vertical wind velocity distributions (PDF), 2) power spectral density (PSD) functions, 3) turbulent kinetic energy (TKE).

The validation of the RPA wind measurements was conducted at the Centre de Recherches Atmospheriques (CRA), an instrumented site of the Pyrenean Platform of Observation of the Atmosphere (P2OA), near Lannemezan, France. A 60 m meteorological tower is instrumented to measure atmospheric state parameters as well as turbulence at multiple levels. In particular, sonic anemometers at 60 m.agl and 30 m.agl (Campbell CSAT3 3-D Sonic Anemometer) were used to validate the RPA measurements of 3D winds. The measurement uncertainties for the sonic anemometers provided by the constructor are 0.04 m s^{-1} for u and v -components, and 0.02 m s^{-1} for w -component. As the errors associated with the sonic anemometers are low, the instruments are considered as a reference for the analysis in this chapter. Five flights have been selected for this analysis based on availability of the data and variability of the state of the atmosphere; these flights are summarized in Table 3.1. During the experiment, the wind-RPA flew straight N-S and E-W legs at 60 m.agl in the vicinity of the mast. The flight paths were in the form of hippodromes in both cardinal directions for Flights 1 to 3 (Fig.3.1), and as N-S legs for Flights 4 and 5. The leg length was 1600 m. The duration of each leg was approximately 100 secs with a total flight duration of approximately 1.5 hours. The five flights were conducted at different times of the day and in different seasons, including three flights conducted on 15 October 2015 spanning morning and afternoon development of the boundary layer, one flight in the morning on 20 May 2016, and the last flight was in the afternoon on 7 July 2016 (Table 3.1). While all flights were conducted in low wind conditions, the turbulent conditions differed from one flight to another. Each flight presented specific constraints for the analysis particularly related to missing data or flight characteristics of the RPA. On 15 October 2015, the sonic anemometer at 60 m.agl did not operate, therefore comparison is done between the wind-RPA flight at 60 m.agl and the sonic anemometer at 30 m.agl (Flight 1 to 3). On 20 May 2016, the wind-RPA flew with an airspeed close to stall speed (ca. 12 m s^{-1}), which impacted the 3D wind measurements of Flight 4. Before the flight on 7 July 2016, the INS had been re-parametrized and the magnetometer re-calibrated, which improved the accuracy of the attitude angles for Flight 5.

TABLE 3.1: Description of flights conducted at P2OA, Lannemezan, France.

ID	Date	Time (local)	Duration	Horizontal wind speed	Wind direction	Remarks
Flight 1	15 Oct 2015	08:05	1h30	0.6 m s ⁻¹	NE	sonic anemometer at 30 m.agl only
Flight 2	15 Oct 2015	12:47	1h22	1.9 m s ⁻¹	N	sonic anemometer at 30 m.agl only
Flight 3	15 Oct 2015	15:35	1h18	2.7 m s ⁻¹	NW	sonic anemometer at 30 m.agl only
Flight 4	20 May 2016	09:15	1h35	3.2 m s ⁻¹	SW	airspeed close to stall speed
Flight 5	7 Jul 2016	15:18	1h06	1.7 m s ⁻¹	NE	magnetometer re- calibrated

3.2 Vertical wind velocity distributions

Vertical wind velocity distributions (PDFs) are compared between sonic anemometers and wind-RPA for the five flights described in Table 3.1. To calculate w from the wind-RPA, angle of attack α and pitch angle θ are calculated such that average vertical velocity w is 0 m s⁻¹ over the length of the leg (1.5 km or larger). This re-centering step is needed because the alignment of the 5-hole probe with reference to Earth's frame may change with meteorological conditions (such as wind speed) and flight parameters (such as airspeed and nominal pitch angles owing to subtle changes in the wings and control surfaces of the RPA). The re-centering step of the 5-hole probe on the RPA is further supported by results from the sonic anemometers on the mast, which also show vertical velocity approaching 0 m s⁻¹ over similar length scales (based on nominal wind speed and averaging time). Distributions of vertical wind velocity from RPA and sonic anemometers are compared in Fig.3.2. Overall, the shape of the histograms, particularly, the width of the histograms between the RPA and sonic anemometers compare well. As expected, the wind-RPA does not measure the low vertical wind velocities (between ca. ± 0.3 m s⁻¹) as precisely as the sonic anemometer. For one of the flights (Flight 4), the calculation of w is biased by the extra-motion induced on the wind-RPA due to an airspeed that was close to the stall speed, which creates an unstable platform. As the flights occur in different turbulent conditions, it is important to point out the variation of distribution shapes (Fig.3.2).

The 'intersection method' is used to quantify the relative agreement between histograms (i.e., the vertical velocity distributions). For an exact match, the intersection method result is 1, for a complete mismatch, the result is 0. The calculation of the intersection number is obtained from $\sum_{i=1}^N \min(I_i, M_i)$ with I and M as the normalized distributions to be compared, and N as the total number of bins. Table 3.2 summarizes the intersection numbers between the wind-RPA and anemometer vertical wind PFD. The intersection numbers between RPA and anemometer vertical wind distribution are higher than 70 %, indicating relatively good agreement between the wind-RPA and the sonic anemometer on the mast. Note that the intersection number does not account for the shape of the distributions,

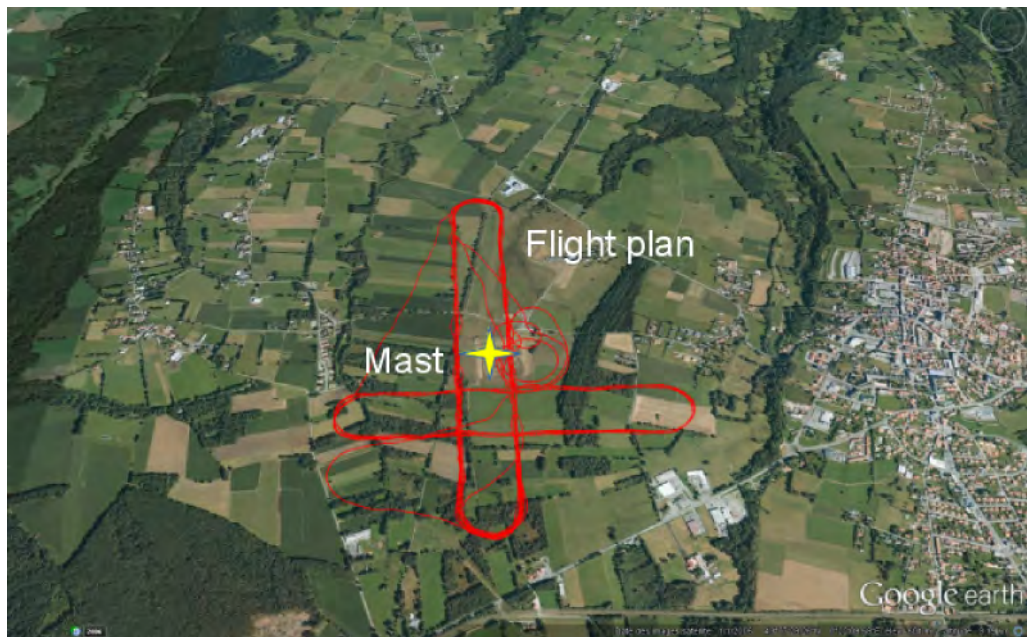


FIG. 3.1: N-S and E-W hippodromes flight plan in the vicinity of a 60 m.agl meteorological mast, conducted at CRA, Lannemezan, France

TABLE 3.2: Intersection numbers for comparison of PDFs for five flights conducted at P2OA, Lannemezan, France.

ID	Intersection number
Flight 1	0.72
Flight 2	0.79
Flight 3	0.90
Flight 4	0.71
Flight 5	0.88

and similar numbers may correspond to different conditions. It is observed between Flight 1 (early morning flight, low vertical wind, which is better measured by the sonic anemometer rather than the RPA), and Flight 4 (RPA close to stall speed, which produces mistakenly wide distribution).

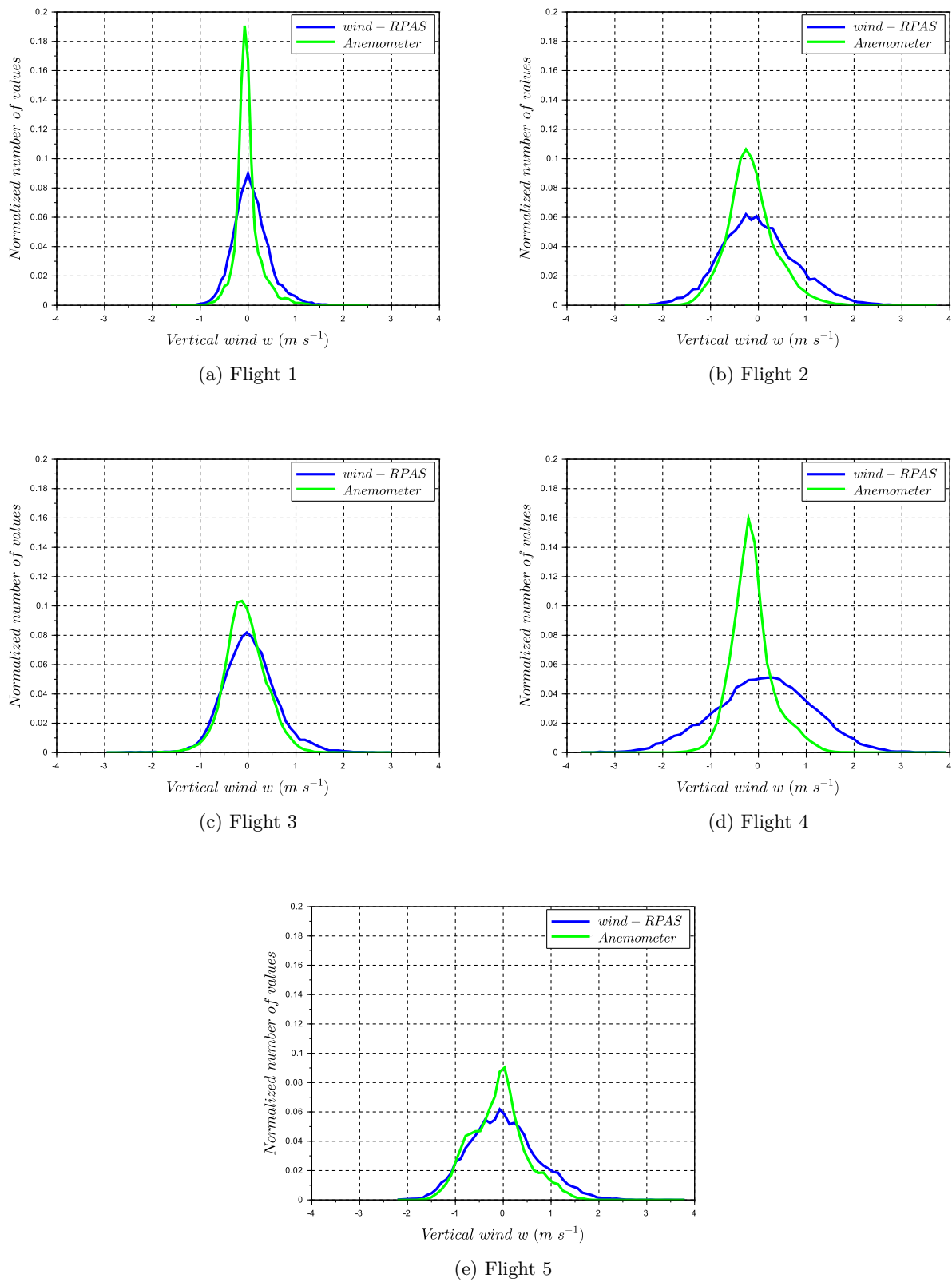
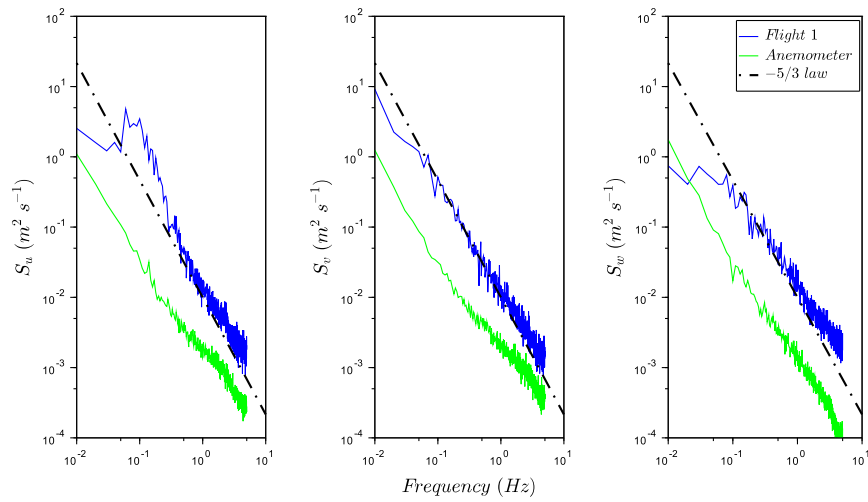


FIG. 3.2: Vertical wind velocity distributions for five flights at CRA Lannemezan, comparison between sonic anemometer and wind-RPA.

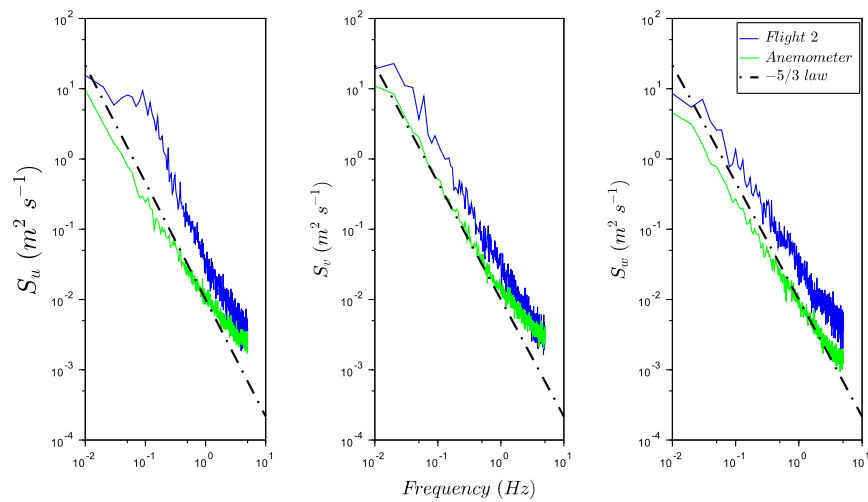
3.3 Power spectral density functions

In this section, the Power Spectrum Density (PSD) functions of wind-RPA are compared to PSD from sonic anemometers. The PSDs transform the wind components into a frequency domain, and reveal the contribution of the RPA in the wind velocity components. In a well-mixed boundary layer, PSD is expected to follow the $-5/3$ slope from Kolmogorov law. The PSD functions from the RPA and sonic anemometers were averaged with the Welch's method, and shown in Fig.3.2. For several flights (Flights 2, 3 and 5), biases are visible higher than 1 Hz (Fig.3.2b, c and e), particularly on the v -component, which are primarily related to the INS noise. For Flights 1, 2, 3 and 4, the RPA motions are still visible at 0.1 Hz in the horizontal u -component due to inaccuracy of the heading measurement in the INS. Flight 5 was conducted after improved after a new parametrization of the INS and a calibration of the magnetometer measurement. A notable improvement in the PSDs (Fig.3.2e) clearly demonstrates the importance of precise heading measurements. The PSDs of the wind velocities from RPA and sonic anemometers follow the $-5/3$ slope as expected from the Kolmogorov law. We note, however, that the PSD from the RPA is overall higher than the wind from anemometer.

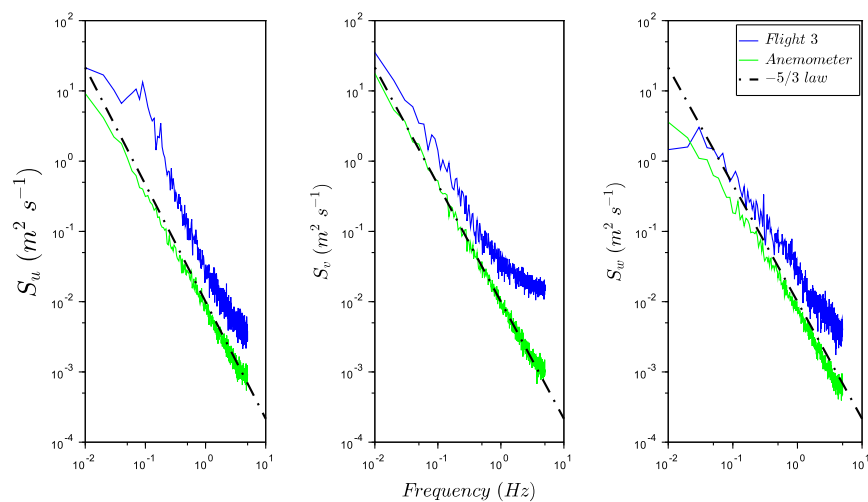
For the three wind components calculated from RPA measurements, the energy level of ground speeds obtained from the INS (V_x , V_y , and V_z) are higher than the other terms in wind equations for frequencies less than 0.3 Hz. To assess the origin of the different energy levels, the decomposition of the vertical wind equation w (Lenschow et al., 1989) is based on the simplified form shown as Equation 2.9. PSDs of each component of w , V_z (vertical ground speed) and A_w (defined as $-V_a \sin(\theta - \alpha)$), are calculated to assess biases related to the INS (Earth frame) and the 5-hole probe (RPA frame). The average results from the RPA flights and the sonic anemometers are presented in Fig.3.3. The high energy levels at low frequencies seem to be related to uncertainties (even a drift) associated with the vertical velocity measurement. The higher energy levels do translate to systematically higher TKE values (Section 3.4); however, these concerns do not significantly impact the results in aerosol-cloud interaction studies (Chapter 5). The relatively high energy levels associated with the PSDs are not unique; yet, it has not been adequately explained in the literature.



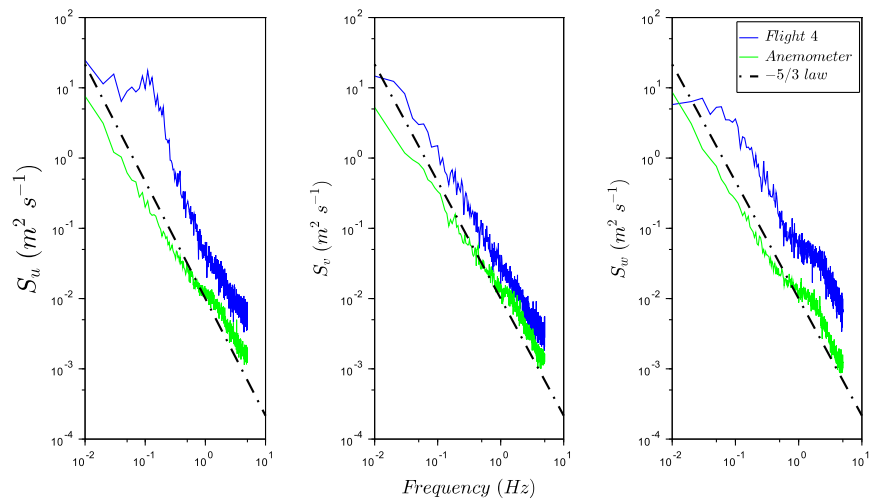
(a)



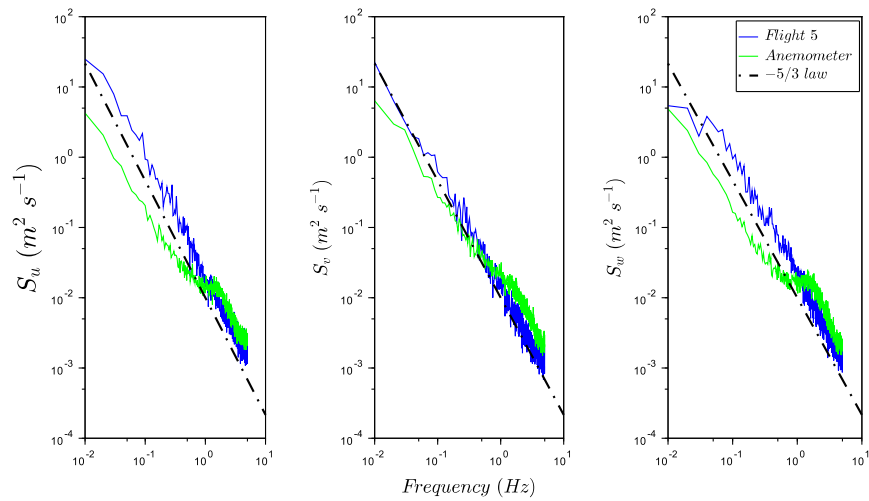
(b)



(c)



(d)



(e)

FIG. 3.2: Power spectral density function for five flights at CRA Lannemezan, comparison between sonic anemometers and wind-RPA wind measurements. a) Flight 1, b) Flight 2, c) Flight 3, d) Flight 4, e) Flight 5.

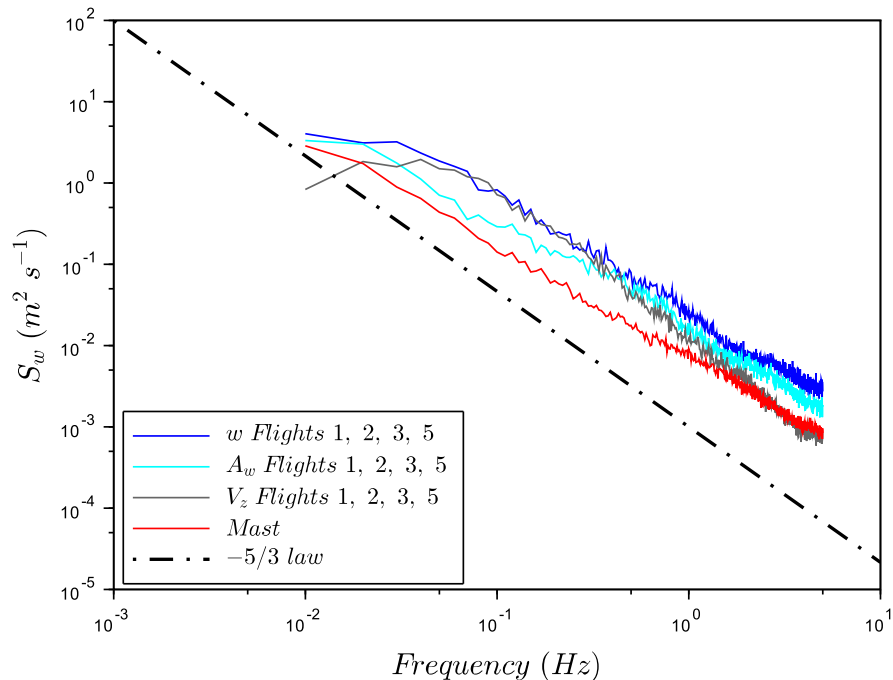


FIG. 3.3: Comparison of averaged PSDs from sonic anemometers (Mast : red) and RPA wind measurements averaged for Flights 1, 2, 3 and 5 (blue). Spectral energy S of decomposed w -wind component with $w = A_w$ (cyan) + V_z (grey) function of frequency. The dashed line represents the $f^{-5/3}$ law.

Båserud et al. (2016) and Reuder et al. (2016) reported systematically high energy levels of the vertical wind component from the SUMO compared to sonic anemometers on a mast (also at CRA in Lannemezan, France). The issue of higher energy levels was then to “be further investigated in the future.” Other studies have compared turbulent kinetic energy (TKE) values between RPA platforms and a reference; the TKE is linked to PSD energy levels via the variance of each wind component. For example, Lampert et al. (2016) compare TKE between 5-hole probe on the M²AV and sonic anemometers (also on the mast at CRA, Lannemezan) and show higher TKE values associated with the M²AV during the afternoon and the night, which also implies higher energy levels of the PSDs. Canut et al. (2016) also compare 5-hole probe measurements of M²AV and manned aircraft (Piper Aztec) to sonic anemometer measurements on a tethered-balloon. The TKE measurements from the M²AV compare well to the tethered balloon measurements (which indirectly compare well to the sonic anemometer on the mast); however, the results show that TKE measured from the manned aircraft were biased towards higher TKEs. Thomas et al. (2012) conclude that direct comparisons between the RPA and the sonic anemometer are tenuous in their study as the Manta RPA flew at 520 m.agl, while the sonic anemometer was only at 10 m.agl. Reineman et al. (2013) is the only study that shows similar vertical wind component PSD between a RPA and a ground-based mast (albeit for a relatively short flight above a flat desert). The main difference between the RPAs listed above and the system described in Reineman et al. (2013) is the INS, as no other group has deployed as precise an INS. Since the energy levels of the PSDs for the

configuration presented in this manuscript, are higher, one cannot calculate divergence/convergence; however, the PSDs from the measurements presented here show slopes approaching the expected -5/3 Kolmogorov regime and the RPA observations reproduce trends in TKE over a range of meteorological conditions. There is certainly more work that needs to be done to improve the turbulence measurements – particularly by improving the INS measurements.

3.4 Turbulent kinetic energy (TKE)

In the atmospheric boundary layer, the turbulent kinetic energy (TKE) quantifies the intensity of turbulence, which controls mixing of the atmosphere (Wyngaard et al. (1971); Lenschow (1974)). TKE is defined as:

$$TKE = \frac{1}{2}(\sigma_u^2 + \sigma_v^2 + \sigma_w^2) \quad (3.1)$$

with σ_u^2 as the variance of E-W wind, σ_v^2 as the variance of N-S wind, and σ_w^2 as the variance of vertical wind. For the climate prediction, TKE is used in mesoscale model (MesoNH) as a prognostic scheme to determine the boundary layer depth (Couvreur et al., 2016). In the atmospheric general circulation model (CAM-5.1 AGCM), TKE defines the vertical velocity used to drive the activation process of aerosols into cloud droplet for studying aerosol-cloud interactions (Morales-Betancourt et al., 2014). As TKE is an important parameter in models, experimental measurements are needed to reinforce model predictions. Airborne platforms, such as manned aircraft, meteorological balloons and RPA, provide the 3D wind measurements necessary for TKE calculations. Previous results of TKE at P2OA, Lannemezan have been published for the BLLAST campaign, and TKE from the SUMO and M²AV have been compared to the sonic anemometer at 60 m.agl (Båserud et al. (2016); Lampert et al. (2016)). The reported values of TKE from the SUMO and M²AV are within 50 % of TKE from the sonic anemometers. Canut et al. (2016) also showed a good agreement of TKE between a tethered balloon and the M²AV, as well as, a manned aircraft (Piper Aztec aircraft from SAFIRE). Correlation coefficients (R^2) between the tethered balloon and the sonic anemometers for the three variance components were between 0.8 and 0.9, as reported in Canut et al. (2016). In this study, for the comparison between the wind-RPA and sonic anemometers (Fig.3.7), the slope of the linear regression for the RPA observations is 1.32 ($R^2 = 0.97$) and improves to 0.95 ($R^2 = 0.91$) with the isotropy assumption ($\sigma_{u,RPA}^2 = \sigma_{v,RPA}^2$).

Variations of each wind components, u, v, w , for the sonic anemometers on the mast at 30 m.agl and 60 m.agl and the RPA are shown in Fig.3.4. Each data point corresponds to the variance on one leg. The variance on v -component (N-S wind component) is ca. 10 % higher in general than variance from the anemometer, while the variance related to the u -component (E-W wind component; $\sigma_{u,RPA}^2$) is up to a factor of ten higher than that of the mast. The variances of the w -component ($\sigma_{w,RPA}^2$ and $\sigma_{w,mast}^2$) are the same within the measurement uncertainties. As

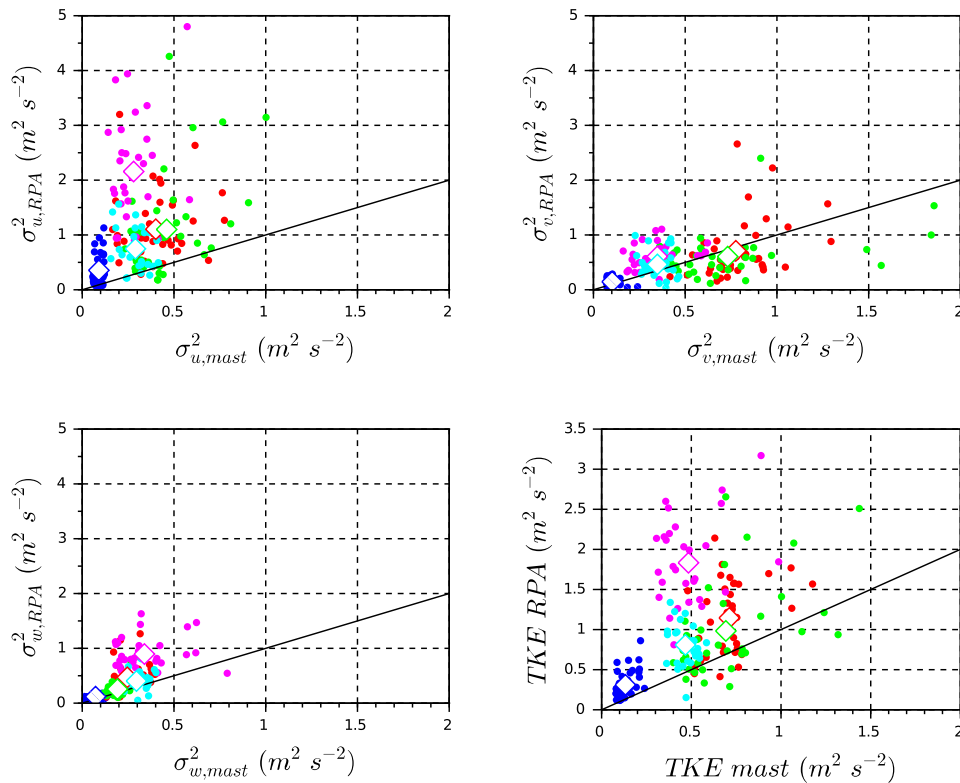


FIG. 3.4: Variances of each wind components, u, v, w , comparison between sonic anemometers on the mast and RPA. Each color corresponds to one flight, blue=Flight 1, red=Flight 2, green=Flight 3, magenta=Flight 4, cyan=Flight 5. Each dot corresponds to one leg measurement. Diamonds correspond to the mean value per flight.

variances of RPA measurements of u and v (horizontal wind components) are larger, the resulting value of TKE is also larger for the RPA compared to the mast. Higher variances for RPA depend on relative flight directions, as wind measurements on the transversal direction (normal to the axis of the RPA fuselage) are less accurate compared to measurements on the longitudinal direction (parallel to the axis of the RPA fuselage). The increase in variances in the transversal wind direction is related primarily to uncertainties in the INS measurements of the RPA heading relative to the Earth's coordinate system. This drift in INS heading manifests itself as sawtooth pattern in the estimation of the horizontal winds over a series of legs, as well as the bump in the PSD distribution for the u -component in Fig.3.2. Note when the RPA is flying along N-S legs, the transversal wind in RPA coordinate system is the E-W wind component; likewise, the transversal wind in the N-S wind component corresponds to RPA flights along E-W legs.

As the drift in INS heading increases the variances of the horizontal wind components and results in an artificially high value of TKE, a method has been explored to compensate for this systematic bias. To explore the increase in variances on the transversal wind direction of RPA, an isotropy assumption ($\sigma_u^2 = \sigma_v^2$) is tested using the wind measurements from the sonic anemometers at multiple levels on the mast. The TKE values at 30 m.agl and 60 m.agl on the mast are calculated

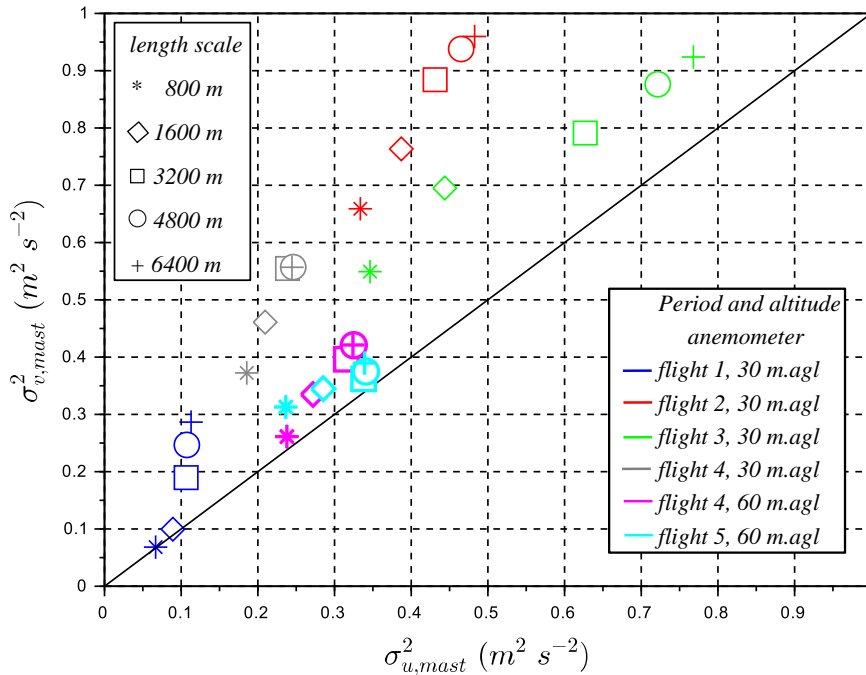


FIG. 3.5: Comparison of variances $\sigma_{u,mast}^2$ and $\sigma_{v,mast}^2$ from the sonic anemometers for the associated flight periods.

for different length scales. The horizontal length scales are the product of nominal wind speeds and time periods that correspond to the length of each leg.

The variances on u (E-W wind component), and v (N-S wind component) of the sonic anemometers are shown in Fig.3.5. At 30 m.agl, the variances ($\sigma_{u,mast}^2$ and $\sigma_{v,mast}^2$) increase with the length scale, creating a range in variances between 0.1 to 0.4 $\text{m}^2 \text{s}^{-2}$ depending on the flight. The isotropy assumption is not satisfied at 30 m.agl. However, at 60 m.agl, the range in variances remains less than 0.1 $\text{m}^2 \text{s}^{-2}$ for $\sigma_{u,mast}^2$ and 0.15 $\text{m}^2 \text{s}^{-2}$ for $\sigma_{v,mast}^2$ across all length scales. The isotropy assumption between the N-S and E-W directions is confirmed when variances in u and v are similar and implies isotropy for altitudes in the boundary layer above 60 m.agl. Differences observed in variances between the horizontal wind components at 30 m.agl are related to surface topography (e.g., nearby trees, fields, and changes in the terrain in the immediate vicinity of the mast). The validation of the isotropy assumption at 60 m.agl using the sonic anemometers allows one to apply a relationship of $\sigma_{u,RPA}^2 = \sigma_{v,RPA}^2$, such that only wind components in the longitudinal direction (i.e., parallel to the axis of the RPA fuselage) are selected to calculate TKE_{RPA} (Fig.3.6).

To compare TKE calculated from the wind-RPA (TKE_{RPA}) and TKE from the sonic anemometer on the mast (TKE_{mast}), a length scale for calculated TKE on the mast is selected based on the length of the leg flown by the RPA (i.e., 1600 m). The RPA generally flies at an airspeed of 16 m s^{-1} , which translates to nearly 100 seconds per leg. The time necessary for the

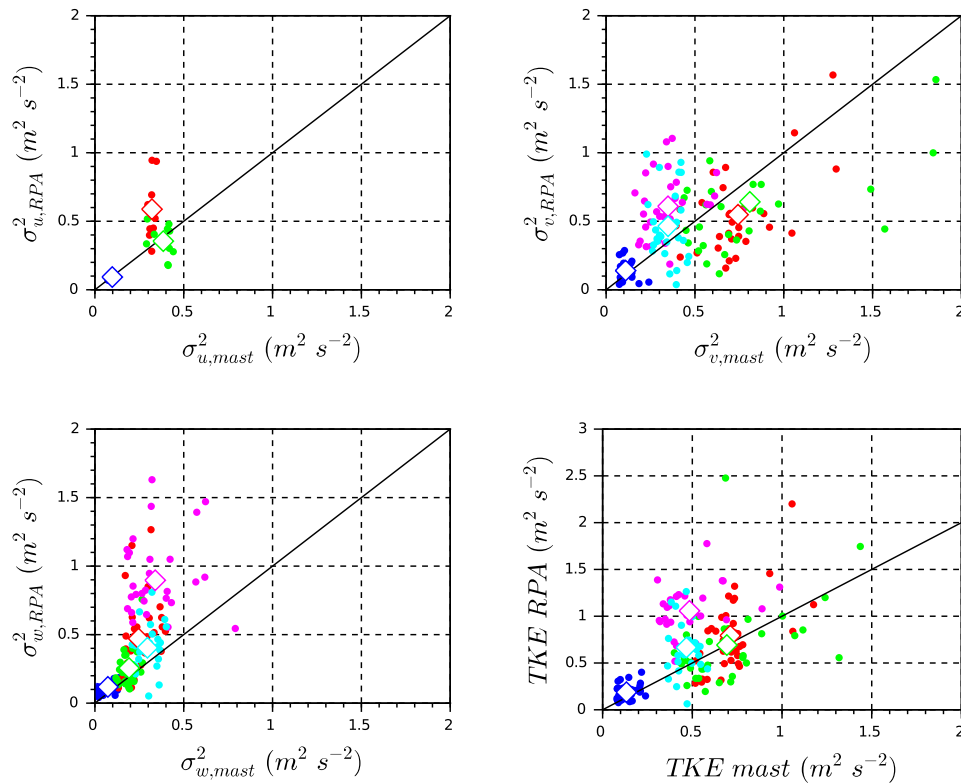


FIG. 3.6: Variances of each wind components, u, v, w , comparison between sonic anemometers on the mast and RPA with only wind components in the longitudinal direction (i.e., parallel to the axis of the RPA fuselage). Each color corresponds to one flight, blue=Flight 1, red=Flight 2, green=Flight 3, magenta=Flight 4, cyan=Flight 5. Each dot corresponds to one leg measurement. Diamonds correspond to the mean value per flight.

anemometer to sample wind traveling the equivalent distance for each reference leg length is calculated using the horizontal wind speed at 30 or 60 m.agl (Table 3.1). TKE is then calculated leg-by-leg before being averaged. For example, the horizontal wind velocity during Flight 5 is 1.7 m s^{-1} ; thus, TKE_{mast} is calculated based on the time required for the air to travel 1600 m, which is 940 s. The variances of the horizontal wind components from the mast are obtained for length scales between 800 m to 6400 m at 30 m.agl and 60 m.agl. The uncertainty bars in Fig.3.7 correspond to 1-sigma, using all the legs during the RPA flights, and using each length scale from 800 m to 6400 m for the sonic anemometers. After obtaining a value of TKE for each leg, the values are averaged to show a single TKE over the entire flight for both the mast and RPA (Fig.3.7). The slope of the linear regression between TKE_{RPA} and TKE_{mast} , without Flight 4, is 1.32 ($R^2 = 0.97$), which is similar to results reported by other studies at P2OA (Lampert et al. (2016); Båserud et al. (2016)).

The open diamonds in Fig.3.7 corresponds to TKE calculated with the three wind components of RPA measurements (no isotropy assumption); the solid diamonds are obtained imposing the isotropy assumption. A clear improvement in the estimation of TKE result from using the isotropy assumption. It is worth noting that the TKE calculated for Flight 4 is significantly different from

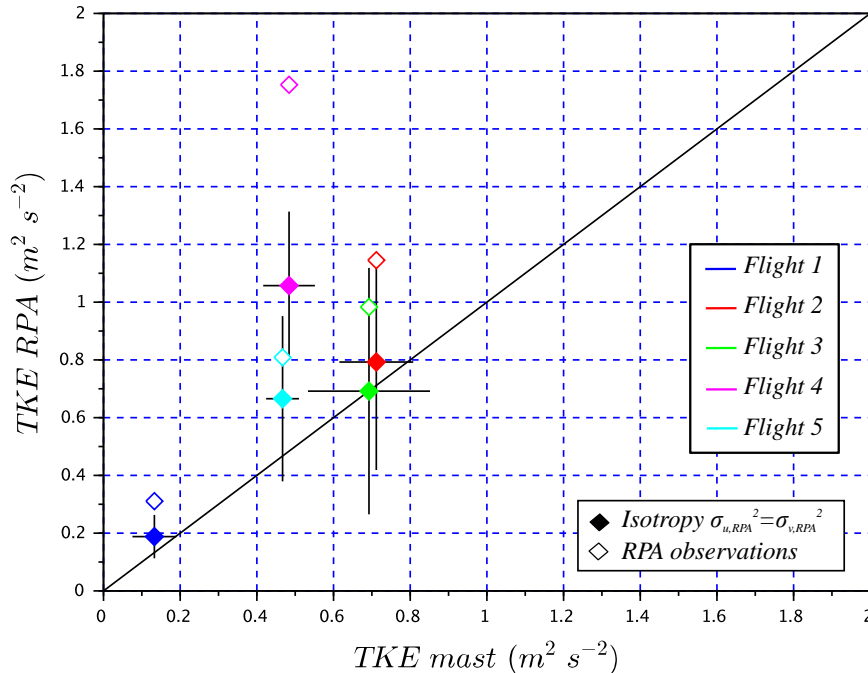


FIG. 3.7: Comparison of TKE_{RPA} and TKE_{mast} . Open diamonds TKE_{RPA} are calculated with the three wind variances of RPA, solid diamonds are obtained with the isotropy assumption $\sigma_{u,RPA}^2 = \sigma_{v,RPA}^2$ observed at 60 m.agl by the sonic anemometer in Fig.3.5. The uncertainty bars correspond to 1-sigma, using all the legs during the RPA flights, and using each length scale from 800 m to 6400 m for the sonic anemometers.

the other flights as the RPA was close to stall speed (as mentioned in Section 3.1). These results suggest that improving the measurement of horizontal winds and reducing biases in the horizontal wind-components of the variances may be achieved by 1) improvement of the INS heading measurement (also noted in Elston et al. (2015)), and 2) verified with a flight plan in a cross pattern (i.e., orthogonal legs, Kroonenberg et al. (2008); Drüe et al. (2013)) as presented in Fig.2.11.

3.5 Conclusions and perspectives

As established in the state of the art of RPAS measurements in the atmospheric boundary layer, light-weight RPA are well-suited to study ABL processes, and provide complementary results to other airborne platforms and ground-based instruments. In the present study, sonic anemometers on a meteorological mast (30 m.agl and 60 m.agl) are the reference for the wind-RPA measurements of 3D winds to be compared. Vertical wind velocity distributions are in good agreement between sonic anemometers and wind-RPA results, with an intersection number higher than 70% when the RPA flies under normal conditions along straight-and-level legs. PSD functions follow the -5/3 power law in turbulent inertial subrange. TKE_{RPA} are within 50 % of TKE_{mast} , when the isotropy assumption ($\sigma_u^2 = \sigma_v^2$) is applied to the wind-RPA data. However, wind measurement accuracy still needs to be

improved, particularly for the horizontal wind (Section 2.6). This is a known issue and we will change the INS model to INS with differential GPS systems that provide faster and more accurate measurements of heading.

As mentioned previously, comparison between the wind-RPA and sonic anemometers on a meteorological tower validated 3D winds from the RPA platform, and assessed our results compared to the ABL literature. Even if meteorological state parameters from the M²AV (temperature, relative humidity, wind direction, and horizontal wind) have been compared with remote-sensing instruments (sodar and wind profiler) in Martin et al. (2011), no direct comparison of RPA with cloud radar or lidar for vertical wind velocity has been found in the literature. During the BACCHUS field campaign at Mace Head Research Station, the collocation of the RPA operations and a Doppler cloud radar allows conducting a direct comparison of vertical wind velocity near cloud base of the two platforms. The following chapter details three case studies and provides a first reference for validation of RPA measurements of vertical wind in cloud with a cloud radar.

Chapter 4

Comparison of vertical wind velocities from RPA and cloud radar

Contents

4.1	Vertical wind measurement for aerosol-cloud closure study	47
4.2	Mace Head field campaign, Ireland	48
4.3	Stratocumulus deck with light precipitation (Flight 26: 2015/08/11) . .	49
4.4	Cloud fields within changing meteorology (Flight 38: 2015/08/21)	51
4.5	Fair weather cumulus clouds (Flight 30: 2015/08/15)	53
4.6	Conclusion and perspectives	54

4.1 Vertical wind measurement for aerosol-cloud closure study

To better understand aerosol-cloud interactions (ACI), closure studies have been conducted to compare simulated and observed cloud optical properties. The purpose of a closure is to reproduce the same parameter with independent methods, particularly using a model to confirm the underlying physical principle. In Conant et al. (2004), airborne measurements (Twin Otter aircraft) are compared with results from a cloud activation parcel model (Nenes et al., 2003) to achieve a degree of closure of cloud droplet number within 20 %. The study was conducted on 20 clouds sampled during the CRYSTAL-FACE experiment (South Florida, USA, Conant et al. (2004)). Aerosol activation was measured by CCN counters and updraft velocities obtained from a 5-hole probe and an INS on the Twin Otter aircraft. Fountoukis et al. (2007) analyzes highly polluted clouds during the ICARTT experiment, in New York State, USA. Cloud droplet number concentrations were sampled from an aircraft, and a comparison is conducted with an adiabatic cloud parcel model with a cloud droplet activation parameterization. Model results and observations agree within 10 % on average. The error in predicted cloud droplet concentration is found to correlate mostly with updraft velocity (Fountoukis et al., 2007), which incites to improve vertical wind measurements. The importance of updraft measurements for ACI is also highlighted in Schmidt et al. (2015) using lidar observations. Aerosol-cloud-dynamics relationship is studied for 29 clouds over central Europe (Germany). Remote-sensing Raman lidar and Doppler lidar observations are used to quantify the aerosol effect on cloud properties. Using updraft measurements remarkably

improves their ACI parameters compared to other remote-sensing ACI studies, and provides results similar to airborne studies.

Sanchez et al. (2017) present the first ACI closure study comparing RPA observations to aerosol-cloud parcel model simulations. RPA measures in-cloud lapse-rate, and deviations from adiabatic conditions suggests mixing between air at cloud top and cloud base. This mixing can be represented in the aerosol-cloud parcel model as entrainment from cloud top. Moreover, in case of a decoupled boundary layer, RPA observations characterize aerosol concentrations at cloud base leading to better estimate cloud top shortwave radiative flux. The aerosol-cloud parcel model requires CCN spectra and a distribution of vertical wind velocities at cloud base. The vertical wind velocity distribution is provided in Sanchez et al. (2017) by the Mace Head cloud radar and the multi-hole probe. As shown in Sanchez et al. (2017) and described in detail in the following section, vertical wind velocities from the cloud radar and the wind-RPA are in good agreement. The aim of the development of the wind-RPA is to be able to measure updraft near cloud base for more accurate aerosol-cloud closure studies. In addition, the wind-RPA distinguishes vertical wind in clouds from clear sky conditions, and identifies different types of cloud regimes. In the following section, vertical wind velocity near cloud base is compared between the cloud radar and the wind-RPA during the BACCHUS field campaign at Mace Head. Three case studies illustrate the different conditions in each cloud regime.

4.2 Mace Head field campaign, Ireland

A BACCHUS field campaign took place at the Mace Head Atmospheric Research Station on the West coast of Ireland in August 2015. The purpose was to study aerosol-cloud interactions linking ground-based and satellite observations using RPA (Sanchez et al., 2017). Among the four instrumented RPAs which flew at Mace Head, the wind-RPA was equipped with the 5-hole probe and the INS, described and validated in Chapters 2 and 3, to obtain 3D wind vectors, as well as upward and downward facing pyranometers to measure downwelling and upwelling broadband solar irradiance (400 to 1100 nm wavelengths). During the campaign, we concentrated on measurements of vertical wind velocity near cloud base to study aerosol-cloud interactions. After identifying the cloud base from the ceilometer or a vertical profile of an earlier flight, the wind-RPA was sent to an altitude close to cloud base, flying 6 km-long straight-and-level legs. Horizontal wind speeds varied from 6 to 12 m s⁻¹ from the West during the case studies presented here. The presence of clouds during the flight was determined using the ratio of the upwelling to downwelling solar fluxes; when the RPA was underneath or within a cloud, the ratio approaches unity.

During this field campaign, the wind-RPA flew in 10 of the 45 scientific flights for a total of 15 hours. Here, we focus on three flights with the wind-RPA (Table 4.1), in which the vertical wind is compared to vertical wind from the cloud radar at Mace Head (Cloud Radar MIRA-35, METEK). Of the 10 flights with the wind-RPA, three provided reliable measurements of updraft inside the clouds, while the other flights were not selected for a number of reasons: water in the 5-hole probe (2 flights), insufficient number of cloud radar data for comparison (2 flights), no cloud (1 flight), no

TABLE 4.1: Description of BACCHUS case study flights, Mace Head, Ireland.

ID	Date	Time (local)	Duration	Horizontal wind speed	wind direction
Flight 26*	11 Aug 2015	16:17	1h20	6 m s ^{-1**}	WNW to SW
Flight 30	15 Aug 2015	14:19	50 min	10 m s ^{-1**}	W to WSW
Flight 38	21 Aug 2015	16:10	1h30	10 m s ^{-1**}	SSW

* no pyranometer data

** the uncertainty associated with RPAS horizontal wind is ± 2 m s⁻¹

pyranometer data to identify clouds (1 flight), and aborted mission due to strong winds (1 flight). The Doppler cloud radar (35.5-GHz, Ka band) is adapted to the observation of the cloud structure over the whole vertical range (Görsdorf et al., 2015). The cloud radar is equipped with a vertically pointed antenna with a polarization filter, a magnetron transmitter and two receivers for polarized signals. Measurements are available up to 15-km height at a temporal resolution of 10 seconds. In this study, a single altitude bin of the cloud radar is selected for the comparison; either cloud top or RPA flight altitude. The vertical resolution of the cloud radar is 29 m between each measurement.

While the flight altitude for the wind-RPA was estimated to be near the cloud base, uncertainties in retrieving cloud base height or an evolution in cloud base height related to diurnal cycles of the boundary layer inevitably lead to the possibility of the RPA flying in the clouds rather than just below cloud base. Consequently, data from two wind-RPA flights during the field campaign are not presented due to the accumulation of water in the probe. We are currently improving the instrumentation to address the issue. Note that direct comparison of instantaneous data between the RPA and cloud radar was not possible, as the RPA did not fly directly over the cloud radar, and did not observe the same air mass. Moreover, the cloud radar reports vertical velocities every 10 s (and only when a cloud is present); therefore relatively long averaging periods are needed to compare with the RPA observations. Hence, we present selected time series of the cloud radar measurements that represent the state of the atmosphere during the flight; for cases with sufficient cloud cover, we present different averaging periods of the cloud radar (a short period that coincides with the RPA flight and a long periods for better counting statistics). Normalized distributions are plotted on the same interval divided into 30 bins of vertical wind velocities. In the present study, comparisons of the vertical wind velocity of the cloud radar serve to validate the RPA results, as well as to provide insight on different atmospheric states related to the measurement techniques.

4.3 Stratocumulus deck with light precipitation (Flight 26: 2015/08/11)

On 11 August, the sky was covered by a stratocumulus deck, and the wind-RPA flew at 1160 m.asl (at least 100 m above the cloud base). Time series of vertical wind from the cloud radar are

TABLE 4.2: BACCHUS field campaign at Mace Head, Ireland. The intersection number compares vertical wind velocity distributions between RPA and cloud radar.

ID	Intersection number* (comparison with RPA)		
	radar flight altitude	radar flight time	radar cloud top
Flight 26	0.53	0.67	0.74
Flight 30	0.78	—	—
Flight 38	0.82	0.78	—

* intersection number described in Section 4.1

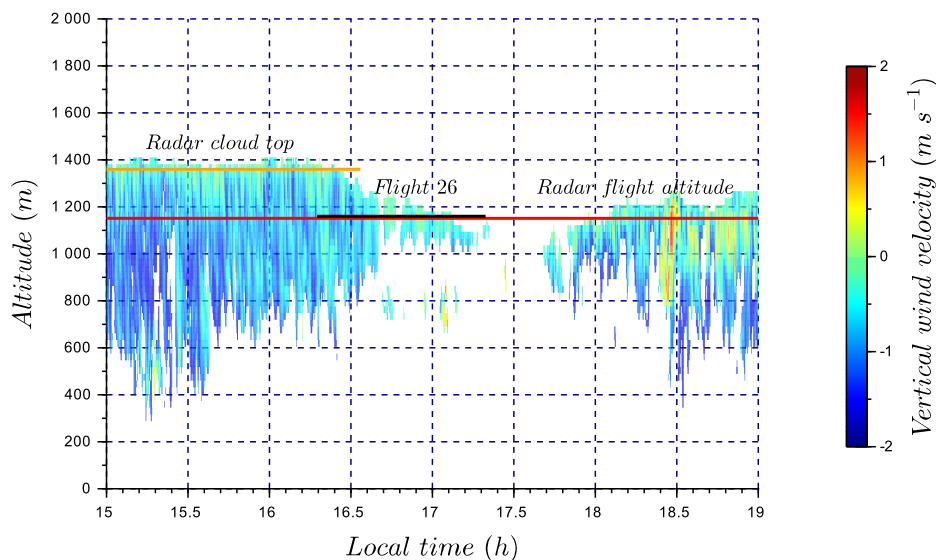


FIG. 4.1: Time series of vertical wind velocity for a stratocumulus deck with light precipitation (Flight 26). The color bar represents the cloud radar vertical wind velocity. Flight 26 sampling time is identified by the black segment. The red horizontal line corresponds to radar data at the altitude of the RPA (1160 m.asl), and the orange line corresponds to radar data at cloud top (1360 m.asl). Cloud radar vertical wind velocity at 1160 m.asl and 1360 m.asl are used in Fig.4.2 to compare with RPA measurements.

presented in Fig.4.1, along colored horizontal lines that indicate observation periods of the cloud radar and RPA, and Fig.4.2 presents a comparison of the vertical wind distribution obtained by cloud radar measurements and the RPA flight. The standard deviation of RPA vertical wind distribution is $\sigma_{RPA} = 0.19 \text{ m s}^{-1}$ (or 0.11 m s^{-1} for positive vertical velocities for comparison with the literature). This result is similar to the range of vertical wind standard deviations obtained in Lu et al. (2007) for stratocumulus clouds observed in the Eastern Pacific Ocean off the coast of Monterey, California. In the Mace Head case study, the presence of falling cloud droplets to an altitude as low as 300 m.agl (Fig.4.1) negatively biases the vertical wind distribution of the cloud radar (Fig.4.2). Previous measurements have also shown that precipitation negatively biases cloud radar observations of vertical wind velocities, as the radar indirectly measures vertical wind by using the motion of scatterers (i.e., hydrometeors; Lothon et al. (2005), Bühl et al. (2015)). These negative biases related to the falling drops are largely removed by obtaining vertical velocity at the

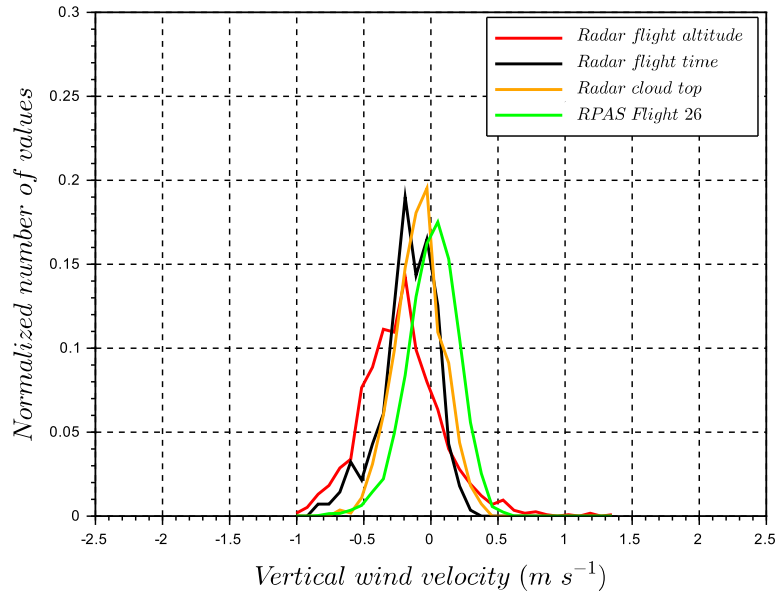


FIG. 4.2: A comparison of vertical wind velocity distributions in a lightly precipitating stratocumulus deck between RPA (1160 m.asl) and cloud radar at RPA altitude (1160 m.asl) for 4 h and flight time periods, and cloud radar at cloud top (1360 m.asl).

top of the cloud (Bühl et al., 2015). Similar results are obtained for our case study, as the cloud radar is strongly influenced by falling droplets, yet only slightly negatively biased at the cloud top. The intersection method, described in Section 3.2, is used to compare the three radar vertical wind distributions with the distribution of RPA measurements (Table 4.2). The intersection number of 0.53 between radar at flight altitude and RPA vertical wind distributions confirms the low match as a result of the negative bias from the precipitating droplets. However, a much better agreement is found between the cloud radar vertical velocity at the top of the cloud (1360 m.asl) and the RPA measurements (intersection number = 0.74). These results show that the 5-hole probe can indeed be used inside clouds and its results are not directly impacted by precipitation. Nonetheless, there is a risk that cloud water plugs a port on the 5-hole probe and renders the measurement of 3D winds invalid. We will address this issue in a redesign of the probe.

4.4 Cloud fields within changing meteorology (Flight 38: 2015/08/21)

A comparison of results from the RPA and cloud radar emphasizes the differences in vertical winds depending on the regions within the cloud field. During Flight 38, the RPA flew within a cloud above the ocean and in clear sky above land for three legs, after which the local meteorology changed into a formation of developing clouds above land (where a cloudless sky had previously been observed; Fig.4.3). The vertical wind velocity for the Flight 38 is presented using a

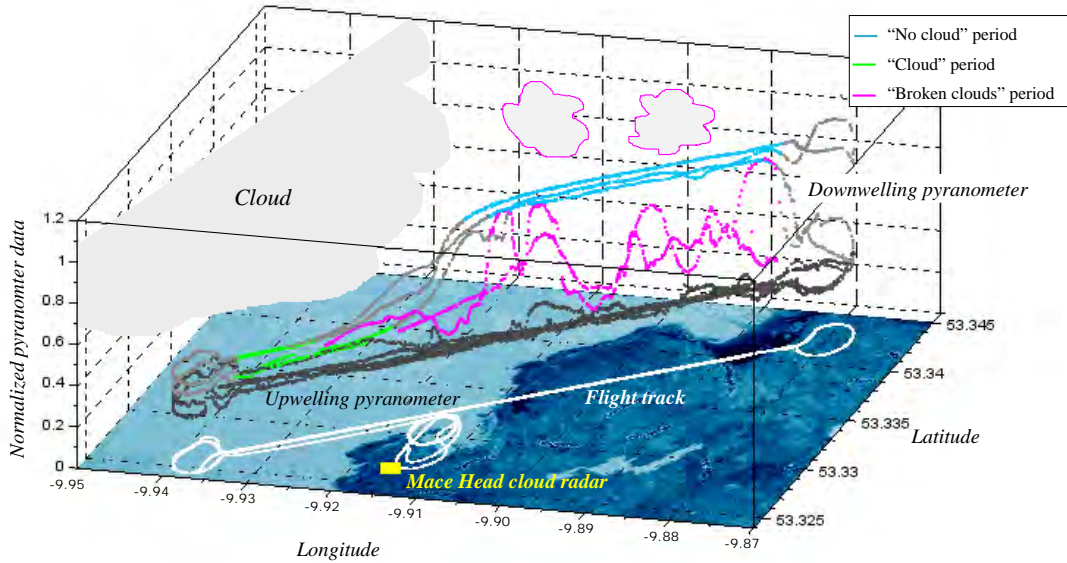


FIG. 4.3: Coastal map and flight tracks for the case study of a convective cloud with changing meteorology (Flight 38). Downwelling and upwelling pyranometers data are color-coded based on the three flight periods (“cloud”, “no cloud” and “broken clouds”). The developing field of broken clouds (magenta contour clouds) appeared during the last two legs. The cloud radar (yellow square) operated at the Mace Head research station.

combination of information shown in a series of figures: downwelling and upwelling pyranometer observations, and three periods corresponding to distinct meteorological conditions (Fig.4.3); the time series cloud radar data (Fig.4.4); and the vertical wind distributions from the RPA flight and the cloud radar (Fig.4.5). These meteorological periods are defined in Fig.4.3 as “cloud” (both pyranometers approach similar values), “no cloud” (downwelling pyranometer is significantly higher than upwelling pyranometer), and a third period associated to a developing field of broken clouds (spatially variable downwelling pyranometer). Combining information from Figs.4.3, 4.4, and 4.5, we deduce a cloudless sky (cyan) was observed by the RPA above land for the first three legs (Fig.4.3). The corresponding cloud radar time series also showed a cloudless sky above land for the beginning of the flight (Fig.4.4). In the meantime, the RPA flew within a cloud above the ocean (green), which was not observed by the cloud radar. Figure 4.5 shows that the standard deviation of vertical velocity within the cloud is larger than for clear sky conditions ($\sigma_{cloud} = 0.29 \text{ m s}^{-1}$, $\sigma_{no\text{ cloud}} = 0.17 \text{ m s}^{-1}$), which highlights the presence of stronger vertical winds in the presence of clouds. During the last two legs of Flight 38, the wind-RPA flew through a developing field of broken clouds above land (magenta), which also appeared in the cloud radar time series and in the satellite image (Fig.4 in Sanchez et al. (2017)). The standard deviation of the “broken cloud” RPA period of vertical wind is larger than the other periods ($\sigma_{broken\text{ cloud}} = 0.48 \text{ m s}^{-1}$). Similar vertical wind distributions are found for cloud radar and the RPA during the “broken clouds” period (Fig.4.5). While not shown here, the vertical wind distributions observed by the cloud radar are similar at radar cloud base (380 m.asl) and at the flight altitude (660 m.asl), as well as at different cloud radar

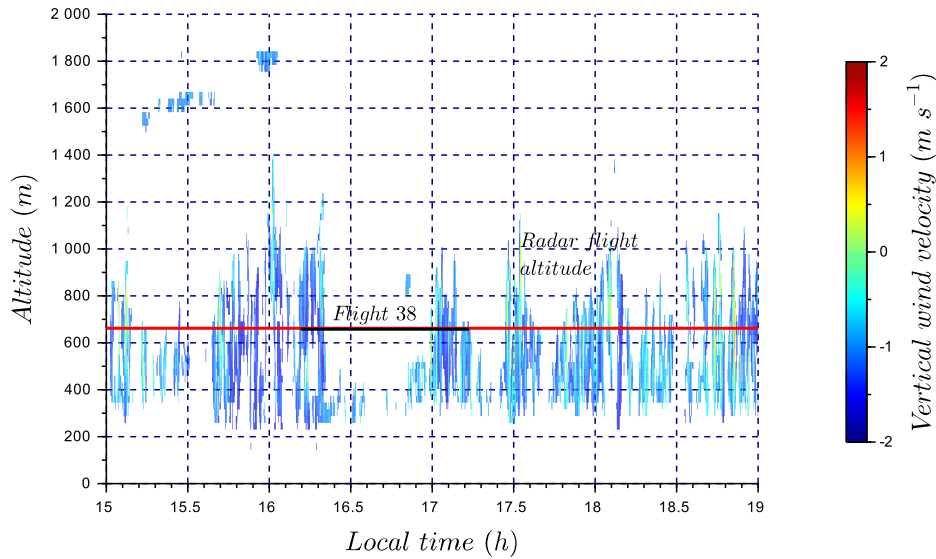


FIG. 4.4: Time series of vertical wind velocity associated with Flight 38. The color bar represents the cloud radar vertical wind velocity. Flight 38 sampling time is identified by the black segment. The red horizontal line corresponds to radar data at flight altitude (660 m.asl), used to plot vertical wind velocity distributions in Fig.4.5.

averaging periods (1.5 and 4 hours). In Table 4.2, intersection numbers illustrate the relatively close matches (ca. 80 %) in comparing the “broken cloud” RPA period and the cloud radar for 4 hours (radar flight altitude) and for 1.5 hours (radar flight time). For comparison, the values of intersection numbers between “broken cloud” and “cloud” periods is 0.73, while between “broken cloud” and “no cloud” periods is 0.56 (based on RPA measurements). The similar results for the observations of a field of broken clouds independently reinforces RPA and cloud radar observational methods, and the changes meteorological conditions highlight the ability to identify distinct states of the atmosphere with the RPA. Relating these differences in updraft velocity to the meteorological conditions of the boundary layer will be explored in future studies.

4.5 Fair weather cumulus clouds (Flight 30: 2015/08/15)

During Flight 30, the cloud field was scattered with small clouds as shown in Fig.4.7 by the cloud radar time series. The wind-RPA flew through one of these clouds as shown by the pyranometer measurements in Fig.4.6. However, the number of data points from the cloud radar during the flight time (black segment) was insufficient to establish a vertical wind distribution, therefore only the cloud radar data for 4 hours (red segment) are presented in Fig.4.8. To compare cloud radar and RPA data, vertical winds from the RPA are divided into “cloud” and “no-cloud” periods based on pyranometer observations. The respective standard deviations for the periods are $\sigma_{cloud} = 0.37 \text{ m s}^{-1}$ and $\sigma_{no\text{ cloud}} = 0.36 \text{ m s}^{-1}$, which are not statistically different. However, the variability in vertical winds between legs is significantly greater in the “no cloud” period (as represented by the

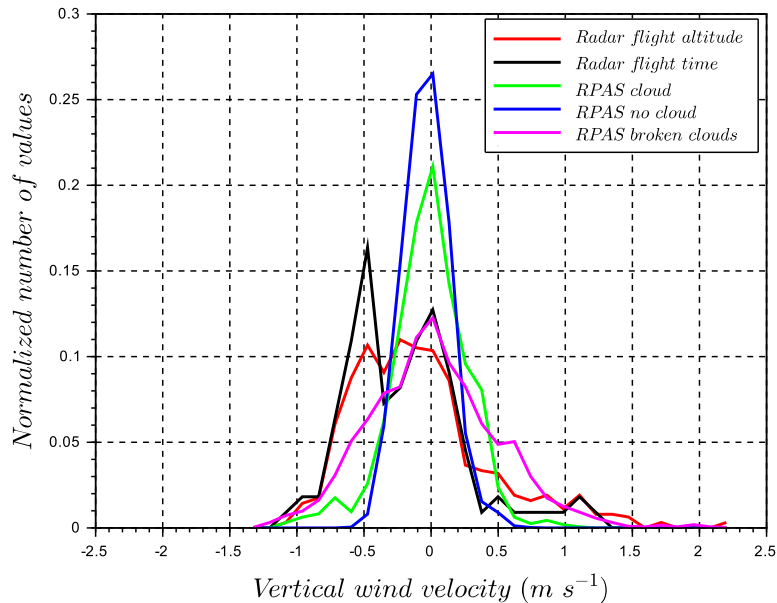


FIG. 4.5: Comparison of vertical wind velocity distributions for RPA and cloud radar for Flight 38 at RPA flight altitude from Fig.4.4. RPA measurements are divided into periods defined in Fig.4.3 (“cloud”, “no cloud” and “broken clouds” periods). The cloud radar detected cloud only for the “broken clouds” period during the RPA flight.

envelope in blue dashed lines in Fig.4.8) compared to the “cloud” period (envelope in green dashed lines). In Fig.4.8, the RPA and cloud radar measurements show similar results during the “cloud” period, with an intersection number equal to 0.78. Kunz et al. (2000) have observed an upward component in the air flow from the ocean at the Mace Head Research Station as a result of the terrain. Systematic differences between the RPA and cloud radar were not observed for our case studies, so we cannot quantify the role of surface heating or orography on the cloud radar vertical distributions compared to those of the RPA. Nonetheless, Ansmann et al. (2010) have observed asymmetry in the vertical wind distributions related to the heterogeneity in surface heating owing to the spatial distribution of the cloud field.

4.6 Conclusion and perspectives

During the Mace Head field experiment, three flights of the wind-RPA are successfully compared with the cloud radar data. Updraft velocities distributions near cloud base are obtained for distinct meteorological conditions, and presented as probability density functions in this chapter. A good agreement is found between RPA vertical wind distributions in the cloud and cloud radar data for each of the three flights (to within $\sim 0.1 \text{ m s}^{-1}$). The range of the vertical velocities encountered during the experiment extends from -1.5 m s^{-1} to 2 m s^{-1} , and the distributions are broader near the cloud base than in clear sky conditions. Higher and asymmetric updrafts are also observed in cloud compared to clear sky, which is consistent with atmospheric conditions required to generate conditions

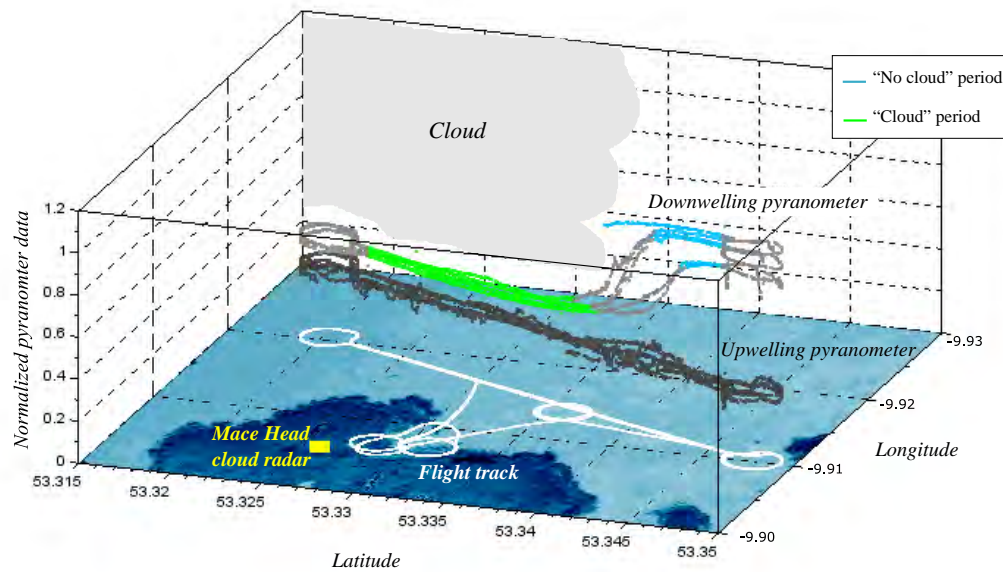


FIG. 4.6: Coastal map and flight tracks for the non-convective cloud case study (Flight 30). Downwelling and upwelling pyranometers data are color-coded based on two flight periods, “cloud” and “no cloud” periods. The cloud radar (yellow square) operated at the Mace Head research station.

for supersaturation and activate aerosols to CCN. The distinct meteorological conditions encountered during the case studies, from slightly precipitating cloud to fair weather cumulus cloud, provide a range of situations to validate the 5-hole probe with a cloud radar and to assess the ability of the RPA to obtain vertical velocity near cloud base. A pair of downwelling and upwelling pyranometers identifies the periods when the RPA flies in clear sky or in cloud. Description of the observations, the aerosol-cloud parcel model input parameters and results of the model are details in the next chapter.

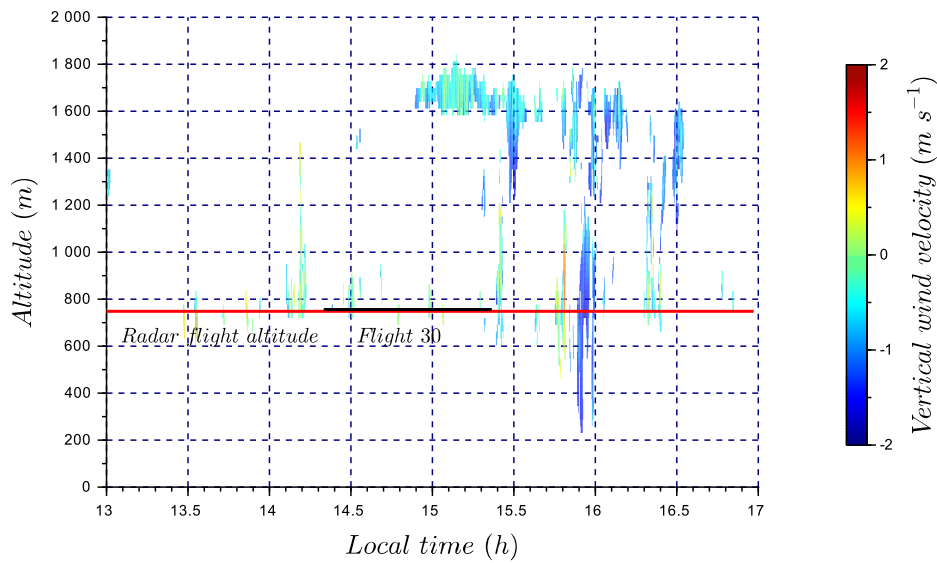


FIG. 4.7: Time series of vertical wind velocity associated with Flight 30. The color bar represents the cloud radar vertical wind velocity. Flight 30 sampling time is identified by the black segment. The red horizontal line corresponds to radar data at flight altitude (750 m.asl) used in Fig.4.8 to plot vertical wind velocity distribution.

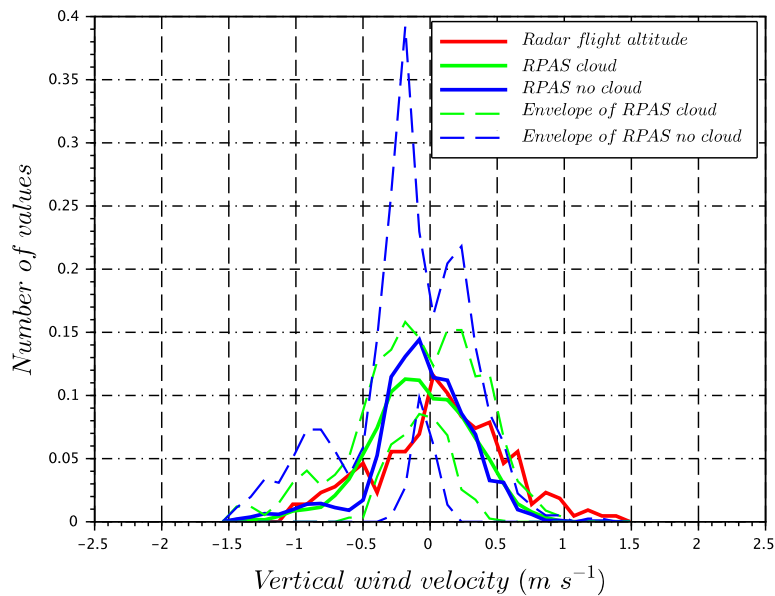


FIG. 4.8: Comparison of normalized vertical wind velocity distributions for RPAS during Flight 30 and cloud radar at RPA flight altitude (750 m.asl; Fig.4.7). RPA measurements are divided into “cloud”, and “no cloud” periods. The envelope of each period is plotted based on the minimum and maximum number per bin vertical velocity distributions on a leg-by-leg basis.

Chapter 5

Closure study, Cyprus field experiment

Contents

5.1	From updraft velocity measurements to aerosol-cloud closure study . . .	57
5.2	Overview of the BACCHUS field campaign in Cyprus	59
5.2.1	Ground-based measurements	59
5.2.2	RPAS Operations	60
5.2.3	Case study : stratocumulus layer	60
5.3	Aerosol-Cloud Parcel Model	61
5.3.1	Description of the Aerosol-Cloud Parcel Model (ACPM)	62
5.3.2	Model inputs from ground measurements and RPAs	64
5.4	Ground-based measurements	65
5.4.1	Particle size distribution	65
5.4.2	Aerosol-CCN closure	67
5.5	RPA measurements and in-cloud extinction	67
5.5.1	RPA vertical profiles	67
5.5.2	Updraft velocity measurements and in-cloud extinction	69
5.6	Aerosol-cloud closure study	72
5.6.1	Cloud droplet number concentration	72
5.6.2	Cloud optical properties	75
5.6.3	Sensitivity study on cloud optical properties	77
5.7	Concluding remarks	77

5.1 From updraft velocity measurements to aerosol-cloud closure study

The present case study focuses on a RPA flight on 1 April 2015, which measured convective updrafts at cloud base and cloud optical properties of a stratocumulus layer (Fig.5.2). Few clouds were observed during the field experiment in the flight zone, and meteorological conditions during this case study provided one of the few opportunities to conduct an aerosol-cloud closure.

The aerosol-cloud parcel model (ACPM) requires input parameters from observations as temperature profile, updraft velocities, aerosol size distribution and CCN concentrations. To describe cloud formation, the formation of droplets in a cooling air parcel and subsequent growth of cloud droplets is investigated. The Köhler theory defines the evolution of water vapor pressure at the surface of a droplet. Two effects impact the Köhler curves: 1) the Kelvin effect, which corresponds to the equilibrium of a pure water droplet owing to the surface tension, and 2) the Raoult effect, which describes the water activity influence of a solute. $p_w(D_p)$, the water vapor pressure over a droplet of diameter D_p , and p^0 , the water vapor pressure over a flat surface at the same temperature are expressed as (Seinfeld et al., 2006) :

$$\ln\left(\frac{p_w(D_p)}{p^0}\right) = \frac{4M_w\sigma_w}{RT\rho_w D_p} - \frac{6n_s M_w}{\pi\rho_w D_p^3} \quad (5.1)$$

where M_w is the molecular weight of water, σ_w is the solution surface tension, ρ_w is the water density, and n_s is the moles of solute. The Kelvin effect, also described as the curvature term, tends to increase saturation water vapor pressure, and the solute effect (Raoult's law) tends to decrease saturation vapor pressure. The maximum of the equilibrium vapor pressure of a droplet with dissolved solute is characterized by a critical wet diameter D_{pc} associated with a critical supersaturation S_c , which represents the maximum of the Köhler curve (Seinfeld et al., 2006), beyond which the droplet experiences unconstrained growth.

The updraft velocity distribution described in Chapter 4 relates to cloud droplet growth through the rate of change in temperature for the displacement of the air parcel. This rate of change in temperature determines the resulting water vapor mixing ratio (i.e., supersaturation). The equation describing the evolution of the thermodynamic energy of the air parcel is given by the vertical temperature gradient (i.e., Sanchez et al. (2017)):

$$dT = -\frac{gwdt + Ldq_l}{c_p} \quad (5.2)$$

where dT is the change in temperature corresponding to the dt time step in the aerosol-cloud parcel model, w is the updraft velocity, g is the acceleration due to gravity, L is the latent heat of water condensation, q_l is liquid water mixing ratio, and c_p is the specific heat of water.

The updraft distribution and the rate of deposition of water vapor on the cloud droplets determine the cooling rate (lapse rate of the vertical temperature profile), and so, the supersaturation inside the cloud (Seinfeld et al., 2006). When there is entrainment, it alters the cooling rate, and therefore the supersaturation, but also the clouds properties such as the droplet size distribution and the total water concentration. The cloud droplet size distribution impacts the cloud optical properties. The cloud extinction is used to derive the optical thickness and albedo (Section 5.6.2), which dictates the shortwave radiative properties of the cloud layer (Sanchez et al., 2017).



FIG. 5.1: Cyprus Atmospheric Observatory at Agia Marina Xyliatou, ground-based instrumentation to study aerosol-cloud interactions.

Closure studies in the present chapter are conducted on aerosol size distribution/CCN properties, cloud droplet number concentrations and the resulting cloud optical properties.

5.2 Overview of the BACCHUS field campaign in Cyprus

The BACCHUS field campaign in Cyprus took place from 2015/03/05 to 2015/04/02. Ground-based instruments, remote-sensing, and RPAS activities contributed to the field campaign. This case study contains all of the necessary elements to study aerosol-cloud interactions by combining the RPA measurements with aerosol and CCN measurements at the ground. The purpose of this case study is to use in situ ground-based and airborne observations to initialize an aerosol-cloud parcel model and compare in situ observations of cloud optical properties to those simulated in the ACPM.

5.2.1 Ground-based measurements

Cyprus Atmospheric Observatory (CAO) at Agia Marina Xyliatou (40 km West of Nicosia, 35.038697N; 33.057711E; 535 m.asl) is operated by the Cyprus Institute, and provided complementary measurements of physicochemical properties of aerosols during the BACCHUS field campaign. Among the instrumentation installed at the ground-based site, multiple instruments provided input to conduct an aerosol-cloud closure study. A miniature CCN instrument provides the number of activated particles at 0.24 % supersaturation (Roberts et al., 2005). A scanning mobility particle sizer (Grimm 5400 SMPS) measures the aerosol number size distribution from 10 to 360 nm diameter. An optical particle counter (Grimm OPC) gives the number of particles per bin for sizes between 0.3 and 20 μm (14 bins). A condensation particles counter (CPC) counts the total aerosol concentration ($D_p > 10$ nm) and is also used to adjust the SMPS measurements as a

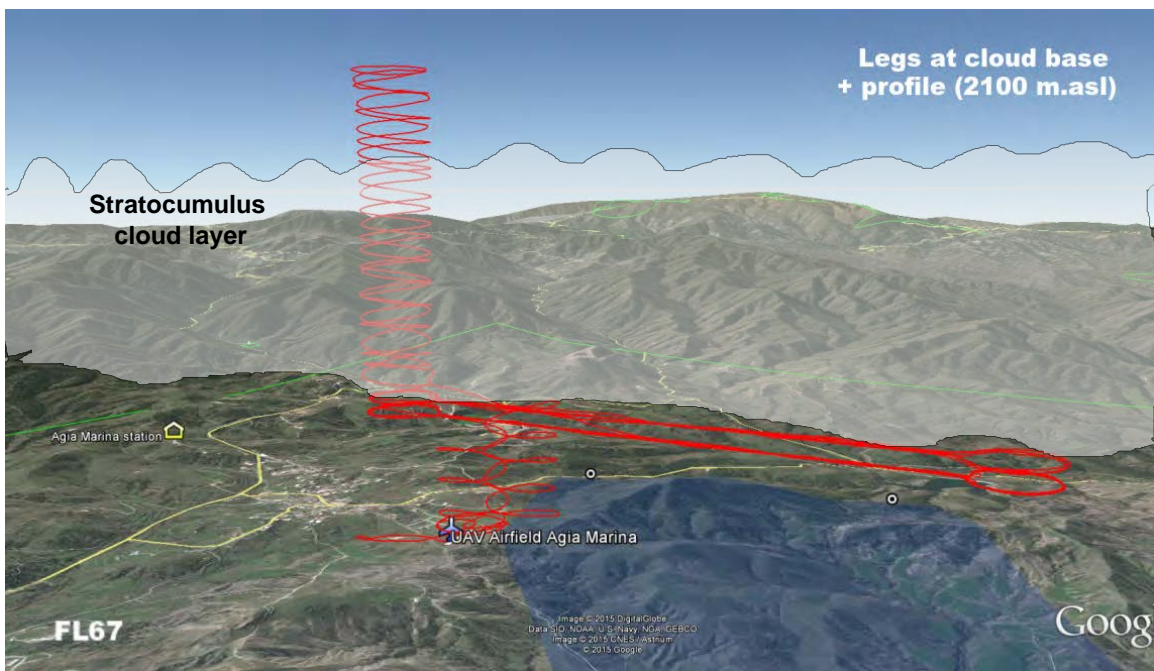


FIG. 5.2: Flight plan for Flight 67, legs at 1000 m.asl, profile up to 2100 m.asl and legs at 950 m.asl. The approximate location of the stratocumulus layer is overlaid on the flight track.

bias was observed in the time series. An aerosol chemical speciation monitor (Q-ACSM) provides the chemical composition of the aerosol particles. A picture of the equipped container is presented in Fig.5.1.

5.2.2 RPAS Operations

The field to operate RPAS (35.056429N; 33.055761E; 450 m.asl) was located 1 km north of the instrumented site. A rectangular airspace approximately $2.6 \times 1.7 \text{ km}^2$ was used for the flight operations with a ceiling at 2286 m.asl; 7500 ft.asl. The field campaign consisted of 52 research flights in 38 hours. The CNRM group deployed three different types of instrumented RPAs: an aerosol-RPA equipped with an optical particle counter (OPC), an optical-RPA instrumented with an aethalometer for black carbon measurements, and a wind-RPA equipped with a 5-hole probe/INS to measure vertical velocities near cloud base and pyranometers to measure cloud optical properties. All the RPAs measured temperature, pressure, relative humidity. They had a video camera attached to the wing.

5.2.3 Case study : stratocumulus layer

Flight 67 with the wind-RPA took place on 1 April 2015 at 2 pm local time (11 am UTC time) for duration of 1 hour and 20 min. The flight plan, as shown in Fig.5.2, consisted of a first set of 1.5 km straight-and-level legs at 1000 m.asl near cloud base, then a profile up to 2100 m.asl through the stratocumulus layer, and another set of straight-and-level legs at 950 m.asl. Note that after a profile through the cloud layer, the 5-hole probe measures nearly the same vertical velocity wind



FIG. 5.3: Pictures of Flight 67 from the on board video camera (Table 5.1), a) near cloud base (1000 m.asl), b) above clouds (2000 m.asl)

distribution at cloud base during the second set of legs (Fig.5.11). The pictures in Fig.5.3 captured during Flight 67 by the video camera show the cloud base and cloud top of the stratocumulus layer. By combining information between the video camera and the altitude of the wind-RPA, the history of the flight is described in Table 5.1. Each period is also confirmed by pyranometer measurements (Fig.5.12). Note that the boundaries of the cloud are not well defined, and are evolving with time between the ascent and the descent of the RPA.

Figure 5.4 shows the Hysplit model (Stein et al., 2015) run for 3 days ending at 1000 m.asl (altitude of cloud base) over the field site on 12 UTC 1 April 2015. The back trajectories show air masses originated from the Western Mediterranean Basin, with trajectories carrying anthropogenic sources from Southern Europe, Northern Africa, and Turkey.

5.3 Aerosol-Cloud Parcel Model

The term closure is used in a number of aerosol-cloud interactions studies to evaluate the cloud droplet number concentration obtained from a parcel model against observations of aerosol and updraft

TABLE 5.1: Profile history from cloud base (1000 m.asl) to the ceiling (2100 m.asl) and down near cloud base again (950 m.asl) during Flight 67

Video time (min)	Altitude (m.asl)	Observations
30:44	1072	cloud base, start of the ascent profile
32:55	1295	change in visibility, enter in the cloud
36:17	1602	cloud top
39:40	1904	below a convection cell
41:00	2102	maximum altitude of the profile
46:43	1730	cloud cell, video-camera sees in cloud
51:42	1121	first sight of ground
53:11	996	cloud base, end of the descent profile

velocities (Conant et al. (2004); Fountoukis et al. (2007); Kulmala et al. (2011); Sanchez et al. (2017)). In the present work, as no direct measurements of cloud droplet number concentration were available, the closure is addressed through the in-cloud extinction profile deduced from the ACPM and measured with the pyranometers. The parcel model is used as a proxy for cloud droplet number concentration. An entrainment parameterization is implemented in the model to obtain a better agreement between the model and observations. The known parameters for the ACPM are CCN measurements, aerosol number size distribution, and updraft velocity. CCN are used to derive hygroscopicity parameters for the measured aerosol size distribution (Fig.5.6).

5.3.1 Description of the Aerosol-Cloud Parcel Model (ACPM)

The Aerosol-Cloud Parcel Model (ACPM) is based on Russell et al. (1999) and Russell et al. (1998), where the main equations explicitly described the processes of activation of aerosol particles and the condensation of water vapor on the resulting cloud droplets. The ACPM uses a fixed section approach for distinct aerosol populations to calculate particle growth and evaporation under supersaturated conditions (Russell et al., 1998). Deposition is also included but negligible for the study here. Droplet collision, coalescence and drizzle rates are negligible for the simulated values of liquid water content and cloud droplet number concentration in the present case (i.e. droplet diameter $D_p < 20$ nm). The present model does not look into homogenous mixing as the results are completely dependent on the homogenous entrainment parameters selected as input for the parcel model. 3D or 4D models would need to complement the study to assess the impact of other in-cloud processes, which might be active on the cloud droplet number. The model is designed to be initialized from aircraft-based field observations, and employs dual-moment (number and mass) algorithm to calculate the particle growth. The aerosol population employed in our studies is assumed to be internally mixed as the particles generally undergo long-range transport from their source (Fig.5.4). However, liquid water is treated in a moving section representation to take into account varying atmospheric conditions such as temperature and humidity (Russell et al., 1998). To simulate drops in the model, aerosol particles are divided into 70 bins that are log spaced. The minimum size is $0.02 \mu\text{m}$, and the maximum size is $3.0 \mu\text{m}$. The relative humidity is corrected to be 100 % at cloud base (adjustment within 3 %). The equation describing the evolution of the thermodynamic energy of the air parcel is given by the

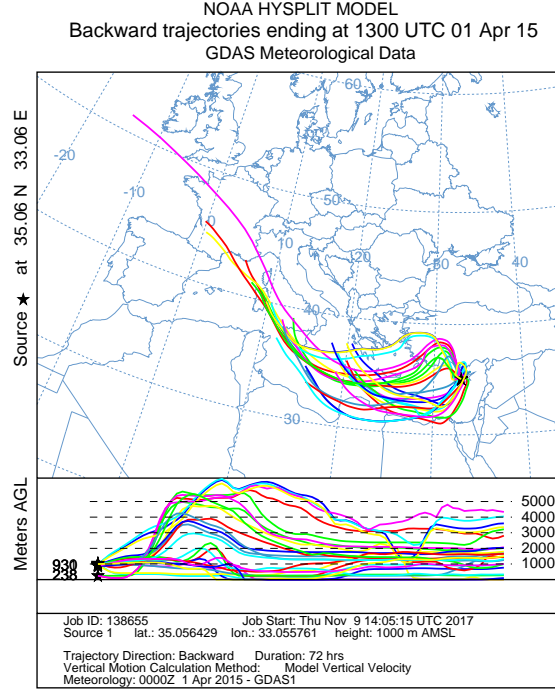


FIG. 5.4: Hysplit model showing 3-day backtrajectories 1 April 2015. Black Star shows the location of the ground station and RPA operations near Agia Marina Xyliatou in Cyprus.

vertical temperature gradient :

$$dT = -\frac{gwdt + Ldq_l}{c_p} \quad (5.3)$$

where dT is the change in temperature corresponding to the dt time step in the ACPM, w is the updraft velocity, g is the acceleration due to gravity, L is the latent heat of water condensation, q_l is liquid water mixing ratio, and c_p is the specific heat of water. Equation 5.3 relates the vertical wind velocity with the condensation of heat and moisture of a rising air parcel in the adiabatic case. The vertical velocities (updraft and downdraft) are measured near the cloud base or within the cloud. For the 1D model, positive updrafts generate supersaturated conditions in which aerosol particles are activated into cloud droplets. Therefore, the downdrafts are not considered in the simulation. The measured cloud temperature profile is used to parametrize entrainment, as the entrainment is described by the mixing of a fraction of air at cloud base and a fraction of air above cloud top, using conserved variables (equivalent potential temperature (Sanchez et al., 2017)). The gradient in the

conserved variable is nearly linear, and is then used to adjust the liquid water content by assuming inhomogeneous mixing. The fraction of air masses originating from below and above the cloud layer is determined as :

$$\theta_{e,c}(z) = \theta_{e,ent}X(z) + \theta_{e,CB}(1 - X(z)) \quad (5.4)$$

where $\theta_{e,c}(z)$ is the equivalent potential temperature in cloud as a function of height, $\theta_{e,ent}$ is the equivalent potential temperature of the cloud-top entrained air, $\theta_{e,CB}$ is the equivalent potential temperature of air at cloud base, and $X(z)$ is the fraction of cloud-top entrained air as a function of height. Then, the entrainment fraction $X(z)$ is given by :

$$X(z) = \frac{\theta_{e,c}(z) - \theta_{e,CB}}{\theta_{e,ent} - \theta_{e,CB}} \quad (5.5)$$

Sanchez et al. (2017) illustrate the importance of including entrainment to simulate cloud optical properties using the ACPM. A similar approach for this case study is presented in the following sections.

5.3.2 Model inputs from ground measurements and RPAs

To initiate the APCM model, in-situ measurements of aerosol size distribution and hygroscopic properties from the ground-station are combined with vertical profiles of temperature and relative humidity and vertical wind velocity distributions from the RPA. The aerosol size distribution described in Fig.5.6, along with the hygroscopicity parameter obtained in Section 5.4.2 are implemented in the ACPM to approximate the CCN spectra at cloud base. The temperature and humidity profiles (Fig.5.8, magenta lines) derived from observations of the RPA profile are used as input parameters in the ACPM model. The temperature profile in the ACPM follows the lapse rate in well-mixed layer and in the cloud layer.

Conant et al. (2004), Hsieh et al. (2009), and Sanchez et al. (2017) have shown that a distribution of updraft velocities and a weighted distribution of in-cloud supersaturations better reproduce cloud microphysical properties than a single-updraft approximation. Consequently, positive vertical wind velocity distribution near cloud base is used as model input (updraft velocities from 0 to 4 m s⁻¹ in Fig.5.11). The APCM model simulates the cloud droplet growth using 40 bins of vertical wind velocities between 0 and 4 m s⁻¹ (Sanchez et al., 2016). Each bin corresponds to a maximum supersaturation and a number of CCN activated into cloud droplets. The overall cloud microphysical properties are weighted based on the vertical wind velocity distribution. The cloud droplet number concentration corresponds to the summation of the number of CCN activated weighted with updraft.

$$N_d = \sum_{i=1}^{40} f(w_i) \cdot N_{CCN}(w_i) \cdot w_i \quad (5.6)$$

Where N_d is the cloud droplet number, i is the bin number, $f(w_i)$ is the occurrence of updraft w_i at the supersaturation S_{c_i} , and $N_{CCN}(w_i)$ is the number of activated particles based on the cloud droplet distribution for S_{c_i} and w_i . N_d is volume weighted by the factor w_i . Results are in line with the case studies (marine environment) presented in Sanchez et al. (2017).

5.4 Ground-based measurements

5.4.1 Particle size distribution

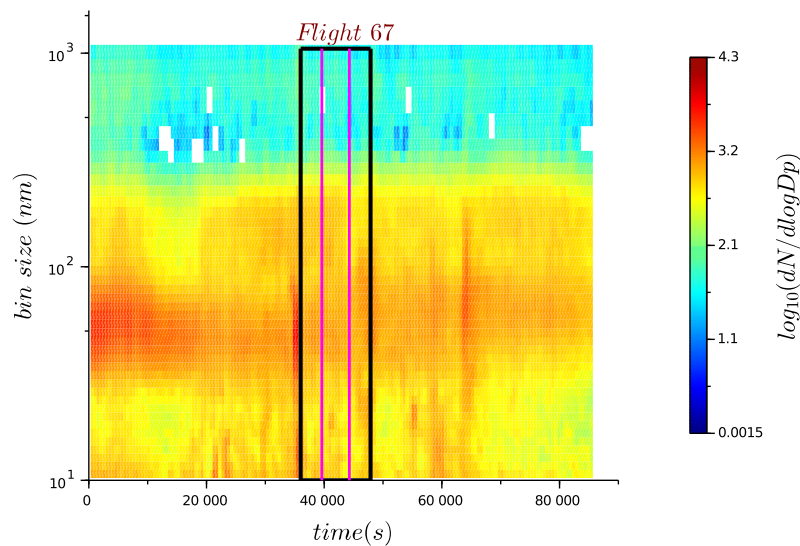


FIG. 5.5: Counter plot showing time series of SMPS data, 1 April 2015. The black rectangle represents the selected data for the analysis (3 hours) and the magenta lines delimit the Flight 67.

Figure 5.5 shows the time series of the aerosol particle number distributions for 1 April 2015 measured at the Cyprus Atmospheric Observatory, where the black rectangle represents the 3-hour period selected to average the aerosol size distribution and the magenta lines represents the time period of Flight 67. The aerosol particle number size distribution shows the presence of modes at 50 and 150 nm, with a trough near 100 nm implying cloud-processed aerosol. Figure 5.6a presents the average size distribution from normalized SMPS, as well as ground-based and RPA OPC measurements. A minimum at 100 nm (known as the Hoppel minimum) is visible in Fig.5.6a. OPC concentrations of ground-based and RPA measurements (from surface to cloud base) are within a factor of two, which is within variability observed on 1 April 2015. As the CPC instrument was

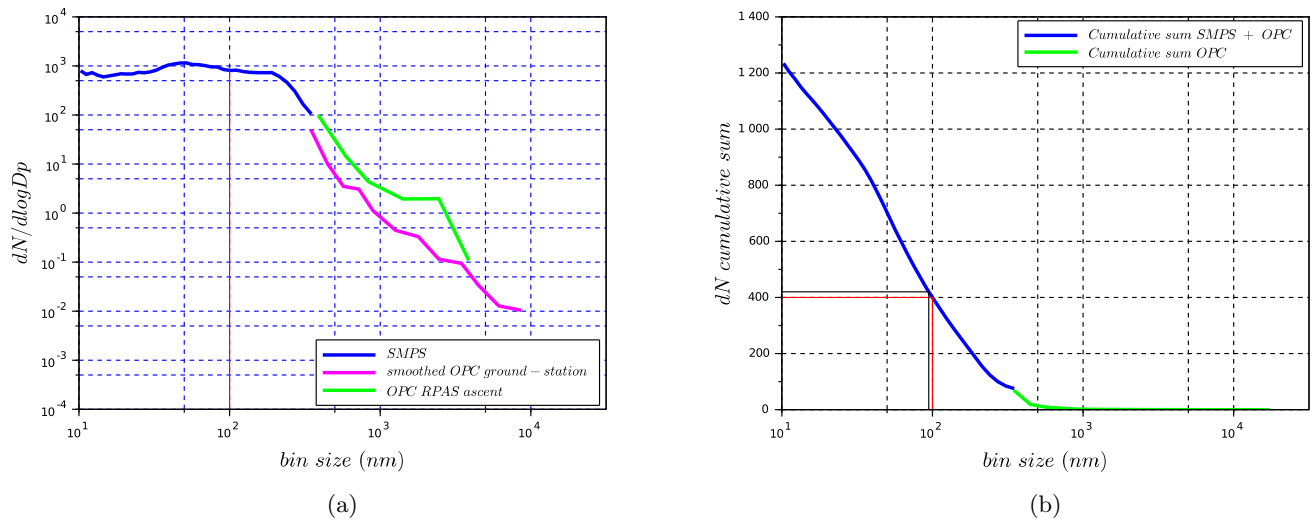


FIG. 5.6: a) Particle size distribution showing combined data from the SMPS (blue), the ground-based OPC (magenta) and the RPA-OPC (green). The red line indicates the Hoppel minimum diameter. b) Particle size cumulative distribution with a combination of data from the SMPS and the ground-based OPC. The red lines indicate the number of particles at the Hoppel minimum diameter (100 nm), the black lines correspond to the aerosol diameter for 420 cm^{-3} particles ($S_c = 0.24 \%$).

stopped on 27 March 2015 (end of the BACCHUS field campaign), no direct measurements of aerosol number concentrations with the SMPS are available for the case study day. Therefore, to quantify systematic biases between the integrated SMPS and CPC aerosol number concentrations, CPC and SMPS data were compared for one week period (20 to 27 March 2015). Integrated SMPS number size distributions were normalized by integrated CPC concentrations. The ratio integrated SMPS/CPC total shows a mean value = 0.63 ± 0.16 .

TABLE 5.2: Particle number distribution from SMPC and OPC during the 3-hour period including Flight 67

total number of particles	Hoppel minimum diameter (nm)	particle number at the Hoppel minimum	number of particles at 0.24 % S_c	diameter at 0.24 % S_c (nm)
1234	100	400	420	94.5

Hoppel et al. (1990) studied the evolution of aerosol size distributions under different meteorological conditions to highlight the growth undergoing cloud processing. The aerosol size distribution in the present study evolves from mono-modal to having a distinct trough around 100 nm in the presence of clouds. Therefore, two modes in the original aerosol size distribution that activates are distinguished. Cloud processing promotes the uptake of water-soluble material on the activated cloud droplets (particularly the uptake of sulfates and nitrates). When the cloud droplet evaporates, the dry particles after cloud processing are larger, and have more water-soluble material with a lower critical supersaturation S_c . The Hoppel minimum corresponds to the size at which the

activated CCN grow to droplets at the maximum in-cloud S_c . On the time scale of hours, the inactivated CCN, or interstitial aerosol, do not change size or supersaturation S_c (Hudson et al., 2015). The cumulative distribution of particle number (based on SMPS and OPC measurements) is calculated and shown in Fig.5.6b. In Fig.5.6, the Hoppel minimum diameter at 100 nm corresponds to an estimate of 400 cm^{-3} particles that activate to form cloud droplets. Similarly, based on the CCN measurements at the ground-station, the CCN concentration at 0.24 % S_c corresponds to 420 cm^{-3} . These results imply that a characteristic in-cloud supersaturation is close to 0.24 % S_c . The critical diameter at 0.24 % S_c provides a diameter of 94.5 nm. Table 5.2 summarizes these parameters, diameters and concentrations.

5.4.2 Aerosol-CCN closure

To describe the relationship between particle dry diameter and CCN activity, Petters et al. (2007) define the hygroscopicity parameter, κ , which represents a quantitative measure of water soluble ions on CCN activity.

$$\kappa = \frac{4A^2}{27D_p^3 \ln^2 S_c} \quad (5.7)$$

where D_p is the droplet diameter, S_c is the critical supersaturation, and A is expressed as:

$$A = \frac{4\sigma_w M_w}{RT\rho_w} \quad (5.8)$$

where the parameters in A are defined as in Eq.5.1. κ calculated using the CCN measurement with a critical dry diameter at 100 nm for a supersaturation of 0.24 % gives 0.3. The value of κ calculated from the aerosol size distribution and CCN measurement is compared to κ obtained from chemical constituents measured by the ACSM instrument at the ground station (Fig.5.7). From the ratio provided by the ACSM approximated to 50 % ammonium sulfate/insoluble matter, κ is estimated to be 0.26. These values are in good agreement, and confirm a closure between aerosol physical and chemical properties and the CCN measurements.

5.5 RPA measurements and in-cloud extinction

RPA measurements are used to link the ground-based aerosol/CCN measurements to cloud-base by showing a well-mixed boundary layer. The vertical wind velocity measurements at cloud base and the cloud extinction profiles from the RPA are then used to study aerosol-cloud interactions.

5.5.1 RPA vertical profiles

Figure 5.8 presents ascent profiles of the atmosphere sampled by the wind-RPA during Flight 67. Profiles of temperature and relative humidity during the ascent and the descent of the RPA are similar, particularly in cloud. The temperature in the boundary layer decreases $-10.1 \text{ }^\circ\text{C km}^{-1}$, which

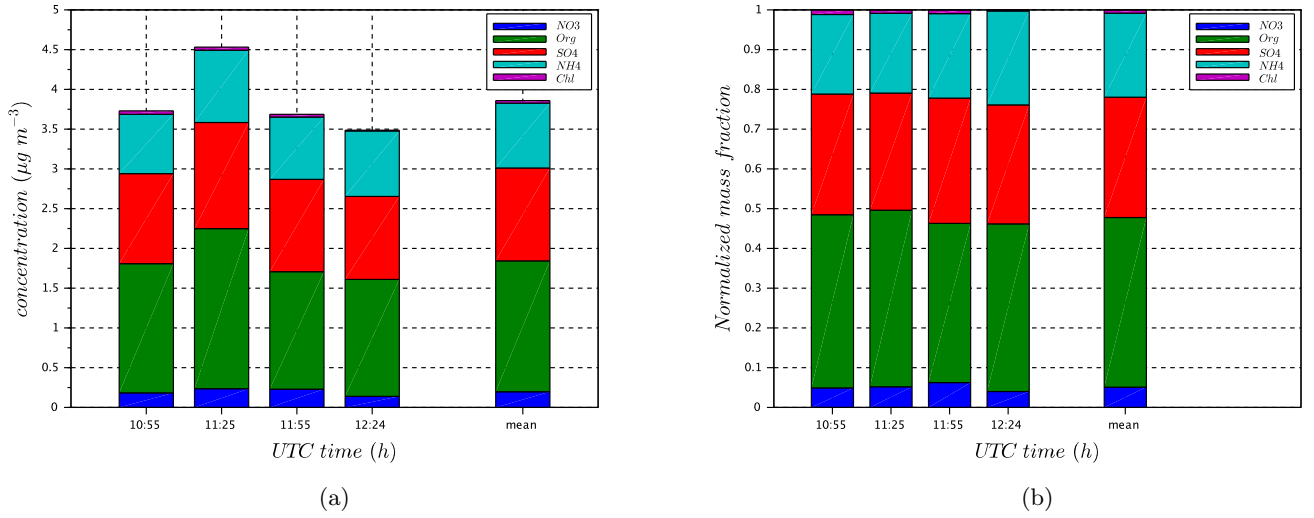


FIG. 5.7: a) Concentration of aerosol chemical composition during Flight 67 (Aerosol chemical speciation monitor measurement). b) Normalized mass fraction of aerosol chemical composition during Flight 67.

is close to a dry adiabatic lapse rate. In cloud, the lapse rate changes to $-4.5 \text{ }^\circ\text{C km}^{-1}$ (Fig.5.8a). The relative humidity increases from 75 % at the ground to 100 % at the cloud base (1020 m.asl), and then decreases again closer to the cloud top (Fig.5.8b). The in-situ measurements have been approximated by linear expressions that serve as input parameters for the aerosol-cloud parcel model in Section 5.3.2 (magenta lines in Fig.5.8). The equivalent potential temperature θ_e is calculated as :

$$\theta_e = T \frac{p_0}{p_d}^{R_d/(c_{pd}+r_t c)} H^{-r_v R_v/(c_{pd}+r_t c)} \exp\left(\frac{L_v r_v}{(c_{pd} + r_t c)T}\right) \quad (5.9)$$

Where T is the temperature, p_0 is the reference pressure (100 kPa), p_d is the partial pressure of dry air, R_d is the gas constant for dry air, c_{pd} is the heat capacity at constant pressure of dry air, r_t is the total water mixing ratio, c is the heat capacity of liquid water, H is the relative humidity, R_v is the gas constant for water vapor, r_v is the vapor mixing ratio, L_v is the latent heat of vaporization. The profile of equivalent potential temperature, which is conserved for changes in the air parcel pressure in Fig.5.8c, shows a neutrally buoyant layer below the cloud base, which implies a well-mixed boundary layer. The skew-T log-P diagram (Fig.5.9) shows the ascent vertical profile of temperature measured during Flight 67.

In addition, profiles of aerosol number concentrations (Fig.5.10) are measured during an earlier flight on the same day (Flight 65, aerosol-RPA, 8:50 am UTC, 11:50 am local time), and present similar concentrations in the atmospheric boundary layer from the ground to cloud base (1020 m.asl). This observation also confirms a well-mixed boundary layer, such that ground-based CCN and aerosol size distribution are then representative of the aerosol concentrations at cloud base (Fig.5.10).

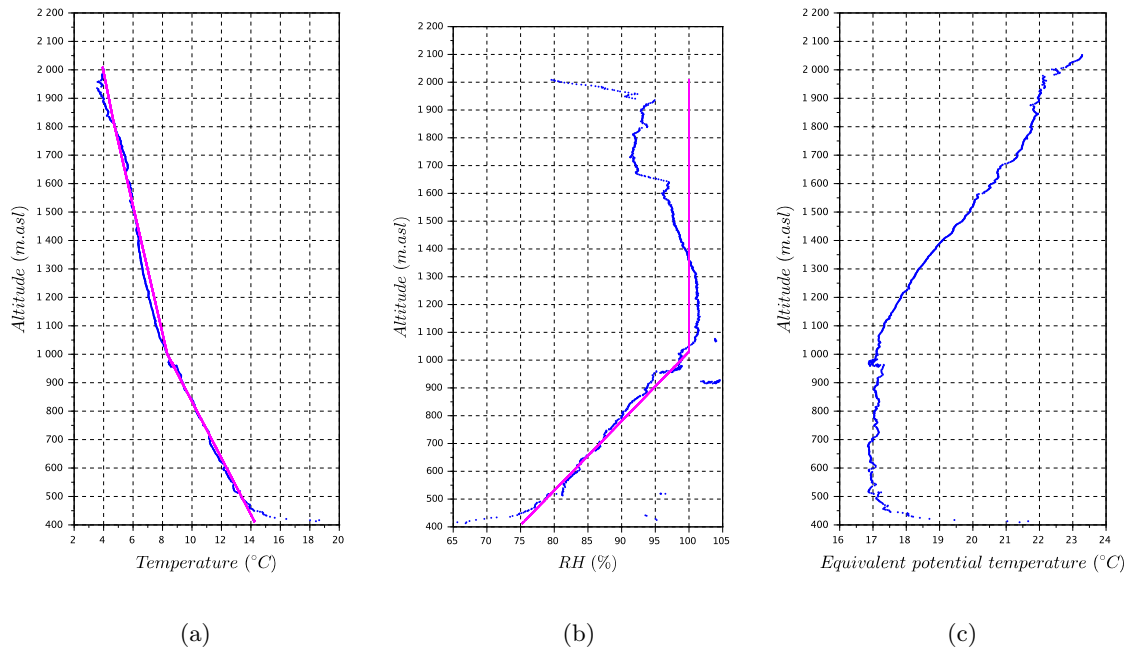


FIG. 5.8: Flight 67, Cyprus, 2015/04/01, meteorologic profiles a) temperature, b) relative humidity. The magenta curves correspond the linear best fit implemented in ACPM. c) Equivalent potential temperature

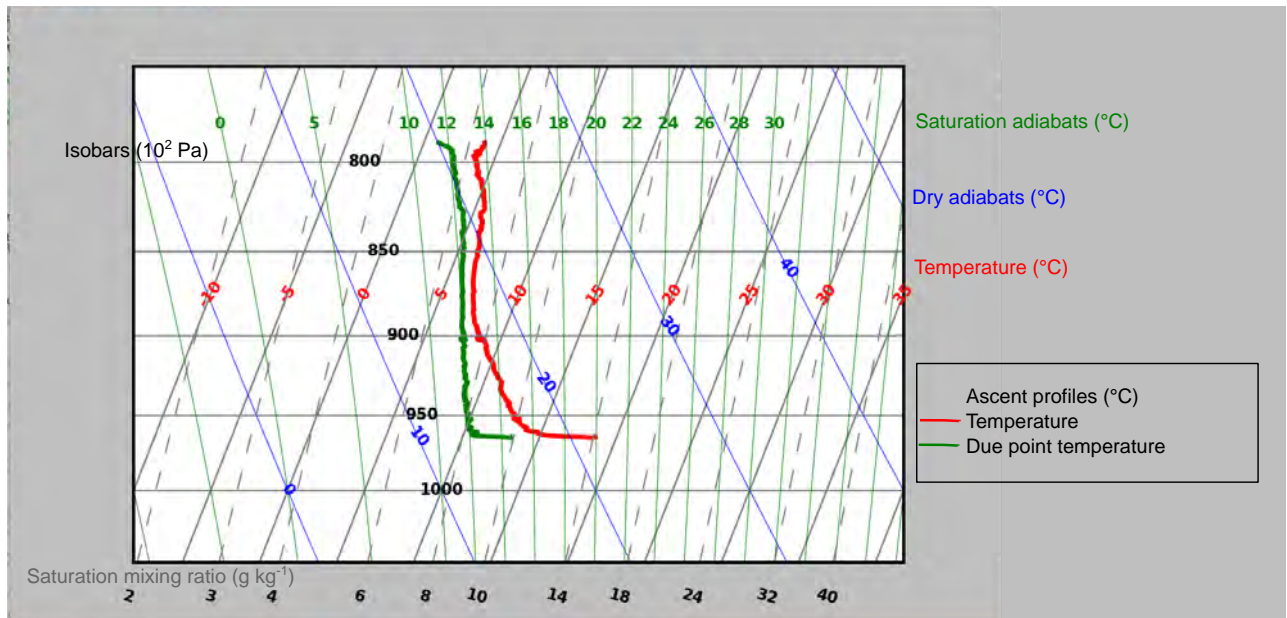


FIG. 5.9: Ascent vertical profile of temperature and due point temperature for Flight 67 displayed on a skew-T log-P diagram.

5.5.2 Updraft velocity measurements and in-cloud extinction

As presented in Section 5.2.3, the wind-RPA flew near cloud base during a first set of legs, profiled the cloud layer up to 2100 m.asl, and then flew on straight-and-level legs again (second set of legs).

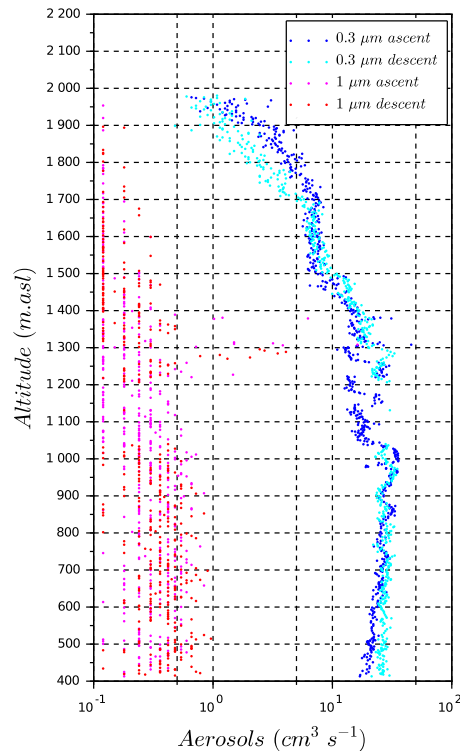


FIG. 5.10: Vertical profiles of aerosol number concentration for Flight 65 at $0.3 \mu\text{m}$ and $1 \mu\text{m}$.

Figure 5.11 shows the vertical wind distributions measured by the wind-RPA for the two sets of legs before (green) and after (magenta) the profile through the cloud layer. Even as the altitude of the legs were slightly different (1000 m.asl and 950 m.asl) because of an evolving boundary layer, nearly the same vertical wind velocity distributions are obtained before and after the cloud layer sampling. The similarity between the vertical wind velocity distributions demonstrate that the boundary layer dynamics were relatively constant throughout the flight and that the 5-hole probe functioned well even after a profile through the cloud layer. Comparing Fig.5.11 with vertical wind distributions obtained during the BACCHUS field campaign at Mace Head Research Station in Ireland (Calmer et al. (2018); Sanchez et al. (2017)), it is noticeable that the vertical wind velocity distribution for the Cyprus case study is wider than the distributions obtained in Ireland (Cyprus: $-2.5 < \text{vertical wind} < 4 \text{ m s}^{-1}$; Ireland: $-1.5 < \text{vertical wind} < 2 \text{ m s}^{-1}$).

Broadband shortwave pyranometers mounted on the top and at the bottom of the RPA fuselage provided upwelling and downwelling profiles of solar irradiance. Normalized pyranometer profiles are shown without correction of the oscillations due to the cosine-angle response of direct sunlight on the sensor (Fig.5.12). These oscillations are particularly visible on the downwelling pyranometer above the cloud layer. Results highlight the extinction of the incoming solar irradiance through the cloud

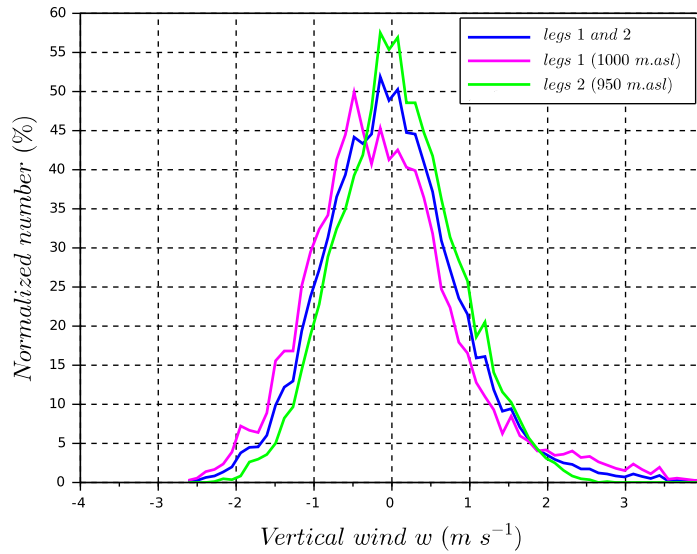


FIG. 5.11: Vertical wind distributions from straight-and-level legs near cloud base during Flight 67.

layer. The profiles of cloud measured optical properties from the RPA are compared in the next section with those of the aerosol-cloud parcel model.

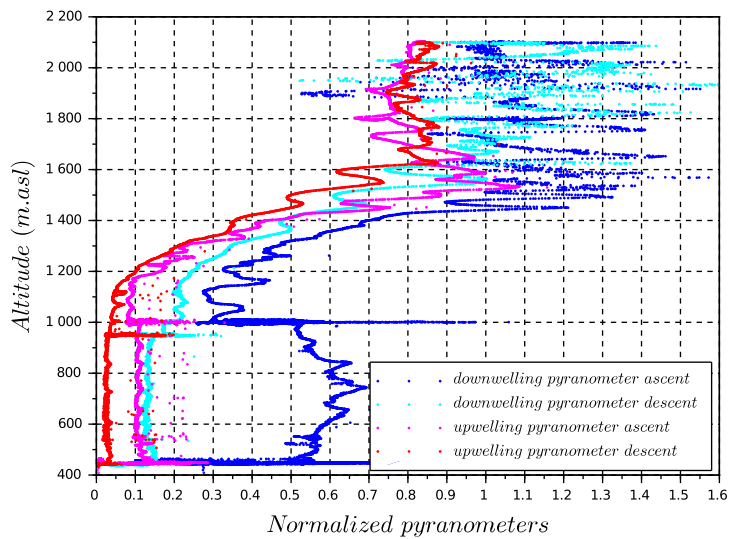


FIG. 5.12: Solar irradiance profiles from pyranometer measurements during Flight 67. The normalization parameter is the measured solar irradiance for clear sky, above the cloud layer, validated from the pyranometer profiles and the video camera (above 1600 m.asl)

5.6 Aerosol-cloud closure study

The purpose of the parcel model is to serve as the link between in-situ measurements of aerosol and vertical velocity distributions to the observed cloud microphysical properties. 1D aerosol-parcel models with explicit cloud microphysics are specifically designed to explore droplet growth/evaporation for a given CCN spectra and vertical velocity distribution. The procedure is to run the 1D model adiabatically, then use the observations of mixing of the conservative variable to calculate how much water has to evaporate in the model. The amount of evaporated water is driven by reducing the droplet number concentration (and not the droplet size) as we approximate the evaporation through inhomogeneous mixing (Jacobson et al., 1994). Coagulation, scavenging and deposition are negligible for the short simulation time. Collision can also be neglected as the diameter of particles mainly lies between 0.1 and 1 μm (Seinfeld et al., 2006).

5.6.1 Cloud droplet number concentration

Results of the ACPM for the profile of cloud droplet number and effective radius are presented in Fig.5.13. For the adiabatic reference case, the cloud droplet number is around 420 cm^{-3} . As shown in Section 5.4.1, the number of activated droplets associated with the Hoppel minimum diameter (ca. 400 cm^{-3}), which is a proxy for the number of aerosol activated into cloud droplets, also agrees well with the ACPM results (Fig.5.13a).

The adiabatic profile of cloud droplet number concentration is compared to the profile incorporating the entrainment parameterization that forces the model to the observed temperature lapse rate (Eq.5.4). Most closure studies neglect entrainment (Snider et al. (2003); Conant et al. (2004); Peng et al. (2005)), however, for the case studies at Mace Head (Sanchez et al., 2017), the difference between observed and simulated parameters suggested a source of heating in the cloud, and a closer approximation of cloud radiative properties was obtained when the entrainment term was added in the model. The entrainment parameterization approximates the impact of inhomogeneous mixing on cloud droplet number due to evaporation of a subset of the cloud droplet population. For the entrainment case, the cloud droplet number shows a peak at a lower number (ca. 210 cm^{-3}), and then decreases with altitude, as the inhomogeneous mixing is assumed. However, the cloud droplet number is sensitive to the entrainment fraction at cloud base, as the droplets are small so even a small change in the amount of water evaporated (from entrainment) will cause a large difference in the number concentration. To illustrate model sensitivity in obtaining droplet number near cloud base, Nd is calculated with a variation of liquid water content (LWC) of $\pm 0.05 \text{ g m}^{-3}$ (close to lower detection limit of in situ cloud probes) for the adiabatic and entrainment profiles (Fig.5.13c). Liquid water contents is calculated as :

$$LWC = \int_0^{\infty} \frac{4}{3} \rho \pi r^3 n(r) dr \quad (5.10)$$

where r is the radius of the cloud droplet, $n(r)$ is the number of cloud droplets with a radius r , and ρ is liquid water density. Based on the small variations of LWC, the cloud droplet number

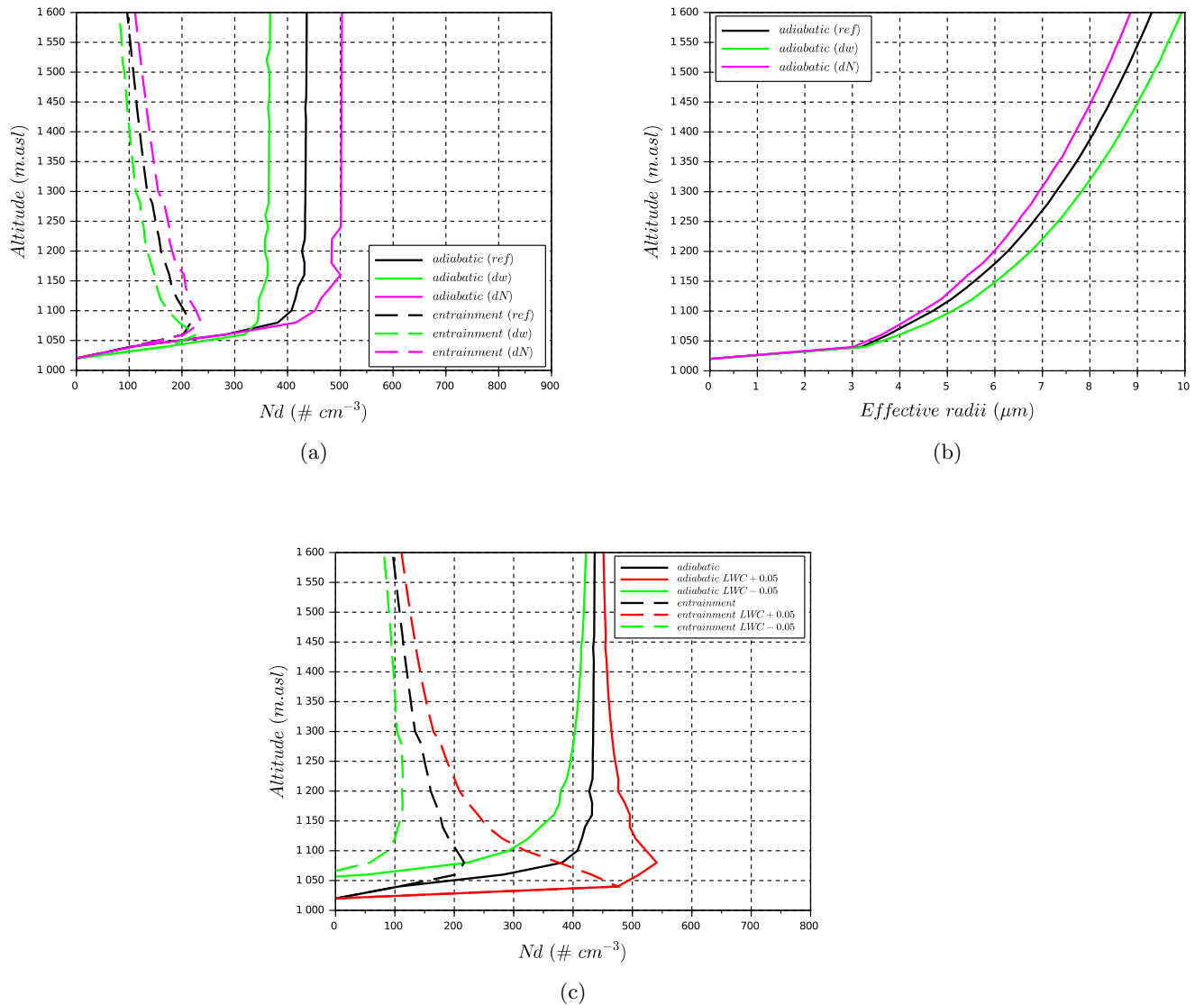


FIG. 5.13: a) Simulated cloud droplet number function of the cloud height, for the adiabatic and the entrainment cases, with variation of updraft velocity (dw) and particle number (dN). b) Cloud effective radii for the adiabatic case with variation of updraft velocity (dw) and particle number (dN). c) Sensitivity of cloud droplet number with $\pm 0.05 \text{ g m}^{-3}$ variation of liquid water content.

concentrations in the adiabatic profiles vary within $\pm 160 \text{ cm}^{-3}$ near cloud base (ca. 45 % variation relative to the adiabatic reference case). However, variations up to 230 cm^{-3} are observed for the entrainment profiles near cloud base (ca. 230 % variation relative to the entrainment reference case). Yet, higher in cloud, the impact of LWC variation on N_d is less pronounced. The peaks of cloud droplet number concentrations for the entrainment profile are then sensitive to observed temperature profiles; however, as clouds are optically thin at cloud base, the impact of this sensitivity on overall cloud optical properties is small. Yet, at cloud top, the maximum difference in cloud droplet number between the entrainment and adiabatic ACPM profiles is $\sim 300 \text{ cm}^{-3}$, which

ultimately, plays a large role in the overall cloud optical properties. Profiles of direct observations of cloud droplet numbers show a similar large variability at cloud base and a decrease in number with altitude (Roberts et al. (2008); Rauber et al. (2007)).

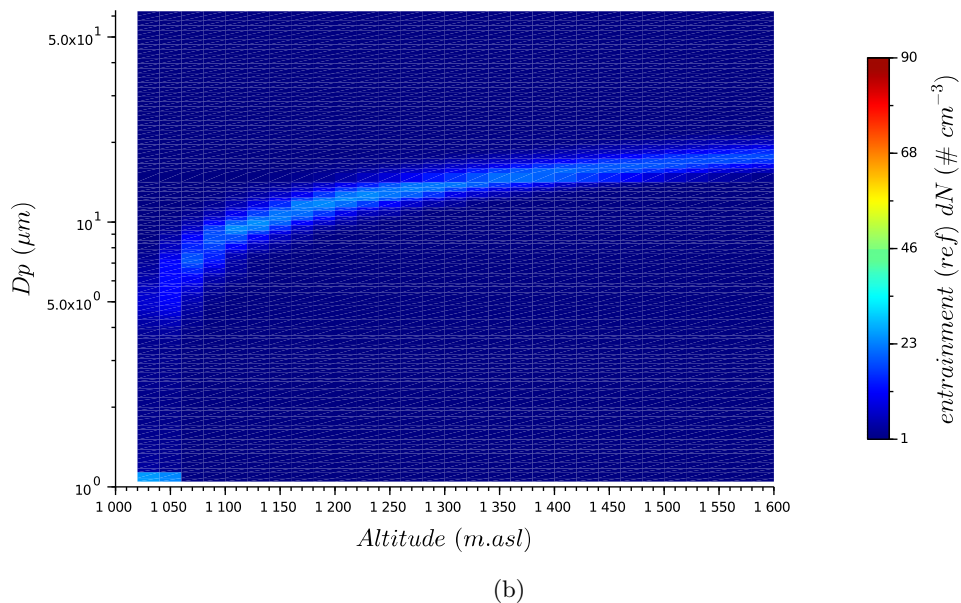
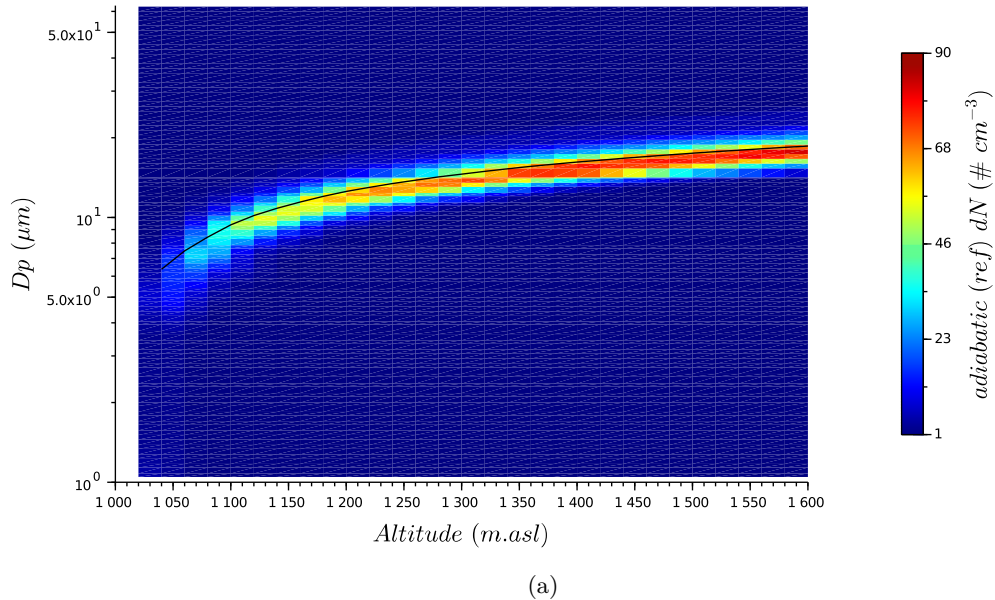


FIG. 5.14: a) Cloud droplet spectrum in the adiabatic case, the black line represents the effective diameter from Fig.5.13b ($2*r_{eff}$). b) Cloud droplet spectrum in the entrainment case.

The cloud droplet effective radius is defined as the integrated volume of the droplets divided by the integrated surface area:

$$r_{eff} = \int_0^{\infty} r^3 n(r) dr / \int_0^{\infty} r^2 n(r) dr \quad (5.11)$$

where r is the radius of the cloud droplet and $n(r)$ is the number of cloud droplets with a radius r . It is assumed that any mixing that occurred between the cloud and cloud-free air are inhomogeneous; this implies that the actual r_{eff} is equal to the adiabatic r_{eff} (Sanchez et al., 2017), therefore only r_{eff} for the adiabatic cases are presented in Fig.5.13b.

Figure 5.14a shows the effective diameter of the droplet distribution at each altitude (also shown in Fig.5.13b). Figures 5.14 show similar features including the nearly constant droplet number concentration for the adiabatic vertical profile and a peak in the number concentration near cloud base for the profile that includes entrainment (as shown in Fig.5.13a). We also point out that the droplet distribution tends to get narrower above cloud base in both adiabatic and entrainment cases.

5.6.2 Cloud optical properties

To study the cloud optical properties, solar irradiance obtained from the pyranometers mounted on the wind-RPA is compared to ACPM in-cloud extinction profiles, which represents the solar irradiance transmission through the cloud layer. The transmission through the cloud layer is approximated by downward integration of the calculation of albedo and subtracting from unity. For example, an infinitely thin cloud has an albedo of zero; therefore, 100 % of incoming solar irradiance is transmitted through the cloud top. As the cloud thickens, the albedo approaches unity meaning that all incoming solar irradiance is reflected back to space (Fig.5.15). To derive the cloud optical properties from the ACPM, the method presented in Sanchez et al. (2017), is followed here. The cloud extinction is proportional to the total droplet surface area and has the form :

$$\sigma_{ext} = \int_0^{\infty} Q_{ext}(r) \pi r^2 n(r) dr \quad (5.12)$$

where r is the radius of the droplet, $n(r)$ is the number of the cloud droplets with a radius of r , and $Q_{ext}(r)$ is the Mie efficiency factor. $Q_{ext}(r)$ asymptotically approaches 2 for water droplets at large size ($r > 2 \mu\text{m}$; Seinfeld et al. (2006)). The cloud optical depth is defined as:

$$\tau = \int_0^H \sigma_{ext}(h) dh \quad (5.13)$$

where H is the cloud thickness and σ_{ext} is the cloud extinction calculated from the simulated cloud droplet size distribution (Eq.5.12). The cloud albedo is then calculated with τ :

$$albedo = \frac{\sqrt{3}(1-g)\tau}{2 + \sqrt{3}(1-g)\tau} \quad (5.14)$$

with g the asymmetric scattering parameter. The albedo is estimated based on the cloud optical depth and the asymmetric scattering parameter (approximated as 0.85 based on the Mie scattering calculation).

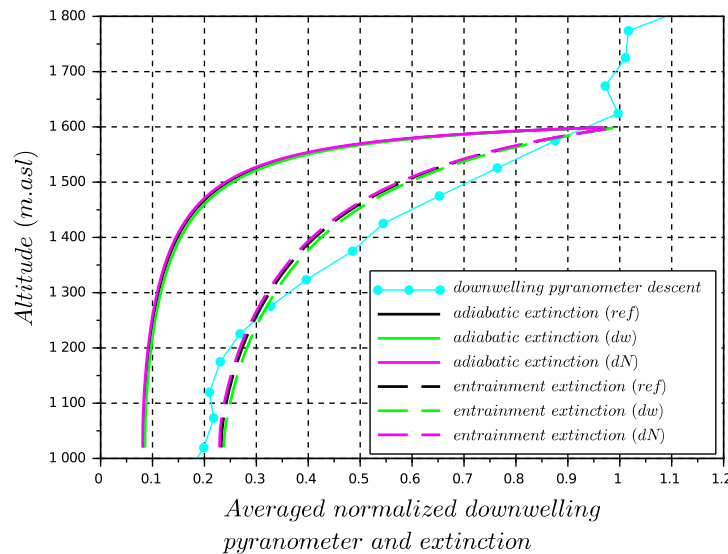


FIG. 5.15: Optical cloud profile, comparison of pyranometer profiles and model simulations for the normalized transmission, with adiabatic and entrainment processes. Cloud top is at 1600 m.asl. Cloud base is at 1020 m.asl

The solar irradiance profile from the RPA, based on the normalized downwelling pyranometer measurements during the descent, is used to compare simulated and observed cloud optical properties (Fig.5.15). To facilitate comparison with the model results, normalized pyranometer is averaged every 50 m (which averages the oscillations related to pitch-and-roll cosine-angle response of the pyranometer). Note that solar cosine-angle corrections will be applied in a future analysis to remove the oscillations in the profile – particularly near and above cloud top. Observations show a sharp gradient in the attenuation of downwelling solar irradiance near cloud top and decrease to ca. 0.2 at cloud bottom. Overlaid on Fig.5.15 are model results from ACPM for adiabatic and entrained cases. In order to compare ACPM and RPA observations, albedo of the cloud layer is calculated top-down using the profiles of simulated cloud droplet number and size distribution in Fig.5.13 to estimate the amount of solar irradiance reflected back to space and subtracted from unity to compare with the downwelling pyranometer profile. Comparison between RPA observations and ACPM for adiabatic and entrainment extinction profiles suggests that cloud optical properties are best represented when including entrainment mixing of cloud-top air.

5.6.3 Sensitivity study on cloud optical properties

In addition to comparing ACPM results between entrainment and adiabatic cases, a sensitivity analysis presented here explores the impact of a change in aerosol particle number concentrations as well as changes in the vertical velocity distribution on the cloud optical properties. Profiles of the cloud droplet number and effective radii (Fig.5.13) and cloud optical properties (Fig.5.15) are also simulated with the inputs of aerosol number concentration multiplied by two ($2N$) and the updraft velocity distribution divided by two ($w/2$). Increasing the aerosol concentrations by a factor of two results in an aerosol concentration of $\sim 2400 \text{ cm}^{-3}$ representing more polluted conditions. Such an increase in aerosol/CCN concentrations also increases cloud droplet number concentration (Fig.5.13a), smaller effective radii (Fig.5.13b), and presents a cloud with a higher albedo. In addition, halving the vertical wind velocity distribution results in a distribution with maximum vertical wind velocities near 2 m s^{-1} , which also happen to be similar to the updraft velocities observed in marine stratocumulus cloud layers over Mace Head Research Station, Ireland (Calmer et al., 2018). The lower vertical wind velocities also results in lower cloud droplet number concentrations and larger effective radii owing to lower in-cloud supersaturations (Fig.5.13). The lower cloud droplet number and smaller effective radii results in lower albedo of the cloud layer (Fig.5.15). A decrease of 70 cm^{-3} in cloud droplet number is observed when the updraft velocity distribution is divided by two (dw); and an increase of 70 cm^{-3} droplet number occurs when the number of dry particles is multiplied by two (dN) for the adiabatic case. Only variations of $\pm 20 \text{ cm}^{-3}$ in cloud droplet number are observed for the entrainment case in cloud. For the entrained extinction profiles, the variability for dN and dw have a smaller impact on the albedo, as dN presents a higher droplet number, but also a smaller diameter. For dw , fewer droplets are generated, but with larger diameters. In the three cases (*ref*, dN , dw), the LWC is the same, therefore opposite tendencies of droplet number and diameter compensate to provide similar in-cloud extinction profiles. Similar observations on the variability of adiabatic extinction profiles are also conducted, showing even less difference to the reference profile than in the entrainment cases. The change in the extinction profile between adiabatic and entrainment cases is 0.15 at cloud base, corresponding to a much larger factor of change in cloud albedo compared to changes in droplet number and vertical wind velocity distributions.

5.7 Concluding remarks

An aerosol-cloud closure is conducted on a case study for a cloud extinction profile. The measurements were conducted during the BACCHUS field campaign in Cyprus (2015/04/01). Ground-based measurements at Agia Marina Xyliatou are combined with RPA observations to implement in an aerosol-cloud parcel model to compare observed and simulated cloud optical properties. Input parameters of the model include the aerosol size distribution obtained from joined SMPS and OPC distributions averaged for the studied period as well as the vertical velocity distribution at cloud base as measured by the RPA. The aerosol size distributions reveal a Hoppel minimum diameter around 100 nm, which suggests that 400 cm^{-3} aerosol particles activated into cloud droplets. These results are also similar to the CCN concentrations of 420 cm^{-3} at 0.24 %

supersaturation. From the aerosol size distribution and the CCN measurements, the critical diameter corresponding to CCN at 0.24 % supersaturation is 94.5 nm, which is equivalent to a hygroscopicity parameter $\kappa = 0.3$. Likewise, a κ value obtained from the ACSM observations of aerosol chemistry is 0.26. Both κ values agree well – suggesting that aerosol particles behave roughly as 50 % ammonium sulfate and 50 % organic material.

Vertical profiles of temperature and relative humidity measured during a RPA flight are implemented in the model. The in-cloud lapse rate is larger than calculated for adiabatic conditions, suggesting cloud-top mixing. In addition, the RPA obtained updraft velocity distribution from straight-and-level legs near cloud base. The aerosol distribution, updraft velocity distribution and temperature profile provide the inputs for the aerosol-cloud parcel model. Two different simulation cases are studied with the ACPM, including an adiabatic case and an entrainment case where the in-cloud temperature profile is taken into account. The adiabatic ACPM simulations yield cloud droplet number concentrations (ca. 400 cm^{-3}) that are similar to those derived from the Hoppel minimum analysis (420 cm^{-3}). Cloud optical properties have been inferred using the extinction profile measured by a downwelling pyranometer. The observed extinction profile is then compared to simulations from the ACPM, and show a better agreement with the entrainment profile rather than with the adiabatic profile. These results highlight the importance of accounting for entrainment in deriving cloud optical properties.

To better evaluate the sensitivity of the ACPM results, variation of input parameters are implemented by multiplying the aerosol concentrations by two (from 1234 to $\sim 2400 \text{ cm}^{-3}$; even more polluted conditions), and dividing the updraft velocity distribution by two (max w from 4 to 2 m s^{-1} ; conditions similar to Mace Head Research Station). A doubling of N increases the maximum cloud droplet number by 70 cm^{-3} , whereas a reduction in w decreases the maximum cloud droplet number by 70 cm^{-3} . These changes in cloud droplet number concentrations by varying N and w lead to a small change (0.003) in the extinction at cloud base (which also corresponds to a 0.003 change in albedo). The impact on cloud effective radius is relatively small ($< \pm 1 \mu\text{m}$ changes in the radius). In comparison, the change in albedo related to entrainment is ca. 0.15. These results are in agreement with the conclusion of closure studies conducted at Mace Head Research Station (Sanchez et al., 2017), whereby the incorporation of a parameterization for entrainment improves the estimate for shortwave radiative flux. The case studies in Cyprus and at Mace Head illustrate the significance of the entrainment processes to estimate the cloud optical properties with ACPM in two different environments. More observations in climatically different regions are needed to understand the relative impact of aerosol, updraft and entrainment on cloud radiative properties.

Chapter 6

Conclusions

Contents

6.1 Conclusion	79
6.2 Conclusion en Français	81

6.1 Conclusion

Aerosol-cloud interactions remain one of the main “poorly understood and unrepresented interactions” when calculating the effective radiative forcing (ERF) (Boucher et al., 2013), an important assessment to understand climate changes. A large uncertainty is still associated with aerosol-cloud ERF estimation, and global climate models (GCM) underestimate ERF (Boucher et al., 2013), possibly because secondary effects of aerosols on clouds have not been well parameterized in simulations yet. The European BACCHUS (impact of Biogenic versus Anthropogenic emissions on Clouds and Climate: towards a Holistic UnderStanding) project specifically focuses on aerosol-cloud interactions, gathering a community of experimentalists and modelling scientists to address the uncertainties associated with these atmospheric processes. Considering small scale models, closure studies are conducted to evaluate the understanding of a given process, for example, the growth of aerosol particles into cloud droplets and their resulting optical properties of the cloud. The input parameters for aerosol-cloud parcel models (particularly updraft velocities and cloud condensation nuclei, CCN), obtained from ground-based and/or airborne measurements, play an important role in simulating cloud microphysical and optical properties. This work shows that entrainment processes also impact cloud optical properties.

Remotely piloted aircraft systems (RPAS) are relatively new platforms in atmospheric science compared to traditionally piloted research aircrafts. Remotely piloted aircraft (RPA) have been successfully implemented in field experiments and have provided new insights on clouds, aerosols, and albedo (Ramanathan et al. (2007); Roberts et al. (2008); Corrigan et al. (2007)), and on atmospheric boundary-layer processes (Reuder et al. (2016); Lampert et al. (2016)). However, as a relatively new tool for atmospheric research, RPA still require significant instrumental development, particularly related to miniaturization of sensors, and validation to address current observational

needs.

Vertical wind velocities near cloud base, and CCN spectra, are the two most important input parameters for aerosol-cloud parcel models in determining cloud microphysical and optical properties. Therefore, the present study focuses on the development and implementation of vertical wind measurements to improve aerosol-cloud closure studies. The validation and deployment of 3D wind measurements obtained by a commercial 5-hole probe with custom electronics on a lightweight RPA has been detailed. The 5-hole probe has been calibrated in a wind tunnel on a dynamic two-axis platform to obtain the angle of attack, angle of sideslip and airspeed (in the RPA reference frame). With an inertial navigation system (INS) providing ground speeds, Euler angles and GPS coordinates, 3D wind vectors in the Earth's reference frame have been calculated with the wind equations from Lenschow et al. (1989). Motions induced by the two-axis platform in the wind tunnel were effectively removed, thereby validating the system performance in a controlled laboratory environment. The uncertainty associated with the vertical wind measurements for the probe/INS system has been determined to be less than 0.12 m s^{-1} . The vertical velocity vectors from the RPA showed good agreement with sonic anemometers on a 60 m.agl meteorological tower at P2OA, Lannemezan, France, with intersection values (a method of comparing histograms) higher than 70 %. The power spectral density (PSD) functions of the three wind components from the sonic anemometers and the RPA generally follow the Kolmogorov law for established turbulent regime; however, RPA motion in the transversal wind component was identified and related to drift in the INS heading measurement. In the future, RPA heading measurements will be improved with an INS that includes differential GPS antennas (dGPS/IMU). Such systems have shown to improve measurements of 3D winds (Reineman et al. (2013); Thomas et al. (2012)); however, such technology has only recently become available for ultralight RPA.

Three case studies from a BACCHUS field campaign (at Mace Head Atmospheric Research Station, Ireland) validated RPA vertical wind velocities near cloud base compared to cloud radar observations. Vertical wind velocity distributions were classified according to the flight periods (clear sky or cloud), emphasizing the impact of meteorology and the state of the atmosphere on the cloud fields. For the first case study, a stratocumulus deck covered the sky and light precipitation was observed. Cloud radar vertical wind velocity distribution was negatively biased and cloud base was not distinctly visible due to falling droplets. The wind-RPA provided a centered vertical wind distribution near cloud base, which was similar to cloud radar observations at cloud-top (in the non-precipitating region of the cloud). The second case study displayed different meteorological conditions during the flight, which were well distinguished by the wind-RPA, including differences between a developing field of broken clouds over land, a small convective cloud over the ocean and clear sky. In the third case study, similar vertical wind distributions were observed near cloud base by the RPA and the cloud radar in fair weather cumulus cloud systems above land and ocean. The distinct meteorological conditions which were encountered for each of the case studies validated RPA results compared to cloud radar and highlighted the ability of the RPA platform to differentiate cloud systems based on vertical wind measurements in different meteorological conditions.

Updraft velocity measurements from the wind-RPA are implemented in the aerosol-cloud parcel model to conduct a closure study for stratocumulus case with convection sampled during a BACCHUS field campaign in Cyprus. Aerosol size distributions and CCN were measured at a ground-site, which served as input to the aerosol-cloud parcel model along with the updraft velocities at cloud base measured by the RPA. In addition, the RPA conducted a vertical profile and measured the shortwave transmission of solar irradiance during its ascent and descent through the cloud layer. Modelled and observed cloud optical properties are similar when entrainment from above the cloud layer is taken into account. The aerosol-cloud parcel model also shows that entrainment has a greater impact on cloud optical properties than variability in updraft velocity and aerosol particle concentration for this case study. Results of the Cyprus case study are consistent with results for closure studies conducted during the Mace Head field campaign (Sanchez et al., 2017), and reinforce the importance of including entrainment processes in cloud models to reduce uncertainties in aerosol-cloud interactions. The closure studies conducted in Mace Head (Sanchez et al., 2017) and in Cyprus (Chapter 5) are the first such closure studies using RPAS. The results are encouraging, and these observations will be expanded in future field campaigns.

6.2 Conclusion en Français

Les interactions aérosols-nuages demeurent l'une des principales interactions "mal comprises et non représentées" dans le calcul du forçage radiatif effectif (ERF) (Boucher et al., 2013), une évaluation importante pour comprendre les changements climatiques. Une grande incertitude est toujours associée à l'estimation du forçage radiatif effectif des aérosols et des nuages, et les modèles climatiques globaux (GCM) sous-estiment ERF (Boucher et al., 2013), probablement étant donné que les effets secondaires des aérosols sur les nuages n'ont pas encore été bien paramétrés dans les simulations. Le projet européen BACCHUS (impact of Biogenic versus Anthropogenic emissions on Clouds and Climate: towards a Holistic UnderStanding) s'intéresse spécifiquement aux interactions aérosol-nuage, réunissant une communauté d'expérimentateurs et de scientifiques modélisateurs pour traiter les incertitudes associées à ces processus atmosphériques. En considérant des modèles à petite échelle, des études de fermeture sont menées pour évaluer la compréhension d'un processus donné, par exemple, la croissance de particules d'aérosol en gouttelettes de nuages et les propriétés optiques résultantes du nuage. Les paramètres d'entrée pour les modèles de parcelle aérosol-nuage (en particulier les vitesses ascendantes et les noyaux de condensation des nuages, CCN), obtenus à partir de mesures au sol et/ou aéroportées, jouent un rôle important dans la simulation des propriétés microphysiques et optiques des nuages. Ce travail montre que les processus d'entraînement ont également un impact sur les propriétés optiques des nuages.

Les systèmes d'aéronefs pilotés à distance (RPAS) sont des plateformes relativement nouvelles dans le domaine de la science atmosphérique par rapport aux avions de recherche pilotés de façon traditionnelle. Des avions pilotés à distance (RPA) ont été opérés avec succès durant des campagnes de mesures et ont ainsi fourni de nouvelles informations sur les nuages, les aérosols et l'albédo

(Ramanathan et al. (2007), Roberts et al. (2008), Corrigan et al. (2007)) et sur la couche limite atmosphérique (Reuder et al. (2016); Lampert et al. (2016)). Cependant, en tant qu'outil relativement nouveau pour la recherche atmosphérique, le RPA nécessite un développement instrumental important, en particulier lié à la miniaturisation des capteurs, et à la validation des mesures afin de répondre aux besoins d'observation actuels.

Les vitesses verticales du vent à de la base des nuages et les spectres CCN sont les deux paramètres d'entrée les plus importants pour les modèles de parcelle aérosol-nuage dans la détermination des propriétés microphysiques et optiques des nuages. Par conséquent, la présente étude se concentre sur le développement et la mise en œuvre de mesures du vent vertical pour améliorer les études de fermeture aérosol-nuage. La validation et le déploiement des mesures de vent 3D obtenues par une sonde commerciale à 5 voies, avec des cartes électroniques assemblées au CNRM, installée sur un RPA ont été détaillés. La sonde à 5 voies a été étalonnée dans une soufflerie sur une plateforme dynamique à deux axes pour obtenir l'angle d'attaque, l'angle de dérapage et la vitesse-air (système de coordonnées du RPA). Avec un système de navigation inertielle (INS) fournissant les vitesses sol, les angles d'Euler et les coordonnées GPS, les vecteurs 3D de vent ont été calculés avec les équations de vent de Lenschow et al. (1989) dans le système de coordonnées terrestres. Les mouvements induits par la plateforme à deux axes dans la soufflerie ont été efficacement déduits, validant ainsi les performances du système dans un environnement contrôlé. L'incertitude associée aux mesures de vent vertical pour le système sonde/INS a été déterminée comme étant inférieure à 0.12 m s^{-1} . Les vecteurs de vitesse verticale du RPA sont en concordance avec les anémomètres soniques sur un mât météorologique de 60 m.agl à P2OA, Lannemezan, France, avec des valeurs d'intersection (une méthode de comparaison des histogrammes) supérieure à 70 %. Les fonctions de densité spectrale de puissance (PSD) des trois composantes du vent des anémomètres soniques et du RPA suivent généralement la loi de Kolmogorov pour le régime de turbulence établie. Cependant, des mouvements du RPA dans la composante transversale du vent ont été identifiés et sont liés à la dérive de la mesure du cap vrai de l'INS. À l'avenir, les mesures de cap vrai du RPA seront améliorées grâce à un INS qui comprend des antennes GPS différentielles (dGPS/IMU). De tels systèmes ont démontré qu'ils amélioreraient les mesures 3D de vent (Reineman et al. (2013); Thomas et al. (2012)). Cependant, cette technologie n'est devenue disponible que récemment pour les RPAs ultralégers.

Trois études de cas d'une campagne de mesures BACCHUS (à la station de recherche atmosphérique de Mace Head, en Irlande) ont validé les vitesses de vent vertical du RPA à la base des nuages comparées aux observations d'un radar de nuage. Les distributions de la vitesse verticale du vent ont été classées en fonction des périodes de vol (ciel dégagé ou nuage), mettant en évidence l'impact de la météorologie et de l'état de l'atmosphère sur les nuages. Pour la première étude de cas, un stratocumulus couvrait le ciel et des précipitations légères ont été observées. La distribution de la vitesse verticale du vent du radar de nuage était biaisée négativement et la base des nuages n'était pas clairement visible en raison de la chute des gouttelettes. Le RPA a fourni une distribution de vent verticale centrée près de la base des nuages, distribution qui était semblable aux

observations du radar dans la partie haute du nuage (dans la région non-précipitante du nuage). La deuxième étude de cas a montré différentes conditions météorologiques pendant le vol, qui furent bien distinguées par le RPA, y compris les différences entre des nuages en développement au-dessus de la terre, un nuage convectif au-dessus de l'océan et un ciel dégagé. Dans la troisième étude de cas, des distributions de vent vertical similaires ont été observées près de la base des nuages par le RPA et le radar de nuage dans les systèmes de cumulus au-dessus des terres et de l'océan. Les conditions météorologiques distinctes rencontrées pour chacune des études de cas ont validé les résultats du RPA en comparaison avec le radar de nuage, et ont mis en évidence la capacité de la plateforme RPA à différencier les systèmes de nuages basés sur des mesures de vent vertical dans différentes conditions météorologiques.

Les mesures de vitesse verticale du RPA sont implémentées dans le modèle de parcelle aérosol-nuage pour mener une étude de fermeture pour un cas de stratocumulus avec convection, échantillonnée lors d'une campagne de terrain BACCHUS à Chypre. Les distributions de taille des aérosols et de CCN ont été mesurés sur un site au sol, qui a servi de paramètres d'entrée au modèle de parcelle aérosol-nuage ainsi que les vitesses verticales à la base des nuages mesurées par le RPA. De plus, le RPA a effectué un profil vertical et a mesuré la transmission d'ondes de rayonnement pendant sa montée et sa descente à travers la couche nuageuse. Les propriétés optiques des nuages modélisées et observées sont similaires lorsque l'entraînement au sommet de la couche nuageuse est pris en compte. Le modèle de parcelle aérosol-nuage montre également que l'entraînement a un plus grand impact sur les propriétés optiques des nuages que la variabilité de la vitesse verticale et que de la concentration en particules d'aérosol pour cette étude de cas. Les résultats de l'étude de cas de Chypre sont cohérents avec les résultats des études de fermeture menées pendant la campagne de mesures de Mace Head, et renforcent l'importance d'inclure les processus d'entraînement dans les modèles de nuages pour réduire les incertitudes liées aux interactions aérosol-nuage. Les études de fermeture menées à Mace Head (Sanchez et al., 2017) et à Chypre (Chapitre 5) sont les premières études de fermeture utilisant des mesures de RPAS. Les résultats sont encourageants et ces observations seront renforcées par des mesures complémentaires lors de futures campagnes de mesures.

Appendix A

**Vertical Wind Velocity Measurements
using a 5-hole Probe with Remotely
Piloted Aircraft to Study
Aerosol-Cloud Interactions, AMT
journal**



Vertical wind velocity measurements using a five-hole probe with remotely piloted aircraft to study aerosol–cloud interactions

Radiance Calmer¹, Gregory C. Roberts^{1,2}, Jana Preissler³, Kevin J. Sanchez^{1,2}, Solène Derrien⁴, and Colin O’Dowd³

¹Centre National de Recherches Météorologiques (CNRM), UMR 3589, Météo-France/CNRS, Toulouse, France

²Scripps Institution of Oceanography, University of California, San Diego, CA, USA

³School of Physics and Centre for Climate and Air Pollution Studies, National University of Ireland Galway, Galway, Ireland

⁴Laboratoire d’Aérologie, University of Toulouse, CNRS, Toulouse, France

Correspondence: Radiance Calmer (radiance.calmer@meteo.fr)

Received: 25 July 2017 – Discussion started: 27 July 2017

Revised: 11 March 2018 – Accepted: 12 March 2018 – Published: 3 May 2018

Abstract. The importance of vertical wind velocities (in particular positive vertical wind velocities or updrafts) in atmospheric science has motivated the need to deploy multi-hole probes developed for manned aircraft in small remotely piloted aircraft (RPA). In atmospheric research, lightweight RPAs (< 2.5 kg) are now able to accurately measure atmospheric wind vectors, even in a cloud, which provides essential observing tools for understanding aerosol–cloud interactions. The European project BACCHUS (impact of Biogenic versus Anthropogenic emissions on Clouds and Climate: towards a Holistic Understanding) focuses on these specific interactions. In particular, vertical wind velocity at cloud base is a key parameter for studying aerosol–cloud interactions. To measure the three components of wind, a RPA is equipped with a five-hole probe, pressure sensors, and an inertial navigation system (INS). The five-hole probe is calibrated on a multi-axis platform, and the probe–INS system is validated in a wind tunnel. Once mounted on a RPA, power spectral density (PSD) functions and turbulent kinetic energy (TKE) derived from the five-hole probe are compared with sonic anemometers on a meteorological mast. During a BACCHUS field campaign at Mace Head Atmospheric Research Station (Ireland), a fleet of RPAs was deployed to profile the atmosphere and complement ground-based and satellite observations of physical and chemical properties of aerosols, clouds, and meteorological state parameters. The five-hole probe was flown on straight-and-level legs to measure vertical wind velocities within clouds. The vertical velocity measurements from the RPA are validated with vertical velocities derived from a ground-based cloud radar by showing that both mea-

surements yield model-simulated cloud droplet number concentrations within 10 %. The updraft velocity distributions illustrate distinct relationships between vertical cloud fields in different meteorological conditions.

1 Introduction

Vertical wind is a key parameter for understanding aerosol–cloud interactions (ACIs). In tracing the evolution of aircraft-based wind measurements in the atmosphere, three axes of development have been pursued since the 1960s: improvements in airborne platforms, inertial navigation systems (INSS) and sensors. Airborne platforms have evolved from large aircraft (e.g., Canberra PR3, Axford, 1968 or NCAR Queen Air, Brown et al., 1983) to ultra-light unmanned aerial systems (e.g., M²AV; Spiess et al., 2007). INSS measure linear and rotational motion of the aircraft (or unmanned aerial system) and are used to back out wind vectors in the Earth’s coordinate system. A major improvement in INSS was the integration of GPS (Global Positioning System) data with fusion sensors (Khelif et al., 1999). The overall accuracy of atmospheric wind vectors has improved drastically, from 1 m s^{−1} with wind vanes (Lenschow and Spyers-Duran, 1989) to 0.03 m s^{−1} with a multi-hole probe and state-of-the-art INS (Garman et al., 2006). Over the past decade, GPS, INSS, and sensors have become sufficiently miniaturized to be deployed on ultra-light remotely piloted aircraft systems

(RPAS)¹, which has extended observational capabilities previously limited to traditional manned aircraft.

A wide range of remotely piloted aircraft (RPA)² has been used to measure atmospheric winds, from a 600 g SUMO (Reuder et al., 2012) to a 30 kg Manta (Thomas et al., 2012). In particular, a multi-hole probe paired with an INS has been the main mechanism for obtaining vertical winds in fixed-wing RPA. Ultimately, the combination of the multi-hole probe, pressure sensors, and the INS dictates the precision of atmospheric wind measurements. The following accuracies for vertical wind measurements w were reported in the literature for different RPA platforms; they were obtained by different methods, which provided either 1σ uncertainty or systematic error analysis associated with a specific pair of probe–INS. In van den Kroonenberg et al. (2008), a custom five-hole probe on the M²AV, implemented with a GPS-MEMS-IMU was reported with an accuracy for w within $\pm 0.5 \text{ m s}^{-1}$. The accuracy was based on a systematic error estimation using characteristic flight parameters with a reference state of $w = 1 \text{ m s}^{-1}$. The uncertainty in w reported for the SUMO (Reuder et al., 2016) is $\pm 0.1 \text{ m s}^{-1}$ as given by the manufacturer (Aeroprobe Corporation); however, the impact of the INS was not included in their analysis. In Thomas et al. (2012), the Manta RPA was also equipped with a commercial Aeroprobe and a C-Migits-III INS to obtain a minimum resolvable w of 0.17 m s^{-1} (1σ). The uncertainty analysis was based on a Gaussian error propagation described in Garman et al. (2006). The Manta and ScanEagle RPAs described in Reineman et al. (2013) achieved precise wind measurements with a custom nine-hole probe and NovAtel INS with reported uncertainties for w within $\pm 0.021 \text{ m s}^{-1}$. Their uncertainty was obtained from a Monte Carlo simulation and was also consistent with reverse-heading maneuvers. The higher precision reported in the latter study (Reineman et al., 2013) is related to probe design and the high precision of the INS. The vertical wind measurements in Reineman et al. (2013) have a similar performance as reported with the BAT probe (Best Air Turbulence probe) on a small piloted aircraft (Garman et al., 2006). For aerosol–cloud studies, vertical wind measurements near 0.1 m s^{-1} are needed, which is within instrument uncertainties for most of the systems described above.

Elston et al. (2015) has identified four main points that still need to be addressed for atmospheric wind measurements using RPAS: (1) true heading remains one of the main sources of inaccuracy in horizontal wind calculation; (2) precise altitude measurement with GPS impacts vertical wind calculations; (3) miniaturization of INS for small RPA with better accuracy of fusion sensors; and (4) RPAS regulations and integration in the airspace, which delay research progress.

¹Commonly called unmanned aerial vehicle (UAV).

²RPA refers to the aircraft, as RPAS represents the airframe and the ground control station.

Until recently, wind measurements from RPA have been mainly used for atmospheric boundary layer studies of turbulence and atmospheric fluxes. In the BLLAST field campaign, multiple RPAs have been deployed to study the evolution of the boundary layer during the transition between afternoon and evening periods (Lothon et al., 2014). Results of sensible and latent heat fluxes, as well as turbulent kinetic energy (TKE), were calculated from the SUMO RPA flights (Reuder et al., 2016; Båserud et al., 2016). The operation of the M²AV and the MASC RPAs during the BLLAST campaign was described in Lampert et al. (2016) with a particular focus on turbulence. A comparison of nearly co-located measurements of TKE between different platforms (tethered balloon, RPA, and manned aircraft) compared the different techniques of obtaining atmospheric wind vectors (Canut et al., 2016). A study of new particle formation in the atmospheric boundary layer has been conducted by Platis et al. (2016), using the MASC and ALADINA RPAs. Vertical profiles during the short morning transition between shallow convective to mixed boundary layer highlight the important role of turbulence in new particle formation processes.

In addition, vertical winds are used to study ACIs, which is the focus of the collaborative project, BACCHUS (impact of Biogenic versus Anthropogenic emissions on Clouds and Climate: towards a Holistic UnderStanding) (BACCHUS, 2016). One critical parameter in ACI studies, not previously measured by RPA, is the vertical wind velocity w at cloud base. Peng et al. (2005) show the importance of measuring vertical velocity in convective clouds for aerosol–cloud closure studies and highlight the need for more cloud microphysical data to further test the sensitivity of cloud droplet number concentration to variations in vertical velocity. Sullivan et al. (2016) investigate the role of updraft velocity in temporal variability of clouds in global climate models (GCMs) and emphasize that simulated vertical velocity distributions are too rarely compared to observations, citing the lack of data. As more than half of the temporal variability in droplet number was due to updraft velocity fluctuations, Sullivan et al. (2016) call for coordinated effort in the atmospheric science community to address the current gap in observations; otherwise uncertainties in modeled cloud droplet number and subsequent radiative properties may remain irreducible. In Conant et al. (2004) and Sanchez et al. (2017), updraft velocity has also been described as a critical parameter, along with cloud condensation nuclei (CCN) spectra, to derive cloud droplet number in ACI studies. Both of these studies show that cloud microphysical and radiative properties are well simulated when CCN spectra and cloud updrafts have been measured.

Therefore, the motivation of the present work is driven by the need for vertical wind measurements to better quantify ACIs. Commercial multi-hole probes do exist (i.e., Aeroprobe Corporation and Vectoflow); however, pressure sensor measurements and integration of the INS have been developed for this study – hence, the need to calibrate and validate

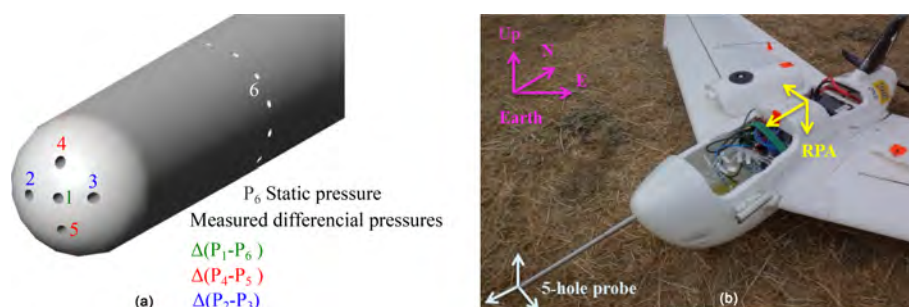


Figure 1. (a) Five-hole probe tip, schematic representation of pressure holes. (b) Five-hole probe mounted on a Skywalker X6 RPA.

the probe–INS pair. Section 2 of the paper describes the RPA platform and the methods used to calculate atmospheric wind vectors. Section 3 presents the calibration of a commercial five-hole probe and its custom electronics in a wind tunnel, complemented by an uncertainty analysis on vertical wind velocity, w . Section 4 shows a comparison of the five-hole probe on a RPA with sonic anemometers on a meteorological mast. Vertical wind velocities from the RPA are compared to those of a cloud radar in different meteorological conditions (Sect. 5). Lastly, the sensitivity of cloud droplet number is investigated as a function of updraft distributions (Sect. 6).

2 Materials and methods

2.1 Remotely piloted aircraft description

The RPAs used here to measure vertical wind velocity and study ACIs are based on the commercially available Skywalker X6 model. The wingspan is 1.5 m long, and take-off weight varies between 1.5 and 2.5 kg depending on the mission specific payload. The RPA's autonomous navigation system is the open-source autopilot Paparazzi from École Nationale de l'Aviation Civile (Brisset et al., 2006). One of the RPAs (wind-RPA) is specially equipped to measure atmospheric wind vectors, particularly vertical wind, whose validation and study of different cloud cases is the purpose of this work. Its take-off weight is 2.3 kg with a 500 g payload. The cruise air speed is approximately 16 m s^{-1} .

2.2 Payload instrumentation

Wind vectors are obtained from a five-hole probe (Aeroprobe Corporation) linked to its differential pressure sensors (All Sensors) by flexible tubing, and an INS (Lord Sensing Microstrain 3DM-GX4-45). The data from both the INS and the pressure sensors are recorded by the same acquisition system to ensure precise synchronization. The acquisition frequency is 30 Hz, and data are averaged to 10 Hz for analysis. The five-hole probe consists of a 6 mm diameter stainless tube with a hemispherical tip (Fig. 1). The associated electronics have been designed at the Centre National de Recherches Météorologiques (CNRM) and consist of three differential

pressure sensors (All Sensors 5-inch-D1-MV) and one absolute pressure sensor (All Sensors MLV-015A). The configuration of pressure sensor connections is similar to Reineman et al. (2013). The tubing length between the probe manifold and the pressure sensors is less than 15 cm and the inner diameter is 0.1 mm. These dimensions are also similar to Wildmann et al. (2014), in which an extensive study of tubing issues is conducted. Figure 1a illustrates the probe schematic: hole 1 gives an estimate of the pressure at the stagnation point of the tip; the differential pressure between holes 2 and 3 provides β , the angle of sideslip; the differential pressure between 4 and 5 gives α , the angle of attack; and hole 6, a ring around the probe, corresponds to the static pressure port. The air speed, V_a , is calculated from the dynamic and static pressure (holes 1 and 6). To obtain atmospheric winds, the five-hole probe system must be calibrated in the probe's coordinate system and converted to the Earth's coordinate system. The INS sends information obtained by an extended Kalman filter to the data acquisition system regarding attitude angles (roll ϕ , yaw ψ , and pitch θ), GPS time and GPS position and altitude, and ground speeds of the RPA in the Earth's coordinate system. Schematics of coordinate systems and angles are shown in Fig. 1b. The payload of the wind-RPA also includes temperature (IST, model P1K0.161.6W.Y.010), absolute pressure (All Sensors, model 15PSI-A-HGRADE-SMINI), and relative humidity sensors (IST, P14 Rapid-W). Two LI-COR LI-200R pyranometers (400 to 1100 nm wavelengths) are installed on the fuselage; one facing up to measure downwelling solar irradiance, and the other facing down to measure upwelling solar irradiance. The ratio of the downwelling and upwelling solar irradiance is used to detect the presence of cloud (when this ratio approaches unity).

2.3 Methods

Atmospheric wind vectors in the Earth's coordinate system are obtained by subtracting the measured motion of the RPA (given by the INS) from the motion of the air (given by the five-hole probe), as stated in Lenschow and Spyers-Duran (1989). The angle of attack α , the angle of sideslip β , and the air speed V_a are measured by the five-hole probe in the probe coordinate system and then transformed to the RPA coordi-

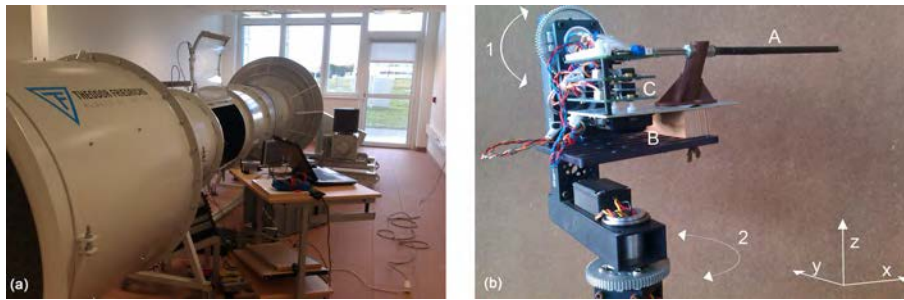


Figure 2. (a) Theodor Friedrichs wind tunnel, Météo-France, Toulouse. (b) Two-axis platform for wind tunnel experiment. 1: rotation on pitch axis; 2: rotation on yaw axis; A: five-hole probe; B: INS; C: pressure sensors.

nate system, while the attitude angles from the INS provide the transformation of α , β , and V_a from the RPA coordinate system to the Earth's coordinate system. The full set of wind equations from Lenschow and Spyers-Duran (1989) are followed throughout this study to derive the atmospheric wind vectors in the Earth's coordinate system. The angular acceleration of the RPA is negligible, particularly during straight-and-level legs, because the distance between the five-hole probe and the INS is on the order of centimeters. More details on wind equations and schematics of coordinate systems are found in Lenschow and Spyers-Duran (1989), Boiffier (1998), and van den Kroonenberg et al. (2008). The calibration of the five-hole probe has been performed in a wind tunnel (Theodor Friedrichs & Co) with a diameter of 70 cm. The uncertainty associated with the wind velocity in the wind tunnel is less than 2 %.

3 Calibration of the five-hole probe

The calibration of the five-hole probe is based on a method described in Wildmann et al. (2014) and consists of a series of wind tunnel experiments to characterize the response of the five-hole probe at different angles. The five-hole probe, the pressure sensors, and the INS are installed in the wind tunnel on a two-axis platform with motion in vertical and horizontal planes (Fig. 2). The calibration of the five-hole probe is a two-step process – first calibrating the differential pressure sensors (Pa), then associating the differential pressures in Pa with angles (α and β ; degrees) and air speed (V_a ; m s^{-1}). The two-axis platform rotates in the pitch axis (motion in the vertical plane) and yaw axis (motion in the horizontal plane), controlled with a LabView program (Fig. 2). The amplitude of pitch and yaw angles varies up to $\pm 15^\circ$ to simulate the largest envelope of expected flight conditions. In the wind tunnel, the angle of attack α (five-hole probe) and the pitch angle θ (INS) are, by definition, the same for a well-aligned system, as for the angle of sideslip β (five-hole probe) and the yaw angle ψ (INS). The INS is used as a reference angle measurement between the five-hole probe and the airflow in the wind tunnel. The determination of α , β ,

and V_a from the five-hole probe depends on four coefficients C_α , C_β , and C_q for the dynamic pressure and C_s for the static pressure (Wildmann et al., 2014; Treaster and Yocum, 1978). To account for offsets in the alignment between the five-hole probe, INS, and wind tunnel, experiments are performed with the probe in the standard orientation shown in Fig. 1, with roll angle equal to 0° (+ markers in Fig. 3), and the probe in inverted orientation for the roll angle equal to 180° (x markers in Fig. 3). Likewise, the same procedure is followed by rotating the five-hole probe by $\pm 90^\circ$ to determine the offset in the horizontal plane for β . INS angles and ratios of differential pressure sensors are recorded for platform positions between $\pm 15^\circ$ for three air speeds in the wind tunnel. Figure 3 shows that calibration coefficients are within instrument uncertainty for air speed between 15 and 25 m s^{-1} , and the calibration shows a nearly linear relationship when the probe is within $\pm 10^\circ$. A systematic offset of 7 % has been found between the calculation of V_a (five-hole probe) and the wind tunnel air speed. The 1σ uncertainty in V_a determined by the five-hole probe is 0.1 m s^{-1} .

To extend the measurements beyond the single-axis of motion described previously, the pitch and yaw angles of the two-axis platform are varied concurrently (Fig. 4a), and the corresponding differential pressure coefficients C_α and C_β are measured (Fig. 4b). This yields a matrix relating the probe's response to the relative vertical (α) and horizontal (β) winds (Fig. 4). The grid in Fig. 4a illustrates the discrete 5° steps in pitch and yaw angles to create a 5×5 calibration matrix for a constant wind speed of 15 m s^{-1} . Similar results are also shown in Wildmann et al. (2014). The horizontal angular bias in Fig. 4 is due to a 3° roll angle in the mounting of the two-axis platform in the wind tunnel. The asymmetry in the calibration matrix (i.e., higher degree of non-linearity on the right side of Fig. 4b) results from a discrepancy in the alignment of the five-hole probe relative to the wind tunnel air flow. The offset between the two-axis platform and the INS is also visible as the grid in Fig. 4a is not centered on 0 (also called the zero-angle offset). The calibration coefficients show a nearly linear relationship for C_α and C_β between values of ± 0.7 , which corresponds to α and β within $\pm 10^\circ$ (Fig. 4).

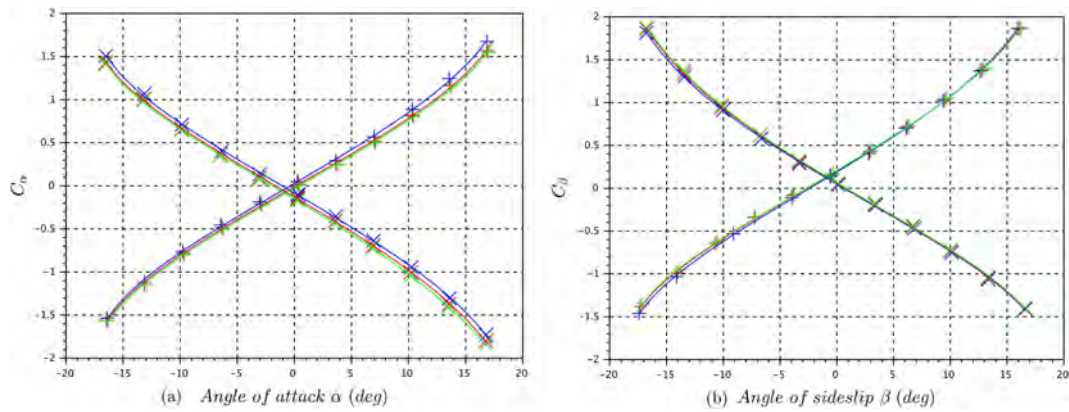


Figure 3. (a) Calibration coefficients C_α for the calculation of the angle of attack α (INS pitch angles as a reference) at different wind tunnel velocities (blue: 15 m s⁻¹; red: 20 m s⁻¹; green: 25 m s⁻¹). The positive slope corresponds to the probe in standard orientation (+ markers). The negative slope corresponds to the probe in inverted orientation (x markers). (b) Calibration coefficients C_β for the calculation of the angle of sideslip β (INS yaw angles as a reference) at different wind tunnel velocities (blue: 15 m s⁻¹; red: 20 m s⁻¹; green: 25 m s⁻¹). The positive slope corresponds to the probe in standard orientation (+ markers). The negative slope corresponds to the probe in inverted orientation (x markers).

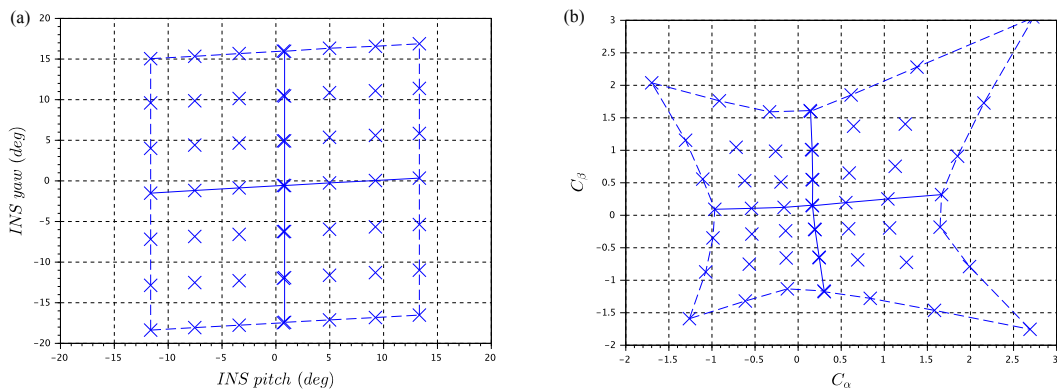


Figure 4. (a) Variation by step of pitch and yaw angles of the two-axis platform in wind tunnel (air speed 15 m s⁻¹). (b) Corresponding C_α and C_β of the five-hole probe to steps of the platform.

3.1 Experimental error analysis on vertical wind velocity

The performance of the five-hole probe–INS pair is verified by using a dynamic platform to generate motion in the controlled environment of the wind tunnel. The wind tunnel provides a laminar flow; thus vertical wind velocity is, by definition, zero even when the two-axis platform is in motion. Therefore, the response of the five-hole probe can be validated in the wind tunnel by controlling the amplitude (up to $\pm 15^\circ$) and the angular rate of change (up to 22° s^{-1}) of the platform in the vertical (pitch) axis. As expected, the estimates of vertical wind velocity, w , in the wind tunnel are close to zero. The 1σ standard deviation of w increases with the angular rate of change of the platform (Fig. 5), which seems to be related to a lag in the INS’s Kalman filtering process. Under the flight conditions reported in this work, the

pitch angle rate of change rarely exceeds $\pm 10^\circ \text{ s}^{-1}$ during straight-and-level legs, implying the minimum resolution of vertical wind velocity measurement with the five-hole probe–INS system is 0.07 m s^{-1} . The uncertainties in w increase when accounting for all parameters, as shown in the next section.

3.2 Gaussian error propagation on vertical wind velocity

To measure vertical wind velocity of a cloud field, the RPA flies straight-and-level legs at a prescribed altitude. Results from such flight legs show that pitch and roll angles are almost always less than 10° with a rate of change within $\pm 10^\circ \text{ s}^{-1}$, as mentioned in the previous section. In such conditions, the five-hole probe response lies in the quasi-linear regime of the calibration coefficients (Fig. 4), and the small-

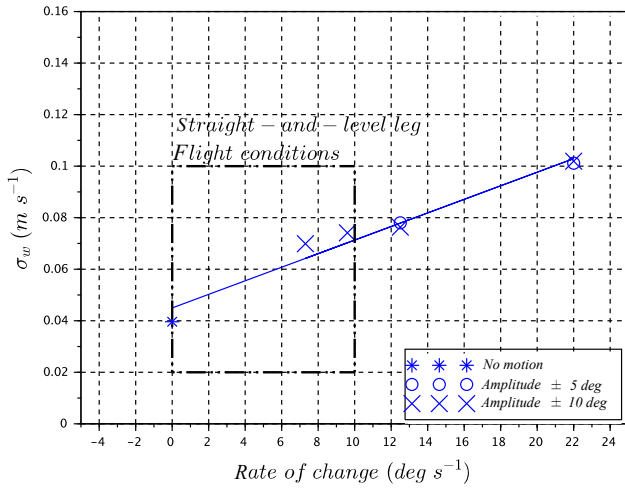


Figure 5. Standard deviation of vertical wind velocity w for each rate of change of the pitch angles on the two-axis platform. For the flight along straight-and-level legs, the rate of change does not exceed 10° s^{-1} .

angle approximations accurately represent the full set of wind equations (Lenschow and Spyers-Duran, 1989). Therefore, the small-angle approximation for the vertical wind velocity equation is used to conduct an uncertainty analysis on w :

$$w = -V_a \sin(\theta - \alpha) + V_z, \quad (1)$$

with V_a the air speed, θ the pitch angle, α the angle of attack, and V_z the vertical RPA speed. The method used to determine the Gaussian error propagation is similar to the uncertainty analysis conducted in Garman et al. (2006). Here, we present the contribution of each component in Eq. (1) (i.e., angle of attack, air speed, pitch, and vertical RPA speed) to the uncertainty in w . The 1σ uncertainty related to the vertical wind velocity is

$$\sigma_w = \sqrt{\left(\frac{\partial w}{\partial \alpha} \sigma_\alpha\right)^2 + \left(\frac{\partial w}{\partial V_a} \sigma_{V_a}\right)^2 + \left(\frac{\partial w}{\partial \theta} \sigma_\theta\right)^2 + \left(\frac{\partial w}{\partial V_z} \sigma_{V_z}\right)^2} \quad (2)$$

where σ_{V_a} is 0.1 m s^{-1} (from wind tunnel measurements), σ_θ is 0.25° , and σ_{V_z} is 0.1 m s^{-1} (both provided by the INS manufacturer). The uncertainties are summarized in Table 1. The error propagation is conducted for α based on C_α in the linear regime (with the slope a_α and the intercept b_α):

$$\alpha = a_\alpha C_\alpha + b_\alpha \quad \text{and} \quad C_\alpha = \frac{\Delta(P_4 - P_5)}{\Delta(P_1 - P_6) - \Delta P}, \quad (3)$$

with $\Delta P = \frac{1}{4}(|\Delta(P_4 - P_5)| + |\Delta(P_2 - P_3)|)$, $\Delta(P_4 - P_5)$ the differential pressure between holes 4 and 5, $\Delta(P_2 - P_3)$ the differential pressure between holes 2 and 3, and $\Delta(P_1 - P_6)$

the differential pressure between holes 1 and 6 (Fig. 1a). Error propagation of Eq. (3) leads to

$$\sigma_\alpha = a_\alpha \sigma_{C_\alpha} \quad (4)$$

and, as C_α is calculated based on the differential pressures measured by the five-hole probe,

$$\sigma_{C_\alpha} = \sqrt{\left(\frac{\partial C_\alpha}{\partial \Delta(P_4 - P_5)} \sigma_{\Delta(P_4 - P_5)}\right)^2 + \left(\frac{\partial C_\alpha}{\partial \Delta(P_2 - P_3)} \sigma_{\Delta(P_2 - P_3)}\right)^2 + \left(\frac{\partial C_\alpha}{\partial \Delta(P_1 - P_6)} \sigma_{\Delta(P_1 - P_6)}\right)^2}. \quad (5)$$

The analysis presented here results in $\sigma_w = 0.12 \text{ m s}^{-1}$, which is similar to the uncertainty in w based on the wind tunnel measurements (from Sect. 3.1) and comparable to the results reported by other studies cited in the introduction.

4 Comparison of vertical winds from RPA and sonic anemometers

The measurements of vertical wind velocity on an RPA were compared to sonic anemometers (Campbell CSAT3 3-D Sonic Anemometer) under calm wind conditions at Centre de Recherches Atmosphériques (CRA), which is an instrumented site of the Pyrenean Platform of Observation of the Atmosphere (P2OA), near Lannemezan, France. The purpose of the comparison is (1) to assess the performance of the RPA measurement of updraft by comparing power spectral density (PSD) and vertical wind w distributions measured by sonic anemometers and (2) to calculate TKE used to study boundary layer dynamics and compare with previous studies. Table 2 summarizes flight and wind conditions encountered during these validation experiments. The sonic anemometers are installed on a meteorological mast at 30 m a.g.l. (meters above ground level) and 60 m a.g.l. as part of permanent installations at the CRA. During the experiment, the RPA flew straight N-S and E-W legs in the vicinity of the mast at 60 m a.g.l. The leg length was 1600 m and the duration of flights was approximately 1.5 h. A total of five flights were conducted in different meteorological conditions: a series of three flights were conducted on 15 October 2015 at different times of the day, one flight was conducted in the morning on 20 May 2016, and the last flight was conducted in the afternoon on 7 July 2016 (Table 2). While all flights were conducted in low wind conditions (wind speed less than 4 m s^{-1}), the turbulent conditions differed from one flight to another. The roll angle exceeded 10° less than 1 % of the time, except during flight 4 when roll exceeded 10° 2 % of the time. The pitch angle never exceeded 10° , except when approaching stall speed and, even then, only exceeded 10° less than 0.1 % of the time.

Table 1. Uncertainty (1σ) associated with parameters from five-hole probe (5HP) and inertial navigation system (INS) for the calculation of error associated with the vertical wind velocity w .

Variable	Symbol	Precision/value
Differential pressure between holes 1 and 6 (5HP)	$\sigma_{\Delta(P_1-P_6)}$	1.2 Pa
Differential pressure between holes 2 and 3 (5HP)	$\sigma_{\Delta(P_2-P_3)}$	1.4 Pa
Differential pressure between holes 4 and 5 (5HP)	$\sigma_{\Delta(P_4-P_5)}$	1.2 Pa
Ratio of differential pressures (5HP)	σ_{C_α}	0.013
Angle of attack (5HP)	σ_α	0.16°
Pitch angle (INS)	σ_θ	0.25°
Air speed (5HP)	σ_{V_a}	0.1 m s ⁻¹ systematic 7 %
Vertical RPA speed (INS)	σ_{V_z}	0.1 m s ⁻¹
Coefficient calibration – slope	a_α	12.52
Coefficient calibration – intersect	b_α	0.039
Uncertainty related to vertical wind velocity	σ_w	0.12 m s ⁻¹

Table 2. Description of flights conducted at CRA, Lannemezan, France.

ID	Date	Time (local)	Duration	Horizontal wind speed	Wind direction	Intersection number*	Remarks
Flight 1	15 Oct 2015	08:05	1 h 30 min	0.6 m s ⁻¹	NE	0.72	Sonic anemometer at 30 m a.g.l. only
Flight 2	15 Oct 2015	12:47	1 h 22 min	1.9 m s ⁻¹	N	0.79	Sonic anemometer at 30 m a.g.l. only
Flight 3	15 Oct 2015	15:35	1 h 18 min	2.7 m s ⁻¹	NW	0.90	Sonic anemometer at 30 m a.g.l. only
Flight 4	20 May 2016	09:15	1 h 35 min	3.2 m s ⁻¹	SW	0.71	Air speed close to stall speed
Flight 5	7 Jul 2016	15:18	1 h 06 min	1.7 m s ⁻¹	NE	0.88	Optimized INS

* Intersection number described in Sect. 4.3.

4.1 Power spectral density functions

To assess the performance of the RPA measurements of atmospheric wind, PSD functions for each of the three wind components of the RPA are compared to PSDs from sonic anemometers. The PSDs of the wind velocities from RPA and sonic anemometers generally follow the $-5/3$ slope from the Kolmogorov law as expected (Fig. 6). The PSDs for flights 1, 2, and 3 are averaged to illustrate the probe–INS performance prior to a magnetometer calibration and revised Kalman filtering of the INS (flight 5). During flight 4, the RPA experienced excess motion due to an air speed close to stall speed, which degraded the wind measurements; consequently, results from flight 4 are not included in the analysis. For flights 1, 2, and 3 (prior to reconfiguring the INS), discrepancies in the PSD energy level are visible at 10⁻¹ Hz particularly on the u component (Fig. 6b). The bump in the u component at 10⁻¹ Hz is related to the uncertainty in the INS heading measurement, which impacts the horizontal wind calculation, particularly the transversal wind component (the wind component perpendicular to RPA heading). Based on the reverse-heading maneuvers, the uncertainty in horizontal winds is estimated to be within ± 1.1 m s⁻¹. After reconfiguring the INS,

a notable improvement in PSDs of all three wind components (particularly u component; transversal wind) was observed (Fig. 6; blue lines). The improvement in INS performance clearly demonstrates the importance of precise INS filtering and heading measurements.

Nonetheless, the PSDs still show a systematic difference between the energy levels related to wind components from the sonic anemometer and the RPA. For the three wind components calculated from RPA measurements, the energy level of ground speeds obtained from the INS (V_x , V_y , and V_z) are higher than the other terms in wind equations for frequencies less than 0.3 Hz. To assess the origin of the different energy levels, the decomposition of the vertical wind equation w (Lenschow and Spyers-Duran, 1989) is based on the simplified form shown as Eq. 1. PSDs of each component of w , V_z (vertical ground speed) and A_w (defined as $-V_a \sin(\theta - \alpha)$), are calculated to assess biases related to the INS (Earth frame) and the five-hole probe (RPA frame). The average results from the RPA flights and the sonic anemometers are presented in Fig. 7. The high energy levels at low frequencies seem to be related to uncertainties (even a drift) associated with the vertical velocity measurement. The higher energy levels do translate to systematically higher TKE val-

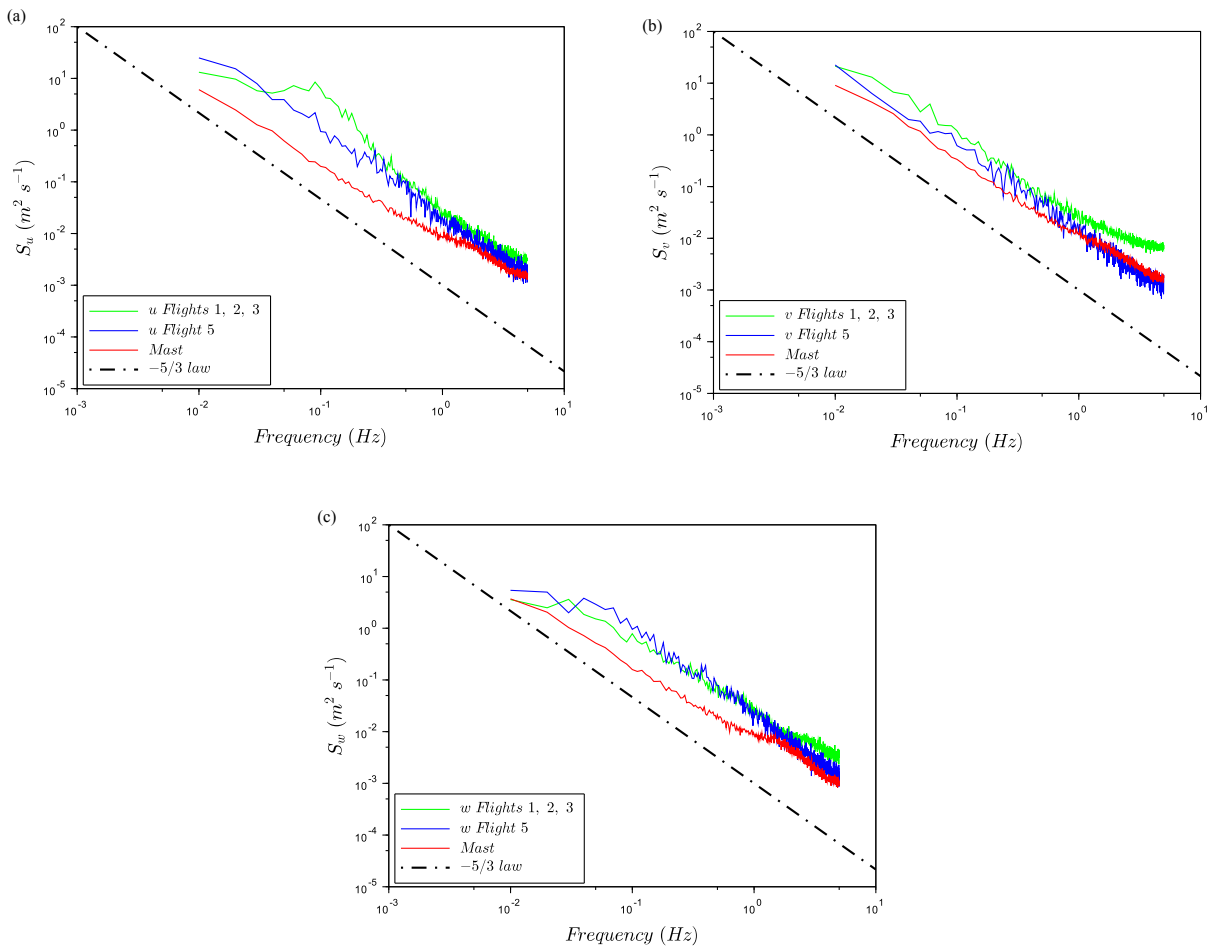


Figure 6. Comparison of averaged PSDs from sonic anemometers (mast: red) and RPA wind measurements averaged for flights 1, 2 and 3 (green), and flight 5 (blue) after the INS has been optimized. The dashed line represents the $f^{-5/3}$ law. **(a)** Spectral energy S of u -wind component function of frequency, **(b)** Spectral energy S of v -wind component function of frequency, **(c)** Spectral energy S of w -wind component function of frequency.

ues (Sect. 4.2); however, these concerns do not significantly impact the results in ACI studies (Sect. 6).

The relatively high energy levels associated with the PSDs are not unique, yet they have not been adequately explained in the literature. Båserud et al. (2016) and Reuder et al. (2016) reported systematically high energy levels of the vertical wind component from the SUMO compared to sonic anemometers on a mast (also at CRA in Lannemezan, France). The issue of higher energy levels was then to “be further investigated in the future”. Other studies have compared TKE values between RPA platforms and a reference; the TKE is linked to PSD energy levels via the variance of each wind component. For example, Lampert et al. (2016) compare TKE between five-hole probe on the M²AV and sonic anemometers (also on the mast at CRA, Lannemezan) and show higher TKE values associated with the M²AV during the afternoon and the night, which also implies higher energy levels of the PSDs. Canut et al. (2016) also com-

pare five-hole probe measurements of M²AV and manned aircraft (Piper Aztec) to sonic anemometer measurements on a tethered balloon. The TKE measurements from the M²AV compare well to the tethered balloon measurements (which indirectly compare well to the sonic anemometer on the mast); however, the results show that TKE measured from the manned aircraft were biased towards higher TKEs. Thomas et al. (2012) conclude that direct comparisons between the RPA and the sonic anemometer are tenuous in their study as the Manta RPA flew at 520 m a.g.l., while the sonic anemometer was only at 10 m a.g.l. Reineman et al. (2013) is the only study that shows similar vertical wind component PSD between a RPA and a ground-based mast (albeit for a relatively short flight above a flat desert). The main difference between the RPAs listed above and the system described in Reineman et al. (2013) is the INS, as no other group has deployed as precise an INS. Since the energy levels of the PSDs for the configuration presented in this paper, are higher,

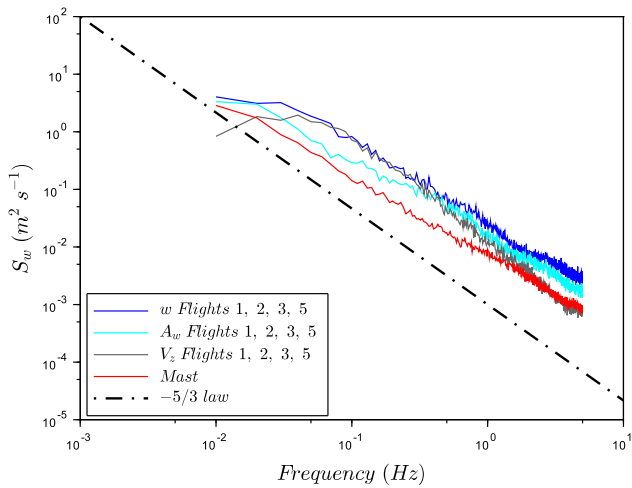


Figure 7. Comparison of averaged PSDs from sonic anemometers (mast: red) and RPA wind measurements averaged for flights 1, 2, 3, and 5 (blue). Spectral energy S of decomposed w -wind component with $w = A_w$ (cyan) + V_z (grey) function of frequency. The dashed line represents the $f^{-5/3}$ law.

one cannot calculate divergence or convergence; however, the PSDs from the measurements presented here show slopes approaching the expected $-5/3$ Kolmogorov regime and the RPA observations reproduce trends in TKE over a range of meteorological conditions. There is certainly more work that needs to be done to improve the turbulence measurements – particularly by improving the INS measurements.

4.2 Turbulent kinetic energy

In the atmospheric boundary layer, the TKE quantifies the intensity of turbulence, which controls mixing of the atmosphere (Wyngaard and Coté, 1971; Lenschow, 1974). TKE is defined as

$$\text{TKE} = \frac{1}{2} (\sigma_u^2 + \sigma_v^2 + \sigma_w^2), \quad (6)$$

with σ_u^2 as the variance of E–W wind, σ_v^2 as the variance of N–S wind, and σ_w^2 as the variance of vertical wind. To assess TKE values between the wind-RPA (TKE_{RPA}) and the sonic anemometers on the mast (TKE_{mast}), we compare different horizontal atmospheric length scales. As the length of each RPA leg is 1600 m, multiples of these legs are chosen for comparison with the sonic anemometers (i.e., 800, 1600, 3200, 4800, 6400 m). The averaging time necessary for the sonic anemometers to record an air mass traveling an equivalent length is calculated using the observed horizontal wind speed and temporally centered with respect to the RPA leg. Mast observations at 30 or 60 m a.g.l. are selected based on data availability (Table 2). Figure 8 clearly shows significant differences between mast-based σ_u^2 (E–W wind component) and σ_v^2 (N–S wind component) at different altitudes and length scales. Such differences, partic-

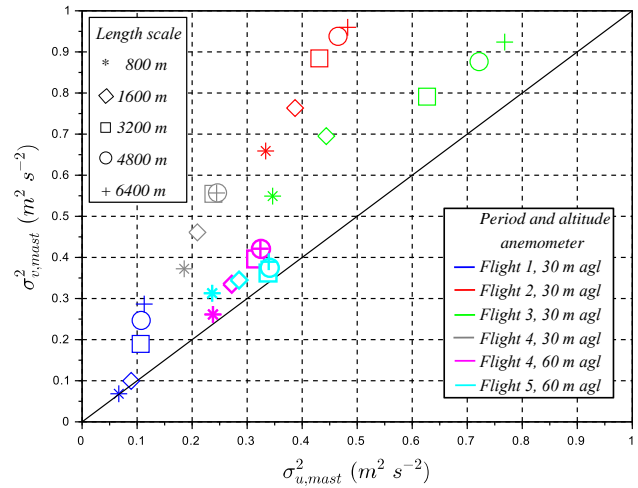


Figure 8. Comparison of TKE_{RPA} and TKE_{mast} . Open diamonds TKE_{RPA} are calculated with the three wind variances of RPA, solid diamonds are obtained with an isotropy assumption $\sigma_{u,\text{RPA}}^2 = \sigma_{v,\text{RPA}}^2$ observed at 60 m a.g.l. by the sonic anemometer in Fig. 8. The uncertainty bars correspond to 1σ , using all the legs during the RPA flights and using each length scale from 800 to 6400 m for the sonic anemometers.

ularly at 30 m a.g.l., are related to surface topography (e.g., terrain, nearby trees and fields). Meanwhile, Fig. 8 confirms that σ_u^2 and σ_v^2 are similar at 60 m a.g.l. (i.e., isotropy in the N–S and E–W directions), which can be used to assess the performance of the five-hole probe–INS on the RPA. Results show that TKE_{RPA} are initially higher than TKE_{mast} (open diamond markers in Fig. 9), as u (the transversal wind component) shows higher variances than v (as described in Sect. 4.1). Applying the observed isotropy shown in Fig. 8 ($\sigma_{u,\text{RPA}}^2 = \sigma_{v,\text{RPA}}^2$ at 60 m a.g.l.) for the RPA observations, the comparison of TKE_{RPA} and TKE_{mast} improves (Fig. 9; solid diamond markers) by replacing σ_u^2 by σ_v^2 in the calculation of TKE_{RPA} . We note, however, the isotropic conditions are not always satisfied (i.e., longitudinal wind rolls affecting crosswind fluxes reported in Reineman et al., 2016). Consequently, a RPA flight strategy, such as parallel and cross-wind legs, is essential in identifying isotropic conditions and measurement errors associated with the five-hole probe–INS system.

As mentioned in Sect. 4.1, studies that report TKE have been published that compare the SUMO and $M^2\text{AV}$ to the sonic anemometer at CRA, Lannemezan (Båserud et al., 2016; Lampert et al., 2016). The reported values of TKE from both of these studies are within 50 % of TKE from the sonic anemometer. Canut et al. (2016) also show a relatively good agreement of TKE between a tethered balloon, the $M^2\text{AV}$, and the manned aircraft with a correlation coefficient $R^2 = 0.88$. In this study, for the comparison between the wind-RPA and sonic anemometers (Fig. 9), the slope of the linear regression for the RPA observations is

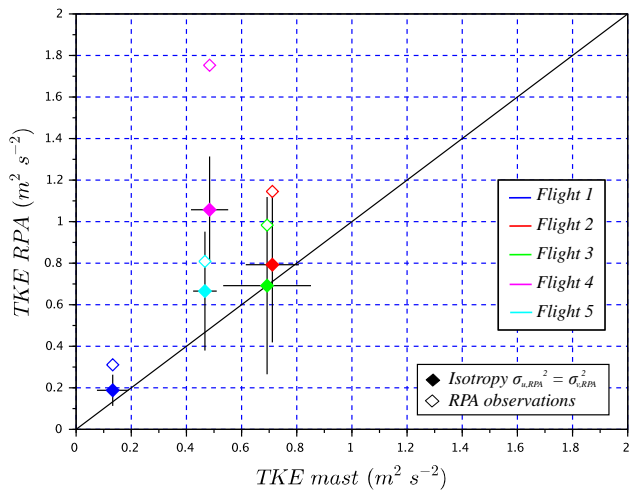


Figure 9. Comparison of variances $\sigma_{u,\text{mast}}^2$ and $\sigma_{v,\text{mast}}^2$ from the sonic anemometers for the associated flight periods and length scales.

1.32 ($R^2 = 0.97$) and improves to 0.95 ($R^2 = 0.91$) with the isotropy assumption ($\sigma_{u,\text{RPA}}^2 = \sigma_{v,\text{RPA}}^2$). Flight 4 is not included in this analysis because of known issues related to flight performance. These results suggest that improving the measurement of horizontal winds and reducing biases in the horizontal components of the variances may be achieved by (1) improvement of the INS heading measurement (also noted in Elston et al., 2015) and (2) verified with a cross-leg flight plan (i.e., orthogonal legs).

4.3 Vertical wind velocity distributions

To compare vertical wind from the RPA to the sonic anemometer, angle of attack α and pitch angle θ are re-centered such that average vertical velocity w is 0 m s^{-1} over the time of the flight. This step is needed because the alignment of the five-hole probe relative to the Earth's frame may change with meteorological conditions (such as wind speed) and flight parameters (such as air speed and nominal pitch angles). The re-centering step of the five-hole probe on the RPA is further justified by results from the sonic anemometers on the mast, which also show an average vertical velocity approaching 0 m s^{-1} over the duration of the flight. Distributions of vertical wind velocities from the RPA and sonic anemometer at 60 m a.g.l. are compared, and the intersection method is used to quantify the agreement between the distributions. An example of the vertical wind distributions are shown in Fig. 10 for flight 5. The calculation of the intersection number is obtained from $\sum_{i=1}^N \min(I_i, M_i)$ with I and M as the normalized distributions to be compared, and N as the total number of bins. For an exact match, the intersection method result is unity; for a complete mismatch, the result is zero. Table 2 summarizes the intersection numbers between

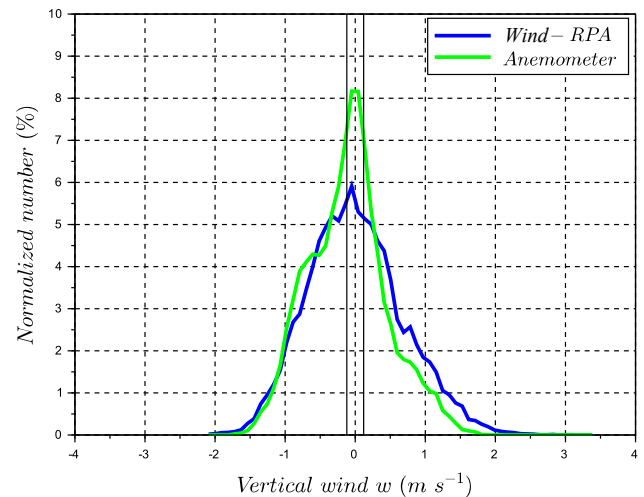


Figure 10. Distribution functions of vertical wind w for RPA and sonic anemometer at 60 m a.g.l. measurements, flight 5. The vertical bars represent the uncertainty ($\sigma_w = 0.12 \text{ m s}^{-1}$) associated with RPA vertical wind measurements.

the RPA and sonic anemometer vertical wind distributions for the five flights. The intersection numbers between RPA and anemometer vertical wind distributions are higher than 70%. As expected, this value is lower during flight 4.

5 Comparison of vertical wind velocities from RPA and cloud radar

A BACCHUS field campaign took place at the Mace Head Atmospheric Research Station on the west coast of Galway, Ireland, in August 2015. The purpose was to study ACIs, linking ground-based and satellite observations using RPAS (Sanchez et al., 2017). Among the four instrumented RPAs which flew at Mace Head, the wind-RPA was equipped with a five-hole probe and an INS to obtain vertical wind velocities, as well as upward- and downward-facing pyranometers to identify cloud sampling periods. During the campaign, we concentrated on measurements of vertical wind velocity near cloud base or within clouds to study ACIs. After identifying the cloud base from the ceilometer or based on a vertical profile of an earlier flight, the wind-RPA was sent to an altitude close to cloud base, flying 6 km long straight-and-level legs. Horizontal wind speeds varied from 6 to 12 m s^{-1} from the west during the case studies presented here. During this field campaign, the wind-RPA flew in 10 of the 45 scientific flights for a total of 15 h. Of the 10 flights with the wind-RPA, three flights contained a complete set of observations (vertical winds, pyranometers, and cloud radar measurements). The other flights were not selected for a number of reasons: water in the five-hole probe (two flights), insufficient number of cloud radar data for comparison (two flights), no cloud (one flight), no pyranometer data to iden-

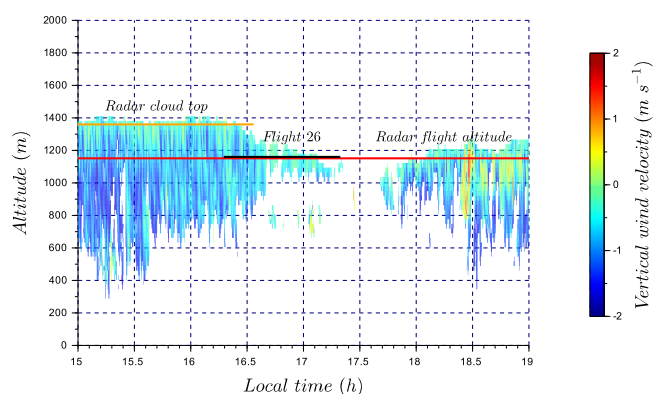


Figure 11. Time series of vertical wind velocity for a stratocumulus deck with light precipitation (flight 26). The color bar represents the cloud radar vertical wind velocity. Flight 26 sampling time is identified by the black segment. The red horizontal line corresponds to radar data at the altitude of the RPA (1160 m a.s.l.), and the orange line corresponds to radar data at cloud top (1360 m a.s.l.). Cloud radar vertical wind velocity at 1160 m a.s.l. and 1360 m a.s.l. are used in Fig. 12 to compare with RPA measurements.

tify clouds (one flight), and aborted mission due to strong winds ($> 15 \text{ m s}^{-1}$, one flight). In this section, we focus on three flights with the wind-RPA (Table 3), in which the vertical wind from the RPA is compared to vertical wind from the cloud radar at Mace Head.

The Doppler cloud radar (cloud radar MIRA-35, METEK, 35.5 GHz, Ka band) at the Mace Head Research Station is adapted to the observation of the cloud structure (Görsdorf et al., 2015). The cloud radar is equipped with a vertically pointed antenna with a polarization filter, a magnetron transmitter, and two receivers for discerning polarized signals. Measurements are available up to 15 km height for a temporal resolution of 10 s. The vertical resolution of the cloud radar is 29 m. In this study, cloud radar data from the cloud top or the RPA flight altitude are selected for the comparison.

While the flight altitude for the wind-RPA was estimated to be near the cloud base, uncertainties in retrieving cloud base height or an evolution in cloud base height related to diurnal cycles of the boundary layer inevitably lead to the RPA flying in the clouds rather than below cloud base. Note that direct comparison of instantaneous data between the RPA and cloud radar is not possible, as the RPA did not fly directly over the cloud radar and did not observe the same air mass. Moreover, the cloud radar reports vertical velocities every 10 s (and only when a cloud is present); therefore, relatively long averaging periods are needed to compare vertical velocity distributions of the cloud radar with RPA observations. In this section, we present selected time series of the cloud radar measurements that represent the state of the atmosphere during the flight; for cases with sufficient cloud cover, we present different averaging periods of the cloud radar (a short period that coincides with the RPA flight and

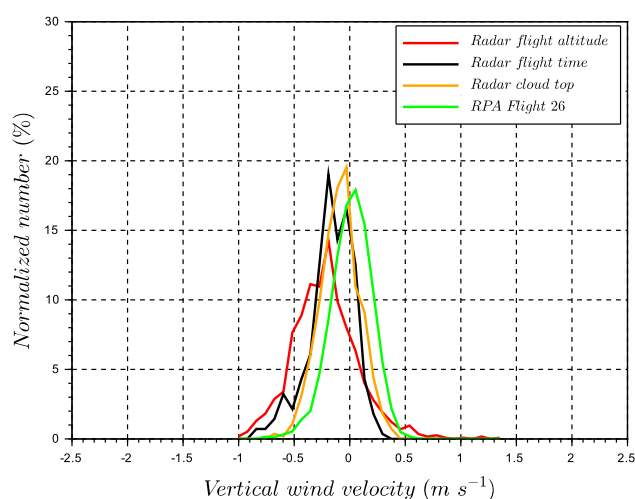


Figure 12. A comparison of vertical wind velocity distributions in a lightly precipitating stratocumulus deck between RPA (1160 m a.s.l.), cloud radar at RPA altitude (1160 m a.s.l.), and cloud radar at cloud top (1360 m a.s.l.). “Radar flight altitude” corresponds to 4 h of cloud radar measurements at the same altitude as the RPA flight. “Radar flight time” corresponds to the cloud radar measurements during the RPA flight period at the same altitude as the RPA. “Radar cloud top” corresponds to cloud radar measurements near the cloud top, which is in the non-precipitating part of the cloud. “RPA flight 26” corresponds to RPA vertical wind measurements during flight 26. Time periods and altitudes are identified in Fig. 11.

longer periods for better counting statistics). In the present study, normalized vertical wind velocity distributions of the cloud radar serve to validate the RPA results. In addition, the vertical velocity distributions provide insight on different atmospheric states (e.g., in–out of cloud, over water or land).

5.1 Stratocumulus deck with light precipitation (flight 26: 11 August 2015)

On 11 August, the sky was covered by a lightly precipitating stratocumulus deck, and the wind-RPA flew at 1160 m a.s.l. (about 100 m above the cloud base). The time series of vertical wind from the cloud radar is presented in Fig. 11, along colored horizontal lines that indicate observation periods of the cloud radar and RPA. Figure 12 presents a comparison of the normalized vertical wind distributions obtained by cloud radar and the RPA measurements. The standard deviation of RPA vertical wind distribution is $\sigma_{\text{RPA}} = 0.19 \text{ m s}^{-1}$ (or 0.10 m s^{-1} if only positive vertical velocities are considered). This result is comparable to the range of vertical wind standard deviations obtained in Lu et al. (2007) for stratocumulus clouds observed off the coast of Monterey, California, in the eastern Pacific ($0.06 < \sigma_w < 0.29 \text{ m s}^{-1}$, for $w > 0 \text{ m s}^{-1}$ from 11 sampled stratocumulus clouds). In this case study, the presence of falling cloud droplets to an altitude as low as 300 m a.g.l. (Fig. 11) negatively biases the vertical wind dis-

Table 3. Description of BACCHUS case study flights, Mace Head Research Station, Ireland. The intersection number compares vertical wind velocity distributions between RPA and cloud radar.

ID	Date	Time (local)	Duration	Horizontal wind speed	Wind direction	Intersection number ² (comparison with RPA)			Figure
						Radar flight alt.	Radar flight time	Radar cloud top	
Flight 26 ¹	11 Aug 2015	16:17	1 h 20 min	6 m s ⁻¹	WNW to SW	0.53	0.67	0.74	Fig. 12
Flight 30	15 Aug 2015	14:19	50 min	10 m s ⁻¹	W to WSW	0.77	–	–	Fig. 18
Flight 38	21 Aug 2015	16:10	1 h 30 min	10 m s ⁻¹	SSW	0.81	0.76	–	Fig. 15

¹ No pyranometer data. ² Intersection number described in Sect. 4.3

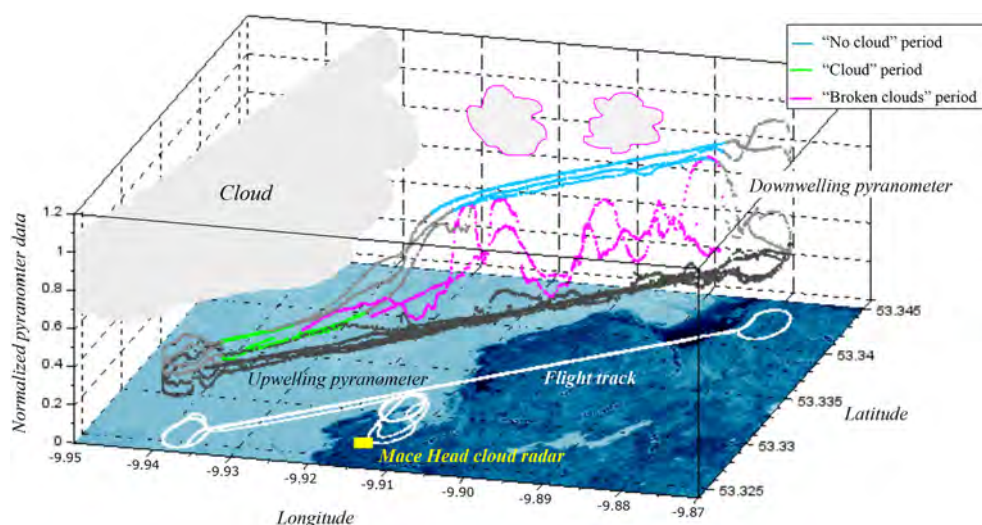


Figure 13. Coastal map and flight tracks for the case study of a convective cloud with changing meteorology (flight 38). Downwelling and upwelling pyranometers data are color-coded based on the three flight periods (“cloud”, “no cloud”, and “broken clouds”). The developing field of broken clouds (magenta contour clouds) appeared during the last two legs. The cloud radar (yellow square) operated at the Mace Head Research Station.

tribution retrieved from the cloud radar (Fig. 12). Previous measurements have also shown that precipitation negatively biases cloud radar observations of vertical wind velocities, as the radar indirectly measures vertical wind by using the motion of scatterers (i.e., hydrometeors; Lothon et al., 2005; Bühl et al., 2015). These negative biases in retrieved vertical winds are largely removed by obtaining vertical velocity distributions at the top of the cloud (Bühl et al., 2015). Similar results are obtained for our case study, as the cloud radar is strongly influenced by falling droplets, yet only slightly negatively biased at the cloud top. The intersection method, described in Sect. 4.3, is used to compare the normalized cloud radar vertical wind distributions to those of the RPA (Table 3). The intersection number is 0.53 between cloud radar and observations at the RPA flight altitude. This relatively low match is a result of the negative bias from the precipitating droplets. A much better agreement is found between the cloud radar vertical velocity distribution retrieved

at the cloud top (1360 m a.s.l.) and the RPA measurements (intersection number = 0.74).

5.2 Cloud fields with changing meteorology (flight 38: 21 August 2015)

In this case study, the results from the RPA and cloud radar emphasizes the differences in vertical wind distributions depending on the meteorological conditions related to cloud field. The wind-RPA flew within a cloud above the ocean and in clear sky above land for three legs, after which the local meteorology changed into a formation of developing clouds above land (where a cloudless sky had previously been observed; Fig. 13). The vertical wind velocity distributions are presented using a combination of information shown in a series of figures: downwelling and upwelling pyranometer observations and three periods corresponding to distinct meteorological conditions (Fig. 13); the time series of cloud radar data (Fig. 14); and the vertical wind distributions from the RPA and the cloud radar (Fig. 15). These meteorological

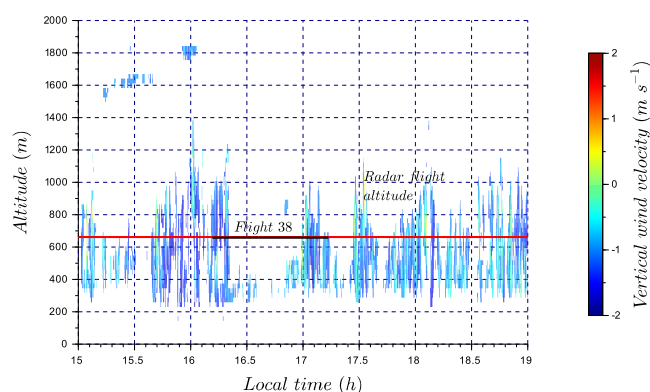


Figure 14. Time series of vertical wind velocity associated with flight 38. The color bar represents the cloud radar vertical wind velocity. Flight 38 sampling time is identified by the black segment. The red horizontal line corresponds to radar data at flight altitude (660 m a.s.l.), used to plot vertical wind velocity distributions in Fig. 15.

periods are defined in Fig. 13 as “cloud” (both pyranometers approach similar values), “no cloud” (downwelling pyranometer is significantly higher than upwelling pyranometer), and a third period associated with a developing field of broken clouds (spatially variable downwelling pyranometer). Based on the pyranometer measurements, we deduce a cloudless sky (cyan) was observed by the RPA above land for the first three legs (Fig. 13). The cloud radar also did not detect clouds above land for the beginning of the flight (Fig. 14). In the meantime, the RPA flew within a cloud above the ocean (Fig. 13, green), which was not observed by the cloud radar. Figure 15 shows that the standard deviation of vertical velocity within the cloud is larger than for clear sky conditions ($\sigma_{\text{cloud}} = 0.28 \text{ m s}^{-1}$, $\sigma_{\text{no cloud}} = 0.17 \text{ m s}^{-1}$), which highlights the presence of stronger vertical winds in the presence of clouds. During the last two legs of flight 38, the wind-RPA flew through a developing field of broken clouds above land (Fig. 13, magenta), which also appeared in the cloud radar time series and in the satellite image (Fig. 4 in Sanchez et al., 2017). The standard deviation during the “broken cloud” RPA period is larger than the other periods ($\sigma_{\text{broken cloud}} = 0.46 \text{ m s}^{-1}$), and the shape of vertical wind distributions is similar for both the cloud radar and the RPA (Fig. 15). While not shown here, the vertical wind distributions observed by the cloud radar are similar at cloud base (380 m a.s.l.) and at the flight altitude (660 m a.s.l.), as well as over different lengths of observing periods (1.5 and 4 h). In Table 3, intersection numbers illustrate the relatively close matches (ca. 80 %) in comparing the “broken cloud” RPA period and the cloud radar for 4 h (radar flight altitude) and for 1.5 h (radar flight time). The similar results for the observations of a field of broken clouds independently reinforces RPA and cloud radar observational methods, and the changes

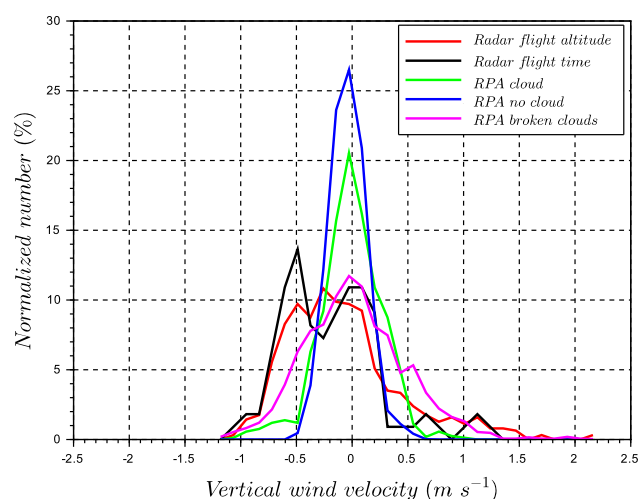


Figure 15. Comparison of vertical wind velocity distributions for RPA and cloud radar for flight 38. “Radar flight altitude” corresponds to 4 h of cloud radar measurements at RPA flight altitude. “Radar flight time” corresponds to the cloud radar measurements during the RPA flight period at the same altitude as the RPA. The time series are defined in Fig. 14. RPA measurements are divided into periods defined in Fig. 13 (“cloud”, “no cloud”, and “broken clouds” periods). The cloud radar detected cloud only for the “broken clouds” period during the RPA flight.

in meteorological conditions highlight the ability to identify distinct states of the atmosphere with the RPA.

5.3 Fair weather cumulus clouds (flight 30: 15 August 2015)

During flight 30, the cloud field was scattered with small clouds as shown in Fig. 17 by the cloud radar time series. However, the number of data points from the cloud radar during the flight time (black segment) was insufficient to establish a vertical wind distribution, therefore only the cloud radar data for 4 h (red segment) are presented in Fig. 18. The wind-RPA flew through one of these clouds as shown by the pyranometer measurements in Fig. 16. To compare cloud radar and RPA data, vertical winds from the RPA are again divided into “cloud” and “no-cloud” periods based on pyranometer observations. The respective standard deviations for the periods are $\sigma_{\text{cloud}} = 0.35 \text{ m s}^{-1}$ and $\sigma_{\text{no cloud}} = 0.34 \text{ m s}^{-1}$, which are not statistically different. However, the variability between legs is significantly greater in the “no cloud” period (as represented by the envelope in blue dashed lines in Fig. 18) compared to the “cloud” period (envelope in green dashed lines). In Fig. 18, the RPA and cloud radar measurements show similar results during the “cloud” period, with an intersection number equal to 0.76. Kunz and de Leeuw (2000) have observed an upward component in the air flow at the surface from the ocean at the Mace Head Research Station as a result of the terrain. However, systematic

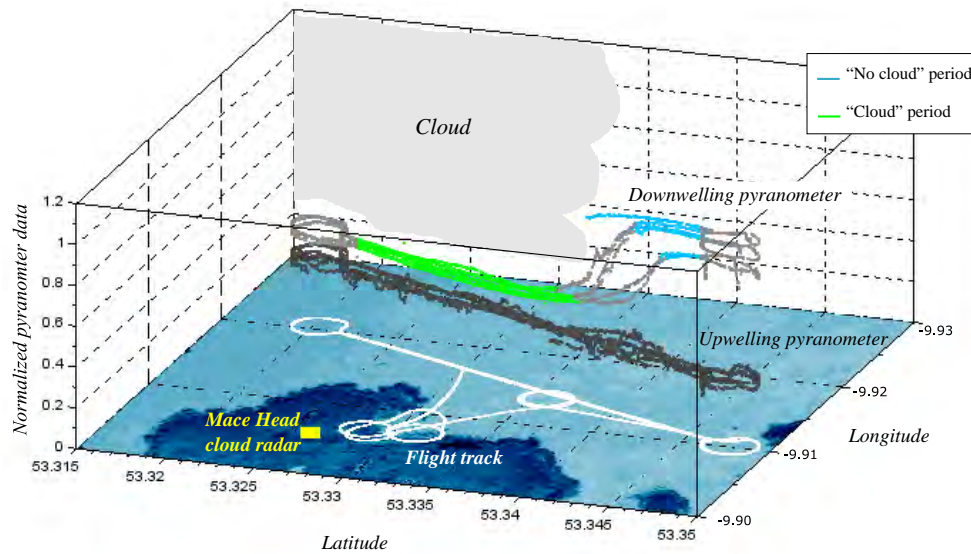


Figure 16. Coastal map and flight tracks for the non-convective cloud case study (flight 30). Downwelling and upwelling pyranometers data are color-coded based on two flight periods, “cloud” and “no cloud” periods. The cloud radar (yellow square) operated at the Mace Head Research Station.

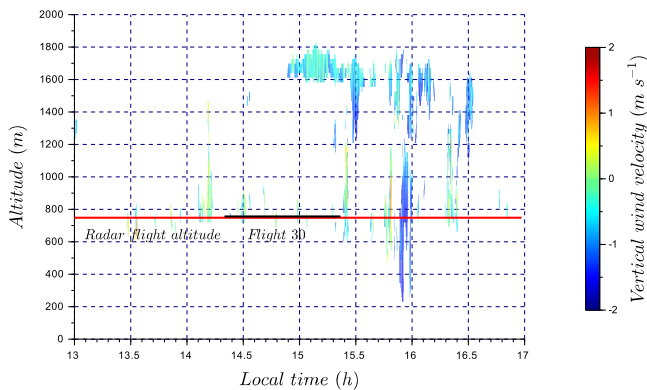


Figure 17. Time series of vertical wind velocity associated with flight 30. The color bar represents the cloud radar vertical wind velocity. Flight 30 sampling time is identified by the black segment. The red horizontal line corresponds to radar data at flight altitude (750 m a.s.l.) used in Fig. 18 to plot vertical wind velocity distribution.

differences between the RPA and cloud radar have not been observed for the other case studies, so we cannot quantify the role of surface heating or orography on the cloud radar vertical distributions compared to those of the RPA.

6 Sensitivity of vertical winds on aerosol–cloud interactions

To study ACIs, the input parameters for an aerosol–cloud parcel model (ACPM) are obtained from vertical profiles (temperature, relative humidity), straight-and-level legs (up-

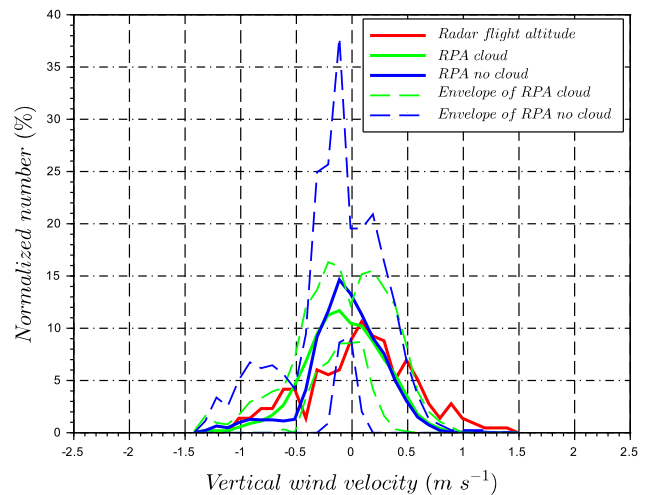


Figure 18. Comparison of normalized vertical wind velocity distributions for RPA during flight 30 and cloud radar at RPA flight altitude (750 m a.s.l.). “Radar flight altitude” period is defined in Fig. 17. RPA measurements are divided into “cloud” and “no cloud” periods. The envelope of each period is plotted based on the minimum and maximum number per bin vertical velocity distributions on a leg-by-leg basis.

draft), and measurements of cloud condensation nuclei spectra and aerosol size distributions. A weighted ensemble of updraft velocities, based on five-hole probe measurements, is used in the parcel model to simulate the cloud droplet distribution, (Sanchez et al., 2016, 2017). A sensitivity study assesses the impact of the vertical velocity distributions between the RPA and anemometer (Sect. 4) or cloud radar

(Sect. 5) on the resulting cloud droplet number concentrations for populations. The sensitivity is equal to $1/N * dN/dw$ with N the cloud droplet number concentration and dN/dw the slope of the cloud droplet number/updraft relationships found in Martin et al. (2017) and Ming et al. (2006). The resulting cloud droplet number concentration is more sensitive at low concentrations ($\sim 1/N$) and at low updraft velocities (when dN/dw is the largest). Based on polluted and clean cases described in Martin et al. (2017), cloud droplet numbers are ca. 100 and 350 cm^{-3} , respectively, with relative differences owing to RPA and anemometer/cloud radar updraft velocities within 10%. While the cloud droplet number concentration simulated with the RPA measurements is systematically higher than from sonic anemometer owing to the broader RPA vertical velocity distributions, a systematic difference in cloud droplet number concentrations is not observed between the RPA and cloud radar. These results suggest that the updraft measurements based on RPA measurements are sufficiently accurate for representing ACIs.

7 Conclusions

The validation of vertical wind measurements in clouds measured by a five-hole probe on a lightweight remotely piloted aircraft (RPA) has been detailed in this study. Atmospheric winds in the Earth's coordinate system are derived using the equations described in Lenschow and Spyers-Duran (1989) with the velocity of the RPA with respect to the Earth (measured by the inertial navigation system, INS), and the velocity of the air with respect to the RPA (measured by the five-hole probe). The attitude angles measured by the INS are used for coordinate system transformation from RPA to the Earth's coordinate system. The five-hole probe has been calibrated in wind tunnel on a two-axis platform to obtain the angle of attack, angle of sideslip, and air speed of the RPA. Motions induced by the dynamic platform in the wind tunnel were effectively removed, thereby validating probe-INS performance. Nonetheless, the rate of the angular rotation of the platform does impact the precision of derived atmospheric winds. The uncertainty associated with the vertical wind measurement w is determined to be 0.12 m s^{-1} using a Gaussian error propagation analysis (and uncertainty related to horizontal wind is 1.1 m s^{-1} based on reverse-heading maneuvers). Vertical velocity distributions from the RPA and sonic anemometers show intersection values higher than 70% in calm wind conditions. Comparisons have also been made between power spectral density (PSD) functions of the sonic anemometer and RPA measurements and demonstrate the impact of optimizing INS heading measurements on the PSD (particularly for the transversal component of wind). The observed isotropy by the sonic anemometer at 60 m a.g.l. is used to improve estimates of turbulent kinetic energy (TKE) obtained from RPA wind measurements. However, orthogonal flight plans must be implemented in order to

account for parallel- and cross-wind atmospheric conditions and measurement biases (particularly related to transversal wind components).

Three case studies from a BACCHUS field campaign (at the Mace Head Atmospheric Research Station, Galway, Ireland) validated RPA vertical wind velocities in clouds compared to cloud radar observations. Vertical wind velocity distributions were classified according to the flight periods (e.g., clear sky or cloud), emphasizing the impact of meteorology and the state of the atmosphere on the distribution of vertical wind velocities in the cloud field. For the first case study, a stratocumulus deck covering the sky and light precipitation was observed. Cloud radar vertical wind velocity distribution was negatively biased and cloud base was not distinctly visible due to falling droplets. The wind-RPA provided a centered vertical wind distribution near cloud base, which was similar to cloud radar observations at cloud top (in the non-precipitating region of the cloud). The second case study displayed different meteorological conditions during the flight, which were well distinguished by the wind-RPA, including differences between a developing field of broken clouds, a small convective cloud, and clear sky. In the third case study, similar vertical wind distributions in clouds were observed by the RPA and the cloud radar in fair weather cumulus cloud systems above land and ocean. The vertical velocity distributions, which were encountered for each of the case studies, highlighted the ability of the RPA platform to differentiate the meteorological conditions associated with the cloud systems based on vertical wind measurements.

To estimate the impact of discrepancies in vertical wind distributions on cloud droplet number concentrations, a sensitivity study was conducted to assess the relationship between cloud droplet number concentrations and updraft for different aerosol populations. The difference in vertical wind distributions between RPA and anemometer/cloud radar generally resulted in differences less than 10%. These results demonstrate that vertical velocity measurements on the RPA are sufficiently accurate to conduct aerosol-cloud closure studies using RPAs.

Data availability. All data are available by contacting the corresponding author or through the following link: https://hal-meteofrance.archives-ouvertes.fr/meteo-01769215/file/data_verticalwind_RPA.zip.

Competing interests. The authors declare that they have no conflict of interest.

Acknowledgements. The research leading to these results received funding from the European Union's Seventh Framework Programme (FP7/2007-2013) project BACCHUS under grant agreement no. 603445. NUI Galway was also supported by the

HEA under PRTL14, the EPA, and SFI through the MaREI Centre. Part of the remotely piloted aircraft system operations presented here have been conducted at Centre de Recherches Atmosphériques of Lannemezan (an instrumented site of the Pyrenean Platform of Observation of the Atmosphere, P2OA), supported by the University Paul Sabatier, Toulouse (France), and CNRS INSU (Institut National des Sciences de l'Univers). The RPAS used for the experiments presented in this work have been developed by the École Nationale de l'Aviation Civile (ENAC). We also thank Marie Lothon from CRA, Lannemezan, Bruno Pigué, William Maurel, and Guylaine Canut from Centre National de Recherches Météorologiques (CNRM) for their advices on wind measurements and Joachim Reuder and Line Båserud from the Geophysical Institute, University of Bergen, Norway, for their advices on TKE calculation.

Edited by: Ad Stoffelen

Reviewed by: two anonymous referees

References

- Axford, D. N.: On the Accuracy of Wind Measurements Using an Inertial Platform in an Aircraft, and an Example of a Measurement of the Vertical Mesostucture of the Atmosphere, *J. Appl. Meteorol.*, 7, 645–666, [https://doi.org/10.1175/1520-0450\(1968\)007<0645:OTAOWM>2.0.CO;2](https://doi.org/10.1175/1520-0450(1968)007<0645:OTAOWM>2.0.CO;2), 1968.
- BACCHUS: BACCHUS, Impact of Biogenic versus Anthropogenic emissions on Clouds and Climate: towards a Holistic Understanding, <http://www.bacchus-env.eu/> (last access: March 2018), 2016.
- Båserud, L., Reuder, J., Jonassen, M. O., Kral, S. T., Paskyabi, M. B., and Lothon, M.: Proof of concept for turbulence measurements with the RPAS SUMO during the BLLAST campaign, *Atmos. Meas. Tech.*, 9, 4901–4913, <https://doi.org/10.5194/amt-9-4901-2016>, 2016.
- Boiffier, J.: The dynamics of flight, the equations, John Wiley and Sons, ISBN: 0 471 94237 5, 1998.
- Brisset, P., Drouin, A., Gorraz, M., Huard, P.-S., and Tyler, J.: The Paparazzi Solution, <https://hal-enac.archives-ouvertes.fr/hal-01004157> (last access: March 2018), 2006.
- Brown, E. N., Friehe, C. A., and Lenschow, D. H.: The Use of Pressure Fluctuations on the Nose of an Aircraft for Measuring Air Motion, *J. Clim. Appl. Meteorol.*, 22, 171–180, [https://doi.org/10.1175/1520-0450\(1983\)022<0171:TUOPFO>2.0.CO;2](https://doi.org/10.1175/1520-0450(1983)022<0171:TUOPFO>2.0.CO;2), 1983.
- Bühl, J., Leinweber, R., Görsdorf, U., Radenz, M., Ansmann, A., and Lehmann, V.: Combined vertical-velocity observations with Doppler lidar, cloud radar and wind profiler, *Atmos. Meas. Tech.*, 8, 3527–3536, <https://doi.org/10.5194/amt-8-3527-2015>, 2015.
- Canut, G., Couvreur, F., Lothon, M., Legain, D., Pigué, B., Lampert, A., Maurel, W., and Moulin, E.: Turbulence fluxes and variances measured with a sonic anemometer mounted on a tethered balloon, *Atmos. Meas. Tech.*, 9, 4375–4386, <https://doi.org/10.5194/amt-9-4375-2016>, 2016.
- Conant, W. C., VanReken, T. M., Rissman, T. A., Varutbangkul, V., Jonsson, H. H., Nenes, A., Jimenez, J. L., Delia, A. E., Bahreini, R., Roberts, G. C., Flagan, R. C., and Seinfeld, J. H.: Aerosol–cloud drop concentration closure in warm cumulus, *J. Geophys. Res.-Atmos.*, 109, d13204, <https://doi.org/10.1029/2003JD004324>, 2004.
- Elston, J., Argrow, B., Stachura, M., Weibel, D., Lawrence, D., and Pope, D.: Overview of Small Fixed-Wing Unmanned Aircraft for Meteorological Sampling, *J. Atmos. Ocean. Tech.*, 32, 97–115, <https://doi.org/10.1175/JTECH-D-13-00236.1>, 2015.
- Garman, K. E., Hill, K. A., Wyss, P., Carlsen, M., Zimmerman, J. R., Stirm, B. H., Carney, T. Q., Santini, R., and Shepson, P. B.: An Airborne and Wind Tunnel Evaluation of a Wind Turbulence Measurement System for Aircraft-Based Flux Measurements, *J. Atmos. Ocean. Tech.*, 23, 1696–1708, <https://doi.org/10.1175/JTECH1940.1>, 2006.
- Görsdorf, U., Lehmann, V., Bauer-Pfundstein, M., Peters, G., Vavriv, D., Vinogradov, V., and Volkov, V.: A 35-GHz Polarimetric Doppler Radar for Long-Term Observations of Cloud Parameters – Description of System and Data Processing, *J. Atmos. Ocean. Tech.*, 32, 675–690, <https://doi.org/10.1175/JTECH-D-14-00066.1>, 2015.
- Khelif, D., Burns, S. P., and Friehe, C. A.: Improved Wind Measurements on Research Aircraft, *J. Atmos. Ocean. Tech.*, 16, 860–875, [https://doi.org/10.1175/1520-0426\(1999\)016<0860:IWMORA>2.0.CO;2](https://doi.org/10.1175/1520-0426(1999)016<0860:IWMORA>2.0.CO;2), 1999.
- Kunz, G. and de Leeuw, G.: Micrometeorological characterisation of the Mace Head field station during PARFORCE, in: *New Particle Formation and Fate in the Coastal Environment*, Rep. Ser. in Aerosol Sci., edited by: O'Dowd, C. D. and Hämeri, K., vol. 48, 2000.
- Lampert, A., Pätzold, F., Jiménez, M. A., Lobitz, L., Martin, S., Lohmann, G., Canut, G., Legain, D., Bange, J., Martínez-Villagrasa, D., and Cuxart, J.: A study of local turbulence and anisotropy during the afternoon and evening transition with an unmanned aerial system and mesoscale simulation, *Atmos. Chem. Phys.*, 16, 8009–8021, <https://doi.org/10.5194/acp-16-8009-2016>, 2016.
- Lenschow, D. and Spyers-Duran, P.: Measurement Techniques : Air motion sensing, National Center for Atmospheric Research, Bulletin No.23, <https://www.eol.ucar.edu/content/raf-bulletin-no-23> (last access: April 2018), 1989.
- Lenschow, D. H.: Model of the Height Variation of the Turbulence Kinetic Energy Budget in the Unstable Planetary Boundary Layer, *J. Atmos. Sci.*, 31, 465–474, [https://doi.org/10.1175/1520-0469\(1974\)031<0465:MOTHVO>2.0.CO;2](https://doi.org/10.1175/1520-0469(1974)031<0465:MOTHVO>2.0.CO;2), 1974.
- Lothon, M., Lenschow, D. H., Leon, D., and Vali, G.: Turbulence measurements in marine stratocumulus with airborne Doppler radar, *Q. J. Roy. Meteor. Soc.*, 131, 2063–2080, <https://doi.org/10.1256/qj.04.131>, 2005.
- Lothon, M., Lohou, F., Pino, D., Couvreur, F., Paradyak, E. R., Reuder, J., Vilà-Guerau de Arellano, J., Durand, P., Hartogensis, O., Legain, D., Augustin, P., Gioli, B., Lenschow, D. H., Faloona, I., Yagüe, C., Alexander, D. C., Angevine, W. M., Bargain, E., Barrié, J., Bazile, E., Bezombes, Y., Blay-Carreras, E., van de Boer, A., Boichard, J. L., Bourdon, A., Butet, A., Campistron, B., de Coster, O., Cuxart, J., Dabas, A., Darbieu, C., Deboudt, K., Delbarre, H., Derrien, S., Flament, P., Fourmentin, M., Garai, A., Gibert, F., Graf, A., Groebner, J., Guichard, F., Jiménez, M. A., Jonassen, M., van den Kroonenberg, A., Magliulo, V., Martin, S., Martinez, D., Mastrotrillo, L., Moene, A. F., Molinos, F., Moulin, E., Pietersen, H. P., Pigué, B., Pique, E., Román-Cascón, C.,

- Rufin-Soler, C., Saïd, F., Sastre-Marugán, M., Seity, Y., Steeneveld, G. J., Toscano, P., Traullé, O., Tzanos, D., Wacker, S., Wildmann, N., and Zaldei, A.: The BLLAST field experiment: Boundary-Layer Late Afternoon and Sunset Turbulence, *Atmos. Chem. Phys.*, 14, 10931–10960, <https://doi.org/10.5194/acp-14-10931-2014>, 2014.
- Lu, M.-L., Conant, W. C., Jonsson, H. H., Varutbangkul, V., Flagan, R. C., and Seinfeld, J. H.: The Marine Stratus/Stratocumulus Experiment (MASE): Aerosol-cloud relationships in marine stratocumulus, *J. Geophys. Res.-Atmos.*, 112, d10209, <https://doi.org/10.1029/2006JD007985>, 2007.
- Martin, A. C., Cornwell, G. C., Atwood, S. A., Moore, K. A., Rothfuss, N. E., Taylor, H., DeMott, P. J., Kreidenweis, S. M., Peters, M. D., and Prather, K. A.: Transport of pollution to a remote coastal site during gap flow from California's interior: impacts on aerosol composition, clouds, and radiative balance, *Atmos. Chem. Phys.*, 17, 1491–1509, <https://doi.org/10.5194/acp-17-1491-2017>, 2017.
- Ming, Y., Ramaswamy, V., Donner, L. J., and Phillips, V. T. J.: A New Parameterization of Cloud Droplet Activation Applicable to General Circulation Models, *J. Atmos. Sci.*, 63, 1348–1356, <https://doi.org/10.1175/JAS3686.1>, 2006.
- Peng, Y., Lohmann, U., and Leaitch, R.: Importance of vertical velocity variations in the cloud droplet nucleation process of marine stratus clouds, *J. Geophys. Res.-Atmos.*, 110, d21213, <https://doi.org/10.1029/2004JD004922>, 2005.
- Platis, A., Altstädter, B., Wehner, B., Wildmann, N., Lampert, A., Hermann, M., Birmili, W., and Bange, J.: An Observational Case Study on the Influence of Atmospheric Boundary-Layer Dynamics on New Particle Formation, *Bound.-Lay. Meteorol.*, 158, 67–92, <https://doi.org/10.1007/s10546-015-0084-y>, 2016.
- Reineman, B. D., Lenain, L., Statom, N. M., and Melville, W. K.: Development and Testing of Instrumentation for UAV-Based Flux Measurements within Terrestrial and Marine Atmospheric Boundary Layers, *J. Atmos. Ocean. Tech.*, 30, 1295–1319, <https://doi.org/10.1175/JTECH-D-12-00176.1>, 2013.
- Reineman, B. D., Lenain, L., and Melville, W. K.: The Use of Ship-Launched Fixed-Wing UAVs for Measuring the Marine Atmospheric Boundary Layer and Ocean Surface Processes, *J. Atmos. Ocean. Tech.*, 33, 2029–2052, <https://doi.org/10.1175/JTECH-D-15-0019.1>, 2016.
- Reuder, J., Ablinger, M., Ágústsson, H., Brisset, P., Brynjólfsson, S., Garhammer, M., Jóhannesson, T., Jonassen, M. O., Kühnel, R., Lämmlein, S., de Lange, T., Lindenberg, C., Malardel, S., Mayer, S., Müller, M., Ólafsson, H., Rögnvaldsson, Ó., Schäper, W., Spengler, T., Zängl, G., and Egger, J.: FLOHOF 2007: an overview of the mesoscale meteorological field campaign at Hofsjökull, Central Iceland, *Meteorol. Atmos. Phys.*, 116, 1–13, <https://doi.org/10.1007/s00703-010-0118-4>, 2012.
- Reuder, J., Bäserud, L., Jonassen, M. O., Kral, S. T., and Müller, M.: Exploring the potential of the RPA system SUMO for multi-purpose boundary-layer missions during the BLLAST campaign, *Atmos. Meas. Tech.*, 9, 2675–2688, <https://doi.org/10.5194/amt-9-2675-2016>, 2016.
- Sanchez, K. J., Russell, L. M., Modini, R. L., Frossard, A. A., Ahlm, L., Corrigan, C. E., Roberts, G. C., Hawkins, L. N., Schroder, J. C., Bertram, A. K., Zhao, R., Lee, A. K. Y., Lin, J. J., Nenes, A., Wang, Z., Wonaschütz, A., Sorooshian, A., Noone, K. J., Jonsson, H., Toom, D., Macdonald, A. M., Leaitch, W. R., and Seinfeld, J. H.: Meteorological and aerosol effects on marine cloud microphysical properties, *J. Geophys. Res.-Atmos.*, 121, 4142–4161, <https://doi.org/10.1002/2015JD024595>, 2016.
- Sanchez, K. J., Roberts, G. C., Calmer, R., Nicoll, K., Hashimshoni, E., Rosenfeld, D., Ovadnevaite, J., Preissler, J., Ceburnis, D., O'Dowd, C., and Russell, L. M.: Top-down and bottom-up aerosol–cloud closure: towards understanding sources of uncertainty in deriving cloud shortwave radiative flux, *Atmos. Chem. Phys.*, 17, 9797–9814, <https://doi.org/10.5194/acp-17-9797-2017>, 2017.
- Spiess, T., Bange, J., Buschmann, M., and Vörsmann, P.: First application of the meteorological Mini-UAV 'M2AV', *Meteorol. Z.*, 16, 159–169, <https://doi.org/10.1127/0941-2948/2007/0195>, 2007.
- Sullivan, S. C., Lee, D., Oreopoulos, L., and Nenes, A.: Role of updraft velocity in temporal variability of global cloud hydrometeor number, *P. Natl. Acad. Sci. USA*, 113, 5791–5796, <https://doi.org/10.1073/pnas.1514039113>, 2016.
- Thomas, R. M., Lehmann, K., Nguyen, H., Jackson, D. L., Wolfe, D., and Ramanathan, V.: Measurement of turbulent water vapor fluxes using a lightweight unmanned aerial vehicle system, *Atmos. Meas. Tech.*, 5, 243–257, <https://doi.org/10.5194/amt-5-243-2012>, 2012.
- Treaster, A. L. and Yocum, A. M.: The calibration and application of five-hole probes, NASA STI/Recon Technical Report N, 78, 1978.
- van den Kroonenberg, A., Martin, T., Buschmann, M., Bange, J., and Vörsmann, P.: Measuring the Wind Vector Using the Autonomous Mini Aerial Vehicle M2AV, *J. Atmos. Ocean. Tech.*, 25, 1969–1982, <https://doi.org/10.1175/2008JTECHA1114.1>, 2008.
- Wildmann, N., Ravi, S., and Bange, J.: Towards higher accuracy and better frequency response with standard multi-hole probes in turbulence measurement with remotely piloted aircraft (RPA), *Atmos. Meas. Tech.*, 7, 1027–1041, <https://doi.org/10.5194/amt-7-1027-2014>, 2014.
- Wyngaard, J. C. and Coté, O. R.: The Budgets of Turbulent Kinetic Energy and Temperature Variance in the Atmospheric Surface Layer, *J. Atmos. Sci.*, 28, 190–201, [https://doi.org/10.1175/1520-0469\(1971\)028<0190:TBOTKE>2.0.CO;2](https://doi.org/10.1175/1520-0469(1971)028<0190:TBOTKE>2.0.CO;2), 1971.

Appendix B

**Top-down and bottom-up
aerosol–cloud closure: towards
understanding sources of uncertainty
in deriving cloud shortwave radiative
flux, ACP journal**



Top-down and bottom-up aerosol–cloud closure: towards understanding sources of uncertainty in deriving cloud shortwave radiative flux

Kevin J. Sanchez^{1,2}, Gregory C. Roberts^{1,2}, Radiance Calmer², Keri Nicoll^{3,4}, Eyal Hashimshoni⁵, Daniel Rosenfeld⁵, Jurgita Ovadnevaite⁶, Jana Preissler⁶, Darius Ceburnis⁶, Colin O’Dowd⁶, and Lynn M. Russell¹

¹Scripps Institution of Oceanography, University of California, San Diego, CA, USA

²Centre National de Recherches Météorologiques, Météo-France & CNRS UMR3589, Toulouse, France

³Department of Meteorology, University of Reading, Reading, UK

⁴Department of Electronic and Electrical Engineering, University of Bath, Bath, UK

⁵Institute of Earth Sciences, The Hebrew University of Jerusalem, Jerusalem, Israel

⁶School of Physics and Centre for Climate and Air Pollution Studies, National University of Ireland Galway, Galway, Ireland

Correspondence to: Kevin J. Sanchez (kjsanche@ucsd.edu)

Received: 4 March 2017 – Discussion started: 21 March 2017

Revised: 13 July 2017 – Accepted: 15 July 2017 – Published: 22 August 2017

Abstract. Top-down and bottom-up aerosol–cloud shortwave radiative flux closures were conducted at the Mace Head Atmospheric Research Station in Galway, Ireland, in August 2015. This study is part of the BACCHUS (Impact of Biogenic versus Anthropogenic emissions on Clouds and Climate: towards a Holistic UnderStanding) European collaborative project, with the goal of understanding key processes affecting aerosol–cloud shortwave radiative flux closures to improve future climate predictions and develop sustainable policies for Europe. Instrument platforms include ground-based unmanned aerial vehicles (UAVs)¹ and satellite measurements of aerosols, clouds and meteorological variables. The ground-based and airborne measurements of aerosol size distributions and cloud condensation nuclei (CCN) concentration were used to initiate a 1-D microphysical aerosol–cloud parcel model (ACPM). UAVs were equipped for a specific science mission, with an optical particle counter for aerosol distribution profiles, a cloud sensor to measure cloud extinction or a five-hole probe for 3-D wind vectors. UAV cloud measurements are rare and have only become possible in recent years through the miniaturization of instrumentation. These are the first UAV measurements at Mace Head. ACPM simulations are compared to

in situ cloud extinction measurements from UAVs to quantify closure in terms of cloud shortwave radiative flux. Two out of seven cases exhibit sub-adiabatic vertical temperature profiles within the cloud, which suggests that entrainment processes affect cloud microphysical properties and lead to an overestimate of simulated cloud shortwave radiative flux. Including an entrainment parameterization and explicitly calculating the entrainment fraction in the ACPM simulations both improved cloud-top radiative closure. Entrainment reduced the difference between simulated and observation-derived cloud-top shortwave radiative flux (δRF) by between 25 and 60 W m^{-2} . After accounting for entrainment, satellite-derived cloud droplet number concentrations (CDNCs) were within 30% of simulated CDNC. In cases with a well-mixed boundary layer, δRF is no greater than 20 W m^{-2} after accounting for cloud-top entrainment and up to 50 W m^{-2} when entrainment is not taken into account. In cases with a decoupled boundary layer, cloud microphysical properties are inconsistent with ground-based aerosol measurements, as expected, and δRF is as high as 88 W m^{-2} , even high ($>30 \text{ W m}^{-2}$) after accounting for cloud-top entrainment. This work demonstrates the need to take in situ measurements of aerosol properties for cases where the boundary layer is decoupled as well as consider cloud-top

¹The regulatory term for UAV is remotely piloted aircraft (RPA).

entrainment to accurately model stratocumulus cloud radiative flux.

1 Introduction

One of the greatest challenges in studying cloud effects on climate are that the clouds are literally out of reach. Many ground-based measurement sites have a long historical record that are useful for identifying climatological trends; however, it is difficult to quantify such trends in cloud microphysical and radiative properties at these stations based solely on remote-sensing techniques such as radar and lidar. In situ aerosol measurements at the surface are often used to estimate cloud properties aloft, but the simulations used to estimate above surface conditions require many idealized assumptions such as a well-mixed boundary layer (BL) and adiabatic parcel lifting. Satellites have the advantage to infer cloud properties over a much larger area than ground-based observations; however, they can only see the uppermost cloud layer, and satellites need in situ observations to improve their retrievals. In this study, we combine ground-based and airborne measurements with satellite observations to determine cloud radiative properties and compare these results to an aerosol–cloud parcel model (ACPM) to identify sources of uncertainty in aerosol–cloud interactions.

The atmospheric research station at Mace Head has been a research platform for studying trace gases, aerosols and meteorological variables since 1958 (O'Connor et al., 2008). The station is uniquely exposed to a variety of air masses, such as clean marine air and polluted European air. Over the long history of observations and numerous field campaigns held at the Mace Head Atmospheric Research Station, few airborne field experiments have been conducted. During the PARFORCE campaign in September 1998, aerosol and trace gas measurements were made to map coastal aerosol formation (O'Dowd et al., 2001). During the second PARFORCE campaign in June 1999, measurements of sea spray plumes were made on an aircraft installed with a lidar (Kunz et al., 2002). In the NAMBLEX campaign in August 2002, flights were conducted to measure aerosol chemical and physical properties in the vicinity of Mace Head (Heard et al., 2006; Norton et al., 2006; Coe et al., 2006). None of the research flights thus far have studied aerosol–cloud interactions and cloud radiative properties at Mace Head.

For ground-based observations, it is often assumed that measured species are well mixed throughout the boundary layer. Often this assumption is valid, and many observational studies have shown that models which use ground-based measurements can accurately simulate cloud droplet number concentrations (CDNCs; Russell and Seinfeld, 1998; Conant et al., 2004; Fountoukis et al., 2007), making bottom-up closure a viable method for predicting cloud properties. Closure is defined here as the agreement between observa-

tions and model simulations of CDNC and cloud-top short-wave radiative flux (δRF). This well-mixed boundary layer simplification, however, has been shown to be inaccurate in many field experiments (e.g., the Atlantic Stratocumulus Transition Experiment (ASTEX; Albrecht et al., 1995) and the Aerosol Characterization Experiments, ACE1 (Bates et al., 1998) and ACE2 (Raes et al., 2000)). Previous studies at Mace Head have shown that decoupled boundary layers can be observed with scanning backscatter lidar measurements (Kunz et al., 2002; Milroy et al., 2012). Such decoupled layers often contain two distinct cloud layers, distinguished as a lower layer within the well-mixed surface mixed layer and a higher decoupled layer between the free troposphere and surface mixed layer (Kunz et al., 2002; Milroy et al., 2012; Stull, 1988). General characteristics associated with decoupled boundary layers are a weak inversion and a decrease in aerosol concentration relative to the surface mixed layer, and they are most commonly occur in relatively deep marine boundary layers (> 1400 m; Jones et al., 2011). Dall'Osto et al. (2010) showed the average height of the surface mixed layer, over Mace Head, varies from 500 to 2000 m, and the decoupled layers have heights ranging from 1500 to 2500 m. Marine boundary layer decoupling is often seen in the tropics and has been attributed to processes that involve cloud heating from cloud-top entrainment, leading to decoupling of the boundary layer (Bretherton and Wyant, 1997; Bates et al., 1998; Albrecht et al., 1995; Zhou et al., 2015; Stevens, 2002). In addition, Bretherton and Wyant (1997) have shown that the decoupling structure is mainly driven by a high latent heat flux that results in a large buoyancy jump across the cloud base. This high latent heat flux is attributed to easterlies bringing air over increasing sea surface temperature, where the boundary layer becomes deeper and more likely to decouple (Albrecht et al., 1995). The cloud layer drives the turbulent motion, and a zone of negative buoyancy flux develops below cloud. The turbulent motion is driven by radiative cooling at cloud top, causing air to sink (Lilly, 1968). The zone of negative buoyancy exists because the deepening of the boundary layer causes the lifting condensation level of the updraft and downdraft to separate. This is important because latent heating in the cloud contributes significantly to the buoyancy in the cloud (Schubert et al., 1979). If this zone of negative buoyancy flux becomes deep enough, it is dynamically favorable for the cloud layer to become decoupled from the cloud layer (Bretherton and Wyant, 1997). Bretherton and Wyant (1997) also show that drizzle can have a substantial impact on enhancing the negative buoyancy flux below cloud, but drizzle is not necessary for the decoupling mechanism they proposed. Other factors, such as the vertical distribution of radiative cooling in the cloud and sensible heat fluxes, play less important roles. Turton and Nicholls (1987) used a two-layer model to show that decoupling can also result from solar heating of the cloud layer, albeit only during the day. Furthermore, Nicholls and Leighton (1986) showed observations of decoupled clouds with cloud-top radiative

cooling, and the resulting in-cloud eddies do not mix down to the surface (further suggesting radiative cooling plays a less important role). Russell et al. (1998) and Sollazzo et al. (2000) showed that in a decoupled atmosphere the two distinct layers have similar characteristics (e.g., aerosol and trace gases composition), with different aerosol concentrations that gradually mix with each other, mixing air from the surface mixed layer into the decoupled layer and vice versa. These previous studies also show that aerosol concentrations in the decoupled layer are lower than those in the surface mixed layer, implying an overestimation in cloud shortwave radiative flux when using ground-based aerosol measurements.

Satellite measurements of microphysical properties, such as CDNC, have the potential to be independent of ground-based measurements and therefore be reliable for studying decoupled clouds. Satellite estimates of CDNC have only become possible recently due to the increased resolution in measurements (Rosenfeld et al., 2012, 2014, 2016; Painemal and Zuidema, 2011). Therefore, current measurements still require ground-based validation until the method is further developed.

The focus of this manuscript is on the top-down closure between satellite retrievals and airborne measurements of cloud microphysical properties, as well as traditional bottom-up closure coupling below and in-cloud measurements of cloud condensation nuclei (CCN), updraft and cloud microphysical properties. In situ measurements of CDNC are not available, so bottom-up closure is expressed in terms of cloud-top shortwave radiative flux rather than CDNC, and top-down closure of satellite CDNC is compared to ACPM-simulated CDNC. The Methods section describes how observations were collected, as well as the methods for estimating CDNC with satellite measurements and calculating shortwave radiative flux with the ACPM. The Results/discussion section summarizes the bottom-up and top-down closure for coupled and decoupled clouds and quantifies the differences in cloud shortwave radiative flux for cases that were affected by cloud-top entrainment.

2 Methods

The August 2015 campaign at the Mace Head Atmospheric Research Station (Galway, Ireland; 53.33° N, 9.90° W) focused on aerosol–cloud interactions at the eastern North Atlantic Ocean by coupling ground-based in situ and remote-sensing observations with airborne and satellite observations. This section summarizes the measurements used for this study and the model used to simulate the observations.

2.1 Ground-based measurements

At the Mace Head research site, aerosol instruments are located in the laboratory at about 100 m from the coastline.

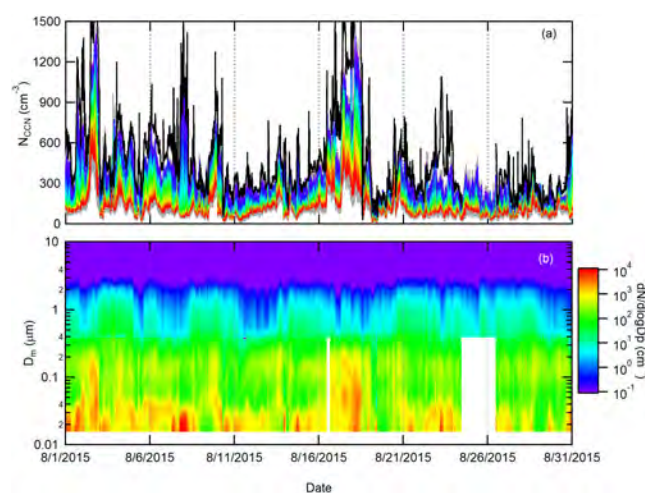


Figure 1. Time series for the month of August 2015 at Mace Head, Ireland, of ground-based CCN concentrations (a) and merged SMPS and APS number size distributions (b).

They are connected to the laminar flow community air sampling system, which is constructed from a 100 mm diameter stainless-steel pipe with the main inlet at 10 m above ground level, so that samples are not impacted by immediate coastal aerosol production mechanisms, such as wave breaking and biological activity (Norton et al., 2006; O’Dowd et al., 2004, 2014; Coe et al., 2006; Rinaldi et al., 2009). The performance of this inlet is described in Kleefeld et al. (2002). Back trajectories during the period of the experiment show that the origin of air masses is predominantly from the North Atlantic; therefore, the air masses sampled at Mace Head generally represent clean open-ocean marine aerosol. Mace Head contains a variety of aerosol sampling instrumentation, spanning particle diameter range of 0.02–20 μm . Size spectral measurements are performed at a relative humidity (RH) < 40 % using Nafion driers. Supermicron particle size distributions were measured using an Aerodynamic Particle Sizer (APS, TSI model 3321, $0.5 < D_p < 20 \mu\text{m}$). The remaining submicron aerosol size range was retrieved from a scanning mobility particle sizer (SMPS, $0.02 < D_p < 0.5 \mu\text{m}$), comprised of a differential mobility analyzer (DMA, TSI model 3071), a condensation particle counter (TSI model 3010, $D_p > 10 \text{ nm}$) and a Kr-85 aerosol neutralizer (TSI 3077). CCN measurements were performed with a miniature continuous-flow stream-wise thermal gradient chamber, which measures the concentration of activated CCN over a range of supersaturations (Roberts and Nenes, 2005). During this study, the supersaturation range spanned 0.2 to 0.82 %. Aerosol hygroscopicity was calculated using κ -Köhler theory (Petters and Kreidenweis, 2007) with the sampled CCN concentrations at a particular supersaturation and corresponding integrated aerosol number concentration at a critical diameter (Roberts et al., 2001). Figure 1 shows time series of CCN spectra and aerosol number size distributions throughout the campaign.

The ground-based remote-sensing measurements utilized in this study are the 35.5 GHz Ka-band Doppler cloud radar MIRA36 (Melchionna et al., 2008; Goersdorf et al., 2015) to obtain vertical velocity distributions at cloud base and the Jenoptik CHM15K ceilometer (Heese et al., 2010; Martucci et al., 2010) to obtain cloud-base height.

2.2 UAV vertical profiles

The UAV operations were conducted directly on the coast about 200 m from the Mace Head Atmospheric Research Station. UAVs were used to collect vertical profiles of standard meteorological variables, temperature (IST, Model P1K0.161.6W.Y.010), pressure (Bs rep GmbH, Model 15PSI-A-HGRADE-SMINI) and relative humidity (IST, P14 Rapid-W), as well as aerosol size distributions with an optical particle counter (OPC, Met One Model 212-2), cloud droplet extinction (Harrison and Nicoll, 2014) updraft velocity at cloud base with a five-hole probe. A list of the various UAV flights and their instrumentation is given in Table 1. Measurement errors for the relative humidity and temperature sensors are $\pm 5\%$ and $\pm 0.5\text{ }^\circ\text{C}$, respectively. As RH sensors are not accurate at high RH ($> 90\%$), the measured values have been scaled such that RH measurements are 100 % in a cloud. At altitudes where the UAV is known to be in cloud (based on in situ cloud extinction measurements) the air mass is considered saturated ($\text{RH} \sim 100\%$). The temperature and relative humidity sensors are protected from solar radiative heating by a thin-walled aluminum shroud positioned outside of the surface layer of the UAV. A helical cone, mounted in front of the sensors, ejects droplets to protect the sensors. The temperature measurements for both cases in which cloud-top entrainment is explored (see Sect. 3.2) are verified to remain in stratocumulus clouds throughout the ascents and descents, and they are not affected by evaporative cooling. The temperature and relative humidity measurements were used to initialize the ACPM below cloud. The UAVs were flown individually in separate missions up to 1.5 h, and each UAV was instrumented to perform a specific science mission (referred to here as aerosol, cloud and 3-D winds).

The OPC measured aerosol number size distributions in eight size bins between 0.3 and $10\text{ }\mu\text{m}$ diameter. Aerosols were sampled via a quasi-isokinetic shrouded inlet mounted on the nose of the UAV. Aerosols samples were heated upon entering the UAV ($\Delta T > 5\text{ K}$ due to internal heating by the electronics), reducing the relative humidity of the sampled air to less than 60 %, and decreased with height ($< 50\%$ above 150 m) before aerosol size was measured. Figure 2 shows a two-instrument redundancy cross-check between ground-based APS and UAV OPC measurements (collected between 40 and 80 m a.g.l.) of aerosol sizes, which are in agreement ($r^2 = 0.48$).

In-cloud extinction was measured in situ using a miniature optical cloud droplet sensor developed at the University of Reading (Harrison and Nicoll, 2014). The sensor operates

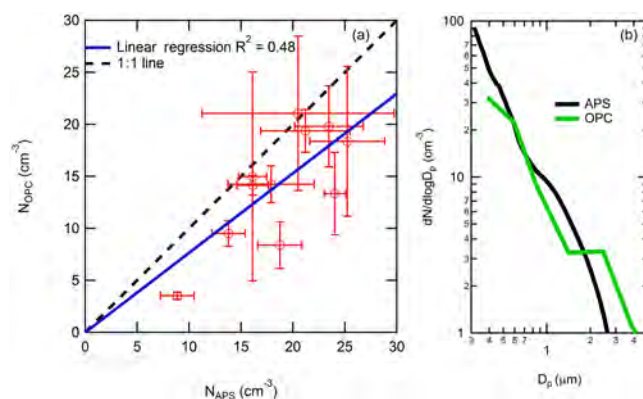


Figure 2. OPC concentrations with particle diameters (D_p) greater than $0.3\text{ }\mu\text{m}$ (a) from 11 UAV research flights, listed in Table 1, plotted against APS concentrations ($D_p > 0.3\text{ }\mu\text{m}$) at Mace Head Atmospheric Research Station (red circles). Error bars represent ± 1 standard deviation. The points are fit with a linear regression (blue line). OPC data were averaged between 40 and 80 m a.s.l. OPC and APS number size distributions averaged for the 11 flights (b).

by a backscatter principle using modulated LED light which is backscattered into a central photodiode. Comparison of the sensor with a Cloud Droplet Probe (Droplet Measurement Technologies) demonstrates good agreement for cloud droplet diameters $> 5\text{ }\mu\text{m}$ (Nicoll et al., 2016). The extinction measurements were used to calculate cloud-top shortwave radiative flux and are further discussed in Sect. 2.4.

Finally, a five-hole probe for measuring three-dimensional wind vectors was mounted on a third UAV. The 3-D wind vectors are determined by subtracting the UAV motion given by an inertial measurement unit (IMU) from the total measured flow obtained by differential pressures in the five-hole probe (Wildmann et al., 2014; Lenschow and Spyers-Duran, 1989; Calmer et al., 2017). UAV five-hole probe measurements were collected along 6 km long straight and level legs at cloud base. Normalized cloud radar vertical velocity distributions are compared to vertical wind distributions obtained from the UAV in Fig. 3. The positive updraft velocities in Fig. 3 are used to initialize the ACPM to produce simulated cloud droplet size distributions throughout the depth of the cloud. The droplet distributions for each updraft velocity are averaged and weighted by the probability distribution of the measured positive velocities. Differences in results when using the cloud radar updrafts versus the UAV five-hole probe updrafts (Fig. 3) are discussed in Sect. 3.1.2.

2.3 Satellite measurements

Research flights with the UAV were conducted in conjunction with satellite overpasses to compare retrieved CDNC and maximum supersaturation (S_{max}) with ACPM-simulated values using the NASA Suomi National Polar-orbiting Partnership (NPP) satellite. The satellite estimations of CDNC

Table 1. UAV research flights conducted at Mace Head, Ireland, and measured parameters in 2015. Flight start and end times are in UTC. NASA’s Suomi National Polar-orbiting Partnership satellite overpasses occurred at approximately 13:00 UTC. Measurements include relative humidity (RH), temperature (T), pressure (P), three-dimensional wind vectors (3-D winds), optical particle counter (OPC) and cloud sensor measurements of cloud droplet extinction.

Date	Flight	Start time	End time	RH	T	P	3-D winds	OPC	Cloud
30-Jul	4	12:41	13:19	x	x	x		x	
30-Jul	5	14:00	14:44	x	x	x			x
30-Jul	6	16:04	16:42	x	x	x		x	
01-Aug	7	11:30	12:13	x	x	x		x	
01-Aug	8	12:35	13:16	x	x	x			x
01-Aug	9	14:00	15:20	x	x	x	x		
01-Aug	10	15:54	16:43	x	x	x		x	
05-Aug	11	11:47	12:29	x	x	x			x
05-Aug	13	13:36	14:26	x	x	x	x		
05-Aug	14	14:42	15:29	x	x	x			x
06-Aug	16	11:55	12:37	x	x	x			x
06-Aug	17	13:51	15:16	x	x	x	x		
10-Aug	19	13:41	14:10	x	x	x			x
10-Aug	20	14:42	15:45	x	x	x	x		
10-Aug	21	16:00	16:45	x	x	x			x
11-Aug	23	12:00	12:47	x	x	x			x
11-Aug	24	13:11	14:05		x	x	x		
11-Aug	25	14:25	15:10	x	x	x			x
11-Aug	26	15:29	16:22		x	x	x		
11-Aug	27	16:58	17:33		x	x		x	
15-Aug	29	12:19	13:03	x	x	x		x	
15-Aug	30	13:46	14:31		x	x	x		
15-Aug	31	15:08	16:14	x	x	x			x
16-Aug	32	12:30	13:20	x	x	x		x	
16-Aug	33	13:40	14:00	x	x	x		x	
17-Aug	34	11:30	12:24	x	x	x			x
17-Aug	35	13:45	14:34	x	x	x		x	
21-Aug	36	12:21	13:12		x	x		x	
21-Aug	37	13:40	14:25	x	x	x			x
21-Aug	38	15:17	16:26	x	x	x	x		
21-Aug	39	16:53	17:27	x	x	x			x
22-Aug	40	9:29	10:12	x	x	x			x
22-Aug	41	10:47	11:37	x	x	x		x	
22-Aug	42	12:52	13:53	x	x	x	x		
22-Aug	43	14:22	14:59	x	x	x		x	
27-Aug	45	10:21	11:10	x	x	x		x	
27-Aug	46	11:27	12:13	x	x	x			x
27-Aug	47	13:11	13:45			x			x
27-Aug	48	15:09	15:23	x	x	x	x		
27-Aug	49	17:20	17:50	x	x	x		x	
28-Aug	50	14:25	14:49	x	x	x		x	

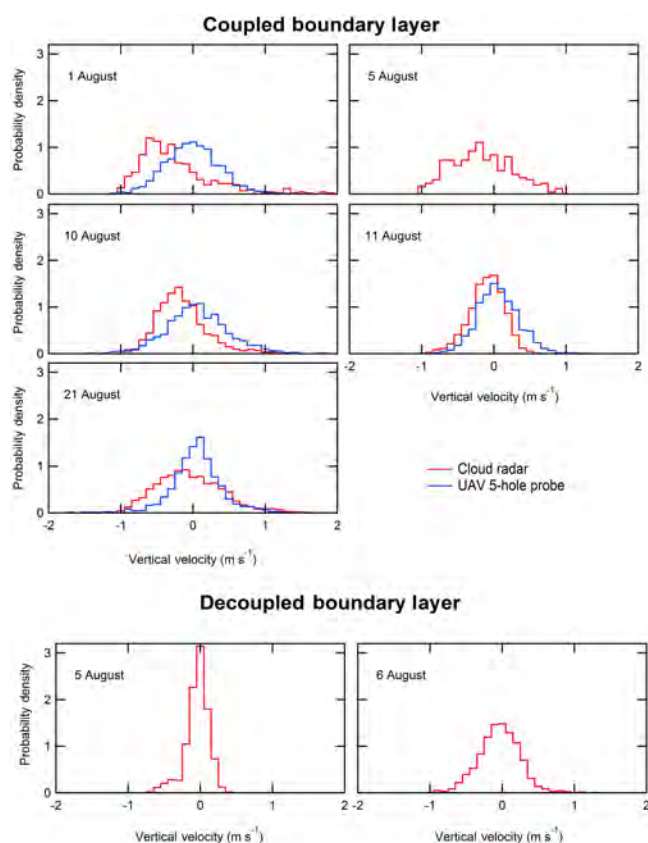


Figure 3. Normalized observed vertical velocity distributions measured by the cloud radar and UAV for each case presented in Table 2.

and S_{\max} are based on methods described by Rosenfeld et al. (2012, 2014, 2016), which are briefly summarized in the following paragraph. The case selection criteria for satellite observations required the overpass to occur at a zenith angle between 0 and 45° to the east of the ground track, to have convective development that spans at least 6 K of cloud temperature from base to top (~ 1 km thick) and to not precipitate significantly. In situ observations were often of thin clouds (< 1 km thick), and the satellite observations consist primarily of the more developed clouds in the same system.

To obtain CDNC, cloud droplet effective radius profiles were extracted from the Suomi NPP satellite. Figure 4 shows an image from the Suomi Visible Infrared Imaging Radiometer Suite on 21 August overlapped on a map of western Ireland. The vertical profile in Fig. 4 shows satellite-retrieved and ACPM-simulated effective radius. To estimate the CDNC, the satellite effective radius (Fig. 4) is first converted to mean volume radius (r_v) using a linear relationship (Freud et al., 2011). Next, it is assumed that any mixing that occurred between the cloud and cloud-free air was inhomogeneous; this implies that the actual r_v is equal to the adiabatic r_v . CDNC can be calculated by dividing the adiabatic water content in the cloud by r_v (Rosenfeld et al., 2012; Beals et al., 2015). The cloud-base height and pressure were used to

calculate the adiabatic water content. Cloud-base height and pressure were obtained from the height of the NCEP reanalysis of the cloud-base temperature, as retrieved from satellite. The cloud-base height was validated against the ceilometer. Freud et al. (2011) showed that the inhomogeneous assumption resulted in an average overestimate in CDNC of 30 %, so the CDNC is reduced by 30 % to account for the bias with the assumption. Finally, to calculate S_{\max} , the cloud-base updraft velocity, from the UAV or cloud radar, is needed, and when paired with the CDNC it can be used to empirically calculate S_{\max} (Rosenfeld et al., 2012; Pinsky et al., 2012). The methodology was validated by Rosenfeld et al. (2016).

2.4 Aerosol–cloud parcel model simulations

A detailed description of the ACPM is presented in Russell and Seinfeld (1998) and Russell et al. (1999). The ACPM is based on a fixed-sectional approach to represent the (dry) particle size domain, with internally mixed chemical components. Aerosols are generally internally mixed at Mace Head because there are no immediate strong sources of pollution. The model employs a dual-moment (number and mass) algorithm to calculate particle growth from one size section to the next for non-evaporating compounds (namely, all components other than water) using an accommodation coefficient of 1.0 (Raatikainen et al., 2013). The dual-moment method is based on Tzivion et al. (1987) to allow accurate accounting of both aerosol number and mass, and it incorporates independent calculations of the change in particle number and mass for all processes other than growth. The model includes a dynamic scheme for activation of particles to cloud droplets. Liquid water is treated in a moving-section representation, similar to the approach of Jacobson et al. (1994), to account for evaporation and condensation of water in conditions of varying humidity. In subsaturated conditions, aerosol particles below the cloud base are considered to be in local equilibrium with water vapor pressure (i.e., relative humidity < 100 %).

Coagulation, scavenging and deposition of the aerosol were included in the model, but their effects are negligible given the relatively short simulations used here (< 2 h) and low marine total aerosol particle concentrations (< 500 cm^{−3}; $D_p > 10$ nm). Feingold et al. (2013) showed that autoconversion and accretion rates are negligible for the simulated values of liquid water content (LWC) and CDNC except for the C21Cu case, which had $LWC > 1$ g m^{−3}. Thus, droplet number loss by collision coalescence can be neglected for all cases except for the C21Cu case. Aerosol hygroscopicity as a function of size (and supersaturation) is determined from CCN spectra and aerosol size distributions as mentioned in Sect. 3.1, and it is used as model input. The ACPM is also constrained by measured temperature profiles, cloud-base height and updraft velocity distribution (Fig. 3). The in-cloud lapse rate is assumed to be adiabatic unless specified otherwise, so simulation results represent an upper bound on

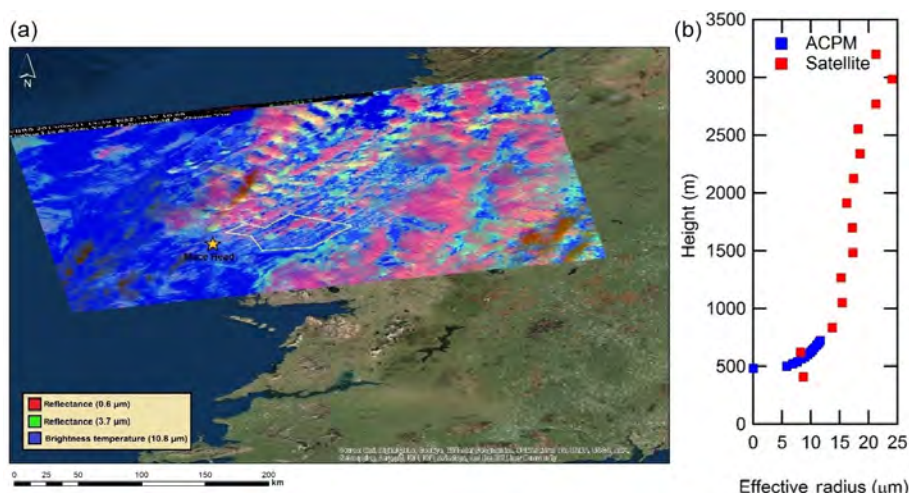


Figure 4. Suomi NPP satellite RGB composite image for 21 August 2015 (a). Mace Head Atmospheric Research Station and UAV flight location are indicated by the yellow star. The white polygon represents the zone for retrieving cloud properties – which is represented by the profile of cloud effective radius (b). Effective radius profiles are presented for both the Suomi NPP satellite (red) and the ACPM (blue).

CDNC and LWC that is unaffected by entrainment. To account for release of latent heat in the cloud, the vertical temperature gradient is calculated as $dT = -(gwdt + Ldq_1)/c_p$, where dT is change in temperature for the vertical displacement of an air parcel, g is acceleration due to gravity, w is updraft velocity at cloud base, dt is time step, L is latent heat of water condensation, q_1 is liquid water mixing ratio and c_p is specific heat of water (Bahadur et al., 2012). A weighted ensemble of positive updraft velocities measured with the cloud radar and UAV five-hole probe were applied to the ACPM (Sanchez et al., 2016).

The simulated cloud droplet size distribution is used to calculate the shortwave cloud extinction. Cloud extinction is proportional to the total droplet surface area (Hansen and Travis, 1974; Stephens, 1978) and is calculated from

$$\sigma_{\text{ext}} = \int_0^{\infty} Q_{\text{ext}}(r) \pi r^2 n(r) dr, \quad (1)$$

where r is the radius of the cloud droplet; $n(r)$ is the number of cloud droplets with a radius of r ; and $Q_{\text{ext}}(r)$ is the Mie efficiency factor, which asymptotically approaches 2 for water droplets at large sizes ($r > 2 \mu\text{m}$).

Finally, the shortwave radiative flux (RF) is calculated as $\text{RF} = \alpha Q$, where Q is the daily-average insolation at Mace Head and α is the cloud albedo. α is estimated using the following equation (Geresdi et al., 2006; Bohren and Battan, 1980):

$$\alpha = \frac{(\sqrt{3}(1-g)\tau)}{(2 + \sqrt{3}(1-g)\tau)}, \quad (2)$$

where τ is the cloud optical depth defined as

$$\tau = \int_0^H \sigma_{\text{ext}}(h) dh; \quad (3)$$

H is the cloud height or thickness; and g , the asymmetric scattering parameter, is approximated as 0.85 based on Mie scattering calculations for supermicron cloud drops. RF is calculated for both simulated cloud extinction and measured UAV extinction.

3 Results/discussion

3.1 Closure of CDNC and cloud-top shortwave radiative flux

For this study, closure is defined as the agreement between observations and model simulations of CDNC and cloud-top shortwave radiative flux. In situ measurements of clouds were made by UAVs on 13 days during the campaign. Of these, a subset of six are chosen here for further analysis, which includes comparison with satellite CDNC as well as simulation of cloud properties with the ACPM (Table 2). The remaining days with UAV measurements did not contain sufficient cloud measurements for analysis. A satellite overpass occurred on each of the 6 days; however only 4 of the days contained clouds that were thick enough to analyze with the satellite. The 10 August case experienced a light drizzle, so ACPM simulations were not conducted for this case; however analysis with satellite imagery was still conducted. On 5 August, two cloud layers were examined, for a total of seven case studies shown in Table 2. Aerosols were occasionally influenced by anthropogenic sources; however, the

Table 2. UAV observations of cloud heights and temperatures and cloud property estimates based on ground measurements. Ground-based Hoppel minimum diameter (D_{\min}) is used to estimate CDNC. ACPM simulation and satellite results are also presented, as well as differences between simulated and observation-derived cloud-top extinction and cloud-top radiative flux. Case abbreviations include if they are coupled (C) or decoupled (D); the day of the month; and cloud type: cumulus (Cu) or stratocumulus (Sc).

	Coupled BL					Decoupled BL	
	01 Aug Cumulus (C01Cu) ^a	05 Aug Cumulus (C05Cu)	10 Aug ^b Cumulus (C10Cu)	11 Aug ^c StratoCu (C11Sc)	21 Aug ^d Cumulus (C21Cu)	05 Aug ^c StratoCu (D05Sc)	06 Aug Cumulus (D06Cu)
	In situ ground-based and UAV measurements						
Cloud-base height (m)	800	430	650	1200	460	1490	2180
Cloud-base temperature (°C)	7.4 ± 0.1	10.6 ± 0.2	8.1 ± 0.1	3.7 ± 0.1	10.4 ± 0.1	6.5 ± 0.2	−2.1 ± 0.2
Cloud-top height (m)	1040	710	1720	1460	960	1630	2400
Cloud-top temperature (°C)	5.7 ± 0.1	8.7 ± 0.2	1.8 ± 0.1	2.4 ± 0.2	7.6 ± 0.1	5.8 ± 0.2	−3.1 ± 0.4
Measured lapse rate in cloud (K km ^{−1})	5.7	6.1	5.1	4.7	6.0	4.1	6.3
Number of cloud layers	1	2 ^g	1	1	1	2 ^h	2 ^h
Hoppel D_{\min} (nm)	74 ± 6	78 ± 16	73 ± 8	83 ± 7	83 ± 5	78 ± 16	80 ± 9
Hoppel D_{\min} CDNC (>Hoppel D_{\min} , cm ^{−3})	129 ± 5	69 ± 8	105 ± 11	87 ± 5	94 ± 12	69 ± 8	164 ± 13
Measured cloud τ	–	11.7	–	8.3	29.1	1.3	4.9
Hoppel minimum critical supersaturation (S_{crit})	0.43 ± 0.03	0.61 ± 0.10	0.37 ± 0.11	0.37 ± 0.05	0.41 ± 0.10	0.61 ± 0.10	0.31 ± 0.06
	ACPM simulation and satellite-derived cloud properties ^e						
Simulated moist adiabatic lapse rate (K km ^{−1})	5.0	4.5	4.9	5.7	4.5	5.1	6.4
Simulated cloud-top droplet r_e (μm)	10.3 ± 0.1	14.4 ± 0.3	–	11.3 ± 0.2	14.2 ± 0.4	10.0 ± 0.1	8.2 ± 0.2
Simulated cloud τ	–	13.2 ± 1.9	–	18.7 ± 2.7	42.1 ± 11.2	4.4 ± 0.5	9.0 ± 1.1
Cloud-top extinction difference ($\delta\sigma_{\text{ext}}$, km ^{−1})	–	11 ± 25	–	36 ± 12	52 ± 42	37 ± 6	34 ± 7
Cloud-top shortwave radiative flux difference (δRF , W m ^{−2}) ^f	–	11 ± 26	–	48 ± 11	20 ± 6	88 ± 8	74 ± 12
Simulated CDNC (cm ^{−3})	135 ± 16	60 ± 12	105 ± 18	88 ± 12	105 ± 31	86 ± 10	171 ± 17
Satellite-estimated CDNC (cm ^{−3})	109	–	85	58 (83) ⁱ	104	–	–
Simulated S_{max} (%)	0.45 ± 0.09	0.45 ± 0.18	0.36 ± 0.15	0.36 ± 0.09	0.40 ± 0.20	0.76 ± 0.04	0.33 ± 0.06
Satellite-estimated S_{max} (%)	0.34	–	0.27	0.48	0.34	–	–

^a C/D – coupled/decoupled; xx – date in August 2015; Sc/Cu – stratocumulus/cumulus cloud. ^b Precipitation occurred on 10 August. ^c Accounting for entrainment improves model/measurement closure (Table 2). ^d The C21Cu case is susceptible to droplet coalescence due to its high liquid water content (Feingold et al., 2013). ^e The error includes the potential error of ± 20 % in updraft velocity and the standard error of the CCN concentration measurements. ^f The difference between the observed (calculated from UAV extinction measurements) and simulated radiative flux. The error includes the potential error of ± 20 % in updraft velocity and the standard error of the CCN concentration measurements. ^g The measurements and results in this column represent the lower of the two clouds. ^h Altitude of top cloud level that is used to calculate cloud radiative flux. ⁱ Excluding the correction for the inhomogeneous entrainment assumption in parentheses.

cases shown consist of aerosol of marine origin with concentrations under 1000 cm^{−3} (Fig. 1).

3.1.1 Ground-based measurement closure

The columns in Table 2 represent the different cases for both clouds that were (a) coupled with and (b) decoupled from the surface BL (“C” and “D”, respectively). The first row in Table 2 includes the state of atmospheric mixing, the date, the type of cloud present and the abbreviation used for each case. The top portion of Table 2 consists of in situ airborne measurements; the bottom portion presents ACPM simulation results and their relation to in situ cloud extinction and satellite-retrieved observations. The ground-based in situ measurements in Table 2 include the Hoppel minimum diameter² (D_{\min}), as well as the aerosol concentration of aerosol with diameters greater than the Hoppel D_{\min} and the inferred in-cloud critical supersaturation (S_c ; Hop-

pel, 1979). The dry aerosol particles with diameters greater than the Hoppel D_{\min} have undergone cloud processing and are used here to estimate the CDNC. For each of the case study days, Fig. 5 demonstrates the aerosol size distribution measurements, from the SMPS and APS, that are used to find the Hoppel D_{\min} and Hoppel CDNC and used to initialize the ACPM. The Hoppel CDNC is calculated by integrating the SMPS and APS combined size distributions for aerosol sizes greater than Hoppel D_{\min} . Figure 6 shows Hoppel-based CDNC estimates are within 30 % of simulated CDNC for the seven cases. The presence of the Hoppel minimum occurs on average at 80 nm diameter throughout the campaign (Figs. 1b, 5), implying in-cloud supersaturations near 0.25 % using a campaign-averaged hygroscopicity (K) of 0.42, which is in agreement with K values observed in the North Atlantic marine planetary boundary layer in Pringle et al. (2010).

²The Hoppel minimum diameter is the diameter with the lowest aerosol concentration between Aitken mode and accumulation mode.

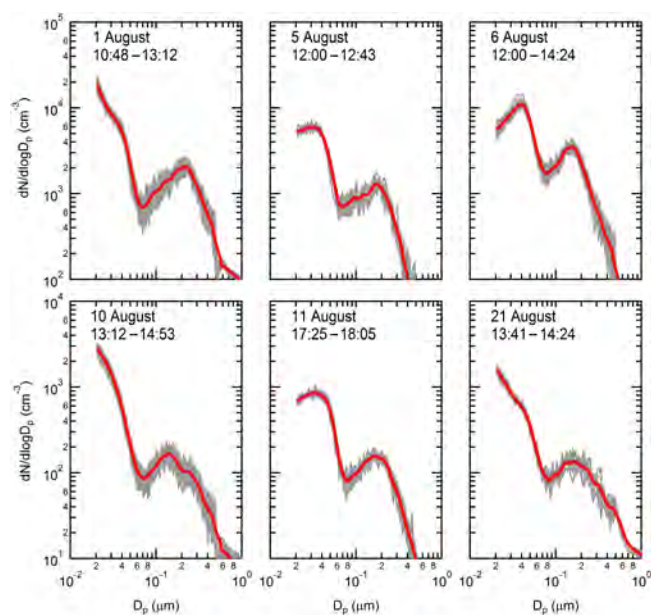


Figure 5. SMPS and APS derived size distributions used for each case study in Table 2. The 5 August size distribution is used for both the coupled and decoupled case. Individual distributions (grey) are from the indicated time ranges in the figure. The time ranges are in UTC. Average distributions are shown in red.

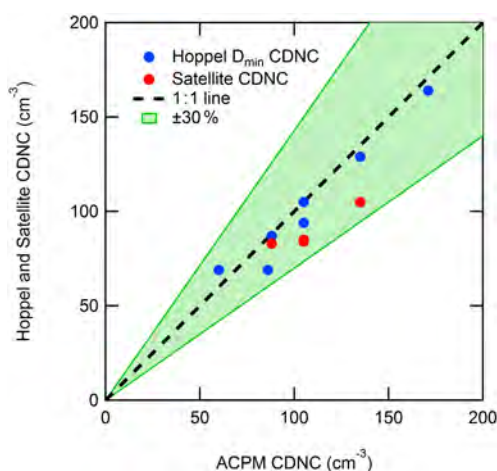


Figure 6. Comparison of simulated CDNC from ACPM with both Hoppel minimum diameter (D_{\min}) derived CDNC (blue) and satellite-estimated CDNC (red). CDNCs plotted are from the listed cloud cases in Table 2. The green shaded region represents Hoppel and satellite CDNCs within 30 % of ACPM simulation CDNC.

3.1.2 UAV measurements closure

Figure 7 displays vertical profiles of meteorological parameters, as well as OPC aerosol number concentration (N_{OPC} ; $D_p > 0.3 \mu\text{m}$) and cloud extinction from two flights (23 and 27) on 11 August. The UAV used on flight 23 (conducted between 12:00 and 12:47 UTC) contained the cloud sensor for

cloud extinction measurements, and flight 27 (conducted between 16:58 and 17:33 UTC) contained the OPC for droplet size distribution measurements. During this time period the cloud base reduced from 1200 m on flight 23 to 980 m on flight 27, but cloud depth remained approximately the same. In the OPC vertical profiles, in Fig. 7d, an aerosol layer is shown above the cloud at ~ 1400 m. OPC measurements are removed inside cloud layers (as aerosol data are contaminated by cloud droplets), hence the gap in OPC data in Fig. 7d. The OPC and temperature measurements, in Fig. 7a and d, are used to show if the boundary layer was coupled (well mixed) or if it was decoupled. The state of the boundary layer and the OPC and temperature measurements are further discussed at the end of this section. The observed temperature and relative humidity profiles, in Fig. 7a and b, are also used to initialize the ACPM. In situ cloud extinction measurements, in Fig. 7c, are then compared to the ACPM-simulated cloud extinction (Fig. 8c).

Figure 8a, c and e present the observed and simulated adiabatic cloud extinction profile for three of the case studies (C11Sc, D05Sc and C21Cu)³. The measurements are binned into in-cloud, cloud-free and cloud-transition (or cloud-edge) samples. Many clouds had a small horizontal extent, making it difficult for the UAVs to remain in cloud as they ascended and descended in a spiral pattern. Also, high horizontal winds ($10\text{--}15 \text{ m s}^{-1}$) will generally move the cloud outside the field of measurement of the aircraft very quickly. For cases where the UAV did not remain in cloud throughout the ascent or descent, the in-cloud samples are identified as the largest extinction values at each height and are seen in the measurements as a cluster of points (Fig. 8e). Since lateral mixing with cloud-free air exerts an influence near the cloud edges, the cloud-transition air is not representative of the cloud core and adiabatic simulations. The amount of sampling within individual clouds varied from case to case, but the UAVs were generally able to make multiple measurements of the same cloud during each vertical profile. C11Sc was unique in that it involved stratocumulus clouds with a large horizontal extent, allowing the UAV to remain entirely in cloud during the upward and downward vertical profiles around a fixed waypoint. Figure 8f shows how the difference between simulated and observed extinction ($\delta\sigma_{\text{ext}}$) is calculated throughout the cloud based on a discrete sampling of in-cloud measurements. It is not certain that the UAV measured the cloud core for cumulus cases, so $\delta\sigma_{\text{ext}}$ is an upper limit (Table 2).

All ACPM simulation results, including those in Table 2, use the cloud radar updraft velocity as input and not the five-hole probe updraft velocity because five-hole probe updraft velocities are not available for all cases. Nonetheless, the differences in ACPM-simulated shortwave radiative flux between using the five-hole probe and cloud radar updraft ve-

³C/D – coupled/decoupled; xx – date in August 2015; Sc/Cu – stratocumulus/cumulus cloud.

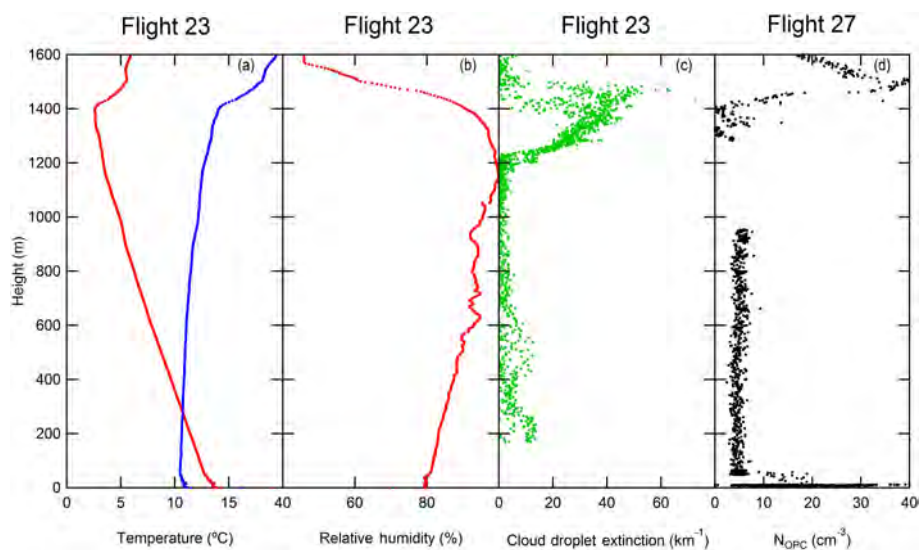


Figure 7. Vertical profiles of temperature, virtual potential temperature (θ_v), relative humidity, cloud droplet extinction and OPC total aerosol concentration. The figure consists of measurements collected from flights 23 and 27 on 11 August 2015 at 12:00–12:47 and 16:58–17:33, respectively. The cloud level is 1200–1480 m in flight 23 and lowered to approximately 980–1280 m in flight 27. OPC measurements that occurred in the cloud have been removed.

locities (Fig. 3) is less than 3 W m^{-2} for the four cases that had both measurements.

The integrated effect of $\delta\sigma_{\text{ext}}$ leads to a difference in cloud observed and simulated δRF for both clouds that were coupled with and decoupled from the surface boundary layer (Table 2). Figure 9 presents a vertical profile of N_{OPC} and equivalent potential temperature. OPC measurements within a thin cloud layer at $\sim 2000 \text{ m}$ are removed. N_{OPC} and equivalent potential temperature (θ_e) clearly illustrate this decoupling as shown in an example vertical profile (Fig. 9) at 900 and 2200 m a.s.l., with the latter representing the inversion between the boundary layer top and free troposphere. N_{OPC} decreases from an average of 31 to 19 cm^{-3} at the same altitude as the weak inversion (700–1000 m). In this study, decoupled boundary layers are often observed, and aerosol number concentrations ($D_p > 0.3 \mu\text{m}$) in the decoupled layer were $44\% \pm 14\%$ of those measured at the ground. While N_{OPC} are not directly representative of CCN concentrations, a reduction in aerosol number with height (and potential differences in hygroscopicity) will nonetheless affect aerosol–cloud closures and, ultimately, the cloud radiative properties. Similarly, Norton et al. (2006) showed results from the European Centre for Medium-Range Weather Forecasts (ECMWF) model reanalysis in which surface winds at Mace Head are often decoupled from synoptic flow and, therefore, the air masses in each layer have different origins and most likely different aerosol properties. Consequently, the CCN number concentrations measured at the surface do not represent those in the higher decoupled cloud layer, which ultimately dictates cloud shortwave radiative flux in the region and δRF in Table 2. While aerosol profiles were not collected

by UAVs for the decoupled cases presented in Table 2, the θ_e profiles and ceilometer measurements show evidence of boundary layer decoupling. These two decoupled cases have larger $\delta\sigma_{\text{ext}}$ than the coupled boundary layer cases in this study, leading to larger cloud-top δRF as well. ACPM simulations were conducted using aerosol concentrations based on the approximate average decoupled-to-coupled aerosol concentration ratio (50 %, Fig. 9) to estimate the difference in shortwave radiative flux. For the D05Sc case, simulations with 50 % decreased cloud-base aerosol concentrations show only slight differences in δRF of 2 W m^{-2} and decreases in CDNC of 10 %. The decrease in aerosol concentration resulted in increased supersaturation due to the low water uptake from fewer activating droplets. The increased supersaturation caused smaller aerosols to activate (Raatikainen et al., 2013) and, therefore, little change in CDNC. The D05Sc case has very low updraft velocities ($0\text{--}0.3 \text{ m s}^{-1}$). At low updraft velocities, the CDNC is often updraft limited (Reutter et al., 2009). This means the CDNC is very sensitive to the updraft velocities and less sensitive to aerosol concentration. Small errors in updraft velocity and low modeled updraft resolution (0.1 m s^{-1}) likely contribute significantly to the error in this case. D06Cu was not influenced as much by low water uptake because the CDNC was much higher at 171 cm^{-3} than 86 cm^{-3} for D05Sc. D06Cu the CDNC decreased by 42 %, and δRF decreased by 18 W m^{-2} . The updraft velocity range for the D06Cu case is significantly higher than the D05Cu case ($0\text{--}1.6 \text{ m s}^{-1}$). The higher velocities for D05Sc and greater sensitivity to aerosol concentration suggest this case is aerosol limited (Reutter et al., 2009). Both decoupled cases still have a δRF greater than the coupled cases.

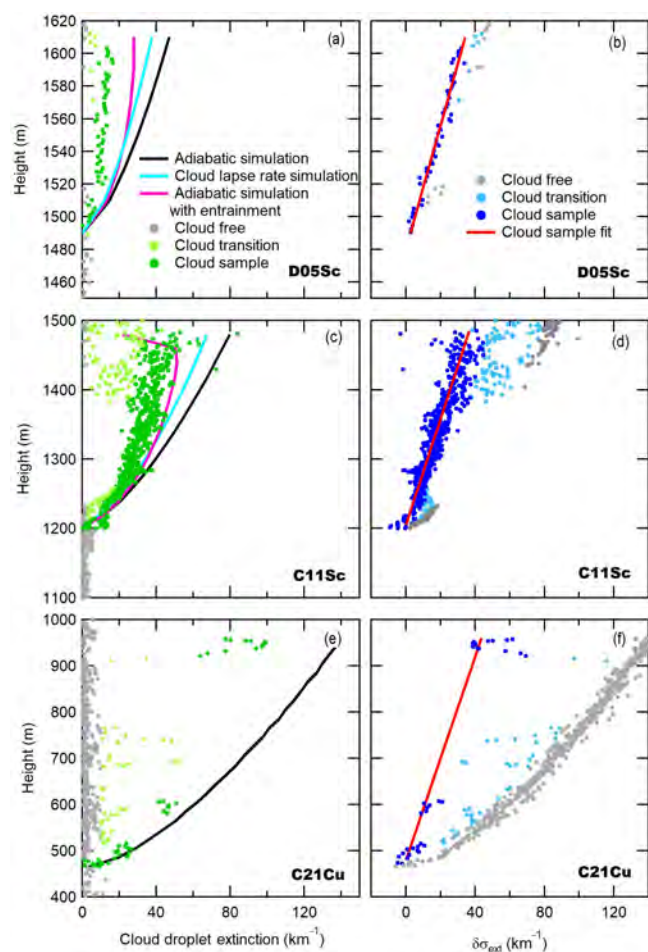


Figure 8. Vertical profiles of measured and simulated cloud extinction from flights D05Sc, C11Sc and C21Cu (a, c and e, respectively; Table 2). In situ measurements are classified into cloud, cloud-transition and cloud-free observations. The differences between UAV-observed and ACPM-simulated cloud extinction (black line) in left figures (a, c, e) are used to calculate $(\delta\sigma_{\text{ext}})$ as a function of altitude in the right figures (b, d, f). The slope of the best fit through in-cloud measurements (red line) represents the increase in $\delta\sigma_{\text{ext}}$ as a function of cloud thickness.

3.1.3 Satellite measurement closure

The satellite and simulated CDNC and S_{max} measurements are presented in the bottom of Table 2. The method for satellite retrieval of cloud properties could not be used for cases when cloud layers were too thin, which unfortunately was the situation during the flights with the decoupled cloud layers. Nonetheless, Fig. 4 shows the satellite image used to identify the clouds to calculate CDNC for C11Sc. Satellite-retrieved cloud-base height and temperature are verified by ground-based ceilometer and temperature measurements. Figure 6 shows the top-down closures, which demonstrate that satellite-estimated CDNC and simulated CDNC are within a $\pm 30\%$ expected concentrations, which is lim-

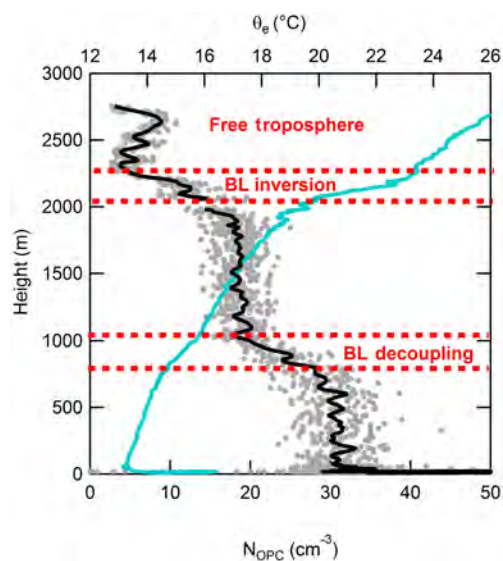


Figure 9. UAV vertical profile of OPC aerosol number concentrations ($D_p > 0.3 \mu\text{m}$; grey) with a 20 s running mean (black) and equivalent potential temperature (θ_e , light blue) illustrate decoupling of the boundary layer. In-cloud OPC measurements (2000–2050 m) have been removed.

ited by the retrieval of effective radius (Rosenfeld et al., 2016). The stratocumulus deck at the top of a well-mixed boundary layer (C11Sc) shows evidence of cloud-top inhomogeneous entrainment (see Sect. 3.2). Freud et al. (2011) found that the inhomogeneous mixing assumption used to derive CDNC from satellite measurements resulted in an average overestimate in CDNC of 30 % (considering an adiabatic cloud droplet profile). Consequently, satellite-retrieved CDNC is reduced by 30 % to account for the inhomogeneous entrainment assumption, which does not necessarily reflect the actual magnitude of entrainment in the clouds. For the C11Sc case, before the correction proposed by Freud et al. (2011) is applied, the satellite-derived CDNC (83 cm^{-3}) is within 30 % of the ACPM CDNC (88 cm^{-3}), similar to the other cases (Fig. 6). However, if the correction is applied, the satellite-derived CDNC (58 cm^{-3}) is not within 30 % of the ACPM CDNC. This indicates cloud-top entrainment for the C11Sc case is already inhomogeneous, and the usual 30 % reduction in CDNC, to correct for the inhomogeneous assumption, should not be applied. Both stratocumulus cases (C11Sc, D05Sc) with cloud-top entrainment (Table 2) are similar to a case studied by Burnet and Brenguier (2007), in which cloud-top entrainment resulted in inhomogeneous mixing. In the following section, C11Sc and D05Sc are re-analyzed to include the effect of cloud-top entrainment on simulated cloud properties using the inhomogeneous mixing assumption.

3.2 Entrainment

Based on the ground-based and UAV measurements, ACPM simulations overestimate cloud shortwave radiative flux significantly for three cases (C11Sc, D05Sc, D06Cu). Section 3.1.2 identified that clouds in decoupled layers (D05Sc, D06Cu) have smaller radiative effects than predicted based on ground-based observations as aerosol (and CCN) number concentrations in the decoupled layer are often smaller than in the surface mixed layer. In this section, cloud-top entrainment is also shown to influence the radiative properties of two sub-adiabatic stratocumulus clouds, C11Sc and D05Sc.

The UAV observations show that both C11Sc and D05Sc have sub-adiabatic lapse rate measurements, compared to simulated moist-adiabatic lapse rates within the cloud (Table 2). The difference between the observed and simulated lapse rates therefore suggests a source of heating in the cloud. The sub-adiabatic lapse rate is attributed to cloud-top entrainment by downward mixing of warmer air at cloud top. The D06Cu case has a slightly sub-adiabatic observed lapse rate (Table 2); however the difference with respect to an adiabatic lapse rate is within instrument error. For this reason, cloud-top entrainment is not explored for this case, though it may contribute to the error.

Further evidence of cloud-top entrainment is shown through conserved variable mixing diagram analysis. In previous studies, a conserved variable mixing diagram analysis was used to show lateral or cloud-top entrainment by showing linear relationships between observations of conserved variables (Paluch, 1979; Neggers et al., 2002; Burnet and Brenguier, 2007). Paluch (1979) first observed a linear relationship of conservative properties (total water content, q_t , and liquid water potential temperature, θ_l) between cumulus cloud cores and cloud edge, to show the cloud-free source of entrained air. Paluch (1979), Burnet and Brenguier (2007), Roberts et al. (2008) and Lehmann et al. (2009) observed decreases in CDNC and liquid water content in cumulus clouds as a function of distance from the cloud cores that indicate inhomogeneous mixing at the cloud edge. Burnet and Brenguier (2007) also show that q_t is linearly proportional to liquid water potential temperature specifically for a stratocumulus cloud with cloud-top entrainment and inhomogeneous mixing. Direct observations of CDNC and liquid water content were not measured at Mace Head, so direct comparisons of CDNC and q_t with Paluch (1979) and Burnet and Brenguier (2007) cannot be investigated here. However, UAV measurements of cloud extinction (Eq. 1), which are related to CDNC ($\text{CDNC} = \int_0^\infty n(r) dr$) and liquid water content ($\text{LWC} = \int_0^\infty \frac{4}{3} \rho \pi r^3 n(r) dr$, where ρ is liquid water density), were measured and are found to be systematically lower than the adiabatic simulated cloud extinction (Fig. 8).

To apply the cloud-top mixing, a fraction of air at cloud base and a fraction of air above cloud top are mixed, conserving q_t and θ_e . The fraction of air from cloud base and cloud top is determined with the measured equivalent poten-

tial temperature:

$$\theta_{e,c}(z) = \theta_{e,\text{ent}}X(z) + \theta_{e,\text{CB}}(1 - X(z)), \quad (4)$$

where $\theta_{e,c}(z)$ is the equivalent potential temperature in cloud as a function of height, $\theta_{e,\text{ent}}$ is the equivalent potential temperature of the cloud-top entrained air, $\theta_{e,\text{CB}}$ is the equivalent potential temperature of air at cloud base and $X(z)$ is the fraction of cloud-top entrained air as a function of height (referred to as the entrainment fraction). $\theta_{e,\text{ent}}$, $\theta_{e,c}(z)$ and $\theta_{e,\text{CB}}$ are measured parameters by the UAV and are not affected by latent heating from evaporation or condensation. The equivalent potential temperature, by definition, accounts for the total water content by including the latent heat released by condensing all the water vapor. Equation (4) takes into account latent heating caused by evaporation of droplets. By rearranging Eq. (4), the entrained fraction is calculated as

$$X(z) = \frac{\theta_{e,c}(z) - \theta_{e,\text{CB}}}{\theta_{e,\text{ent}} - \theta_{e,\text{CB}}}. \quad (5)$$

Figure 10a and b present the relationships between two conservative variables measured by the UAV (water vapor content, q_v and θ_e) for C11Sc and D05Sc. The q_v is derived from relative humidity measurements and is equivalent to the q_t for subsaturated, cloud-free air (i.e., < 100 %RH). The cloud-free air is shown in blue in Fig. 10, where the below-cloud measurements have lower θ_e than in cloud and the above-cloud measurements have higher θ_e than in cloud.

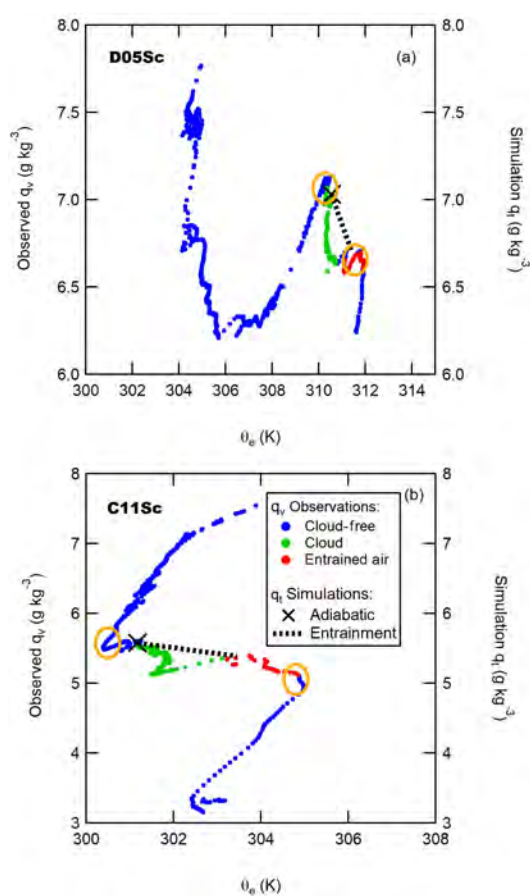
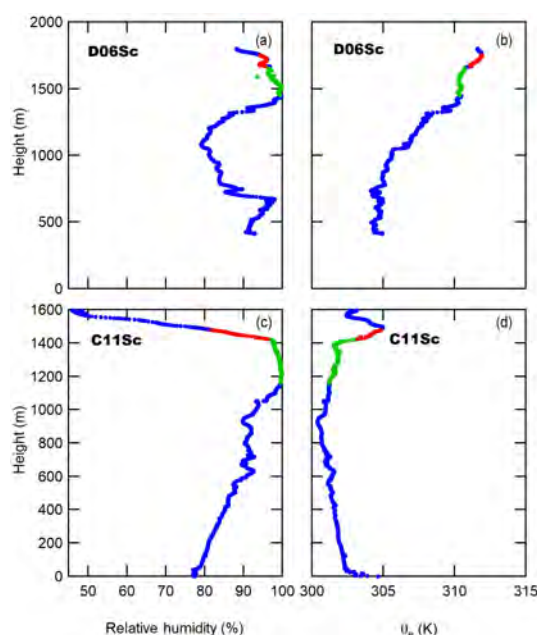
Figure 11 shows the relative humidity and θ_e profiles used in Fig. 10. For both C11Sc and D05Sc, $\theta_{e,c}(z)$ is directly measured in cloud, and q_t and θ_e exhibit an approximately linear relationship (Fig. 10; Eq. 4). The linear relationship of q_t and θ_e (between the non-mixed sources of air indicated by orange circles in Fig. 10) is assumed to be a result of the cloud reaching a steady state, with air coming from cloud base and cloud top (e.g., cloud lifetime \gg mixing time). The observed in-cloud q_v in Fig. 10a and b is less than the conservative variable q_t ; however, the figure also includes q_t based on simulated adiabatic (marked with an “X”) and cloud-top entrainment (dashed black line) conditions. Under adiabatic conditions q_t and θ_e do not change in the cloud, which is why the adiabatic simulations only consist of one point in Fig. 10. Equation (4) is used to derive the simulated cloud-top entrainment conditions (Fig. 10a and b), where the fraction entrained is used to calculate q_v and shows a linear relationship between q_t and θ_e . Measurements above cloud top (RH < 95 %), labeled entrained air, with $q_v > 5.1$ and $q_v > 6.5 \text{ g kg}^{-1}$ are used to represent the properties of the entrained air for C11Sc and D05Sc, respectively (Fig. 10). These conditions were chosen because these values are on the mixing line, between the non-mixed sources identified by the orange circles.

Figure 12 shows the sensitivity of the simulated cloud extinction profile, for the 11 August case, based on measurement uncertainties related to the entrained q_t and θ . The key

Table 3. Results of the application of entrainment fraction and the measured lapse rate entrainment parameterization for two clouds with observed cloud-top entrainment.

Entrainment method	Coupled BL (C11Sc)		Decoupled BL (D05Sc)	
	Homogeneous mixing entrainment	Lapse rate adjustment	Homogeneous mixing entrainment	Lapse rate adjustment
Cloud-top extinction difference ($\delta\sigma_{\text{ext}}$, km^{-1})	16 ± 10	23 ± 11	16 ± 5	26 ± 6
Simulated cloud τ	10.1 ± 1.5	10.3 ± 1.6	2.2 ± 0.3	3.5 ± 0.5
Cloud-top shortwave radiative flux difference (δRF , W m^{-2}) ^a	20 ± 16	32 ± 17	33 ± 9	61 ± 12
Cloud-base simulated CDNC ^b	88 ± 12	83 ± 12	86 ± 10	68 ± 10

^a The difference between the observed (calculated from UAV extinction measurements) and simulated shortwave radiative flux. The error includes the potential error of $\pm 20\%$ in updraft velocity and the standard error of the CCN concentration measurements. ^b The simulated CDNC is unchanged at the cloud base for the entrainment fraction method; however the CDNC decreases with height.

**Figure 10.** Conservative variables, water vapor content (q_v , conservative in subsaturated conditions and derived from RH measurements) and equivalent potential temperature (θ_e) identify mixing between cloud air and entrained air for flights D06Sc (a) and C11Sc (b). Measurements are defined as cloud-free (blue), in-cloud (green) or entrained-air properties used in simulations (red). The orange circles highlight what is suggested to be the non-mixed sources of air.**Figure 11.** UAV vertical profiles of relative humidity (a, c) and θ_e (b, d) for flights D06Sc and C11Sc, used in Fig. 10. Profiles are defined as cloud-free (blue), in-cloud (green) or entrained-air sources (red).

variable for identifying the entrained fraction (Eq. 5), $\theta_{e,\text{ent}}$, is a function of q_t and θ , so a decrease in either parameter results in a proportional decrease in $\theta_{e,\text{ent}}$. Equation (5) shows that entrainment fraction becomes more sensitive to the uncertainty related to the measurement of θ_e as the difference between $\theta_{e,\text{ent}}$ and $\theta_{e,\text{CB}}$ approaches zero. This is also shown in Fig. 12, where σ_{ext} is more sensitive to lower entrained q_t and θ values.

Table 3 shows $\delta\sigma_{\text{ext}}$, δRF and CDNC for two cases with cloud-top entrainment (C11Sc and D05Sc) using two methods of accounting for the cloud-top entrainment. One method (labeled the “inhomogeneous mixing entrainment method” in Table 3) applies the entrainment fraction calculated in

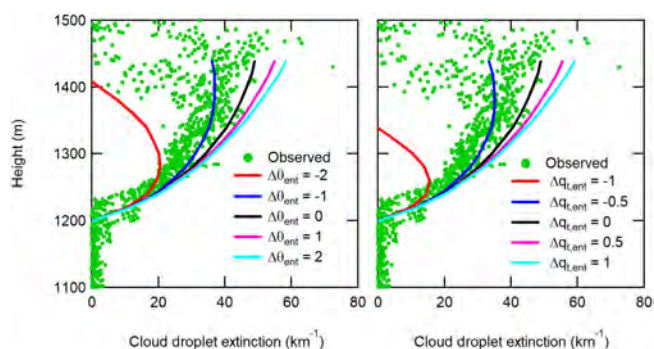


Figure 12. Sensitivity of simulated cloud extinction based on variability of entrained-air potential temperature (θ_{ent} , K) and entrained-air total water mixing ratio ($q_{t,\text{ent}}$, g kg^{-1}) for the C11Sc case. The $\Delta\theta_{\text{ent}}$ and $\Delta q_{t,\text{ent}}$ terms define the change in the entrained θ and q_t values where no change ($\Delta\theta_{\text{ent}} = 0$ and $\Delta q_{t,\text{ent}} = 0$) is equivalent to the adiabatic simulation with entrainment from Fig. 8c.

Eq. (5), and the other an entrainment parameterization presented by Sanchez et al. (2016). The entrainment parameterization constrains the ACPM simulation to use the observed in-cloud lapse rate instead of assuming an adiabatic lapse rate. This is labeled the “lapse rate adjustment” entrainment method in Table 3. In the sub-adiabatic cloud cases (C11Sc and D05Sc), the measured in-cloud lapse rate is lower than the adiabatic lapse rate, which leads to the condensation of less water vapor and subsequent activation of fewer droplets in the ACPM simulation. Similarly, when applying the inhomogeneous mixing entrainment method, the dryer and warmer entrained air (from above cloud top) leads to evaporation of liquid water in the cloud. Previous observations of stratocumulus cloud-top mixing suggest the entrainment is inhomogeneous (Burnet and Brenguier, 2007; Beals et al., 2015), which implies that timescales of evaporation are much less than the timescales of mixing, such that a fraction of the droplets are evaporated completely and the remaining droplets are unaffected by the entrainment. The net decrease in CDNC subsequently results in less extinction of solar radiation compared to the purely adiabatic simulation.

The inclusion of inhomogeneous mixing entrainment improved the ACPM accuracy for both C11Sc and D05Sc using the measured lapse rate and entrainment fraction methods (Fig. 8, Table 3). After accounting for inhomogeneous entrainment, δRF decreased from 88 to 33 and 48 to 20 W m^{-2} for D05Sc and D11Sc, respectively, using the entrainment fraction method. D05Sc simulations still yield significant δRF even after accounting for inhomogeneous mixing entrainment, likely because the cloud is in a decoupled BL, as noted in Sect. 3.1.2 to exhibit lower aerosol concentrations than those measured at the surface. The CDNC presented in Table 3 represents the CDNC at cloud base and did not change after applying the entrainment fraction method; however, the CDNC decreases with height for the entrain-

ment fraction method rather than remaining constant with height. Finally, the lapse rate adjustment entrainment method (Sanchez et al., 2016) does improve ACPM accuracy between in situ and satellite-retrieved cloud optical properties relative to the adiabatic simulations but has greater $\delta\sigma_{\text{ext}}$ throughout the cloud than the inhomogeneous mixing entrainment method. For the lapse rate adjustment entrainment method δRF decreased from 88 to 61 and 48 to 32 W m^{-2} for D05Sc and D11Sc, respectively. The lapse rate adjustment entrainment method resulted in lower δRF than the purely adiabatic simulations; however, δRF was minimized by directly accounting for the entrainment fraction.

4 Conclusions

This work presents measurements conducted in August 2015 at the Mace Head Atmospheric Research Station in Ireland, from multiple platforms including ground-based, airborne and satellite measurements. As part of the BACCHUS (Impact of Biogenic versus Anthropogenic emissions on Clouds and Climate: towards a Holistic UnderStanding) European collaborative project, the goal of this study is to understand key processes affecting aerosol–cloud shortwave radiative flux interactions. Seven cases including cumulus and stratocumulus clouds were investigated to quantify aerosol–cloud interactions using ground-based and airborne measurements (bottom-up closure), as well as cloud microphysical and radiative properties using airborne measurements and satellite retrievals (top-down closure). An aerosol–cloud parcel model was used to link the ground-based, airborne and satellite observations, and to quantify uncertainties related to aerosols, cloud microphysical properties and resulting cloud optical properties.

ACPM simulations represent bottom-up and top-down closures within uncertainties related to satellite retrievals for conditions with a coupled boundary layer and adiabatic cloud development. For these conditions, the difference in shortwave radiative flux between simulations and in situ observed parameters is no greater than 20 W m^{-2} . However, when entrainment and decoupling of the cloud layer occur, the ACPM simulations overestimate the cloud shortwave radiative flux. Of the seven cases, two of the observed clouds occurred in a decoupled layer, resulting in differences in observed and simulated δRF of 88 and 74 W m^{-2} for the decoupled stratocumulus case on 5 August (D05Sc) and the decoupled cumulus case on 6 August (D06Cu) cases, respectively. Adiabatic ACPM simulations resulted in a maximum cloud-top δRF value of 20 W m^{-2} for coupled boundary layer cases and 74 W m^{-2} for the decoupled boundary layer cases, after accounting for cloud-top entrainment. The reduction in aerosol concentrations in the decoupled layer compared to ground-based measurements is a factor in overestimating decoupled cloud-top shortwave radiative flux with the ACPM; however simulations with 50 % decreased aerosol concentra-

tions show only slight differences in δRF of 2 W m^{-2} and decreases in CDNC of 10 % for D05Sc. For D06Cu δRF decreased by 18 W m^{-2} , and the CDNC decreased by 42 %. Even after decreasing the aerosol concentration by 50, both decoupled cases have δRF values significantly higher than the coupled boundary layer cases ($<20\text{ W m}^{-2}$).

For the cases with cloud-top entrainment, D05Sc and the coupled stratocumulus case on 11 August (C11Sc), liquid water content is one of the major factors in overestimating cloud-top shortwave radiative flux with the ACPM. For these cases, the measured in-cloud lapse rates are lower than adiabatic lapse rates, suggesting a source of heat due to entrainment of warmer, drier air from above the cloud. Furthermore, linear relationships between conservative variables (simulated total water vapor, q_t , and equivalent potential temperature, θ_e) also suggest mixing between air at cloud base and cloud top. For D05Sc, after accounting for cloud-top entrainment by applying the entrainment fraction, δRF decreased from 88 to 33 W m^{-2} . For the coupled boundary layer case with entrainment (C11Sc) the δRF decreases from 48 to 20 W m^{-2} after accounting for cloud-top entrainment with the entrainment fraction.

Based on airborne observations with UAVs, decoupling of the boundary layer occurred on 4 of the 13 flight days (two decoupled cloud cases were not discussed due to the lack of in-cloud measurements). However, cloud drop entrainment was only observed on 2 of those days, limited by the ability to make in situ measurements. These measurements occurred during the summer, so additional measurements are needed to look at seasonal trends. These cases illustrate the need for in situ observations to quantify entrainment mixing and cloud-base CCN concentrations particularly when the mixing state of the atmosphere is not known. Using ground-based observations to model clouds in decoupled boundary layers and not including cloud-top entrainment are shown to cause significant differences between observations and simulation radiative forcing and, therefore, should be included in large-scale modeling studies to accurately predict future climate forcing.

UAV measurements were coordinated with 13 days of satellite overpasses, and cloud microphysical properties were retrieved for four of the cases. When accounting for entrainment, the differences between simulated and satellite-retrieved CDNC are within the expected 30 % accuracy of the satellite retrievals (Rosenfeld et al., 2016). However, in situ measurements are necessary to refine satellite retrievals to allow cloud properties to be studied on larger spatial scales.

Data availability. All data are available by contacting the corresponding author or through the following link: https://hal-meteofrance.archives-ouvertes.fr/meteo-01567780/file/MH_data_for_archive.zip.

Competing interests. The authors declare that they have no conflict of interest.

Special issue statement. This article is part of the special issue “BACCHUS – Impact of Biogenic versus Anthropogenic emissions on Clouds and Climate: towards a Holistic Understanding (ACP/AMT/GMD inter-journal SI)”. It is not associated with a conference.

Acknowledgements. The research leading to these results received funding from the European Union’s Seventh Framework Programme (FP7/2007-2013) project BACCHUS under grant agreement no. 603445. EU H2020 project ACTRIS-2 under the grant agreement no. 654109 is also acknowledged for supporting the Mace Head Atmospheric Research Station. Keri Nicoll acknowledges a NERC Independent Research Fellowship (NE/L011514/1). Darius Ceburnis acknowledges the Irish EPA (2012-CCRP-FS.12). Jana Preissler acknowledges the Irish EPA (2015-CCRP-FS.24). Radiance Calmer acknowledges financial support from Météo France. Kevin J. Sanchez acknowledges the Chateaubriand Fellowship. We thank École Nationale de l’Aviation Civile (ENAC) for assistance with construction and operation of the UAVs. The authors also acknowledge Kirsten Fossum for the collection of SMPS data. We applied a sequence-defines-credit approach for the sequence of authorship.

Edited by: Hailong Wang

Reviewed by: four anonymous referees

References

- Albrecht, B. A., Bretherton, C. S., Johnson, D., Scudlark, W. H., and Frisch, A. S.: The Atlantic Stratocumulus Transition Experiment – ASTEX, *B. Am. Meteorol. Soc.*, 76, 889–904, [https://doi.org/10.1175/1520-0477\(1995\)076<0889:TASTE>2.0.CO;2](https://doi.org/10.1175/1520-0477(1995)076<0889:TASTE>2.0.CO;2), 1995.
- Bahadur, R., Russell, L. M., Jacobson, M. Z., Prather, K., Nenes, A., Adams, P., and Seinfeld, J. H.: Importance of composition and hygroscopicity of BC particles to the effect of BC mitigation on cloud properties: Application to California conditions, *J. Geophys. Res.-Atmos.*, 117, D09204, <https://doi.org/10.1029/2011jd017265>, 2012.
- Bates, T. S., Huebert, B. J., Gras, J. L., Griffiths, F. B., and Durkee, P. A.: International Global Atmospheric Chemistry (IGAC) project’s first aerosol characterization experiment (ACE 1): Overview, *J. Geophys. Res.-Atmos.*, 103, 16297–16318, <https://doi.org/10.1029/97jd03741>, 1998.
- Beals, M. J., Fugal, J. P., Shaw, R. A., Lu, J., Spuler, S. M., and Stith, J. L.: Holographic measurements of inhomogeneous cloud mixing at the centimeter scale, *Science*, 350, 87–90, <https://doi.org/10.1126/science.aab0751>, 2015.
- Bohren, C. F. and Battan, L. J.: Radar Backscattering by Inhomogeneous Precipitation Particles, *J. Atmos. Sci.*, 37, 1821–1827, [https://doi.org/10.1175/1520-0469\(1980\)037<1821:RBBIPP>2.0.CO;2](https://doi.org/10.1175/1520-0469(1980)037<1821:RBBIPP>2.0.CO;2), 1980.

- Bretherton, C. S. and Wyant, M. C.: Moisture transport, lower tropospheric stability and decoupling of cloud-topped boundary layers, *J. Atmos. Sci.*, 54, 148–167, [https://doi.org/10.1175/1520-0469\(1997\)054<0148:MTLTA>2.0.CO;2](https://doi.org/10.1175/1520-0469(1997)054<0148:MTLTA>2.0.CO;2), 1997.
- Burnet, F. and Brenguier, J.-L.: Observational study of the entrainment-mixing process in warm convective clouds, *J. Atmos. Sci.*, 64, 1995–2011, <https://doi.org/10.1175/jas3928.1>, 2007.
- Calmer, R., Roberts, G., Preissler, J., Derrien, S., and O’Dowd, C.: 3D Wind Vector Measurements using a 5-hole Probe with Remotely Piloted Aircraft, *Atmos. Meas. Tech. Discuss.*, <https://doi.org/10.5194/amt-2017-233>, in review, 2017.
- Coe, H., Allan, J. D., Alfarra, M. R., Bower, K. N., Flynn, M. J., McFiggans, G. B., Topping, D. O., Williams, P. I., O’Dowd, C. D., Dall’Osto, M., Beddows, D. C. S., and Harrison, R. M.: Chemical and physical characteristics of aerosol particles at a remote coastal location, Mace Head, Ireland, during NAMBLEX, *Atmos. Chem. Phys.*, 6, 3289–3301, <https://doi.org/10.5194/acp-6-3289-2006>, 2006.
- Conant, W. C., VanReken, T. M., Rissman, T. A., Varutbangkul, V., Jonsson, H. H., Nenes, A., Jimenez, J. L., Delia, A. E., Bahreini, R., Roberts, G. C., Flagan, R. C., and Seinfeld, J. H.: Aerosol-cloud drop concentration closure in warm cumulus, *J. Geophys. Res.-Atmos.*, 109, D13204, <https://doi.org/10.1029/2003jd004324>, 2004.
- Dall’Osto, M., Ceburnis, D., Martucci, G., Bialek, J., Dupuy, R., Jennings, S. G., Berresheim, H., Wenger, J., Healy, R., Facchini, M. C., Rinaldi, M., Giulianelli, L., Finessi, E., Worsnop, D., Ehn, M., Mikkilä, J., Kulmala, M., and O’Dowd, C. D.: Aerosol properties associated with air masses arriving into the North East Atlantic during the 2008 Mace Head EUCAARI intensive observing period: an overview, *Atmos. Chem. Phys.*, 10, 8413–8435, <https://doi.org/10.5194/acp-10-8413-2010>, 2010.
- Feingold, G., McComiskey, A., Rosenfeld, D., and Sorooshian, A.: On the relationship between cloud contact time and precipitation susceptibility to aerosol, *J. Geophys. Res.-Atmos.*, 118, 10544–10554, <https://doi.org/10.1002/jgrd.50819>, 2013.
- Fountoukis, C., Nenes, A., Meskhidze, N., Bahreini, R., Conant, W. C., Jonsson, H., Murphy, S., Sorooshian, A., Varutbangkul, V., Brechtel, F., Flagan, R. C., and Seinfeld, J. H.: Aerosol-cloud drop concentration closure for clouds sampled during the International Consortium for Atmospheric Research on Transport and Transformation 2004 campaign, *J. Geophys. Res.-Atmos.*, 112, D10S30, <https://doi.org/10.1029/2006jd007272>, 2007.
- Freud, E., Rosenfeld, D., and Kulkarni, J. R.: Resolving both entrainment-mixing and number of activated CCN in deep convective clouds, *Atmos. Chem. Phys.*, 11, 12887–12900, <https://doi.org/10.5194/acp-11-12887-2011>, 2011.
- Geresdi, I., Meszaros, E., and Molnar, A.: The effect of chemical composition and size distribution of aerosol particles on droplet formation and albedo of stratocumulus clouds, *Atmos. Environ.*, 40, 1845–1855, <https://doi.org/10.1016/j.atmosenv.2005.11.012>, 2006.
- Goersdorf, U., Lehmann, V., Bauer-Pfundstein, M., Peters, G., Vavriv, D., Vinogradov, V., and Volkov, V.: A 35-GHz Polarimetric Doppler Radar for Long-Term Observations of Cloud Parameters-Description of System and Data Processing, *J. Atmos. Ocean. Tech.*, 32, 675–690, <https://doi.org/10.1175/jtech-d-14-00066.1>, 2015.
- Hansen, J. E. and Travis, L. D.: Light-Scattering in Planetary Atmospheres, *Space Sci. Rev.*, 16, 527–610, <https://doi.org/10.1007/bf00168069>, 1974.
- Harrison, R. G. and Nicoll, K. A.: Note: Active optical detection of cloud from a balloon platform, *Rev. Sci. Instrum.*, 85, 066104, <https://doi.org/10.1063/1.4882318>, 2014.
- Heard, D. E., Read, K. A., Methven, J., Al-Haider, S., Bloss, W. J., Johnson, G. P., Pilling, M. J., Seakins, P. W., Smith, S. C., Sommariva, R., Stanton, J. C., Still, T. J., Ingham, T., Brooks, B., De Leeuw, G., Jackson, A. V., McQuaid, J. B., Morgan, R., Smith, M. H., Carpenter, L. J., Carslaw, N., Hamilton, J., Hopkins, J. R., Lee, J. D., Lewis, A. C., Purvis, R. M., Wevill, D. J., Brough, N., Green, T., Mills, G., Penkett, S. A., Plane, J. M. C., Saiz-Lopez, A., Worton, D., Monks, P. S., Fleming, Z., Rickard, A. R., Alfarra, M. R., Allan, J. D., Bower, K., Coe, H., Cubison, M., Flynn, M., McFiggans, G., Gallagher, M., Norton, E. G., O’Dowd, C. D., Shillito, J., Topping, D., Vaughan, G., Williams, P., Bitter, M., Ball, S. M., Jones, R. L., Povey, I. M., O’Doherty, S., Simmonds, P. G., Allen, A., Kinnery, R. P., Beddows, D. C. S., Dall’Osto, M., Harrison, R. M., Donovan, R. J., Heal, M. R., Jennings, S. G., Noone, C., and Spain, G.: The North Atlantic Marine Boundary Layer Experiment (NAMBLEX), Overview of the campaign held at Mace Head, Ireland, in summer 2002, *Atmos. Chem. Phys.*, 6, 2241–2272, <https://doi.org/10.5194/acp-6-2241-2006>, 2006.
- Heese, B., Flentje, H., Althausen, D., Ansmann, A., and Frey, S.: Ceilometer lidar comparison: backscatter coefficient retrieval and signal-to-noise ratio determination, *Atmos. Meas. Tech.*, 3, 1763–1770, <https://doi.org/10.5194/amt-3-1763-2010>, 2010.
- Hoppel, W. A.: Measurement of the size distribution and ccn supersaturation spectrum of sub-micron aerosols over the ocean, *J. Atmos. Sci.*, 36, 2006–2015, [https://doi.org/10.1175/1520-0469\(1979\)036<2006:motsda>2.0.co;2](https://doi.org/10.1175/1520-0469(1979)036<2006:motsda>2.0.co;2), 1979.
- Jacobson, M. Z., Turco, R. P., Jensen, E. J., and Toon, O. B.: Modeling Coagulation Among Particles of Different Composition and Size, *Atmos. Environ.*, 28, 1327–1338, [https://doi.org/10.1016/1352-2310\(94\)90280-1](https://doi.org/10.1016/1352-2310(94)90280-1), 1994.
- Jones, C. R., Bretherton, C. S., and Leon, D.: Coupled vs. decoupled boundary layers in VOCALS-REx, *Atmos. Chem. Phys.*, 11, 7143–7153, <https://doi.org/10.5194/acp-11-7143-2011>, 2011.
- Kleefeld, C., O’Dowd, C. D., O’Reilly, S., Jennings, S. G., Aalto, P., Becker, E., Kunz, G., and de Leeuw, G.: Relative contribution of submicron and supermicron particles to aerosol light scattering in the marine boundary layer, *J. Geophys. Res.-Atmos.*, 107, 8103, <https://doi.org/10.1029/2000jd000262>, 2002.
- Kunz, G. J., de Leeuw, G., Becker, E., and O’Dowd, C. D.: Lidar observations of atmospheric boundary layer structure and sea spray aerosol plumes generation and transport at Mace Head, Ireland (PARFORCE experiment), *J. Geophys. Res.-Atmos.*, 107, 8106, <https://doi.org/10.1029/2001jd001240>, 2002.
- Lehmann, K., Siebert, H., and Shaw, R. A.: Homogeneous and Inhomogeneous Mixing in Cumulus Clouds: Dependence on Local Turbulence Structure, *J. Atmos. Sci.*, 66, 3641–3659, <https://doi.org/10.1175/2009jas3012.1>, 2009.
- Lenschow, D. H. and Spysers-Duran, P.: Measurement Techniques: Air Motion Sensing, NCAR, 1989.

- Lilly, D. K.: Models of cloud-topped mixed layers under a strong inversion, *Q. J. Roy. Meteor. Soc.*, 94, 292–309, <https://doi.org/10.1002/qj.49709440106>, 1968.
- Martucci, G., Milroy, C., and O’Dowd, C. D.: Detection of Cloud-Base Height Using Jenoptik CHM15K and Vaisala CL31 Ceilometers, *J. Atmos. Ocean. Tech.*, 27, 305–318, <https://doi.org/10.1175/2009jtecha1326.1>, 2010.
- Melchionna, S., Bauer, M., and Peters, G.: A new algorithm for the extraction of cloud parameters using multiplex analysis of cloud radar data – First application and preliminary results, *Meteorol. Z.*, 17, 613–620, <https://doi.org/10.1127/0941-2948/2008/0322>, 2008.
- Milroy, C., Martucci, G., Lolli, S., Loaec, S., Sauvage, L., Xueref-Remy, I., Lavric, J. V., Ciais, P., Feist, D. G., Biavati, G., and O’Dowd, C. D.: An Assessment of Pseudo-Operational Ground-Based Light Detection and Ranging Sensors to Determine the Boundary-Layer Structure in the Coastal Atmosphere, *Advances in Meteorology*, 2012, 929080, <https://doi.org/10.1155/2012/929080>, 2012.
- Neggens, R. A. J., Duyenkerke, P. G., Rodts, S. M. A., and Ams, A. M. S.: Shallow cumulus convection: a validation of large-eddy simulation against aircraft and Landsat observations, 15th Symposium on Boundary Layers and Turbulence, 199–202, <https://doi.org/10.1256/qj.02.93>, 2002.
- Nicholls, S. and Leighton, J.: An Observational Study of the Structure of Stratiform Cloud Sheets, 1. Structure, *Q. J. Roy. Meteor. Soc.*, 112, 431–460, <https://doi.org/10.1002/qj.49711247209>, 1986.
- Nicoll, K., Harrison, R. G., and Brus, D.: Optical cloud detection from a disposable airborne sensor, EGU General Assembly, Vienna Austria, 2016.
- Norton, E. G., Vaughan, G., Methven, J., Coe, H., Brooks, B., Gallagher, M., and Longley, I.: Boundary layer structure and decoupling from synoptic scale flow during NAMBLEX, *Atmos. Chem. Phys.*, 6, 433–445, <https://doi.org/10.5194/acp-6-433-2006>, 2006.
- O’Connor, T. C., Jennings, S. G., and O’Dowd, C. D.: Highlights of fifty years of atmospheric aerosol research at Mace Head, *Atmos. Res.*, 90, 338–355, <https://doi.org/10.1016/j.atmosres.2008.08.014>, 2008.
- O’Dowd, C., Ceburnis, D., Ovadnevaite, J., Vaishya, A., Rinaldi, M., and Facchini, M. C.: Do anthropogenic, continental or coastal aerosol sources impact on a marine aerosol signature at Mace Head?, *Atmos. Chem. Phys.*, 14, 10687–10704, <https://doi.org/10.5194/acp-14-10687-2014>, 2014.
- O’Dowd, C. D., Becker, E., and Kulmala, M.: Mid-latitude North-Atlantic aerosol characteristics in clean and polluted air, *Atmos. Res.*, 58, 167–185, [https://doi.org/10.1016/S0169-8095\(01\)00098-9](https://doi.org/10.1016/S0169-8095(01)00098-9), 2001.
- O’Dowd, C. D., Facchini, M. C., Cavalli, F., Ceburnis, D., Mircea, M., Decesari, S., Fuzzi, S., Yoon, Y. J., and Putaud, J. P.: Biogenically driven organic contribution to marine aerosol, *Nature*, 431, 676–680, <https://doi.org/10.1038/nature02959>, 2004.
- Painemal, D. and Zuidema, P.: Assessment of MODIS cloud effective radius and optical thickness retrievals over the Southeast Pacific with VOCALS-REx in situ measurements, *J. Geophys. Res.-Atmos.*, 116, D24206, <https://doi.org/10.1029/2011jd016155>, 2011.
- Paluch, I. R.: Entrainment Mechanism in Colorado Cumuli, *J. Atmos. Sci.*, 36, 2467–2478, [https://doi.org/10.1175/1520-0469\(1979\)036<2467:TEMICC>2.0.CO;2](https://doi.org/10.1175/1520-0469(1979)036<2467:TEMICC>2.0.CO;2), 1979.
- Petters, M. D. and Kreidenweis, S. M.: A single parameter representation of hygroscopic growth and cloud condensation nucleus activity, *Atmos. Chem. Phys.*, 7, 1961–1971, <https://doi.org/10.5194/acp-7-1961-2007>, 2007.
- Pinsky, M., Khain, A., Mazin, I., and Korolev, A.: Analytical estimation of droplet concentration at cloud base, *J. Geophys. Res.-Atmos.*, 117, D18211, <https://doi.org/10.1029/2012jd017753>, 2012.
- Pringle, K. J., Tost, H., Pozzer, A., Pöschl, U., and Lelieveld, J.: Global distribution of the effective aerosol hygroscopicity parameter for CCN activation, *Atmos. Chem. Phys.*, 10, 5241–5255, <https://doi.org/10.5194/acp-10-5241-2010>, 2010.
- Raatikainen, T., Nenes, A., Seinfeld, J. H., Morales, R., Moore, R. H., Latham, T. L., Lance, S., Padro, L. T., Lin, J. J., Cerully, K. M., Bougiatioti, A., Cozic, J., Ruehl, C. R., Chuang, P. Y., Anderson, B. E., Flagan, R. C., Jonsson, H., Mihalopoulos, N., and Smith, J. N.: Worldwide data sets constrain the water vapor uptake coefficient in cloud formation, *P. Natl. Acad. Sci. USA*, 110, 3760–3764, doi10.1073/pnas.1219591110, 2013.
- Raes, F., Bates, T., McGovern, F., and Van Liedekerke, M.: The 2nd Aerosol Characterization Experiment (ACE-2): general overview and main results, *Tellus B*, 52, 111–125, <https://doi.org/10.1034/j.1600-0889.2000.00124.x>, 2000.
- Reutter, P., Su, H., Trentmann, J., Simmel, M., Rose, D., Gunthe, S. S., Wernli, H., Andreae, M. O., and Pöschl, U.: Aerosol- and updraft-limited regimes of cloud droplet formation: influence of particle number, size and hygroscopicity on the activation of cloud condensation nuclei (CCN), *Atmos. Chem. Phys.*, 9, 7067–7080, <https://doi.org/10.5194/acp-9-7067-2009>, 2009.
- Rinaldi, M., Facchini, M. C., Decesari, S., Carbone, C., Finessi, E., Mircea, M., Fuzzi, S., Ceburnis, D., Ehn, M., Kulmala, M., de Leeuw, G., and O’Dowd, C. D.: On the representativeness of coastal aerosol studies to open ocean studies: Mace Head – a case study, *Atmos. Chem. Phys.*, 9, 9635–9646, <https://doi.org/10.5194/acp-9-9635-2009>, 2009.
- Roberts, G. C., Andreae, M. O., Zhou, J. C., and Artaxo, P.: Cloud condensation nuclei in the Amazon Basin: “Marine” conditions over a continent?, *Geophys. Res. Lett.*, 28, 2807–2810, <https://doi.org/10.1029/2000gl012585>, 2001.
- Roberts, G. C. and Nenes, A.: A continuous-flow stream-wise thermal-gradient CCN chamber for atmospheric measurements, *Aerosol Sci. Technol.*, 39, 206–221, <https://doi.org/10.1080/027868290913988>, 2005.
- Roberts, G. C., Ramana, M. V., Corrigan, C., Kim, D., and Ramanathan, V.: Simultaneous observations of aerosol-cloud-albedo interactions with three stacked unmanned aerial vehicles, *P. Natl. Acad. Sci. USA*, 105, 7370–7375, <https://doi.org/10.1073/pnas.0710308105>, 2008.
- Rosenfeld, D., Williams, E., Andreae, M. O., Freud, E., Pöschl, U., and Rennó, N. O.: The scientific basis for a satellite mission to retrieve CCN concentrations and their impacts on convective clouds, *Atmos. Meas. Tech.*, 5, 2039–2055, <https://doi.org/10.5194/amt-5-2039-2012>, 2012.
- Rosenfeld, D., Fischman, B., Zheng, Y., Goren, T., and Giguzin, D.: Combined satellite and radar retrievals of drop concentration and

- CCN at convective cloud base, *Geophys. Res. Lett.*, 41, 3259–3265, <https://doi.org/10.1002/2014gl059453>, 2014.
- Rosenfeld, D., Zheng, Y., Hashimshoni, E., Poehlker, M. L., Jefferson, A., Poehlker, C., Yu, X., Zhu, Y., Liu, G., Yue, Z., Fischman, B., Li, Z., Giguzin, D., Goren, T., Artaxo, P., Barbosa, H. M. J., Poeschl, U., and Andreae, M. O.: Satellite retrieval of cloud condensation nuclei concentrations by using clouds as CCN chambers, *P. Natl. Acad. Sci. USA*, 113, 5828–5834, <https://doi.org/10.1073/pnas.1514044113>, 2016.
- Russell, L. M., Lenschow, D. H., Laursen, K. K., Krummel, P. B., Siems, S. T., Bandy, A. R., Thornton, D. C., and Bates, T. S.: Bidirectional mixing in an ACE 1 marine boundary layer overlain by a second turbulent layer, *J. Geophys. Res.*, 103, 16411–16432, 1998.
- Russell, L. M. and Seinfeld, J. H.: Size- and composition-resolved externally mixed aerosol model, *Aerosol Sci. Technol.*, 28, 403–416, <https://doi.org/10.1080/02786829808965534>, 1998.
- Russell, L. M., Seinfeld, J. H., Flagan, R. C., Ferek, R. J., Hegg, D. A., Hobbs, P. V., Wobrock, W., Flossmann, A. I., O'Dowd, C. D., Nielsen, K. E., and Durkee, P. A.: Aerosol dynamics in ship tracks, *J. Geophys. Res.-Atmos.*, 104, 31077–31095, <https://doi.org/10.1029/1999jd900985>, 1999.
- Sanchez, K. J., Russell, L. M., Modini, R. L., Frossard, A. A., Ahlm, L., Corrigan, C. E., Roberts, G. C., Hawkins, L. N., Schroder, J. C., Bertram, A. K., Zhao, R., Lee, A. K. Y., Lin, J. J., Nenes, A., Wang, Z., Wonaschuetz, A., Sorooshian, A., Noone, K. J., Jonsson, H., Toom, D., Macdonald, A. M., Leitch, W. R., and Seinfeld, J. H.: Meteorological and aerosol effects on marine cloud microphysical properties, *J. Geophys. Res.-Atmos.*, 121, 4142–4161, <https://doi.org/10.1002/2015jd024595>, 2016.
- Schubert, W. H., Wakefield, J. S., Steiner, E. J., and Cox, S. K.: Marine stratocumulus convection, 1 governing equations and horizontally homogeneous solutions, *J. Atmos. Sci.*, 36, 1286–1307, [https://doi.org/10.1175/1520-0469\(1979\)036<1286:mscopy>2.0.co;2](https://doi.org/10.1175/1520-0469(1979)036<1286:mscopy>2.0.co;2), 1979.
- Sollazzo, M. J., Russell, L. M., Percival, D., Osborne, S., Wood, R., and Johnson, D. W.: Entrainment rates during ACE-2 Lagrangian experiments calculated from aircraft measurements, *Tellus B*, 52, 335–347, <https://doi.org/10.1034/j.1600-0889.2000.00010.x>, 2000.
- Stephens, G. L.: Radiation Profiles in Extended Water Clouds 2, Parameterization Schemes, *J. Atmos. Sci.*, 35, 2123–2132, [https://doi.org/10.1175/1520-0469\(1978\)035<2123:rpiewc>2.0.co;2](https://doi.org/10.1175/1520-0469(1978)035<2123:rpiewc>2.0.co;2), 1978.
- Stevens, B.: Entrainment in stratocumulus-topped mixed layers, *Q. J. Roy. Meteor. Soc.*, 128, 2663–2690, <https://doi.org/10.1256/qj.01.202>, 2002.
- Stull, R. B.: *An Introduction to Boundary Layer Meteorology*, Kluwer Academic, Dordrecht, 574–576, 1988.
- Turton, J. D. and Nicholls, S.: A Study of the Diurnal-Variation of Stratocumulus Using a Multiple Mixed Layer Model, *Q. J. Roy. Meteor. Soc.*, 113, 969–1009, <https://doi.org/10.1256/smsqj.47710>, 1987.
- Tzivion, S., Feingold, G., and Levin, Z.: An efficient numerical solution to the stochastic collection equation, *J. Atmos. Sci.*, 44, 3139–3149, [https://doi.org/10.1175/1520-0469\(1987\)044<3139:aenstt>2.0.co;2](https://doi.org/10.1175/1520-0469(1987)044<3139:aenstt>2.0.co;2), 1987.
- Wildmann, N., Ravi, S., and Bange, J.: Towards higher accuracy and better frequency response with standard multi-hole probes in turbulence measurement with remotely piloted aircraft (RPA), *Atmos. Meas. Tech.*, 7, 1027–1041, <https://doi.org/10.5194/amt-7-1027-2014>, 2014.
- Zhou, X., Kollias, P., and Lewis, E. R.: Clouds, Precipitation, and Marine Boundary Layer Structure during the MAGIC Field Campaign, *J. Climate*, 28, 2420–2442, <https://doi.org/10.1175/jcli-d-14-00320.1>, 2015.

Bibliography

- Albrecht, Bruce A. (1989). “Aerosols, cloud microphysics, and fractional cloudiness”. In: *Science* 245.4923, pp. 1227–1230. ISSN: 0036-8075.
- Altstädter, B. et al. (2015). “ALADINA – an unmanned research aircraft for observing vertical and horizontal distributions of ultrafine particles within the atmospheric boundary layer”. In: *Atmospheric Measurement Techniques* 8.4, pp. 1627–1639. DOI: 10.5194/amt-8-1627-2015.
- Anderson, J.D. (2001). *Fundamentals of Aerodynamics, third edition*. 1128 pp, ISBN13: 978-0071289085. McGraw-Hill.
- Ansmann, A., Fruntke, J., and Engelmann, R. (2010). “Updraft and downdraft characterization with Doppler lidar: cloud-free versus cumuli-topped mixed layer”. In: *Atmospheric Chemistry and Physics* 10.16, pp. 7845–7858. DOI: 10.5194/acp-10-7845-2010.
- Axford, D. N. (1968). “On the Accuracy of Wind Measurements Using an Inertial Platform in an Aircraft, and an Example of a Measurement of the Vertical Mesostructure of the Atmosphere”. In: *Journal of Applied Meteorology* 7.4, pp. 645–666. DOI: 10.1175/1520-0450(1968)007<0645:OTAOWM>2.0.CO;2.
- Bange, J., Spieß, T., and Kroonenberg, A. van den (2007). “Characteristics of the early-morning shallow convective boundary layer from Helipod Flights during STINHO-2”. In: *Theoretical and Applied Climatology* 90.1, pp. 113–126. ISSN: 1434-4483. DOI: 10.1007/s00704-006-0272-2.
- Båserud, L. et al. (2016). “Proof of concept for turbulence measurements with the RPAS SUMO during the BLLAST campaign”. In: *Atmospheric Measurement Techniques* 9.10, pp. 4901–4913. DOI: 10.5194/amt-9-4901-2016.
- Boiffier, J.L (1998). *The dynamics of flight, the equations*. ISBN 0 471 94237 5. John Wiley and Sons.
- Boucher, O. et al. (2013). “Clouds and Aerosols Supplementary Material”. In: *Climate Change 2013: The Physical Science Basis. Contribution of Working Group I to the Fifth Assessment Report of the Intergovernmental Panel on Climate Change [Stocker, T.F., D. Qin, G.-K. Plattner, M. Tignor, S.K. Allen, J. Boschung, A. Nauels, Y. Xia, V. Bex and P.M. Midgley (eds.)]* URL: www.climatechange2013.org.
- Brisset, Pascal et al. (2006). “The Paparazzi Solution”. In: pp xxxx. URL: <https://hal-enac.archives-ouvertes.fr/hal-01004157>.
- Brown, E. N., Friehe, C. A., and Lenschow, D. H. (1983). “The Use of Pressure Fluctuations on the Nose of an Aircraft for Measuring Air Motion”. In: *Journal of Climate and Applied Meteorology* 22.1, pp. 171–180. DOI: 10.1175/1520-0450(1983)022<0171:TUOPFO>2.0.CO;2.
- Bühl, J. et al. (2015). “Combined vertical-velocity observations with Doppler lidar, cloud radar and wind profiler”. In: *Atmospheric Measurement Techniques* 8.8, pp. 3527–3536. DOI: 10.5194/amt-8-3527-2015.

- Bunker, A. F. (1955). “Turbulence and shearing stresses measured over the North Atlantic ocean by an airplane-acceleration technique”. In: *Journal of Meteorology* 12.5, pp. 445–455. DOI: 10.1175/1520-0469(1955)012<0445:TASSMO>2.0.CO;2.
- Calmer, R. et al. (2018). “Vertical wind velocity measurements using a five-hole probe with remotely piloted aircraft to study aerosol–cloud interactions”. In: *Atmospheric Measurement Techniques* 11.5, pp. 2583–2599. DOI: 10.5194/amt-11-2583-2018. URL: <https://www.atmos-meas-tech.net/11/2583/2018/>.
- Canut, G. et al. (2016). “Turbulence fluxes and variances measured with a sonic anemometer mounted on a tethered balloon”. In: *Atmospheric Measurement Techniques* 9.9, pp. 4375–4386. DOI: 10.5194/amt-9-4375-2016.
- Conant, W. C. et al. (2004). “Aerosol–cloud drop concentration closure in warm cumulus”. In: *Journal of Geophysical Research: Atmospheres* 109.D13. D13204, n/a–n/a. ISSN: 2156-2202. DOI: 10.1029/2003JD004324.
- Corrigan, C. E. et al. (2007). “Capturing vertical profiles of aerosols and black carbon over the Indian Ocean using autonomous unmanned aerial vehicles”. In: *Atmospheric Chemistry and Physics Discussions* 7.4, pp. 11429–11463. URL: <https://hal.archives-ouvertes.fr/hal-00303026>.
- Corsmeier, Ulrich, Hankers, Rudolf, and Wieser, Andreas (2001). “Airborne turbulence measurements in the lower troposphere onboard the research aircraft Dornier 128-6, D-IBUF”. In: *Meteorologische Zeitschrift* 10.4, pp. 315–329. ISSN: 0941-2948. DOI: doi:10.1127/0941-2948/2001/0010-0315.
- Couvreux, F. et al. (2016). “Boundary-layer turbulent processes and mesoscale variability represented by numerical weather prediction models during the BLLAST campaign”. In: *Atmos. Chem. Phys.*, 16, 8983-9002. DOI: 10.5194/acp-16-8983-2016.
- Crawford, Timothy L. and Dobosy, Ronald J. (1992). “A sensitive fast-response probe to measure turbulence and heat flux from any airplane”. In: *Boundary-Layer Meteorology* 59.3, pp. 257–278. ISSN: 1573-1472. DOI: 10.1007/BF00119816.
- Crumeyrolle, S. et al. (2010). “New particle formation events measured on board the ATR-42 aircraft during the EUCAARI campaign”. In: *Atmospheric Chemistry and Physics* 10.14, pp. 6721–6735. DOI: 10.5194/acp-10-6721-2010. URL: <https://hal-insu.archives-ouvertes.fr/insu-00554263>.
- Ditas, F. et al. (2012). “Aerosols-cloud microphysics-thermodynamics-turbulence: evaluating supersaturation in a marine stratocumulus cloud”. In: *Atmospheric Chemistry and Physics* 12.5, pp. 2459–2468. DOI: 10.5194/acp-12-2459-2012.
- Drüe, Clemens and Heinemann, Günther (2013). “A Review and Practical Guide to In-Flight Calibration for Aircraft Turbulence Sensors”. In: *Journal of Atmospheric and Oceanic Technology* 30.12, pp. 2820–2837. DOI: 10.1175/JTECH-D-12-00103.1.
- Elston, Jack et al. (2015). “Overview of Small Fixed-Wing Unmanned Aircraft for Meteorological Sampling”. In: *Journal of Atmospheric and Oceanic Technology* 32.1, pp. 97–115. DOI: 10.1175/JTECH-D-13-00236.1.
- Fountoukis, Christos et al. (2007). “Aerosol–cloud drop concentration closure for clouds sampled during the International Consortium for Atmospheric Research on Transport and Transformation

- 2004 campaign”. In: *Journal of Geophysical Research: Atmospheres* 112.D10. D10S30, n/a–n/a. ISSN: 2156-2202. DOI: 10.1029/2006JD007272.
- Garman, K. E. et al. (2006). “An Airborne and Wind Tunnel Evaluation of a Wind Turbulence Measurement System for Aircraft-Based Flux Measurements”. In: *Journal of Atmospheric and Oceanic Technology* 23.12, pp. 1696–1708. DOI: 10.1175/JTECH1940.1.
- Görsdorf, Ulrich et al. (2015). “A 35-GHz Polarimetric Doppler Radar for Long-Term Observations of Cloud Parameters—Description of System and Data Processing”. In: *Journal of Atmospheric and Oceanic Technology* 32.4, pp. 675–690. DOI: 10.1175/JTECH-D-14-00066.1.
- Hacker, J.M. and Crawford, T. (1999). “The BAT-probe: the ultimate tool to measure turbulence from any kind of aircraft (or sailplane)”. In: *Technical soaring*.
- Hoppel, W. A. et al. (1990). “Aerosol size distributions and optical properties found in the marine boundary layer over the Atlantic Ocean”. In: *Journal of Geophysical Research: Atmospheres* 95.D4, pp. 3659–3686. ISSN: 2156-2202. DOI: 10.1029/JD095iD04p03659.
- Hsieh, W.C. et al. (2009). *Parameterization of cloud droplet size distributions: comparison with parcel models and observations*. DOI: 10.1029/2008JD011387.
- Hudson, James G., Noble, Stephen, and Tabor, Samantha (2015). “Cloud supersaturations from CCN spectra Hoppel minima”. In: *Journal of Geophysical Research: Atmospheres* 120.8. 2014JD022669, pp. 3436–3452. ISSN: 2169-8996. DOI: 10.1002/2014JD022669.
- Jacobson, Mark Z. et al. (1994). “Modeling coagulation among particles of different composition and size”. In: *Atmospheric Environment* 28.7, pp. 1327–1338. ISSN: 1352-2310. DOI: [https://doi.org/10.1016/1352-2310\(94\)90280-1](https://doi.org/10.1016/1352-2310(94)90280-1).
- Jones, R. F. (1954). “Five flights through a thunderstorm belt”. In: *Quarterly Journal of the Royal Meteorological Society* 80.345, pp. 377–387. DOI: 10.1002/qj.49708034507.
- Khelif, D., Burns, S. P., and Friehe, C. A. (1999). “Improved Wind Measurements on Research Aircraft”. In: *Journal of Atmospheric and Oceanic Technology* 16.7, pp. 860–875. DOI: 10.1175/1520-0426(1999)016<0860:IWMORA>2.0.CO;2.
- Kroonenberg, Aline van den et al. (2008). “Measuring the Wind Vector Using the Autonomous Mini Aerial Vehicle M2AV”. In: *Journal of Atmospheric and Oceanic Technology* 25.11, pp. 1969–1982. DOI: 10.1175/2008JTECHA1114.1.
- Kulmala, M. et al. (2011). “General overview: European Integrated project on Aerosol Cloud Climate and Air Quality interactions (EUCAARI); integrating aerosol research from nano to global scales”. In: *Atmospheric Chemistry and Physics* 11.24, pp. 13061–13143. DOI: 10.5194/acp-11-13061-2011.
- Kunz, G.J. and Leeuw, G. de (2000). “Micrometeorological characterisation of the Mace Head field station during PARFORCE, in New Particle Formation and Fate in the Coastal Environment”. In: *Rep. Ser. in Aerosol Sci., edited by C. D. O’Dowd and K. Hämeri* vol.48.
- Lampert, A. et al. (2016). “A study of local turbulence and anisotropy during the afternoon and evening transition with an unmanned aerial system and mesoscale simulation”. In: *Atmospheric Chemistry and Physics* 16.12, pp. 8009–8021. DOI: 10.5194/acp-16-8009-2016.

- Lawson, R. Paul (1979). "A System for Airborne Measurement of Vertical Air Velocity". In: *Journal of Applied Meteorology* 18.10, pp. 1363–1368. DOI: 10.1175/1520-0450(1979)018<1363:ASFAM0>2.0.CO;2.
- Lenschow, D. H. (1971). "Vanes for Sensing Incidence Angles of the Air from an Aircraft". In: *Journal of Applied Meteorology* 10.6, pp. 1339–1343. DOI: 10.1175/1520-0450(1971)010<1339:VFSIA0>2.0.CO;2.
- (1974). "Model of the Height Variation of the Turbulence Kinetic Energy Budget in the Unstable Planetary Boundary Layer". In: *Journal of the Atmospheric Sciences* 31.2, pp. 465–474. DOI: 10.1175/1520-0469(1974)031<0465:M0THV0>2.0.CO;2.
- Lenschow, D. H., Wyngaard, J. C., and Pennell, W. T. (1980). "Mean-Field and Second-Moment Budgets in a Baroclinic, Convective Boundary Layer". In: *Journal of the Atmospheric Sciences* 37.6, pp. 1313–1326. DOI: 10.1175/1520-0469(1980)037<1313:MFASMB>2.0.CO;2.
- Lenschow, D.H. (1972). "The measurement of air velocity and temperature using the NCAR Buffalo aircraft measuring system". In: *Technical Note T N /S T R -7 J , NCAR, Boulder, Colo.* DOI: 10.5065/D6C8277W.
- Lenschow, D.H. and Spyers-Duran, P. (1989). "Measurement Techniques : Air motion sensing". In: *National Center for Atmospheric Research, Bulletin No.23.* URL: <https://www.eol.ucar.edu/raf/Bulletins/bulletin23.html>.
- Lohmann, U. and Feichter, J. (2004). "Global indirect aerosol effects: a review". In: *Atmospheric Chemistry and Physics Discussions* 4.6, pp. 7561–7614.
- Lothon, M. et al. (2005). "Turbulence measurements in marine stratocumulus with airborne Doppler radar". In: *Quarterly Journal of the Royal Meteorological Society* 131.609, pp. 2063–2080. ISSN: 1477-870X. DOI: 10.1256/qj.04.131.
- Lothon, M. et al. (2014). "The BLLAST field experiment: Boundary-Layer Late Afternoon and Sunset Turbulence". In: *Atmospheric Chemistry and Physics* 14.20, pp. 10931–10960. DOI: 10.5194/acp-14-10931-2014.
- Lu, Miao-Ling et al. (2007). "The Marine Stratus/Stratocumulus Experiment (MASE): Aerosol-cloud relationships in marine stratocumulus". In: *Journal of Geophysical Research: Atmospheres* 112.D10. D10209, n/a–n/a. ISSN: 2156-2202. DOI: 10.1029/2006JD007985.
- Martin, S., Bange, J., and Beyrich, F. (2011). "Meteorological profiling of the lower troposphere using the research UAV "M²AV Carolo"". In: *Atmospheric Measurement Techniques* 4.4, pp. 705–716. DOI: 10.5194/amt-4-705-2011.
- Martin, Sabrina, Beyrich, Frank, and Bange, Jens (2014). "Observing Entrainment Processes Using a Small Unmanned Aerial Vehicle: A Feasibility Study". In: *Boundary-Layer Meteorology* 150.3, pp. 449–467. ISSN: 1573-1472. DOI: 10.1007/s10546-013-9880-4.
- Morales, R. and Nenes, A. (2010). "Characteristic updrafts for computing distribution-averaged cloud droplet number and stratocumulus cloud properties". In: *Journal of Geophysical Research: Atmospheres* 115.D18. D18220, n/a–n/a. ISSN: 2156-2202. DOI: 10.1029/2009JD013233.
- Morales-Betancourt, R. and A.Nenes (2014). "Understanding the contributions of aerosol properties and parameterization discrepancies to droplet number variability in a global climate model". In: *Atmos. Chem. Phys.* DOI: 10.5194/acp-14-4809-2014.

- Nenes, Athanasios and Seinfeld, John H. (2003). “Parameterization of cloud droplet formation in global climate models”. In: *Journal of Geophysical Research: Atmospheres* 108.D14. 4415, n/a–n/a. ISSN: 2156-2202. DOI: 10.1029/2002JD002911.
- Peng, Yiran, Lohmann, Ulrike, and Leitch, Richard (2005). “Importance of vertical velocity variations in the cloud droplet nucleation process of marine stratus clouds”. In: *Journal of Geophysical Research: Atmospheres* 110.D21. D21213, n/a–n/a. ISSN: 2156-2202. DOI: 10.1029/2004JD004922.
- Petters, M. D. and Kreidenweis, S. M. (2007). “A single parameter representation of hygroscopic growth and cloud condensation nucleus activity”. In: *Atmospheric Chemistry and Physics* 7.8, pp. 1961–1971. DOI: 10.5194/acp-7-1961-2007.
- Ramana, M. V. et al. (2007). “Albedo, atmospheric solar absorption and heating rate measurements with stacked UAVs”. In: *Quarterly Journal of the Royal Meteorological Society* 133.629, pp. 1913–1931. ISSN: 1477-870X. DOI: 10.1002/qj.172.
- Ramanathan, Veerabhadran et al. (2007). “Warming trends in Asia amplified by brown cloud solar absorption”. In: *Nature* 448.7153, 575–578. ISSN: 0028-0836. DOI: 10.1038/nature06019.
- Rauber, Robert M. et al. (2007). “Rain in Shallow Cumulus Over the Ocean: The RICO Campaign”. In: *Bulletin of the American Meteorological Society* 88.12, pp. 1912–1928. DOI: 10.1175/BAMS-88-12-1912. URL: <https://doi.org/10.1175/BAMS-88-12-1912>.
- Reineman, Benjamin D. et al. (2013). “Development and Testing of Instrumentation for UAV-Based Flux Measurements within Terrestrial and Marine Atmospheric Boundary Layers”. In: *Journal of Atmospheric and Oceanic Technology* 30.7, pp. 1295–1319. DOI: 10.1175/JTECH-D-12-00176.1.
- Reuder, J et al. (2008). “SUMO: A small unmanned meteorological observer for atmospheric boundary layer research”. In: *IOP Conference Series: Earth and Environmental Science* 1.1, p. 012014. DOI: 10.1088/1755-1307/1/1/012014.
- Reuder, J. et al. (2016). “Exploring the potential of the RPA system SUMO for multipurpose boundary-layer missions during the BLLAST campaign”. In: *Atmospheric Measurement Techniques* 9.6, pp. 2675–2688. DOI: 10.5194/amt-9-2675-2016.
- Reuder, Joachim et al. (2012). “FLOHOF 2007: an overview of the mesoscale meteorological field campaign at Hofsjökull, Central Iceland”. In: *Meteorology and Atmospheric Physics* 116.1, pp. 1–13. ISSN: 1436-5065. DOI: 10.1007/s00703-010-0118-.
- Reutter, P. et al. (2009). “Aerosol- and updraft-limited regimes of cloud droplet formation: influence of particle number, size and hygroscopicity on the activation of cloud condensation nuclei (CCN)”. In: *Atmospheric Chemistry and Physics* 9.18, pp. 7067–7080. DOI: 10.5194/acp-9-7067-2009.
- Roberts, G. C. and Nenes, A. (2005). “A Continuous-Flow Streamwise Thermal-Gradient CCN Chamber for Atmospheric Measurements”. In: *Aerosol Science and Technology* 39.3, pp. 206–221. DOI: 10.1080/027868290913988.
- Roberts, G. C. et al. (2008). “Simultaneous observations of aerosol-cloud-albedo interactions with three stacked unmanned aerial vehicles”. In: *Proceedings of the National Academy of Science* 105, pp. 7370–7375. DOI: 10.1073/pnas.0710308105.
- Russell, Lynn M. and Seinfeld, John H. (1998). “Size- and Composition-Resolved Externally Mixed Aerosol Model”. In: *Aerosol Science and Technology* 28.5, pp. 403–416. DOI: 10.1080/02786829808965534.

- Russell, Lynn M. et al. (1999). "Aerosol dynamics in ship tracks". In: *Journal of Geophysical Research: Atmospheres* 104.D24, pp. 31077–31095. ISSN: 2156-2202. DOI: 10.1029/1999JD900985.
- Sanchez, K. J. et al. (2016). "Meteorological and aerosol effects on marine cloud microphysical properties". In: *Journal of Geophysical Research: Atmospheres* 121.8, pp. 4142–4161. ISSN: 2169-897X. DOI: 10.1002/2015JD024595.
- Sanchez, K.J. et al. (2017). "Top-down and bottom-up aerosol-cloud-closure: towards understanding sources of uncertainty in deriving cloud radiative forcing". In: *Atmos. Chem. Phys.* DOI: 10.5194/acp-2017-201, 2017.
- Schmidt, J. et al. (2015). "Strong aerosol–cloud interaction in altocumulus during updraft periods: lidar observations over central Europe". In: *Atmospheric Chemistry and Physics* 15.18, pp. 10687–10700. DOI: 10.5194/acp-15-10687-2015.
- Seinfeld, J.H. and Pandis, S.N. (2006). *Atmospheric chemistry and physics, from air pollution to climate change*. ISBN 978-0-471-72018-8. John Wiley and Sons.
- Siebert, H. et al. (2013). "The fine-scale structure of the trade wind cumuli over Barbados; an introduction to the CARRIBA project". In: *Atmospheric Chemistry and Physics* 13.19, pp. 10061–10077. DOI: 10.5194/acp-13-10061-2013.
- Siebert, Holger et al. (2006). "Probing Finescale Dynamics and Microphysics of Clouds with Helicopter-Borne Measurements". In: *Bulletin of the American Meteorological Society* 87.12, pp. 1727–1738. DOI: 10.1175/BAMS-87-12-1727.
- Snider, Jefferson R. et al. (2003). "Aerosol activation in marine stratocumulus clouds: 2. Köhler and parcel theory closure studies". In: *Journal of Geophysical Research: Atmospheres* 108.D15. 8629, n/a–n/a. ISSN: 2156-2202. DOI: 10.1029/2002JD002692. URL: <http://dx.doi.org/10.1029/2002JD002692>.
- Spiess, Thomas et al. (2007). "First application of the meteorological Mini-UAV 'M2AV'". In: *Meteorologische Zeitschrift* 16.2, pp. 159–169. DOI: 10.1127/0941-2948/2007/0195.
- Stein, A. F. et al. (2015). "NOAA's HYSPLIT Atmospheric Transport and Dispersion Modeling System". In: *Bulletin of the American Meteorological Society* 96.12, pp. 2059–2077. DOI: 10.1175/BAMS-D-14-00110.1. eprint: <https://doi.org/10.1175/BAMS-D-14-00110.1>. URL: <https://doi.org/10.1175/BAMS-D-14-00110.1>.
- Sullivan, Sylvia C. et al. (2016). "Role of updraft velocity in temporal variability of global cloud hydrometeor number". In: *Proceedings of the National Academy of Sciences* 113.21, pp. 5791–5796. DOI: 10.1073/pnas.1514039113.
- Telpord, J. W. and Warner, J. (1962). "On the Measurement from an Aircraft of Buoyancy and Vertical Air Velocity in Cloud." In: *Journal of Atmospheric Sciences* 19, pp. 415–423. DOI: 10.1175/1520-0469(1962)019<0415:OTMFAA>2.0.CO;2.
- Thomas, R. M. et al. (2012). "Measurement of turbulent water vapor fluxes using a lightweight unmanned aerial vehicle system". In: *Atmospheric Measurement Techniques* 5.1, pp. 243–257. DOI: 10.5194/amt-5-243-2012.
- Treaster, A. L. and Yocum, A. M. (1978). "The calibration and application of five-hole probes". In: *NASA STI/Recon Technical Report N 78*.

- Twomey, S. (1974). "Pollution and the planetary albedo". In: *Atmospheric Environment (1967)* 8.12, pp. 1251–1256. ISSN: 0004-6981. DOI: [http://dx.doi.org/10.1016/0004-6981\(74\)90004-3](http://dx.doi.org/10.1016/0004-6981(74)90004-3).
- Werner, F. et al. (2014). "Twomey effect observed from collocated microphysical and remote sensing measurements over shallow cumulus". In: *Journal of Geophysical Research: Atmospheres* 119.3, pp. 1534–1545. ISSN: 2169-8996. DOI: [10.1002/2013JD020131](https://doi.org/10.1002/2013JD020131).
- Wildmann, N., Mauz, M., and Bange, J. (2013). "Two fast temperature sensors for probing of the atmospheric boundary layer using small remotely piloted aircraft (RPA)". In: *Atmospheric Measurement Techniques* 6.8, pp. 2101–2113. DOI: [10.5194/amt-6-2101-2013](https://doi.org/10.5194/amt-6-2101-2013).
- Wildmann, N., Ravi, S., and Bange, J. (2014). "Towards higher accuracy and better frequency response with standard multi-hole probes in turbulence measurement with remotely piloted aircraft (RPA)". In: *Atmospheric Measurement Techniques* 7.4, pp. 1027–1041. DOI: [10.5194/amt-7-1027-2014](https://doi.org/10.5194/amt-7-1027-2014).
- Wildmann, Norman, Rau, Gerrit Anke, and Bange, Jens (2015). "Observations of the Early Morning Boundary-Layer Transition with Small Remotely-Piloted Aircraft". In: *Boundary-Layer Meteorology* 157.3, pp. 345–373. ISSN: 1573-1472. DOI: [10.1007/s10546-015-0059-z](https://doi.org/10.1007/s10546-015-0059-z).
- Wyngaard, J. C. and Coté, O. R. (1971). "The Budgets of Turbulent Kinetic Energy and Temperature Variance in the Atmospheric Surface Layer". In: *Journal of the Atmospheric Sciences* 28.2, pp. 190–201. DOI: [10.1175/1520-0469\(1971\)028<0190:TBOTKE>2.0.CO;2](https://doi.org/10.1175/1520-0469(1971)028<0190:TBOTKE>2.0.CO;2).